DOT/FAA/TC-13/36,V3

Federal Aviation Administration
William J. Hughes Technical Center
Aviation Research Division
Atlantic City International Airport
New Jersey 08405

Analytical Tools for Residual Stress Enhancement of Rotorcraft Damage Tolerance

Volume 3: Residual Stress Measurements, Crack Growth Testing, and Linear Elastic Fracture Mechanics Analyses

April 2015

Final Report

This document is available to the U.S. public through the National Technical Information Services (NTIS), Springfield, Virginia 22161.

This document is also available from the Federal Aviation Administration William J. Hughes Technical Center at actlibrary.tc.faa.gov.

U.S. Department of Transportation
Federal Aviation Administration

NOTICE

This document is disseminated under the sponsorship of the U.S. Department of Transportation in the interest of information exchange. The U.S. Government assumes no liability for the contents or use thereof. The U.S. Government does not endorse products or manufacturers. Trade or manufacturers' names appear herein solely because they are considered essential to the objective of this report. The findings and conclusions in this report are those of the author(s) and do not necessarily represent the views of the funding agency. This document does not constitute FAA policy. Consult the FAA sponsoring organization listed on the Technical Documentation page as to its use.

This report is available at the Federal Aviation Administration William J. Hughes Technical Center's Full-Text Technical Reports page: actlibrary.tc.faa.gov in Adobe Acrobat portable document format (PDF).

Technical Report Documentation Page

1. Report No.	2. Government Accession No.	3. Recipient's Catalog No.
DOT/FAA/TC-13/36,V3		

4. Title and Subtitle	5. Report Date
ANALYTICAL TOOLS FOR RESIDUAL STRESS ENHANCEMENT OF ROTORCRAFT DAMAGE TOLERANCE VOLUME 3: RESIDUAL STRESS MEASUREMENTS, CRACK GROWTH TESTING, AND LINEAR ELASTIC FRACTURE MECHANICS ANALYSES	April 2015
	6. Performing Organization Code Hill Engineering
7. Author(s) Michael R. Hill, John E. Van Dalen, Daniel H. Stuart, and John R. Minotti, Jr.	8. Performing Organization Report No.
9. Performing Organization Name and Address Hill Engineering, LLC 3035 Prospect Park Drive, Suite 180 Rancho Cordova CA 95670	10. Work Unit No. (TRAIS)
	11. Contract or Grant No. DTFACT-06-C-00025
12. Sponsoring Agency Name and Address U.S. Department of Transportation Federal Aviation Administration Southwest Region-Aircraft Rotorcraft Directorate- Certification Service 2601 Meacham Boulevard Fort Worth, TX 76137	13. Type of Report and Period Covered Final Report
	14. Sponsoring Agency Code ASW-112

15. Supplementary Notes

The Federal Aviation Administration William J. Hughes Technical Center Aviation Research Division COR was Traci Stadtmueller.

16. Abstract

This work develops laboratory data essential to understanding the ability to correlate the growth of one-dimensional (1D) and two-dimensional (2D) fatigue cracks in residual stress-bearing structures, which is a critical gap in current approaches to damage-tolerant design of rotorcraft. Fatigue crack growth tests were carried out in a range of coupons that progressed from very simple to fairly complex. Companion linear elastic fracture mechanics (LEFM) analyses were used to correlate their behavior. The coupon geometries were: 1D cracks in standard compact tension coupons, 1D and 2D cracks in coupons with open holes, 1D cracks in coupons with pin-loaded holes, and 2D cracks at fastener holes in nested-angle coupons with a lap shear joint. Most testing series were performed under constant amplitude cyclic loading, but additional tests of pin-loaded hole and nested-angle coupons were performed under variable-amplitude loading. Each series of tests employed a number of identical coupons (replicate tests) as well as coupons in at least two material conditions: an as-machined (AM) condition (without residual stress) and a residual stress-bearing condition. Tests in compact tension coupons had residual stress induced by laser shock peening and all other tests had residual stress induced by cold hole expansion. Care was taken in the experimental work to accurately: control the test setup to ensure growth of a single crack, determine residual stress fields, measure crack growth, and determine the observed fatigue crack growth rate (FCGR). Replicate tests provided measures of variability in residual stress and fatigue crack growth. In the companion LEFM analyses, care was taken to accurately develop stress intensity factors (SIFs), superpose applied and residual SIFs, and determine the predicted FCGR from the range of SIF ΔK and stress ratio R. Observed crack growth data for 1D cracks were consistent with LEFM predictions for both the AM and residual stress-bearing conditions, though the degree of agreement depended on the applied stress ratio. Variability in observed crack growth behavior was consistent with the variability in measured residual stress. Observed crack growth data from coupons with 2D cracks at an open hole were consistent with LEFM predictions for the AM condition, but not for the residual stress-bearing condition, where the LEFM predictions assumed a quarter-elliptical crack shape. Observed crack size data suggested that crack shape in AM coupons was quarter-elliptical, but in residual stress-bearing coupons was not. The inability to predict the growth of 2D cracks in the residual stress-bearing coupons may, therefore, be due to the lack of appropriate SIFs for the residual stress-bearing condition (for which cracks were not quarter-elliptical).

17. Key Words	18. Distribution Statement
Fatigue, Crack growth, Residual stress, Laser peening, Cold hole expansion, Stress intensity factor	This document is available to the U.S. public through the National Technical Information Service (NTIS), Springfield, Virginia 22161. This document is also available from the Federal Aviation Administration William J. Hughes Technical Center at actlibrary.tc.faa.gov.

19. Security Classif. (of this report)	20. Security Classif. (of this page)	21. No. of Pages	22. Price
Unclassified	Unclassified	164	

Form DOT F 1700.7 (8-72) Reproduction of completed page authorized

ACKNOWLEDGEMENTS

The authors acknowledge George Schneider (a Sikorsky retiree who passed away during the early phases of this research) for his vision in scoping this program. If the reader finds this report useful, please consider it an honor to his memory and a part of his legacy.

We would like to thank the partners in this work: the Federal Aviation Administration for sponsorship; Steve Gould and Michael Urban at Sikorsky Aircraft for providing test coupons and industrial experience; and Professor Jim Newman Jr. and his team at Mississippi State University for assisting in the data analysis.

TABLE OF CONTENTS

		Page
EXECUTIVE SUMMARY		xxii
1.	INTRODUCTION	1
1.1	Background	1
1.2	Project Scope	2
2.	THE 1D CRACK GROWTH IN RESIDUAL STRESS-BEARING COMPACT TENSION COUPONS	2
2.1	Introduction	2
2.2	Methods	3
2.3	Results	6
2.4	Discussion	8
2.5	Summary	10
2.6	Tables	10
2.7	Figures	12
3.	THE 1D CRACK GROWTH AT COLD-EXPANDED OPEN HOLES	22
3.1	Introduction	22
3.2	Methods	24
3.2.1	Coupon Geometry and Material	24
3.2.2	Residual Stress Measurement	24
3.2.3	Fatigue Testing	25
3.2.4	Crack Length Measurement	25
3.3	Results	30
3.3.1	Residual Stress Measurements	30
3.3.2	Crack Length Measurement Method	31
3.3.3	Observed and Predicted Crack Growth Behavior	31
3.4	Discussion	33
3.4.1	Correlation of Observed and Predicted Lifetime Variability	33
3.4.2	Prediction Verification	33
3.4.3	Crack Growth Rate Correlation	33
3.4.4	Methodological Complications	34
3.5	Summary	34

3.6 Tables 35
3.7 Figures 36

4. THE 2D CRACK GROWTH AT COLD-EXPANDED OPEN HOLES 45

4.1 Introduction 45
4.2 Methods 47

4.2.1 Coupon Geometry and Material 47
4.2.2 Residual Stress Measurement 47
4.2.3 Fatigue Testing 47
4.2.4 Crack Length Measurement 48

4.3 Results 51

4.3.1 Residual Stress Measurements 51
4.3.2 Crack Length Measurement Methods 52
4.3.3 Observed and Predicted Crack Growth Behavior 52

4.4 Discussion 55

4.4.1 Crack Length Measurements 55
4.4.2 Prediction Verification 56
4.4.3 The SIF Formulation 56

4.5 Summary 56
4.6 Tables 57
4.7 Figures 58

5. THE 1D CRACK GROWTH AT COLD-EXPANDED LOADED HOLES UNDER CONSTANT AMPLITUDE LOADING 72

5.1 Introduction 72
5.2 Methods 72

5.2.1 Material 72
5.2.2 Geometry 72
5.2.3 Hole Preparation 73
5.2.4 Residual Stress Fields 73
5.2.5 Test Matrix 73
5.2.6 Crack Growth Testing 73
5.2.7 Load Level Determination 74
5.2.8 Test Frame Calibration 74
5.2.9 Data Collection Instrumentation 75
5.2.10 Data Collection 75
5.2.11 Post-Test Measurements 75
5.2.12 DCPD Correlation 75

5.2.13 Crack Growth Predictions 76

5.3 Results 77

5.3.1 Fatigue Crack Growth Predictions 77
5.3.2 Fatigue Crack Growth Test Data Compared to LEFM Predictions 77

5.4 Discussion 78

5.4.1 Correlation Between Observed and Predicted Behavior 78
5.4.2 Methodological Difficulties 79

5.5 Tables 80
5.6 Figures 82

6. THE 1D CRACK GROWTH AT COLD-EXPANDED LOADED HOLES UNDER VARIABLE AMPLITUDE LOADING 89

6.1 Introduction 89
6.2 Methods 89

6.2.1 Block Loading Program 89

6.2.2 Coupon Preparation 90

6.2.3 Test Equipment and Calibration 90

6.2.4 Data Collection 91

6.2.5 The FCGR Calculation 91

6.2.6 Test Matrix 91

6.2.7 The LEFM Predictions of Crack Growth Under Variable Amplitude Loading 91

6.2.8 Tuning the MGWM Model to Test Data 93

6.3 Results 93
6.4 Discussion 94

6.4.1 Correlation Between Observed and Predicted Loaded Hole Crack Growth 94

6.4.2 Effects of Load Interaction 95

6.4.3 Underload Calculation 95

6.4.4 Loaded Hole Fatigue Performance With and Without CX 95

6.5 Tables 96
6.6 Figures 98

7. CRACK GROWTH IN NESTED ANGLES UNDER ALTERNATING CONSTANT AMPLITUDE BLOCK LOADING AND VARIABLE AMPLITUDE LOADING 101

7.1 Introduction 101
7.2 Methods 101

7.2.1 Material 101
7.2.2 Geometry 102
7.2.3 Fastener Hole Manufacturing 102
7.2.4 Residual Stress Measurement 102
7.2.5 Initial Notch 102
7.2.6 Coupon Assembly 103
7.2.7 Grips 103
7.2.8 Fatigue Loading 103
7.2.9 Load Frame Alignment and Calibration 103
7.2.10 Test Matrix 104
7.2.11 Initial Load Levels 105
7.2.12 Fatigue Testing 105
7.2.13 In-Situ Surface Crack Size Measurement 105
7.2.14 Post-test Through-thickness Crack Size Measurement 106
7.2.15 Fatigue Crack Growth Rate Calculations 106
7.2.16 Data Verification 106

7.3 Results 106

7.3.1 Residual Stress Measurements 106
7.3.2 Crack Growth Under Alternating Constant Amplitude Loading 107
7.3.3 Crack Growth Under Variable Amplitude Loading 109

7.4 Discussion 110

7.4.1 The AM Versus CX Test Results 110
7.4.2 Photogrammetric Measurement of Marker Bands 111
7.4.3 Methodological Difficulties 111
7.4.4 Difference Between Test Results and Field Observations 112

7.5 Tables 112
7.6 Figures 115

8. CONCLUSION 127

9. REFERENCES 128

APPENDIX

A—Determination of Loads Applied to the Nested-Angle Coupon for Alignment and Static and Dynamic Calibration

LIST OF FIGURES

Figure		Page
1	The *da/dN* for Clad 7075-T6, 0.090-Inch Thick Sheet, Lab Air	12
2	The 7075-T6 C(T) Coupon	12
3	Contour Measurement Results Illustrating the Residual Stress Distribution on the Plane of the Crack for AM and LSP-3N Coupons	13
4	Through-Thickness Average Stress for AM and LSP-3N Coupons Computed From Contour Results	13
5	The K_{RS} as a Function of Crack Length	14
6	The *a* vs. *N* and *da/dN* vs. ΔK_{app} for an AM Coupon Tested With Constant $P_{\max}$ = 0.98 kN and R = 0.1	14
7	The *a* vs. *N* and *da/dN* vs. *a* for an LSP Coupon Tested With Constant $P_{\max}$ = 2.22 kN and R = 0.1	15
8	The *a* vs. *N* and *da/dN* vs. *a* for an AM Coupon Tested With Constant ΔK_{app} and R_{app} = 0.1	15
9	The *a* vs. *N* and *da/dN* vs. *a* for LSP Coupons Tested With Constant ΔK_{app} and R_{app} = 0.1	16
10	The *a* vs. *N* and *da/dN* vs. *a* for LSP Coupons Tested With Constant ΔK_{app} and R_{app} = 0.5	16
11	The *a* vs. *N* and *da/dN* vs. ΔK_{app} LEFM Predictions for an AM Coupon Tested With Constant $P_{\max}$ = 0.98 kN and R = 0.1	17
12	The *a* vs. *N* and *da/dN* vs. *a* for LEFM Predictions for an LSP Coupon Tested With Constant $P_{\max}$ = 2.22 kN and R = 0.1	17
13	The *a* vs. *N* and *da/dN* vs. *a* for LEFM Predictions for AM Coupons Tested With Constant ΔK_{app} and R_{app} = 0.1	18
14	The *a* vs. *N* and *da/dN* vs. *a* for LEFM Predictions for LSP Coupons Tested With Constant ΔK_{app} and R_{app} = 0.1	18
15	The *a* vs. *N* and *da/dN* vs. *a* for LEFM Predictions for LSP Coupons Tested With Constant ΔK_{app} and R_{app} = 0.5	19
16	The K_{RS} Measured Using the Slitting and Contour Methods	19

17	Through-Thickness Average Residual Stress Computed Using the Contour and Slitting Methods	20
18	Coupons 21 and 22 Showing Rapid Crack Growth During Precracking as a Result of Combined Applied and Residual SIFs, and Subsequent Slowing of Fatigue Crack Growth Rate	20
19	Coupon 20_2 Illustrating How Removal of the Material in the Crack Wake Removes Crack Closure Due to Elastic Relaxation	21
20	Coupon 23_2 Illustrating Crack Growth Behavior for an Arrest Case, Which Had K_{app} Raised and Testing Continued	21
21	Open Hole Coupons Used in This Study: Fatigue Coupon Dimensions and DCPD Lead Locations, and Coupon Blanks Used for Residual Stress Measurements	36
22	Crack Length Measurement System Diagram	36
23	Regression Intervals for the Modified Incremental Method	37
24	Data From Test of Coupon C080-03, With Semi-Log Plot of Crack Size vs. Cycles Above and Comparison of FCGR Calculation Methods Below: at Low FCGR Where Noise is High Compared to FCGR, and at Long Crack Length With High FCGR Gradient	37
25	The FCGR vs. ΔK_{eff} Data From the Literature and Piecewise Log–Log Fit	38
26	Contour Measurement Results Illustrating 2D Stress Distributions for the Left and Right Side of Cold-Expanded Coupons	39
27	Through-Thickness Residual Stress Distribution at Three Different Positions for the Bare Residual Stress Coupon	40
28	Through-Thickness Average Residual Stress for the Left and Right Sides of the Three Residual Stress Coupons	40
29	Standard Deviation in Residual Stress for the Set of Six Stress Distributions in Figure vs. the Distance From the Edge of the Hole	41
30	Comparison of DCPD and DP Crack Length Measurements Made on the Same Coupons	41
31	Comparison of Coupon Surface After Fatigue for Clad and Bare Coupons: a Bare Coupon With Clearly Visible Crack Tip Locations and a Clad Coupon With Microcracking Obscuring the Crack Tip Location	42

32 Nondimensional Geometry Factors for Applied and Residual Stresses for Given Crack Sizes; Reference Stress for Applied Stress Is Gross Applied Stress; Reference Stress for Residual Stress Is Negative Flow Stress 42

33 The FCGR-ΔK_{eff} Literature Data, Current Results for AM Coupons, and the Tabular-Lookup Compared to That for Experimental Data 43

34 The AM Coupons, $R = 0.1$, $S_{max} = 47.2$ MPa: Crack Length as a Function of Life and Crack Growth Rate as a Function of Crack Length 43

35 The AM Coupons, $R = 0.5$, and $S_{max} = 65.0$ MPa: Crack Length as a Function of Life and Crack Growth Rate as a Function of Crack Length 44

36 The CX Coupons, $R = 0.1$, and $S_{max} = 142$ MPa: Crack Length as a Function of Life and Crack Growth Rate as a Function of Crack Length 44

37 The CX Coupons, $R = 0.5$, and $S_{max} = 136$ MPa: Crack Length as a Function of Life and Crack Growth Rate as a Function of Crack Length 45

38 A Comparison Between the Seven-Point Incremental Polynomial Smoothing Algorithm and the Modified Incremental Smoothing Algorithm 45

39 Crack Front Shapes for a CX Coupon as Illustrated by Clark and Johnson, and Pell et al. 58

40 Open Hole Coupons Used in This Study: Fatigue Coupon Dimensions and DCPD Lead Locations, and Coupon Blanks Used for Residual Stress Measurements 58

41 Crack Length Measurement System Diagram 59

42 The KG and Strain Relief Pad Positioning 59

43 Dimension Definitions for the Corner Crack SIF Solution and the Part-Elliptical Through-Thickness SIF Solutions 60

44 Contour Measurement Results Illustrating 2D Stress Distributions for the Left and Right Side of CX Coupons 61

45 Through-Thickness Residual Stress Distribution at Three Different Positions for the Bare Residual Stress Coupon 62

46 Mid-Thickness Average Residual Stress for the Left and Right Sides of the Three Residual Stress Coupons 62

47 Standard Deviation in Residual Stress for the Set of Six Stress Distributions in Figure vs. the Distance from the Edge of the Hole 63

48 Comparison of DCPD to KG Crack Length Measurements Made on the Same Thin Coupon 63

49 The AM coupons, $R = 0.1$ and $S_{max} = 47.2$ MPa: Front Face Crack Length as a Function of Life, and Front Face Crack Growth Rate as a Function of Front Face Crack Length 64

50 The AM Coupons, $R = 0.5$ and $S_{max} = 65.0$ MPa: Front Face Crack Length as a Function of Life, and Front Face Crack Growth Rate as a Function of Front Face Crack Length 64

51 The CX Coupons, $R = 0.1$ and $S_{max} = 130$ MPa: Front Face Crack Length as a Function of Life, and Front Face Crack Growth Rate as a Function of Front Face Crack Length 65

52 The CX Coupons, $R = 0.5$ and $S_{max} = 135$ MPa: Front Face Crack Length as a Function of Life, and Front Face Crack Growth Rate as a Function of Front Face Crack Length 65

53 The AM Coupons, $R = 0.1$ and $S_{max} = 47.2$ MPa: Bore Crack Length as a Function of Life, and Bore Crack Growth Rate as a Function of Front Face Crack Length 66

54 The AM Coupons, $R = 0.5$ and $S_{max} = 65.0$ MPa: Bore Crack Length as a Function of Life, and Bore Crack Growth Rate as a Function of Front Face Crack Length 66

55 The CX Coupons, $R = 0.1$ and $S_{max} = 130$ MPa: Bore Crack Length as a Function of Life, and Bore Crack Growth Rate as a Function of Front Face Crack Length 67

56 The CX Coupons, $R = 0.5$ and $S_{max} = 141$ MPa: Bore Crack Length as a Function of Life, and Bore Crack Growth Rate as a Function of Front Face Crack Length 67

57 Ratio of Crack Length on the Bore or Back Face to Crack Length on the Front Face as a Function of Life for Each Test Variation: AM $R = 0.1$, AM $R = 0.5$, CX $R = 0.1$, and CX $R = 0.5$ 68

58 Through-Thickness Average Crack Length as a Function of Loading Cycles for the Four Test Variations Measured by DCPD or Computed From Surface Measurements Using a Crack-Front Model Based on a Straight Line or Part Ellipse 69

59 The AM Coupons, $R = 0.1$ and $S_{max} = 47.2$ MPa: DCPD Crack Length as a Function of Life, and DCPD Crack Growth Rate as a Function of Front Face Crack Length 70

60 The AM Coupons, $R = 0.5$ and $S_{max} = 65.0$ MPa: DCPD Crack Length as a Function of Life, and DCPD Crack Growth Rate as a Function of Front Face Crack Length 70

61 The CX Coupons, R = 0.1 and S_{max} = 130 MPa: DCPD Crack Length as a Function of Life, and DCPD Crack Growth Rate as a Function of Front Face Crack Length 71

62 The CX Coupons, R = 0.5 and S_{max} = 135 MPa: DCPD Crack Length as a Function of Life, and DCPD Crack Growth Rate as a Function of Front Face Crack Length 71

63 Loaded Hole Coupon Geometry 82

64 Residual Stress vs. Radial Distance From the Loaded Hole Perimeter, Error Bars Marking Residual Stress Variability 82

65 Loaded Hole Instrumentation as Seen Through Inspection Window of Clevis, With the DCPD KG and Strain Gage, Highlighting the 6.35 mm Diameter Loading Pin and Bronze Bushing 83

66 Loaded Hole Instrumentation: KG and Strain Gage 83

67 Resulting Polynomial Relationship Describing DCPD Voltage to Crack Length for Crack Angles of 0° and 15° Plotted Against: Data From the Numerical Results and Data From Controlled DCPD Measurements 84

68 Geometry Factors vs. Crack Length for Applied and Residual Stresses, Normalized by Applied Gross Section Stress and Flow Stress, Respectively 84

69 The SIF vs. Crack Length for Applied and Residual Stresses for $S_{app,max}$ = 60.33 MPa and R = 0.1 85

70 The AM R = 0.1 Crack Growth Data Plotted With LEFM Crack Growth Predictions of Crack Length as a Function of Cycles and FCGR as a Function of Crack Length 85

71 The AM R = 0.5 Crack Growth Data Plotted With LEFM Crack Growth Predictions of Crack Length as a Function of Cycles and FCGR as a Function of Crack Length 86

72 The CX R = 0.1 Crack Growth Data Plotted With LEFM Crack Growth Predictions of Crack Length as a Function of Cycles and FCGR as a Function of Crack Length at an S_{max} = 60.33 MPa 86

73 The CX R = 0.5 Crack Growth Data Plotted With LEFM Crack Growth Predictions of Crack Length as a Function of Cycles and FCGR as a Function of Crack Length at an S_{max} = 62.0 MPa 87

74 Difference in Front and Back Crack Lengths Measured During the Test of Coupon A8 87

75 Normalized Front and Rear Strain and Crack Size Differences Plotted as a Function of Average Crack Length; the Vertical Line Identifies Shim Adjustment and the Response of Strain and Crack Growth 88

76 Fretting Failure at the Perimeter of the Loaded Hole Experienced During Initial Testing Without a Bushing 88

77 In-Flight Stress Calculated From Collected Strain Data: Plotted as a Function of Time, and Binned Into a 26 x 28 Binning Scheme and Sorted by Increasing Mean Stress and Stress Amplitude 98

78 Plot of the Final Block Loading Program as a Function of Cycles Used to Test Loaded Hole Coupons 98

79 Dimensions Used by the MGWM to Define Features at the Crack Tip 99

80 Crack Growth Through Loaded Hole AM Coupons With LEFM Predictions Plotted as Crack Length as a Function of Block Programs and Crack Growth Rate as a Function of Crack Length 99

81 Crack Growth Through Loaded Hole CX Coupons With LEFM Predictions Plotted as Crack Length as a Function of Block Programs and Crack Growth Rate as a Function of Crack Length at 82.7 MPa 100

82 Predictions of CX Crack Growth Using a Stress-Based Underload Ratio or a *K*-Based Underload Ratio Plotted as Crack Length as a Function of Block Programs and Crack Growth Rate as a Function of Crack Length 100

83 Dimensions of the Nested-Angle Coupon Assembly, the Small Piece, and the Large Piece 115

84 Nested-Angle Coupon Shown Gripped at Either End as During Testing, With Arrows Highlighting the Direction of the Applied Force 116

85 Cross Section of a Nested Angle, Definition of the Cross-Sectional Centroid and Principal Axes, and the Location of the Strain Gages and Bending Characterization 116

86 Trimmed KG Placed Between the Critical Fastener Hole and the Coupon Bend; Note the Marking Made by the Fastener Collar and Its Proximity to the KG Foil 117

87 Contour Plots of Residual Stress Measured for Two AM and Two CX Coupons Along the Cut Plane and Axes Provided on the Top Left and Top Middle of the Figure, Respectively 118

88 Variation of Residual Stress Through the Specimen Thickness With Error Bars Providing the Standard Deviation 118

89	Average Mid-Thickness Residual Stress Plotted With Standard Deviation	119
90	Through-Thickness Average Residual Stress for Nested-Angle and Thin Open Hole Coupons	119
91	Crack Growth History Following Crack Breakthrough for Coupons NC A, B, and C	120
92	The FCGR Following Crack Breakthrough as a Function of Free Surface Crack Length for Coupons NC A, B, and C During Blocks With $R = 0.1$ and $R = 0.5$	120
93	Crack Length as a Function of Cycles From Crack Breakthrough for Coupons CW 10 and 11	121
94	The FCGR From Crack Breakthrough as a Function of Free Surface Crack Length, for Coupons CW 10 and 11 During Blocks With $R = 0.1$ and $R = 0.5$	121
95	Marker Bands for Cracks Initiated at Different Locations Along the Notch Front Where NC C and CW 11 Show Crack Initiation Across the Entire Notch and NC A, NC B, and CW 10 Show Crack Initiation at the Intersection of the Notch and the Faying Surface	122
96	Crack Length Down the Bore of the Hole Normalized by Faying Surface Crack Length and Free Surface Crack Length Normalized by Faying Surface Crack Length as a Function of Faying Surface Crack Length	123
97	Cracked Area vs. Faying Surface Crack Length	123
98	Cracked Area Growth Rate vs. Faying Surface Crack Length	124
99	Crack Length Beyond Breakthrough Measured Using Surface DCPD and Marker Bands Plotted as a Function of Cycles for Sample NC A and Marker Band Measurements vs. DCPD Measurements	124
100	The AM Nested-Angle Crack Growth Data Plotted as a Free Surface Crack Length as a Function of Block Programs Beyond Crack Breakthrough, and a Free Surface Crack Growth Rate as a Function of Free Surface Crack Length	125
101	The CX Nested-Angle Crack Growth Data Plotted as Free Surface Crack Length as a Function of Block Programs Beyond Crack Breakthrough, and Free Surface Crack Growth Rate as a Function of Free Surface Crack Length	125
102	Coupon Failures Due to Fretting at the Coupon Grip, Stress at Large Holes Under the Coupon Grip, and Asperity on the Faying Surface	126

LIST OF TABLES

Table		Page
1	Mechanical Properties of 7075–T6 Plate	10
2	Coupon and Loading Conditions Employed in Fatigue Crack Growth Tests	11
3	Crack Lengths Measured by Compliance and Visually	11
4	Mechanical Properties for Clad and Bare 0.080-Inch 7075-T6 Aluminum Sheet	35
5	Maximum Applied Stress Levels for the Four Different Test Variations	35
6	Points to Create Piecewise Log–Log FCGR-ΔK_{eff} Tabular Lookup Curve for 7075-T6 Al	35
7	Material Properties for Clad and Bare 0.19-Inch 7075-T6 Aluminum Sheet	57
8	Applied Stress Levels for the Four Different Test Variations	57
9	Points to Create Multilinear FCGR-ΔK_{eff} Tabular Lookup Curve for 7075-T6 Al	57
10	Mechanical Properties for Clad 0.080-Inch 7075-T6 Aluminum Sheet	80
11	Target Stresses and Loads for Fatigue Testing	80
12	Coefficients to the Power Series Defining Correlations Between DCPD and Crack Length for Cracks at 0º and 15º; Valid for $a \leq 13.2$ mm and 9.5 mm, Respectively	80
13	Test Number, Key Test Parameters, Measurements Made of Test Results, and Prediction Data	81
14	The Bin Boundaries Defining the Refined Binning Scheme Along Stress Amplitude and Mean Stress, Respectively	96
15	Variable-Amplitude Block-Loading Program Listed per Bin Number, Maximum and Minimum Stress, Stress Ratio, and the Number of Cycles per Bin	96
16	Data From Fatigue Crack Growth Tests for Loaded Hole Coupons Under Variable Amplitude Loading	97
17	Mechanical Properties of Extruded, Clad 7075–T651 Aluminum	112
18	Power Series Coefficients for DCPD to Crack Length Correlation With Modified KG for 0°, 15°, and 7° Cracks	113
19	Fatigue Life Measured During Alternating Constant Amplitude Nested-Angle Testing at S_{max} = 62.0 MPa	113

20 Normalized Stress Levels Achieved During Variable-Amplitude Nested-Angle Testing Calculated From Strains Measured During Post-Test Dynamic Calibration 114

21 Fatigue Life Measured During Variable-Amplitude Nested-Angle Testing at S_{max} = 117.0 MPa 114

LIST OF SYMBOLS, ABBREVIATIONS, AND ACRONYMS

α_g	Constraint factor compensating crack tip plasticity for plain stress or strain
α_i	Coefficients for power series relating voltage to crack length
Δa	Crack length interval for regression
ΔK	Stress intensity factor range
ΔK_{eff}	Effective stress intensity factor range
ΔK_{MGWM}	Total stress intensity factor range including load interaction
ΔK_{tot}	Total stress intensity factor range
ΔN	Cycle range for regression
ε_F, ε_R	Strain on front and rear face of sample, respectively
σ	Gross stress
σ_a	Stress amplitude
σ_m	Mean stress
$\sigma_{\max}^{ol}$	Maximum stress applied during overload
σ_{ul}	Underload stress
σ_{ys}	Yield strength of material
v_j	Coefficients for power series relating crack length to voltage
Φ	Reduction factor applied to K_{red} because of underload
Φ_o	Tuning parameter used in the MGWM
a	One-dimensional crack length (most sections) or crack length along hole bore (sections 4 and 7)
a_{ap}	Crack length at present cycle
a_f	Final crack length
a_i	Initial crack length
a_n	Initial notch length
a_{ol}	Crack length at overload cycle
B_{exp}	Measured block loading programs to termination crack length
B_{pred}	Predicted block loading programs to termination crack length
c	Crack length on the surface for a corner crack
C_{cr}	Constraint correction factor
c_t	Crack length on the surface following breakthrough of a corner crack
C(T)	Compact tension test
C_{1i}, C_{2i}	Points to create FCGR versus ΔK piecewise curve
D	Hole diameter
da/dN	Fatigue crack growth rates
dc/dN	Fatigue crack growth rates
f	Geometry factor for stress intensity factor
K	Stress intensity factor
$K_{app,\max}$	Maximum applied stress intensity factor
$K_{app,\min}$	Minimum applied stress intensity factor
$K_{MGWM,\max}$	Maximum total stress intensity factor including load interaction
$K_{MGWM,\min}$	Minimum total stress intensity factor including load interaction
K_{red}	Reduction stress intensity factor compensating for overload
K_{RS}	Residual stress intensity factor
K_{tot}	Total stress intensity factor

$K_{tot,\max}$	Maximum total stress intensity factor
$K_{tot,\min}$	Minimum total stress intensity factor
$K_{tot,\max}^{ol}$	Maximum total stress intensity factor at overload
L	Rolling direction
L-T	Long-transverse to the rolling direction
M(T)	Middle-crack tension fatigue coupon
N	Cycles of loading
N_{obs}	Observed cycles to termination crack length
N_{pred}	Predicted cycles to termination crack length
R	Stress ratio of total stress intensity factor ratio
R_{MGWM}	Total stress ratio, including load interaction
R_u	Underload ratio
$R_u(K)$	Underload ratio calculated from stress intensity factor
$R_u(\sigma)$	Underload ratio calculated from stress
$S_{\max}$	Maximum applied cyclic stress (for constant amplitude loading) or peak applied stress (for variable amplitude loading)
S_o	Opening stress
$S_o/S_{\max}$	Ratio of crack opening stress to maximum cyclic stress
$S(x)$	Crack-line stress in the uncracked geometry under a reference loading
t	Material thickness
u_a	Uncertainty in crack length
V	Voltage
V_f	Voltage measurement at the final crack length
V_o	Initial voltage measurement
W	Coupon width
Z_{ap}	Radius of plastic zone ahead of crack tip due to applied stress
Z_{ol}	Radius of plastic zone ahead of crack tip formed during overload cycle
1D	One-dimensional
2D	Two-dimensional
3D	Three-dimensional
AM	As-machined
CCR	Corner crack regime
CX	Cold expansion
DAQ	Data acquisition unit
DCPD	Direct current potential difference
DP	Digital photomicroscopy
EDM	Electric discharge machine
FCGR	Fatigue crack growth rate
FE	Finite element
FEM	Finite element model
GWM	Generalized Willenborg Model
KG	Krak-Gage
LEFM	Linear elastic fracture mechanics
MGWM	Modified Generalized Willenborg Model
LSP	Laser shock peening
ND	Neutron diffraction

QE	Quarter elliptical
SIF	Stress intensity factor
SR	Surface replica
TCS	Test control software
TTCR	Through-thickness crack regime
XRD	X-ray diffraction

EXECUTIVE SUMMARY

An experimental study was performed to collect data on the growth of fatigue cracks in residual stress-bearing materials typical of rotorcraft structures. Companion analyses were developed to assess the accuracy of typical fatigue crack growth models. Fatigue crack growth tests were performed on a range of coupons that progressed from very simple to fairly complex. The coupon geometries were: one-dimensional (1D) cracks in standard compact tension coupons, 1D and two-dimensional (2D) cracks in coupons with open holes, 1D cracks in coupons with pin-loaded holes, and 2D cracks at fastener holes in nested-angle coupons with a lap shear joint. Most test series were performed under constant amplitude cyclic loading, but additional tests of pin-loaded hole and nested-angle coupons were performed under variable-amplitude loading. Each series of tests employed a number of identical coupons (replicate tests) as well as coupons in at least two material conditions: an as-machined (AM) condition (without residual stress) and a residual stress-bearing condition. Tests in compact tension coupons had residual stress induced by laser shock peening, but all other tests had residual stress induced by cold-hole expansion. Replicate tests provided measures of variability in residual stress and fatigue crack growth. Companion linear elastic fracture mechanics (LEFM) analyses were developed for comparison with the experimental data and made use of measured residual stresses from replicate coupons.

Observed crack growth data for 1D cracks were consistent with LEFM predictions for both the AM and residual stress-bearing conditions, though the degree of agreement depended on the applied stress ratio. Variability in observed crack growth behavior was consistent with the variability in measured residual stress. Observed crack growth data from coupons with 2D cracks at an open hole were consistent with LEFM predictions for the AM condition, but not for the residual stress-bearing condition, where the LEFM predictions assumed a quarter-elliptical crack shape. Observed crack size data suggested that the crack shape in AM coupons was quarter-elliptical, but in residual stress-bearing coupons it was not. The inability to predict the growth of 2D cracks in the residual stress-bearing coupons may therefore be due to the lack of appropriate stress intensity factors for the residual stress-bearing condition (in which cracks were not quarter-elliptical).

The work in this volume is part of a larger project additionally covered in two preceding volumes and was performed by Hill Engineering, LLC under subcontract to Mississippi State University in partnership with Sikorsky Aircraft Company. The program was sponsored by the Federal Aviation Administration.

1. INTRODUCTION.

1.1 BACKGROUND.

Early aircraft design was based on a safe life philosophy for which lifetime calculations were based on idealized gross geometry. This worked fine for early designs made either with fatigue-resilient materials, such as wood, or those that were somewhat conservative (because of the use of new alloys with which many were unfamiliar at the time). However, as performance requirements for aircraft, and familiarity with those alloys increased, designs became less conservative. A number of catastrophic aircraft failures, particularly in the B-47 bomber fleet during the late 1950s [1], motivated an investigation into the cause of the crashes. The conclusion of the investigation was that the design methods used were not conservative enough because they did not account for inevitable damage to the parts, either from manufacturing flaws or damage sustained during service. A new damage-tolerant design philosophy was created to ensure slow crack growth for a given flaw size, such that the critical crack size would not be reached within a given factor of safety during the parts' lifetime. This design philosophy is what is being used today to design aircraft and other high-performance, fatigue-critical parts.

Today's designers are always looking for ways to squeeze the most performance from their designs. In the past, this meant the manipulation of three variables to combat crack growth: the stresses applied to the part, the part material, and the part geometry. In design optimization, often little can be done to change the stresses applied to the part, and material choices are typically constrained, leaving shape as a primary variable for optimization. With the prevalent use of finite element (FE) analysis techniques in design today, many parts already have well-optimized geometry. An alternative method to combating crack growth is to change the internal residual stress field of the part via a residual stress treatment. These treatments induce compressive residual stresses in specific regions and effectively counteract the applied tensile stresses that the part experiences. Residual stress treatments offer the possibility to increase performance beyond the optimization of applied stress, material, and geometry.

Cold-expanded holes are used in the aircraft industry to improve the fatigue life of components with fastener holes, whereas the process of cold expansion (CX) induces compressive residual hoop stress around the hole that slows the growth of fatigue cracks initiating at the hole. The CX process induces compressive residual stress by pulling a tapered mandrel through a split sleeve placed in the hole, which leaves tensile plastic hoop strain adjacent to the hole. Elastic relaxation upon removal of the mandrel produces a region of compressive residual hoop stress. The CX has been found to be very effective in slowing crack growth from fastener holes [2]. However, the industry does not give model-based credit to life improvement from CX in design [1] because of the lack of an established correlation between observed and predicted crack growth in a number of previous studies [3].

The fact that the benefits of residual stress treatments are not adequately included in design analyses makes for overly conservative designs and prevents optimal planning of appropriate damage-inspection intervals, which is a critical component of the damage-tolerant design philosophy. The goal of this work is to support the creation of tools that accurately quantify the benefits of residual stresses in design analyses. This would allow residual stress locations and

amounts to be optimized, thus increasing component lifetimes, decreasing component weights, and creating more useful intervals for damage inspection.

1.2 PROJECT SCOPE.

The work reported in this volume includes laboratory data essential for understanding the ability of models to correlate the growth of one-dimensional (1D) and two-dimensional (2D) fatigue cracks in residual stress-bearing structures, which is a critical gap in current approaches to damage-tolerant design of rotorcraft. Fatigue crack growth tests were carried out in a range of coupons that progressed from very simple to fairly complex, and companion linear elastic fracture mechanics (LEFM) analyses were used to correlate their behavior. The coupon geometries were: 1D cracks in standard compact tension coupons, 1D and 2D cracks in coupons with open holes, 1D cracks in coupons with pin-loaded holes, and 2D cracks at fastener holes in nested-angle coupons having a lap shear joint. Most test series were performed under constant amplitude cyclic loading, but additional tests of pin-loaded holes and nested-angle coupons were performed under variable-amplitude loading. Each series of tests employed a number of identical coupons (replicate tests) as well as coupons in at least two material conditions: an AM condition (without residual stress) and a residual stress-bearing condition. Tests in compact tension coupons had residual stress induced by laser shock peening (LSP) and all other tests had residual stress induced by cold-hole expansion.

This report includes complete test details: materials, coupon geometries, fabrication details, and residual stress measurements, as well as crack growth test methods and results. It also includes a comparison of observed fatigue crack growth data to LEFM predictions for many of the test conditions.

The work was organized into a set of tests with increasing complexity of coupon geometry, crack morphology, loading, and prediction models building up to tests of coupons having a fastened connection between nested angles. The program began with tests in the compact tension coupon geometry from the ASTM standard [4], which is well documented. These tests are described in section 2. Subsequent sections reflect a set of intermediate validation steps that investigate crack growth at open holes, first for 1D crack growth (section 3) and then for 2D crack growth (section 4), for which 1D growth has a constant crack length through the thickness and 2D growth does not. Section 5 reports tests of 1D crack growth at pin-loaded holes, while section 6 reports tests in the same geometry but under variable-amplitude block loading representative of rotorcraft operation. Section 7 describes tests of nested-angle coupons representative of a fatigue-critical structural detail.

2. THE 1D CRACK GROWTH IN RESIDUAL STRESS-BEARING COMPACT TENSION COUPONS.

2.1 INTRODUCTION.

Damage-tolerant fatigue design is becoming a more widely used approach in the rotorcraft industry because of recent advancements in fracture mechanics and successful implementation of damage tolerance in fixed-wing aircraft [5–7]. Current rotorcraft fatigue design practice has been to use a safe life approach, with which the lifetime of a part is calculated based on life to

fatigue crack formation and safety factors based on the life/stress level [8 and 9]. The damage-tolerance approach contrasts with the safe-life approach in that parts, when new, are assumed to contain crack-like damage that will become larger under operational loads. The useful life of a part is determined based on the time it takes for the initial damage to grow to a size that would cause failure, and inspections are used to identify and repair damage at intervals of a fraction of that useful life. Therefore, a part may remain in service until inspection dictates its removal from service (i.e., "retirement for cause"), improving the reliability of many parts and potentially extending part life.

Residual stress treatments, such as shot peening, cold-hole expansion, and case hardening are commonly used in the rotorcraft industry and have affected the operational experience of parts designed to the safe-life approach. These residual stress treatments, when applied correctly, impart compressive residual stresses that have the ability to improve the fatigue performance and damage tolerance of parts [10–12]. If the damage-tolerant approach is to be applied successfully to parts fielded with residual stress treatments, the effects of these residual stress treatments must be included in their analysis or analyses.

To take full advantage of the benefits residual stress treatments offer, engineers and designers must be given analytical approaches (and easy-to-use tools) with which they can model the potential effects of residual stress treatments. To develop these tools, the basic behavior of fatigue cracks growing through residual stress-bearing material must first be understood. This section develops data to support an improved understanding of crack growth through residual stress fields by using a simple, accepted geometry; a 1D crack; and a well-characterized, reliable residual stress distribution. The hope is that by minimizing the potential sources for uncontrolled effects, the essential interaction of residual and applied stresses can be observed and characterized.

The first objective of this study was to produce a set of identical residual stress-bearing coupons that could be used to observe crack growth under combined residual and applied stress. The second objective was to determine if LEFM, with superposition of applied and residual stress, is an accurate predictor of crack growth under combined residual and applied stress.

2.2 METHODS.

Aluminum alloy 7075-T6 was selected for this test program because of its prevalent use in rotorcraft components. The material was received as clad plate 4.8 mm thick. Handbook mechanical properties of 7075-T6 are listed in table 1. Fatigue crack growth rates for this material taken from [13] are illustrated in figure 1.

Compact tension test C(T) coupons as defined in ASTM E647 were used in this study. The C(T) coupon is well suited for this work because of its accepted use in fatigue crack growth testing, its simple geometry, and the fact that it contains a 1D fatigue crack characterized by the crack length, a. Coupon geometry had thickness (B) of 3.8 mm and a characteristic dimension (W) of 50.8 mm (see figure 2.). Coupons were cut such that crack growth occurred in the long-transverse to the rolling direction (L-T) orientation. To obtain the 3.8 mm coupon thickness from the stock material, the material was machined in equal amounts from each side so that the samples lay in the t/2 plane and the original clad layer was removed. The starter notch with

integral knife-edges was fabricated using a wire electric discharge machine (EDM). The EDM notch was 0.3 mm wide and 22.9 mm long (corresponding to an initial notch length of a_n = 10.2 mm).

To produce an identical set of residual stress-bearing coupons, LSP was used. In thin geometries, like the C(T) coupons used in this study, LSP can generate through-thickness compressive residual stress in the treated area. For this work, LSP was applied by Metal Improvement Company, using a parameter set of 4 GW/cm^2 irradiance per pulse, 18 ns pulse duration, and three layers of treatment (denoted 4-18-3). This parameter set was selected because it provided optimal high-cycle fatigue life improvements in previous work with 7050-T7451 coupons [14 and 15]. Coupons were peened on both sides, alternating sides between each layer application. The peened area is shown in figure 2. Values of S and X_p were selected during coupon design as 22.9 mm and 27.9 mm, respectively, to provide a negative residual stress intensity factor (SIF) that would reduce crack growth rate, as observed in earlier work [16]. This LSP condition will be referred to as LSP-3N, indicating LSP with three layers applied near the front face of the coupon.

In addition, three other LSP treatments were selected to examine the effects of LSP intensity (through number of layers) and location of the peened area (through X_p) on the residual SIF (K_{RS}). These additional treatments were: 4-18-3 X_p = 12.7 mm (LSP-3F), 4-18-1 X_p = 12.7 and 27.9 mm (LSP-1F and LSP-1N), all with S = 22.9 mm.

The 2D residual stress distributions were measured on the prospective crack plane of LSP-3N coupons using the contour method [17 and 18]. Wire EDM was used to cut the coupons in half and expose the crack plane. After cutting, a laser triangulation area scanning profilometer was used to measure the resulting out-of-plane deformation of the cut surface on both halves of the coupon. The measured deformations of the two halves were averaged and the inverse averaged deformations were applied as displacement boundary conditions in a three-dimensional (3D) elastic FE model of one-half of the coupon. The stress resulting from the elastic FE model provides the experimental estimate of the original residual stress distribution. Residual stress measurements were performed on C(T) blanks that had holes, but did not have notches. Replicate coupons were measured to validate LSP process control and to demonstrate the consistency of the contour method [17 and 18].

The slitting method was used to measure K_{RS} following Schindler's method for a thin rectangular plate [19]. A strain gage with an active grid length of 0.8 mm was applied to the center of the back face of the coupon. Wire EDM was used to incrementally extend a slit through the coupon, with strain recorded after each increment of slit depth. The K_{RS} was then computed from the influence function $Z(a)$ provided in [19], the plane stress modulus of elasticity E' = 71.7 GPa, and the derivative of strain with respect to slit depth:

$$K_{RS}(a) = \frac{E'}{Z(a)} \frac{d\varepsilon(a)}{da} \tag{1}$$

The influence function $Z(a)$ does not account for the holes present in the C(T) coupon, which were assumed to have negligible effect.

Fatigue crack growth tests were conducted on a computer controlled servo-hydraulic load frame. The crack mouth opening compliance was used to monitor crack length during the tests, as described in ASTM E647. Crack mouth opening displacement was measured at the front face of the coupon using a clip-type displacement gage.

A range of coupon and loading combinations was used to evaluate residual stress effects on fatigue crack growth (see table 2). Two tests were run under constant amplitude load. One AM coupon was tested with a constant maximum load of 0.979 kN and an applied load ratio (R_{app}) of 0.1 to characterize fatigue crack growth rates for applied SIF ranges (ΔK_{app}) from 4.4 to 22.0 $\mathrm{MPa}\sqrt{\mathrm{m}}$. One LSP-3N coupon was tested with maximum applied load of 2.22 kN and $R_{app} = 0.1$ to examine fatigue crack growth through residual stress-bearing material under increasing ΔK_{app} loading. The remaining coupons were run under constant ΔK_{app} loading. Tests were run at various levels of ΔK_{app} and with R_{app} of either 0.1 or 0.5. Initial tests were conducted at 5 Hz (coupons 07, 08, 11, 19, and 20), but difficulties with test control (when crack growth rates were small) required reducing the test frequency to 2 Hz for further tests.

Fatigue pre-cracking per ASTM E647 was performed for initial tests, but was eliminated for expediency in later tests because the compliance crack length data in the initial tests agreed well with fractographic observations. For tests without pre-cracking, the first 1.3 mm of crack growth data were discarded and the cycle count adjusted to be zero at the first data point beyond 1.3 mm of crack growth. Tests were ended when a crack length of 38.1 mm was achieved or when crack arrest—defined as reaching 100,000 cycles with no measureable crack growth—occurred. Test data were reduced following ASTM E647 using the incremental polynomial method for computing crack growth rates (n = 6, provided adequate smoothing of data was used for all coupons).

Upon completion of the fatigue crack growth tests, coupons were fractured through the remaining ligament to expose the fracture surface. The locations of the EDM notch, fatigue pre-crack (where applicable), and final fatigue crack were recorded in accordance with ASTM E647 using a stereo microscope equipped with a two-axis instrumented stage.

The LEFM crack growth predictions were made for each test condition by developing custom software. The $K_{RS}(a)$ measured using the slitting method was included in the analysis using superposition:

$$\Delta K_{tot}(a) = K_{app,\max}(a) - K_{app,\min}(a) \tag{2}$$

$$R_{tot}(a) = \frac{K_{app,\min}(a) + K_{RS}(a)}{K_{app,\max}(a) + K_{RS}(a)} \tag{3}$$

where max and min subscripts on $K_{app}(a)$ denote maximum and minimum resulting from cyclic loading as a function of crack length. $\Delta K_{tot}(a)$ and $R_{tot}(a)$ are the SIF range and total SIF ratio, respectively, that arise as the result of the combination of applied load and residual stress as functions of crack length. The NASGRO equation provided the crack growth rate as a function of crack length from $\Delta K_{tot}(a)$ and $R_{tot}(a)$. The NASGRO equation constants for 7075-T6 sheet

(in the L-T orientation) were available [20] and used in the analysis. Crack growth history (crack length [a] versus number of cycles of loading [N]) was determined by numerically integrating the crack growth rate. To properly model the highly negative stress ratios created by the residual stress in these samples, the NASGRO equation was modified by setting the NASGRO crack opening function [f] equal to zero for values of $R_{tot}(a)$ which cause f to be less than zero [21].

The LEFM predictions were made to match experimental conditions. Analyses used input test loading and initial crack lengths. Predictions were terminated at a crack length of 38.1 mm or upon crack arrest (determined by when the predicted crack growth rate dropped below 2.54×10^{-6} mm/cycle).

2.3 RESULTS.

The results of contour measurements made on two AM and two LSP-3N coupons are illustrated in figure 3. Residual stress in the AM coupons ranged from -44.8 to 15.9 MPa and had a similar through-thickness distribution at all points across the coupon width. The LSP coupons had a maximum compressive residual stress of -289.6 MPa that occurred on the surface near the middle of the coupon and a maximum tensile stress of 351.6 MPa that occurred at the front face of the coupon. In the peened region (from $x = 12.7$ to $x = 35.6$ mm), residual stress was compressive at the surfaces and decreased in magnitude with through-thickness position. Outside of the peened region, residual stress had nearly uniform through-thickness, but varied with position across the width. Replicate coupons confirm LSP process control and demonstrate repeatability of the residual stress measurements.

Through-thickness average residual stress for each coupon, computed from the contour measurements, is plotted in figure 4. The AM coupons have a thickness-average of nearly 0 MPa, as expected. Thickness-average stress in the LSP-3N coupon has maximum tension at the front face with a value of 316 MPa and maximum compression of -137 MPa near the middle of the LSP area (x = 27.4 mm).

In figure 5, K_{RS} from the slitting method is shown. Positioning the LSP region farther from the start of the slit (LSP-1F, LSP-3F) results in a predominantly tensile K_{RS} distribution. For the three-layer case, the tensile peak of 35.9 $\mathrm{MPa}\sqrt{\mathrm{m}}$ is in excess of the material's plane strain fracture toughness, 29.0 $\mathrm{MPa}\sqrt{\mathrm{m}}$. Results for each of the coupons exhibit a most positive (tensile) K_{RS} of magnitude equal to or greater than the most negative (compressive) K_{RS} magnitude, suggesting potential deleterious effects from compressive residual stress treatments. The magnitude of the maximum tensile K_{RS} in coupons LSP-1F and LSP-3F (17.7 and 35.9 $\mathrm{MPa}\sqrt{\mathrm{m}}$) is nearly twice the magnitude of the maximum compressive K_{RS} in coupons LSP-1N and LSP-3N (-10.5 and -16.8 $\mathrm{MPa}\sqrt{\mathrm{m}}$). Both of these facts demonstrate that it is critical to carefully select an LSP location with respect to the expected crack initiation location and part geometry. With the LSP-3N coupon, which was treated identically to the coupons used for fatigue testing, the SIF was measured to have a minimum value of -16.8 $\mathrm{MPa}\sqrt{\mathrm{m}}$ at $a = 20.2$ mm. Replicate coupons illustrate the consistency of the LSP application and of Schindler's method.

The results of the AM coupon constant load test show expected crack growth behavior, with *da/dN* vs ΔK being approximately linear when plotted on log–log axes (see figure 6).

The results of the LSP-3N constant load test show the effects of compressive K_{RS} on crack growth (see figure 7). The large decrease in crack growth rate reaches a minimum at $a = 20.3$ mm, which is consistent with the location of maximum compressive K_{RS} for this treatment (see figure 5). The AM coupons tested at constant ΔK_{app} exhibited constant crack growth rates, as expected (see figure 8). Average crack growth rates at $R_{app} = 0.1$ were 6.25×10^{-4} and 1.88×10^{-3} mm/cycle at ΔK_{app} of 14.8 and 22.0 $\mathrm{MPa}\sqrt{\mathrm{m}}$, respectively.

All of the LSP coupons tested exhibited similar trends in crack growth behavior (see figures 9[a] and 10[a]). Crack growth rates start out with values comparable to AM. As the crack grows into the LSP region, growth rates begin to slow because of decreasing R_{tot} as a result of superposition applied and residual stress. Crack growth rates reach a minimum between $a = 20.3$ and $a = 22.9$ mm, near the location of minimum measured K_{RS} (a = 20.2 mm). Arrest resulted at smaller values of ΔK_{app} used in coupons 19 and 23. For other coupons, in which cracks do not arrest, growth rates begin to increase, at first with the same rate of change at which they slowed, then at reduced rates of change. Crack growth rates are very slow to return to the rates observed in tests of AM coupons. A small local peak in crack growth rate was observed after the initial rise in *da/dN* for coupons 18 and 24 occurring between $a = 22.9$ mm and $a = 24.1$ mm.

For LSP coupons tested with $R_{app} = 0.1$, the crack growth rate was slowed from 1.88×10^{-3} mm/cycle (AM) to a minimum of 4.14×10^{-4} mm/cycle (LSP) with constant $\Delta K_{app} = 22.0$ $\mathrm{MPa}\sqrt{\mathrm{m}}$ (compare figures 8 and 9). The number of cycles required to reach a crack size of 38.1 mm increased 5.6 times from 13,000 in the AM case to 73,000 cycles in the LSP case. Testing at $\Delta K_{app} = 16.5$ $\mathrm{MPa}\sqrt{\mathrm{m}}$ resulted in crack arrest at $a = 19.05$ mm, again near the point of maximum compressive K_{RS}.

For LSP coupons tested with $R_{app} = 0.5$, the minimum crack growth rates witnessed were 1.66×10^{-4} and 9.40×10^{-7} mm/cycle for LSP coupons tested at $\Delta K_{app} = 14.3$ and 11.0 $\mathrm{MPa}\sqrt{\mathrm{m}}$, respectively (figure 10[b]). Coupon 23, tested at $\Delta K_{app} = 8.8$ $\mathrm{MPa}\sqrt{\mathrm{m}}$, exhibited crack arrest at $a = 20.3$ mm.

A summary of crack length measurements is provided in table 3. Under the "EDM Notch" column, "User" indicates values input at the start of the fatigue crack growth test. Compliance-based crack length measurements are included for the fatigue pre-crack and final crack to allow comparisons with post-test measurements. Crack lengths for test 20 could not be measured because of extension of the EDM notch for test 20_2 (which is described later). For coupon 23, the EDM notch length of test 23 is reported and the final crack length is from test 23_2 (described later). The values in the table validate that testing was conducted in accordance with ASTM E647.

The results of LEFM analysis for each test case are compared with the test data in figures 11–15. There is good correlation between the predictions and the test data overall. Discrepancies in the AM coupons tested with constant ΔK_{app} are consistent with the discrepancies seen in the

da/dN vs. ΔK_{app} data from the AM coupon tested with constant applied load (see figure 11) and are due to the NASGRO equation having a simple power-law *da/dN* vs. ΔK relationship for moderate crack growth rates. For the LSP cases at $R = 0.1$, LEFM provides good agreement as the crack growth slows (for $a < 22$ mm). For the LSP cases at $R = 0.5$, LEFM overestimates crack growth rates as crack growth slows ($a < 22$ mm). At longer crack lengths ($a > 22$ mm) in both stress ratios, LEFM predicts that growth rates return quickly to AM rates, but the test data show a more gradual return. The differences between observed and predicted crack growth rates do not produce large differences in crack growth history (a vs. N).

2.4 DISCUSSION.

A comparison of K_{RS} determined using the slitting and contour methods indicates little difference between the two. For the contour method, K_{RS} is calculated using a weight function for a single-edge cracked square plate from Wu and Carlsson [22] and the through-thickness average residual stress profile calculated from the contour results (see figure 4). With the exception of the minimum K_{RS} valley, the profiles calculated by the two methods are nearly identical (see figure 16). The discrepancy in the valley is due to fitting of the contour surface profile data with a 5th order Fourier surface. If the order of the fit is increased to 10th order, the match to the valley becomes better (but the pointwise contour residual stress results become somewhat noisy).

Through-thickness average residual stress computed from the contour method is compared to through-thickness average residual stress calculated from strain measured during slitting experiments. Computation of residual stress from measured strain was performed using regularized unit pulses, as described in Schajer and Prime [23]. It is clear from figure 17 that these two methods agree very well and further that the 10th order contour fit, again, provides a better match with the slitting results.

Selecting the area of a part to treat with residual stress treatment is critical. While the goal of typical residual treatment is to impart beneficial compressive residual stresses to prolong fatigue life, compensating tensile residual stresses will arise to satisfy equilibrium. The magnitude and location of these compensating tensile stresses are dependent on the geometry of the part. However, their effect on crack growth is largely because of the location of these stresses with respect to the location of crack initiation and crack path because this determines K_{RS} and controls the crack tip fields. The effects of crack initiation location can clearly be seen in the results of the K_{RS} measurements for the four different LSP treatments. Extending the slit into the LSP region from the opposite side (modeled by LSP-1F and LSP-3F) results in very high magnitude tensile K_{RS} instead of the highly compressive K_{RS} found in LSP-1N and LSP-3N. In the LSP-3F case, the maximum tensile K_{RS} (35.9 $\mathrm{MPa}\sqrt{\mathrm{m}}$) is greater than K_{Ic} of the material (29.0 $\mathrm{MPa}\sqrt{\mathrm{m}}$). A K_{RS} of this magnitude could be devastating in an actual part, since even low magnitude tensile K_{RS} can result in fracture when combined with applied loads, as seen at the beginning of coupons 21 and 22 (see figure 18).

The initial fatigue crack growth rates of coupons 21 and 22 were slower than expected due to rapid crack growth, and resulting plasticity ahead of the crack tip, combined with a decreasing total stress ratio. This occurred as a result of the combination of the applied and residual SIFs.

For these tests, $K_{\max,app}$ was 28.6 $\mathrm{MPa}\sqrt{\mathrm{m}}$, nearly equal to K_{Ic} (29.0 $\mathrm{MPa}\sqrt{\mathrm{m}}$), which, together with tensile K_{RS} at short crack lengths, caused very fast crack growth (see figure 18).

The slow return to AM crack growth rates in the LSP samples for longer cracks (a > 22 mm) is most likely due to crack face contact (closure) behind the crack tip from elastic relaxation of the residual stress-bearing material. As the crack grows through the residual stress-bearing material, traction-free surfaces are created. These traction-free surfaces result in out-of-plane deformation of the surfaces due to the release of residual stress. Regions containing compressive residual stress deform outward. This outward deformation results in interference between the crack faces and crack closure. This sort of crack face contact affects the cyclic crack tip stress fields, but is not accounted for in the LEFM analysis. Even with this discrepancy, the LEFM analyses indicate that superposition is a good tool for prediction of residual stress effects on crack growth rates.

Two secondary tests were run for better understanding of some of the crack growth results. If a test was stopped before the crack reached 38.1 mm, the remainder of the coupon was available for a secondary test. Coupon 20 was stopped at a = 24.6 mm because of difficulties with test control. A secondary test denoted as 20_2 was conducted with the remaining coupon. Prior to the secondary test, the EDM notch was extended past the location of stoppage, to a = 26.0 mm. Testing then resumed at the same loading conditions (R_{app} = 0.1, ΔK_{app} = 22.0 $\mathrm{MPa}\sqrt{\mathrm{m}}$). The result of this test is illustrated in figure 19. This test is significant because it indicates that elimination of crack face contact (that was present because of elastic release of compressive residual stress) allows the LSP coupons to nearly return to the AM rate once the crack has grown through the region affected by K_{RS} (a = 14.0 to 33.0 mm).

The fatigue crack growth rate behavior witnessed in the LSP coupons is the result of the combination of two sources of crack closure: negative R_{tot} from K_{RS} and elastic relaxation. Negative R_{tot} directly affects the material near the tip of the crack, whereas elastic relaxation occurs in the wake of the crack. Initially, for a < 23.0 mm, the R_{tot} effect dominates the coupon behavior. The LEFM approach includes the R_{tot} effect and, therefore, accurately predicts crack growth rates in this region.

A small peak in fatigue crack growth rate can be seen at approximately a = 23.0 mm in coupons 18, 19, and 24 where this transition occurs. This peak becomes less noticeable in coupon 24 and is not visible in coupons 21 and 22. The smaller, less noticeable peak is likely due to the fact that, in general, as R_{app} and/or ΔK_{app} are increased, the R_{tot} effect is reduced (i.e., less change in da/dN for same change in R_{tot}), resulting in less sharp transition between the R_{tot} and elastic relaxation dominated regions and a less noticeable peak. The transition peak as well as closure from both R_{tot} and elastic relaxation can also be seen in coupon 25, which was tested with constant load (see figure 12). As elastic relaxation begins to occur in the crack wake, it begins to dominate crack closure, and LEFM predictions, which do not have provisions for this behavior, become less accurate. Coupon 20_2 shows that by removing the material in the wake of the crack, the elastic relaxation effect is also removed and crack growth follows the LEFM prediction. The fatigue crack growth rate of coupon 20_2 starts out below that of the AM coupon (coupon 11), but slowly climbs to match the AM fatigue crack growth rate at a = 33.0 mm where K_{RS} is zero.

Coupon 23 was also used for a secondary test. The test started out with ΔK_{app} = 8.8 $\mathrm{MPa}\sqrt{\mathrm{m}}$ and a runout was called at a = 20.32 mm, when the growth rate reached 7.62 x 10^{-6} mm/cycle. The test was continued by increasing ΔK_{app} to 11.0 $\mathrm{MPa}\sqrt{\mathrm{m}}$ and results were denoted as 23_2 (see figure 20). The resulting crack growth behavior agrees with results for coupon 24, which was tested with ΔK_{app} = 11.0 $\mathrm{MPa}\sqrt{\mathrm{m}}$ for its entirety.

2.5 SUMMARY.

While the tests reported in this section used simple sample geometry, different from geometries often used when evaluating damage tolerance methods for rotorcraft structures, they reflect an important step in validating key technologies for measuring for residual stress fields and accounting for their effects on fatigue crack growth. Through careful sample design and well-controlled material processing, we developed a sample set with a consistent and useful residual stress distribution. The contour and slitting methods each provided useful measurements of the residual stress field, and results of the two techniques were in agreement. Slitting method measurements of the residual SIF provided useful input to LEFM crack growth predictions.

Comparison of data and LEFM predictions shows that fatigue crack growth rates in the residual stress-bearing coupons are affected by both SIF ratio effects—from the combination of applied and residual SIFs—and by closure in the crack wake due to elastic relaxation of the residual stress-bearing material. The LEFM with superposition accurately predicted the fatigue crack growth behavior in regions dominated by SIF ratio effects; however, LEFM does not include provisions for the regions dominated by crack closure from elastic relaxation in the crack wake, which degraded prediction accuracy. Further work investigating crack closure due to elastic relaxation of residual stress-bearing material in the crack wake would be useful for developing improved crack growth models. This could include developing prediction methods for the amount of interference created by a given residual stress field and then determining how that interference will translate into crack closure effects. Wang [24] has shown that modifying the strip yield model can provide good predictions of closure due to relaxation and that other approaches might exist.

2.6 TABLES.

Table 1. Mechanical Properties of 7075-T6 Plate [13]

S_u (MPa)	S_y (MPa)	E (GPa)	Poisson's Ratio υ	K_{Ic} ($\mathrm{MPa}\sqrt{\mathrm{m}}$)
572	503	71.7	0.33	29.0

Table 2. Coupon and Loading Conditions Employed in Fatigue Crack Growth Tests

Coupon SN(s)	*Rapp*	*P*max (kN)	*Kapp* ($\mathbf{MPa}\sqrt{\mathbf{m}}$)	Condition
12	0.1	0.98	-	AM
25	0.1	2.22	-	LSP-3N
07	0.1	-	14.8	AM
08, 11	0.1	-	22.0	AM
19	0.1	-	16.5	LSP-3N
18, 20	0.1	-	22.0	LSP-3N
23	0.5	-	8.8	LSP-3N
24	0.5	-	11.0	LSP-3N
21, 22	0.5	-	14.3	LSP-3N

Table 3. Crack Lengths Measured by Compliance and Visually

Coupon Number	EDM Notch (mm)		Fat. Pre-crack (mm)		Final Crack (mm)	
	User	Visual	Comp	Visual	Comp	Visual
7	10.16	9.71	13.34	13.44	38.12	38.53
8	10.16	9.71	13.36	13.34	38.11	38.65
11	10.29	10.12	14.49	14.28	38.13	38.20
12	10.16	10.15	N/A	N/A	35.68	36.06
18	15.44	15.35	N/A	N/A	38.11	38.48
19	10.41	10.43	N/A	N/A	24.89	24.67
20_2	26.37	26.28	N/A	N/A	38.10	38.41
21	10.41	10.41	N/A	N/A	38.12	38.28
22	10.41	10.21	N/A	N/A	38.11	38.18
23, 23_2	10.41	10.39	N/A	N/A	38.11	38.37
24	10.41	10.43	N/A	N/A	38.12	38.13

2.7 FIGURES.

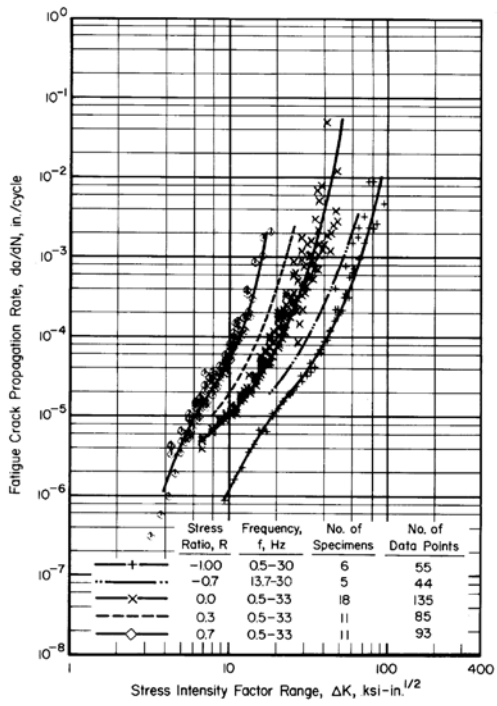

Figure 1. The *da/dN* for Clad 7075-T6, 0.090-Inch Thick Sheet, Lab Air [13]

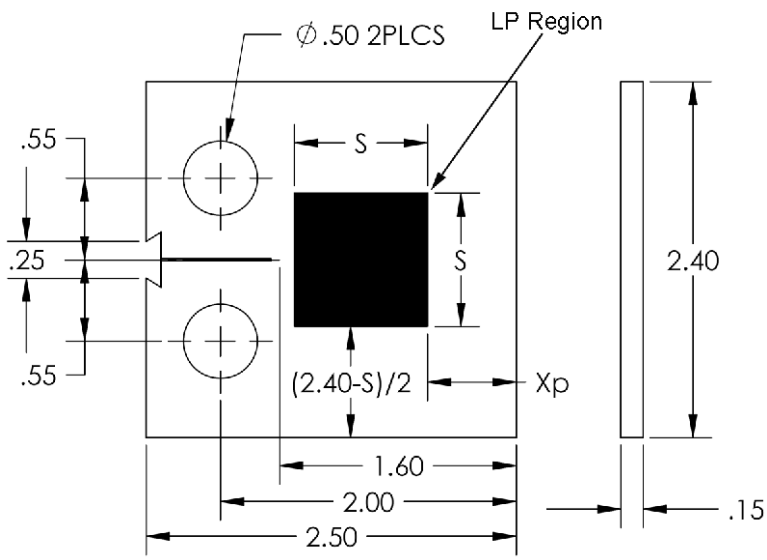

Figure 2. The 7075-T6 C(T) Coupon (dimensions in millimeters)

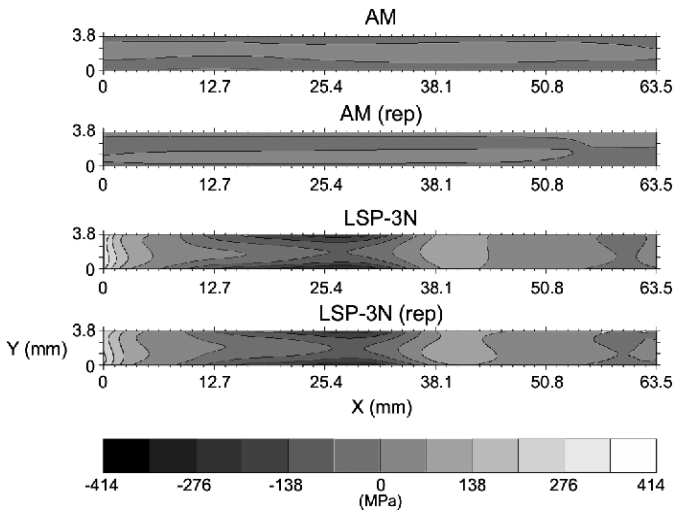

Figure 3. Contour Measurement Results Illustrating the Residual Stress Distribution on the Plane of the Crack for AM and LSP-3N Coupons

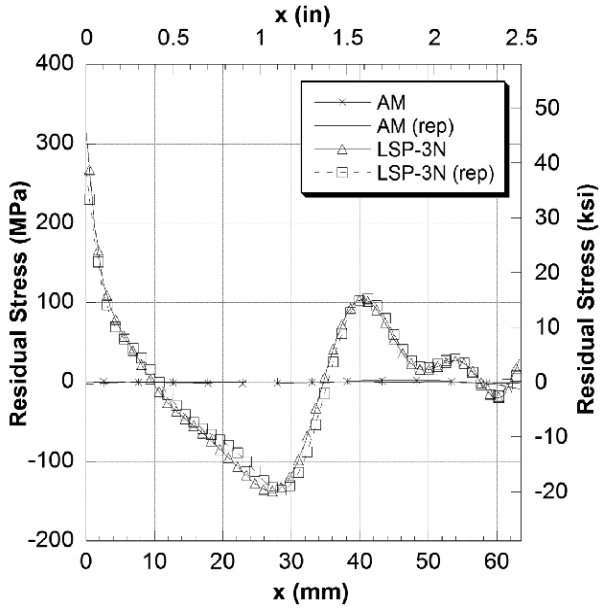

Figure 4. Through-Thickness Average Stress for AM and LSP-3N Coupons Computed From Contour Results

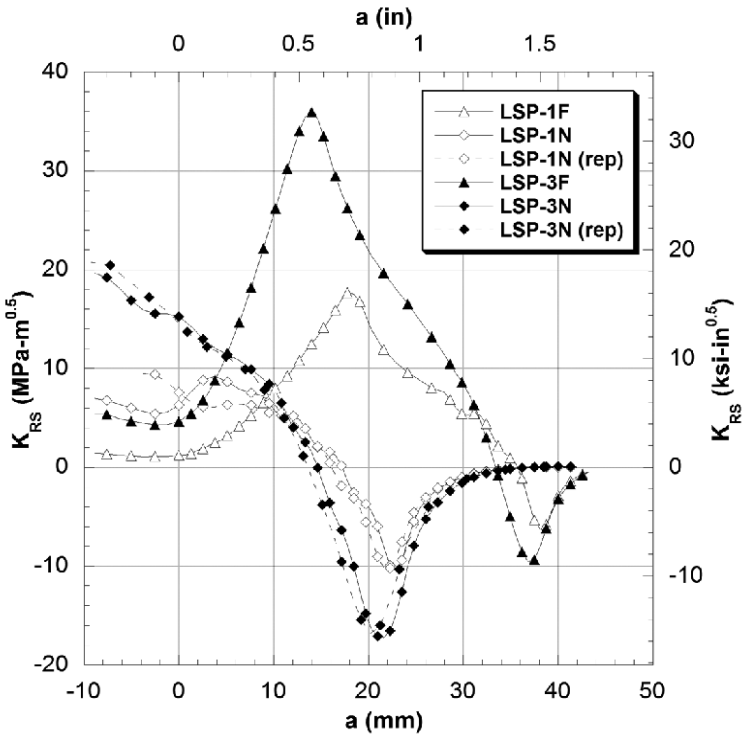

Figure 5. The K_{RS} as a Function of Crack Length (every other data point plotted)

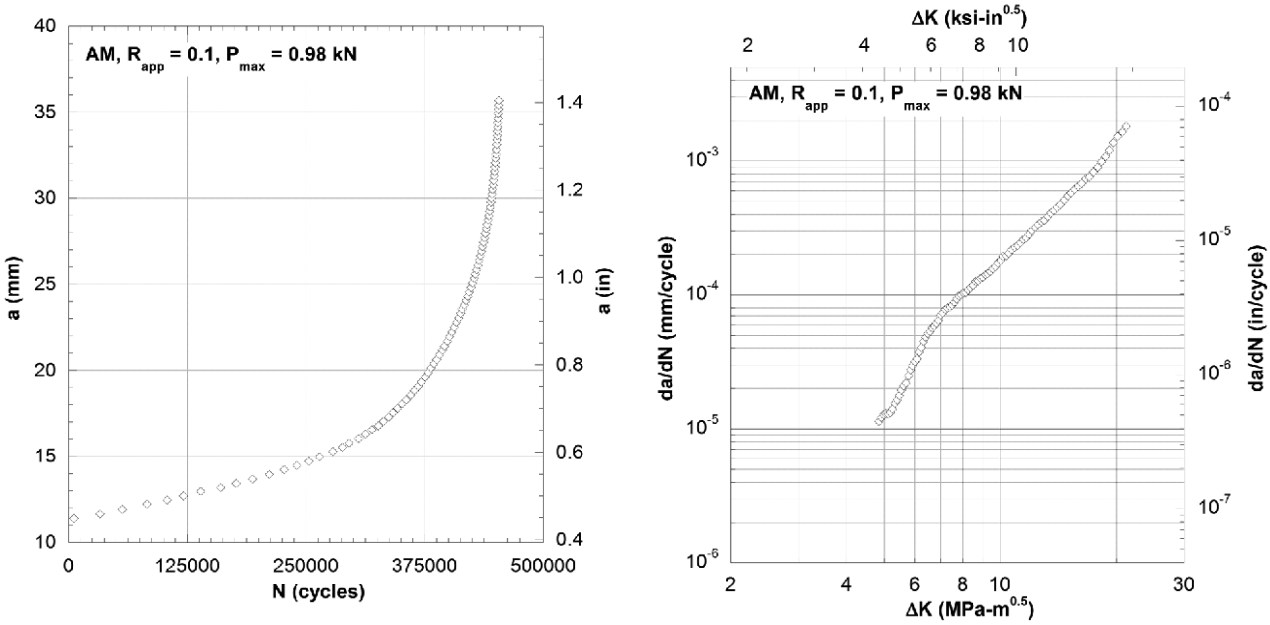

(a) (b)

Figure 6. The (a) a vs. N and (b) da/dN vs. ΔK_{app} for an AM Coupon Tested With Constant $P_{\max}$ = 0.98 kN and R = 0.1 (every third data point plotted)

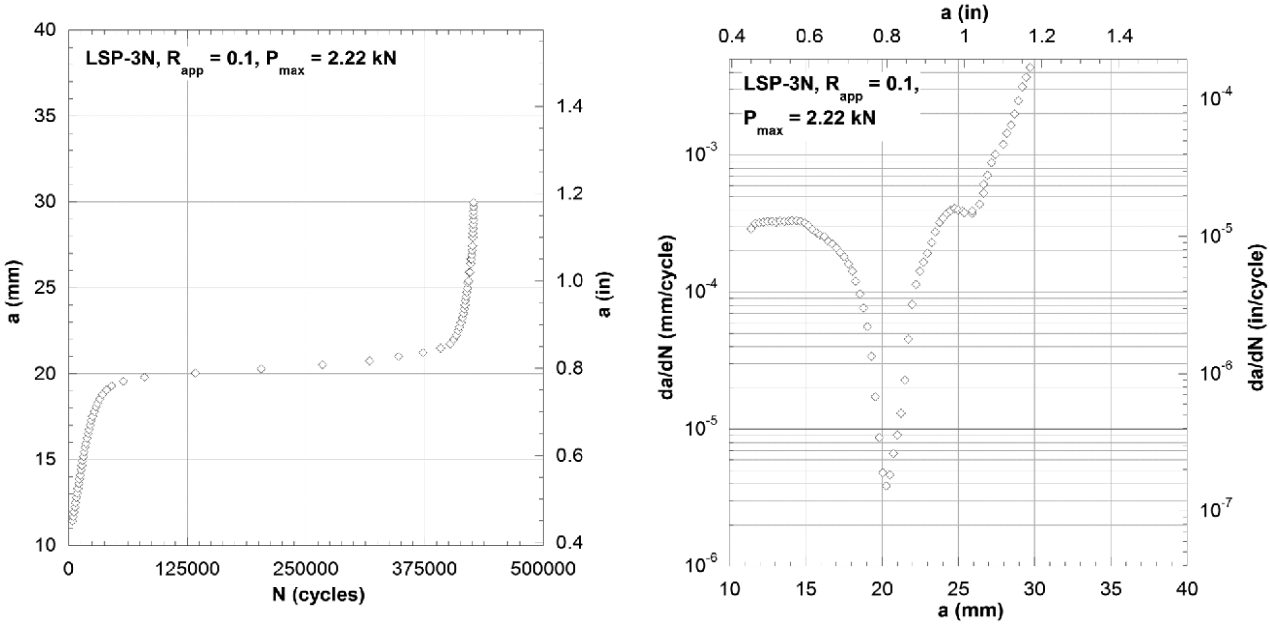

(a) (b)

Figure 7. The (a) *a* vs. *N* and (b) *da/dN* vs. *a* for an LSP Coupon Tested With Constant P_{max} = 2.22 kN and R = 0.1 (every third data point plotted)

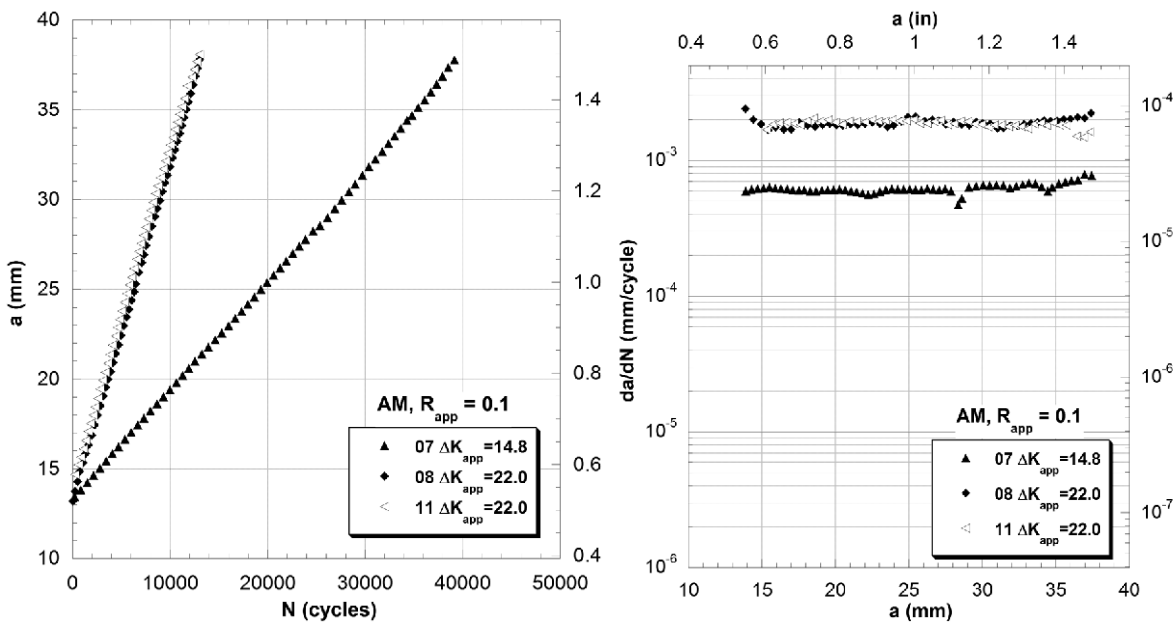

(a) (b)

Figure 8. The (a) *a* vs. *N* and (b) *da/dN* vs. *a* for an AM Coupon Tested With Constant ΔK_{app} and R_{app} = 0.1 (every fifth data point plotted)

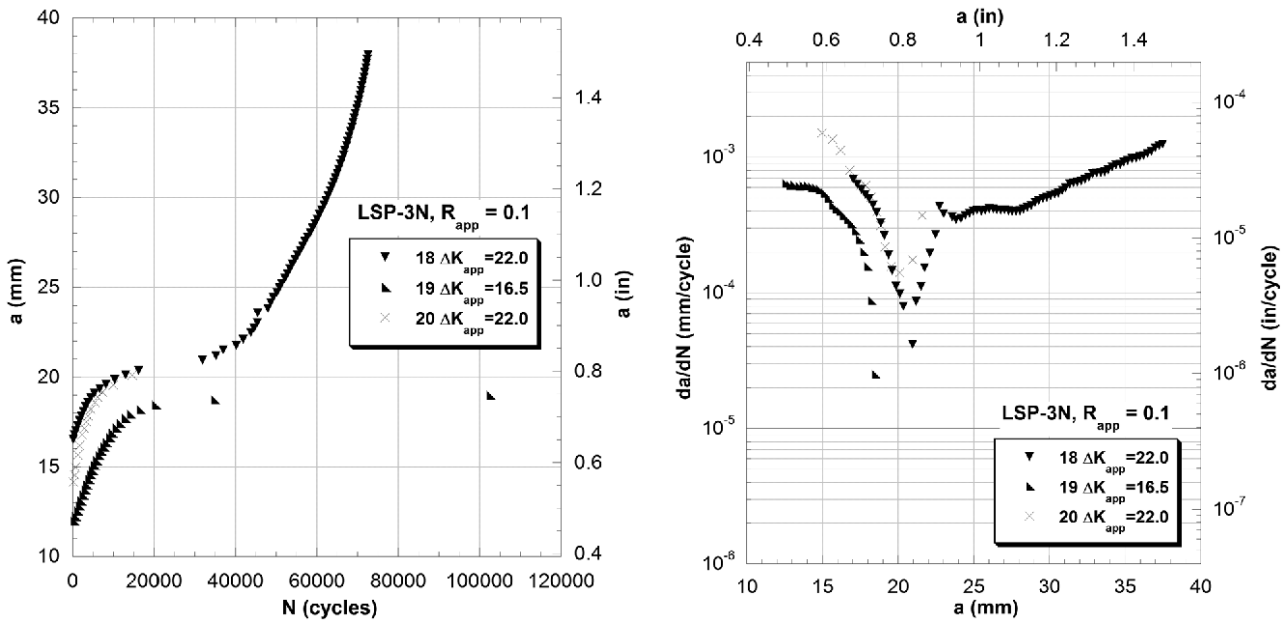

(a) (b)

Figure 9. The (a) *a* vs. *N* and (b) *da/dN* vs. *a* for LSP Coupons Tested With Constant ΔK_{app} and R_{app} = 0.1 (every third data point plotted)

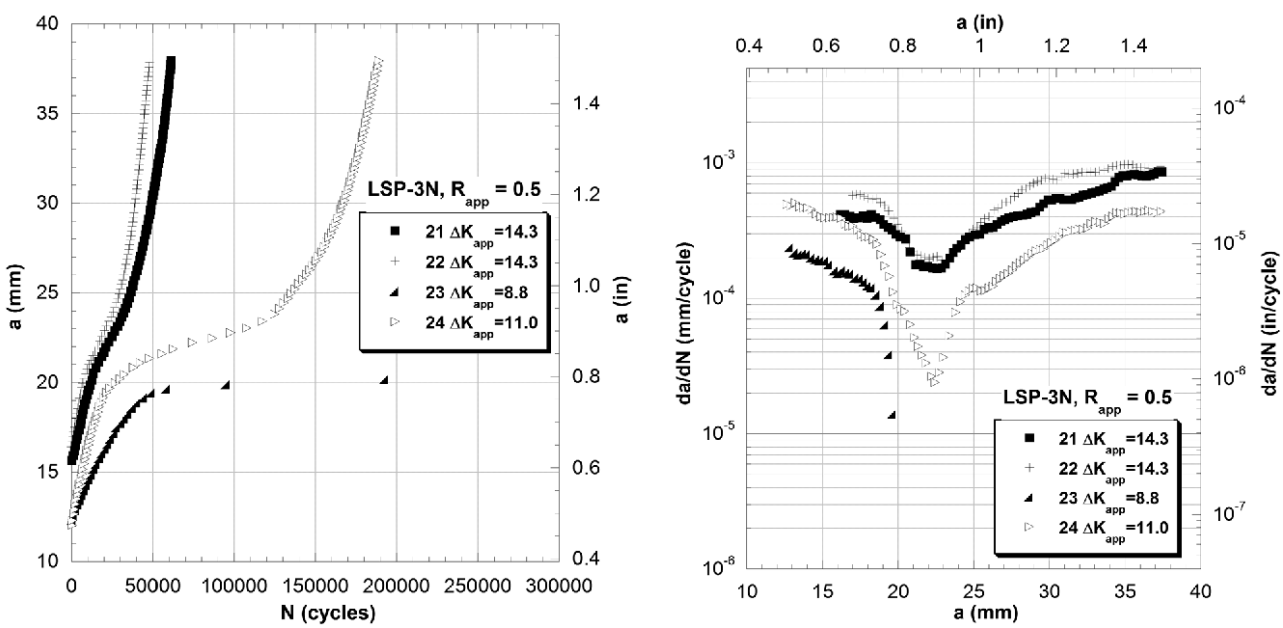

(a) (b)

Figure 10. The (a) *a* vs. *N* and (b) *da/dN* vs. *a* for LSP Coupons Tested With Constant ΔK_{app} and R_{app} = 0.5 (every third data point plotted)

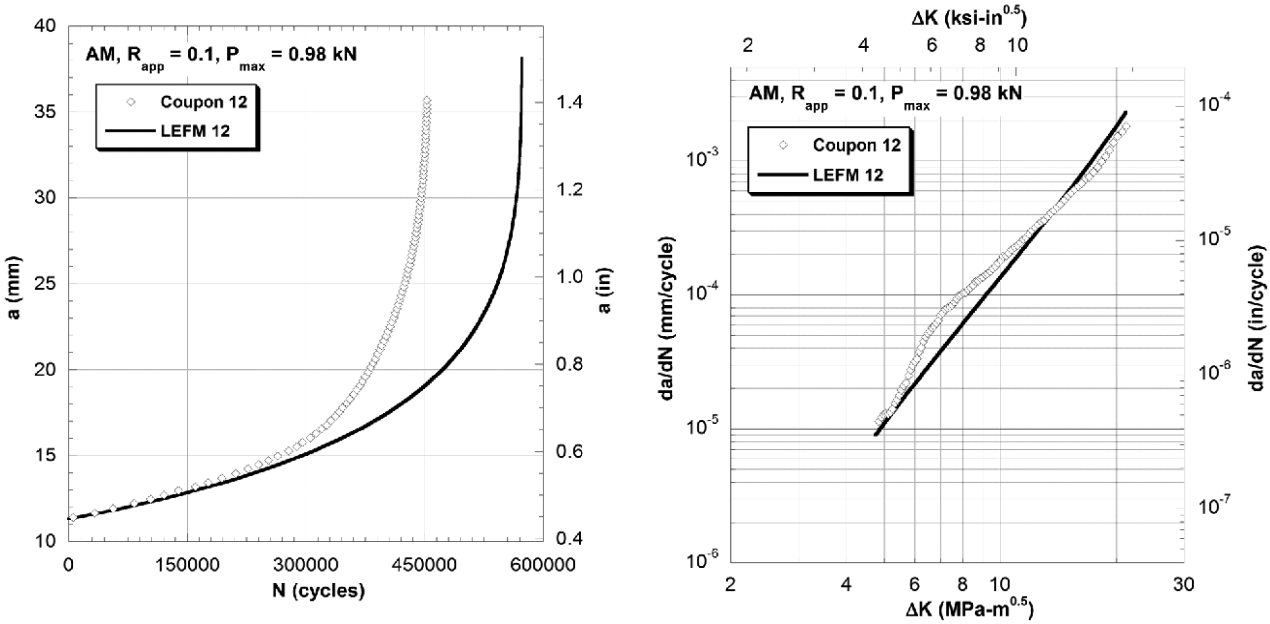

(a) (b)

Figure 11. The (a) a vs. N and (b) da/dN vs. ΔK_{app} LEFM Predictions for an AM Coupon Tested With Constant $P_{\max}$ = 0.98 kN and R = 0.1 (every third data point plotted)

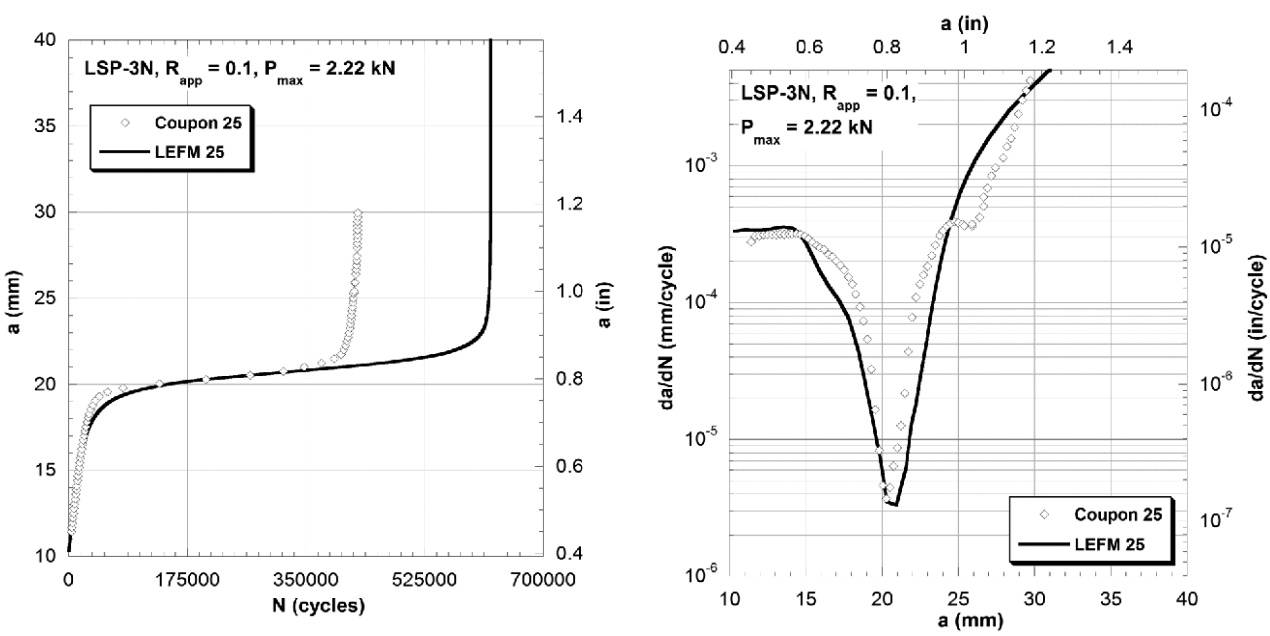

(a) (b)

Figure 12. The (a) a vs. N and (b) da/dN vs. a for LEFM Predictions for an LSP Coupon Tested With Constant $P_{\max}$ = 2.22 kN and R = 0.1 (every third data point plotted)

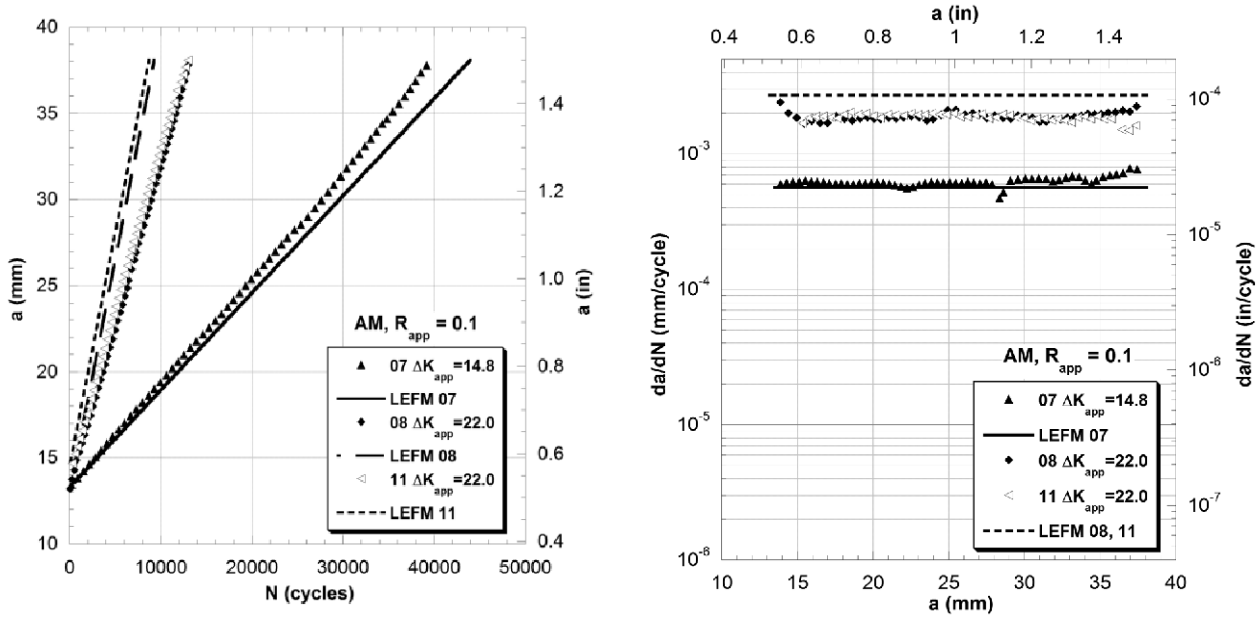

(a) (b)

Figure 13. The (a) *a* vs. *N* and (b) *da/dN* vs. *a* for LEFM Predictions for AM Coupons Tested With Constant ΔK_{app} and R_{app} = 0.1 (every fifth data point plotted)

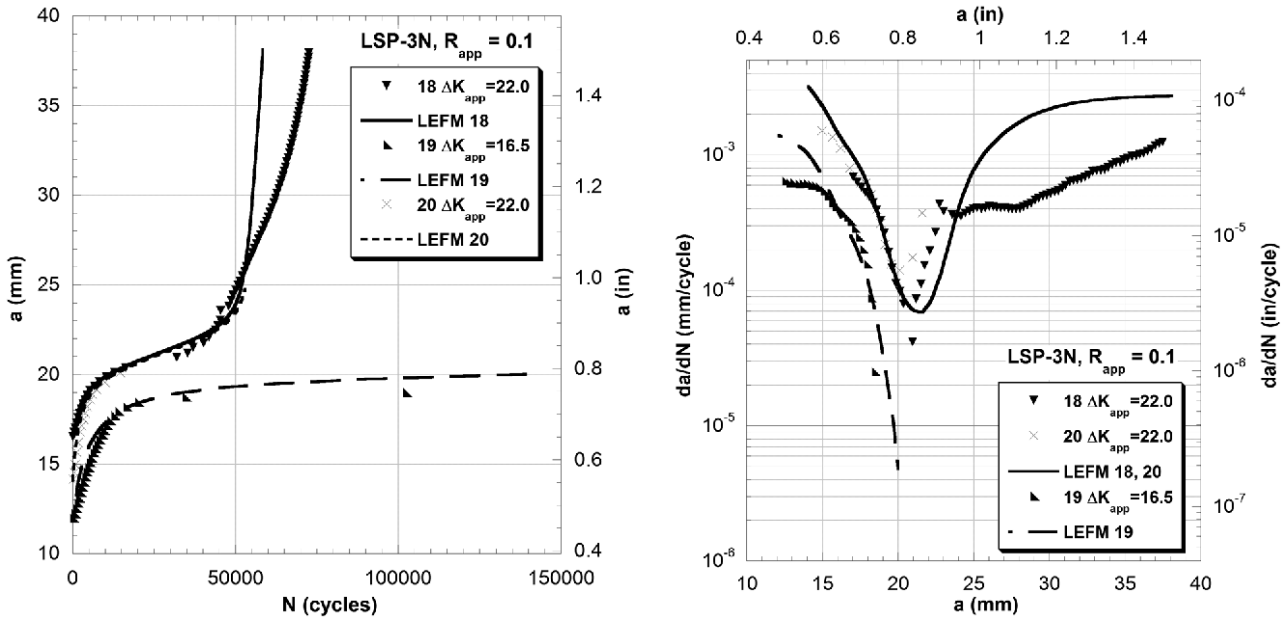

(a) (b)

Figure 14. The (a) *a* vs. *N* and (b) *da/dN* vs. *a* for LEFM Predictions for LSP Coupons Tested With Constant ΔK_{app} and R_{app} = 0.1 (every third data point plotted)

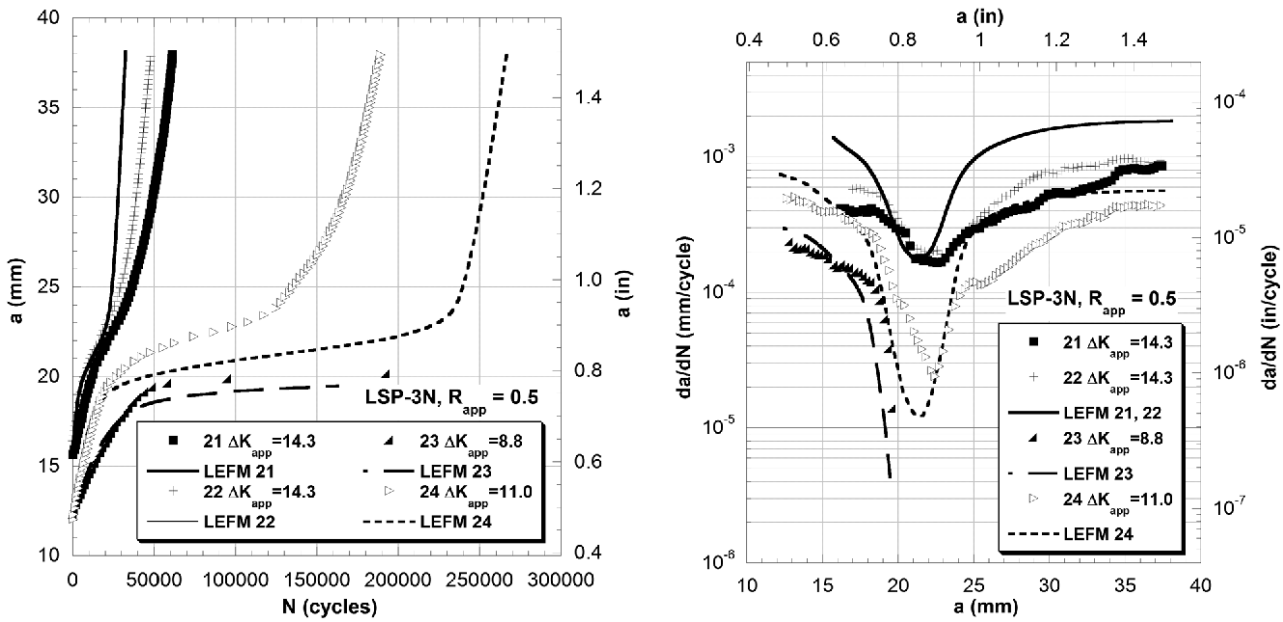

(a) (b)

Figure 15. The (a) *a* vs. *N* and (b) *da/dN* vs. *a* for LEFM Predictions for LSP Coupons Tested With Constant ΔK_{app} and R_{app} = 0.5 (every third data point plotted)

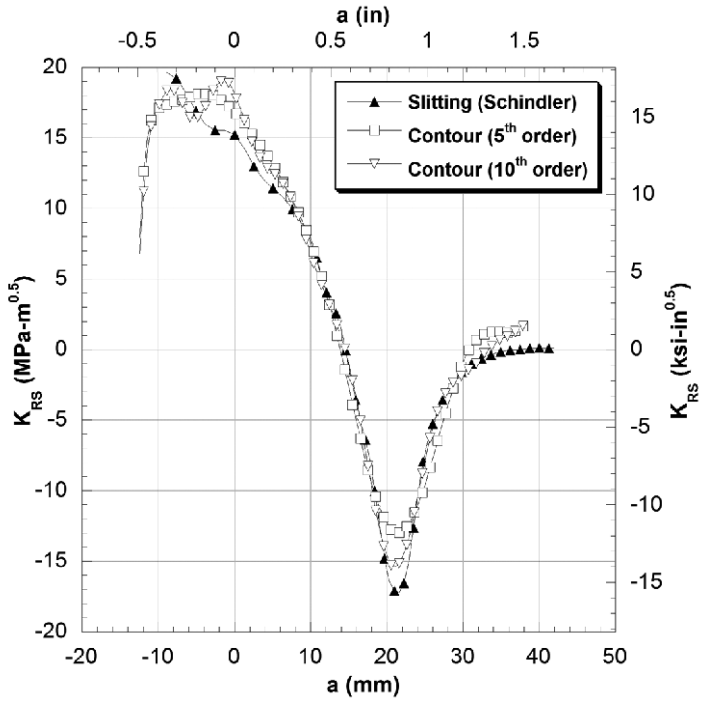

Figure 16. The K_{RS} Measured Using the Slitting and Contour Methods

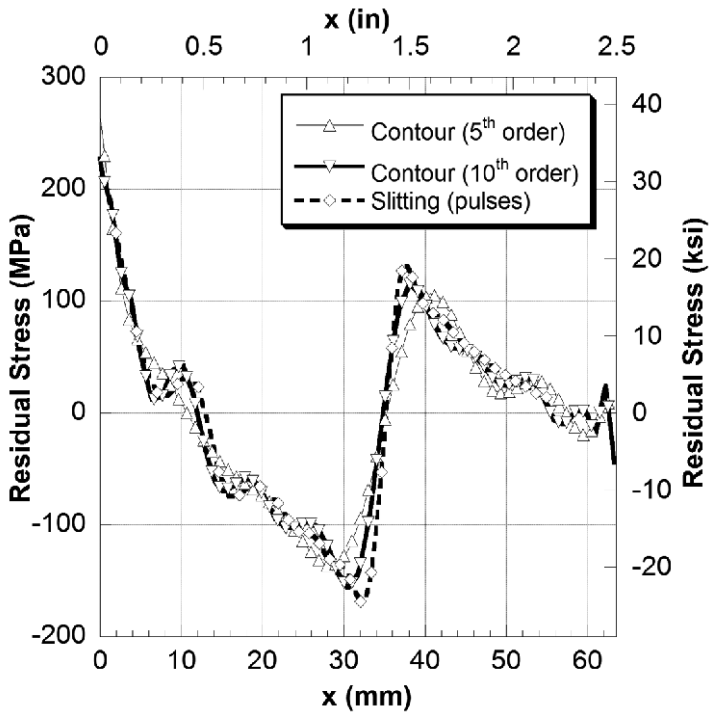

Figure 17. Through-Thickness Average Residual Stress Computed Using the Contour and Slitting Methods (every other data point plotted)

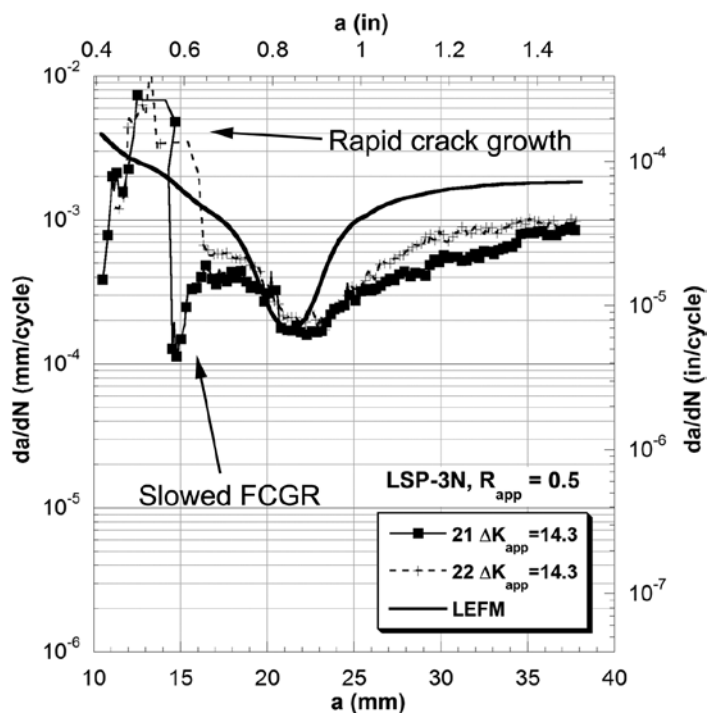

Figure 18. Coupons 21 and 22 Showing Rapid Crack Growth During Precracking as a Result of Combined Applied and Residual SIFs, and Subsequent Slowing of Fatigue Crack Growth Rate

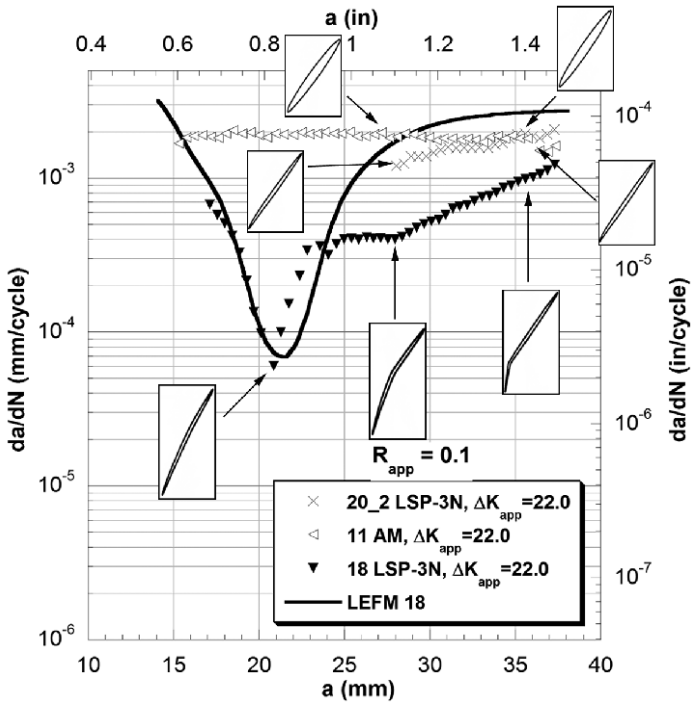

Figure 19. Coupon 20_2 (every fifth data point plotted) Illustrating How Removal of the Material in the Crack Wake Removes Crack Closure Due to Elastic Relaxation (compliance loops for each coupon are included for clarity)

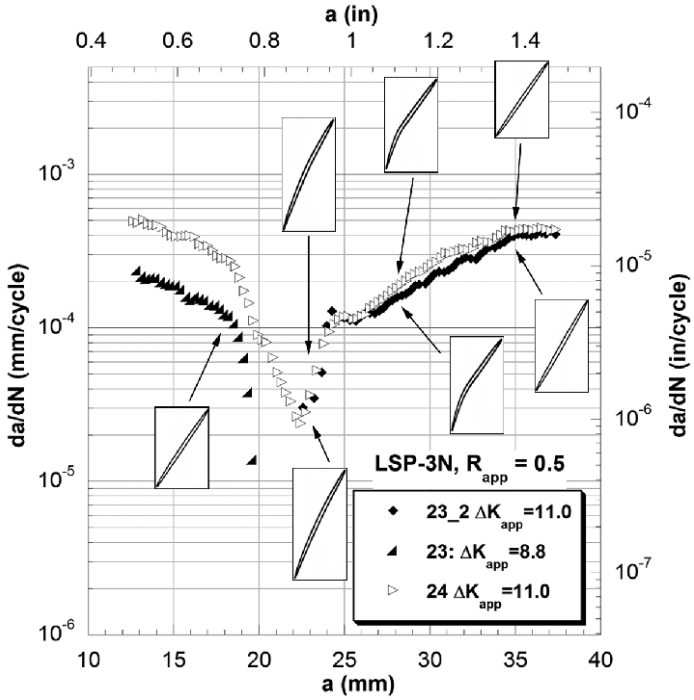

Figure 20. Coupon 23_2 (every third data point plotted) Illustrating Crack Growth Behavior for an Arrest Case, Which Had K_{app} Raised and Testing Continued

3. THE 1D CRACK GROWTH AT COLD-EXPANDED OPEN HOLES.

3.1 INTRODUCTION.

This section presents experimental and analytical work regarding the growth of 1D cracks from CX open holes. To predict the fatigue crack growth history of coupons without residual stresses, LEFM has been widely used with good success [2]. To make the same type of predictions in coupons containing residual stresses, LEFM is used in conjunction with the principle of superposition. In the principle of superposition, SIFs are determined as the sum of SIFs from applied and residual stresses. The LEFM predictions with superposition have also been widely studied [25–28] but have been less successful in correlating observed and predicted crack growth behavior than typically found for tests in AM material.

A review of earlier work suggests that reported inaccuracies of superposition-based predictions might be due to a number of confounding factors rather than a fundamental problem with the superposition method. The presence of residual stresses in coupons and components may cause cracks to become 2D in configurations for which cracks in residual stress-free, AM materials are 1D. While methods to calculate SIFs for 1D cracks are straightforward and well established, SIFs for 2D cracks are more difficult to calculate, and it can be unclear how to use these more complex SIFs to obtain accurate life predictions. In addition, residual stress-bearing materials often exhibit cracking at multiple sites or develop 2D crack shapes that are quite different from the elliptical-based shapes typically observed in tests of AM materials, and for which stress intensity solutions are readily available. Many of the earlier works on CX either included specimens that were quite thick, so that it was difficult to assume 1D crack growth [25–27, 29–39], or included multiple cracks per hole [27, 30, 34, 36, 40]. To understand the ability of superposition to correlate fatigue crack growth behavior at AM and CX holes, the present work uses a test setup that provides 1D crack growth of a single crack.

In fatigue testing of AM material, significant variability in crack growth history will exist within sets of identically prepared tests, and it should be expected that variability will increase where materials are treated with an additional residual stress-inducing process. However, some of the earlier work includes only one [27, 38, and 41] or two [30, 36, and 42] replicate tests per material condition. The present program includes at least three replicate coupons in each test condition in an effort to assess average crack growth behavior and its variation.

Although lifetime prediction is an important metric, reporting predicted lifetime alone, or even plots of crack size versus loading cycles, does not provide sufficient information to allow an understanding of the degree of correlation between models and experiments. Instead, reporting crack growth rate as a function of crack length allows clearer evaluation of model accuracy throughout the life. Further, it has been demonstrated that the method used to compute the FCGR from the basic laboratory data (pairs of crack size and number of cycles) can significantly affect the value of FCGR reported [43]. Much of the earlier work either did not report observed FCGR or did not report the method used to determine it [3, 27, 30–34, 37, 38, 40–42, and 44]. The present work includes a careful assessment of FCGR calculation and reports all test results in terms of FCGR versus crack size.

A model that predicts crack growth history depends on a number of factors that must each be performed accurately to make useful forecasts of FCGR and crack growth history. One basic element included in all LEFM prediction schemes is a correlation of FCGR with the range of intensity factor (ΔK) and stress ratio (R). For a number of materials, including high-strength aluminum alloys, FCGR behavior is not predicted accurately by a simple power law relation. Despite this fact, many studies [25, 27, 33–35, 37, 38, and 40] include predictions using power-law-based approximations (e.g., the NASGRO [45] equation) and this can lead to significant differences between observed and predicted behavior. The present work makes use of an FCGR prediction scheme based on a tabular lookup and significantly improves the agreement between observed and predicted behavior.

Fatigue crack growth behavior can be highly dependent on the residual stress distribution contained in test materials. Kokaly et al. [30], working with CX coupons, found in one instance that a ±1% variation in residual stress led to an approximate ±30% variation in predicted crack growth lifetime where the combination of applied and residual stresses was in the near threshold regime (very slow crack growth). It should be noted, however, that the degree of variability depends on the proximity to the FCGR threshold, with crack growth history at lower levels of applied stress having a greater sensitivity to residual stress variability. It is clear that residual stresses have to be carefully estimated to be able to achieve accurate prediction of fatigue crack growth.

A number of methods have been used to determine residual stress distributions in materials having CX holes [2], including models (both closed-form and FE) and measurements (x-ray diffraction [XRD], neutron diffraction [ND], the Sachs method, and contour method). In predicting fatigue crack growth at CX holes, the fidelity between the residual stress field used in predictions and that contained in the test articles will have a significant effect on the degree of correlation between observed and predicted behavior.

In forecasting the behavior of carefully designed CX test articles, residual stress measurements might be preferred over models, and previous studies have used a number of measurement techniques. Ball [27], de Matos [41], and Lacarac [44] found XRD to be noisy and unable to determine a reliable through-thickness distribution of residual stress. The lack of useful XRD results led to the use of a model in place of measurements (for which Ball used a closed-form model and de Matos used an FE model) or an alternative experimental method (for which Lacarac used the Sachs method). Conversely, Zhang et al. [39] found their XRD results compared well to their closed-form solutions. Stefanescu found ND results similar to XRD [46], and Smith et al. [47] and Lacarac et al. [42] found that Sachs compared well with results of an FE model, except close to the hole (which is the most important region).

Many papers point to the presence and importance of understanding the through-thickness variation in residual stress, which arises from the mechanical details of mandrel entry to and exit from the hole during processing [1]. They also point to the inadequacies of closed-form models, as well as XRD, ND, and the Sachs method to resolve the through-thickness variations. Zhang et al. [48] and Ismonov et al. [49] both found that the contour method provided measured through-thickness residual stress fields that compared fairly well to 3D FE, although it did not perform as well when it was close to the coupon entry and exit surfaces.

The main objective of this research is to evaluate superposition-based LEFM for prediction of crack growth at cold-expanded holes in thin sheet. The following secondary objectives have been set to avoid confounding factors that affected previous work. Fatigue coupon geometry, initial notch size, and applied stress levels are chosen to ensure 1D propagation of a single crack from the hole. Multiple replicate tests are performed for each test variation to robustly establish experimental trends. Experimental FCGR data are carefully computed from the basic test data. Crack growth rates for predictions are determined from tabular lookup FCGR-ΔK relationships based on literature data from various stress ratios. Lastly, residual stresses are measured on multiple coupons using the contour method because of its relatively high accuracy and ability to measure through-thickness residual stress variation; both average residual stress and coupon-to-coupon variation are included in predictions of fatigue cracking.

3.2 METHODS.

3.2.1 Coupon Geometry and Material.

Long, dog-bone shaped open hole coupons were cut from 2.03 mm thick 7075-T6 sheets, with the long axis of the coupons along the rolling (*L*) direction. Equal numbers of coupons were cut from clad and bare sheets, with coupon designations including *C* for those cut from clad sheet and *B* for those cut from bare sheet. Mechanical properties for 7075-T6 sheet are listed in table 4, as found in MIL-HDBK-5H [50]. The 2.03 mm (0.080 in) sheet thickness is typical of rotorcraft fuselage structure, and is thin enough to ensure that crack lengths are approximately constant through the coupon thickness (1D cracks). A dog-bone shape was chosen over a constant-width coupon to avoid problems of failure at the grips due to fretting fatigue, as occurred for earlier tests of straight coupons [51]. The coupon is 381 mm total length and 88.9 mm width at the gripped ends. The gripped ends taper to a central gage section 44.5 mm wide and 88.9 mm long with a centrally located hole 7.09 mm in diameter (figure 21[a]). The long central gage section ensures initial uniform applied stress at the crack plane and is longer than 1.2 multiplied by the gage width, as required for middle-crack tension (M(T)) coupons in ASTM E647 [4].

Split-sleeve CX was used to induce residual stress at the hole in half of the coupons [30]. Hole size and degree of cold working were selected to be typical of rotorcraft applications. Prior to CX, holes are drilled to a 6.35 mm diameter. The CX sleeve is oriented so that the split is parallel to the long axis of the coupon and sized to obtain a 3% interference fit with the tapered mandrel. After CX, the holes are reamed to a 7.09 mm diameter to remove any undesirable features left by the CX process. The AM coupons have holes drilled and are then reamed using the same tooling used on CX coupons so that their final diameter is also 7.09 mm.

A fatigue starter notch at the edge of the hole is cut using a wire EDM; it is 0.127 mm wide, 0.254 mm long, and of constant length through the thickness.

3.2.2 Residual Stress Measurement.

Residual stress distributions (2D) from CX are measured along the crack plane using the contour method. The AM coupons were assumed to have insignificant magnitudes of residual stress and, therefore, were not measured. Full details regarding the contour method for residual stress

measurement are available in the literature [17 and 18]. The method involves four steps: cutting the coupon in half to relieve residual stress on a plane through the coupon, measuring the deformed shape of the cut-plane (which is analogous to the pre-cut residual stress), fitting of the deformation data to a smooth surface, and calculating the pre-cut residual stress using a 3D elastic FE analysis. To economize on material, residual stress measurements are made on small coupon blanks (sized 88.9 x 44.5 mm) without notches (figure 21[b]) and fabricated using the same methods used for fatigue coupons. Following the steps of the contour method, each specimen was carefully clamped and then cut in half along the center plane using a wire EDM (where the center plane corresponds to the plane of crack growth in the fatigue coupons). A laser scanning profilometer was used to measure out-of-plane deformation of the cut surface. To filter out the effects of cut-path wandering and shear stress [17], the deformations from each side of the cut were averaged together; to remove the effects of cut-surface roughness and measurement noise, the surfaces were fit to an analytically smooth surface. A 3D FE model was created using post-cut, half-coupon geometry, and the negative of the averaged, smoothed surface deformations applied as displacements on the cut-surface of the model. The stress distribution on the cut-plane of the FE model provides the estimate of residual stress on the plane of the coupon. Measurements of residual stress were performed on three coupon blanks—one bare and two clad—to quantify average residual stress from CX and its variability: because each measurement included residual stress fields on two sides of the hole (which we refer to as left and right sides), the measurements provided six distributions of residual stress for further analysis.

3.2.3 Fatigue Testing.

Fatigue crack growth tests were performed at constant amplitude stress using a servo-hydraulic computer-controlled load frame. Static calibration was performed to ensure the coupons were stressed in pure tension (no bending) [52]. The machine was also dynamically calibrated to ensure that coupon strain levels at the cyclic testing frequency were as prescribed [53]. Three variables were investigated in the test matrix to determine the influence of each variable on crack growth history. Residual stress condition was compared by testing CX and AM coupons, applied stress ratios were compared by testing coupons at $R = 0.1$ and $R = 0.5$, and material condition was compared by testing clad (*C*) and bare (*B*) coupons. To understand variability, at least one replicate test was performed for each of the eight test variations. Early testing showed no significant or consistent difference between residual stress or crack growth behavior in clad and bare coupons, so that experimental trends were established by considering results from clad and bare coupons as a single population of (at least) four coupons per variation of residual stress and applied stress ratio. Applied stress levels (based on gross section area) for each of the test variations were chosen to achieve lifetimes of approximately 200,000 cycles and were based on preliminary residual stress estimates and LEFM predictions. Initial tests were performed to iterate stress levels and ensure useful test durations. Final stress levels are shown in table 5.

3.2.4 Crack Length Measurement.

During fatigue cycling, tests were stopped at inspection periods to collect crack length data. Two methods were used for making crack length measurements in the coupons: direct current potential difference (DCPD) and digital photomicroscopy (DP). The DCPD method was used to

collect the crack length data while the DP method was used in parallel in early testing to validate the DCPD method.

Test control software (TCS) (see figure 22) was developed to pause cycling at each inspection period, open the crack mouth by applying 80% of maximum applied cyclic stress, trigger measurements, and continue cycling once measurements were complete.

3.2.4.1 The DP Crack Length Measurement.

For the DP method, a digital camera was pointed at a face of the coupon with the field of view such that a 6.35 mm long crack could be measured. A combination of a 25 mm extension tube, a 2X teleconverter, and a 100 mm macro lens allowed for a field of view of roughly 9 mm at a working distance of 127 mm with an optical magnification of 2.4X. A Canon digital Rebel XT DSLR with an 8 megapixel camera body allowed resolution of approximately 2.53 µm per pixel. Images were captured with a small aperture (f 13) and low ISO (100) to maximize depth of field and sharpness, and to minimize noise [54]. Several steps were taken to minimize vibration to ensure sharp images [54], including the use of a stiff camera stand and mirror lockup. A flash was placed at an oblique angle to illuminate and define the crack tip location. Flash location and exposure length were selected to obtain good crack tip illumination.

Coupons were prepared for DP by polishing and marking with a reference scale. The coupons were polished with cotton gauze and 1 µm diamond polish until a mirror finish was achieved. Initial testing identified the importance of a mirror finish to facilitate locating the crack tip in the images [54 and 55]. A reference scale on the coupons was created with small marks, 6.35 mm apart, lightly scored on the surface of the coupon away from the crack plane and parallel to the loading direction using a height gage equipped with a scalpel and granite table.

The TCS triggered DP measurements using 5V signals and relays to wake up the camera, charge the flash, and capture the image (see figure 22).

To obtain crack lengths, images were analyzed in digital image manipulation software [56]. First a correlation was made between the known length between calibration marks and the corresponding number of pixels in the photo. Then, all of the photos were opened as different layers in one file and automatically arranged to ensure they overlapped exactly. This was necessary because as the crack grew, the coupon became more compliant and the crack location shifted in the field of view. In some photos, it was difficult to recognize the crack tip. The layered photographs allowed comparisons between neighboring inspections, making precise location of the crack tip easier. Crack lengths were then measured from the edge of the hole to the crack tip for each inspection period.

3.2.4.2 The DCPD Crack Length Measurement.

The DCPD method correlates a voltage to a cracked area [4]. When current is applied through the coupon, a voltage drop can be measured across discontinuities in the material such as holes and cracks. Leads placed on either side of the crack surface will read an increasing voltage as the crack progresses and reduces the area of conductivity. Crack lengths are determined by

correlating voltage measurements to crack lengths using a calibration function for the coupon geometry and electrical lead locations.

Coupon preparation for the DCPD method required drilling holes to fasten electrical leads and adding plastic sheets to the grip area for electrical isolation. Fasteners were chosen as the attachment method because heat from welding/soldering is more likely to affect the residual stress fields than machining holes. One set of close fit holes was drilled for #0-80 fasteners for the measurement leads while two tapped and threaded holes were made for #6-32 current source leads (see figure 21[a]). Voltage measurement leads were 12.7 mm apart, which was deemed close enough for good DCPD resolution without the small lead holes affecting the CX residual stress. Current leads were placed 254 mm apart, which is more than three times the coupon gage width (133.4 mm); this ensures uniform current density [57]. Styrene sheet 0.508 mm thick was cut to match the size of the coupon's grip area and attached using cyanoacrylate to electrically isolate the coupon [4].

All of the electrical leads were attached to the coupon using ring terminals crimped and soldered to grounded, shielded wires with nuts and bolts. The voltage leads used No. 26 AWG copper wire while the current leads used larger No. 18 AWG copper wire. Positive and negative voltage leads were attached on opposite faces of the coupon to obtain a through-thickness average crack length and compensate for non-uniform crack front shapes [57].

The DCPD measurements were triggered in the same way as for the DP method, through the TCS (see figure 23). The DCPD measurement system is comprised of a computer (separate from the TCS) running DCPD Control Software (DCPD CS), a DC current source, a data acquisition unit (DAQ), a precision voltmeter, and a polarity switching unit. A signal is sent from the TCS to the DAQ, where the DCPD CS recognizes it as the start signal. The DCPD CS then communicates to the current source to turn on and provide 17A of DC current. At the same time, it communicates through the DAQ to the polarity-reversing circuit to switch polarity. The polarity circuit is constructed with a high-capacity DPDT relay to reverse the current direction when triggered. The current reversing circuit was used to help eliminate error due to thermal EMF and drift [58 and 59]. Next, the DCPD CS instructs the voltmeter to take readings and record them in a data file. Five sample measurements are taken in a series and are averaged over 10 power line cycles (60 Hz) to help negate the influence of noise [57]. The DCPD CS then repeats that process, switching the polarity and taking measurements until it has taken 10 sets of measurements for each polarity direction. The DCPD CS then turns off the current supply and awaits the next trigger from the TCS, signaling the beginning of the next inspection period.

3.2.4.3 The DCPD Data Reduction.

By carefully reducing the raw DCPD data, noise and drift in the measurements were decreased. There are 100 voltage measurements taken per inspection period: 10 sets of measurements, each with two polarity directions, and five measurements per polarity direction. First, the mean of the five samples per polarity direction is taken. Next, the differences between the means in each polarity direction are taken and divided by two. Finally, the mean of the resulting 10 measurement sets is taken, reducing the data to a single value per inspection period. For each inspection period, the voltage value is normalized by the voltage measured at 20,000 cycles. A normalization point at 20,000 cycles was chosen to allow sufficient time for the voltage lead

connections to reach a stable contact resistance with the coupon. Before that point, fretting between the coupon and connector surfaces creates variability in contact resistance, which affects measured voltage. The choice of 20,000 cycles was reasonable because no crack growth was found with the DP method before 20,000 cycles for any of the test variations.

3.2.4.4 The DCPD Voltage vs. Crack Length Correlation.

An FE-based correlation was created to convert voltage data into crack length data following methods described by Ritchie and Bath [60]. Boundary conditions were used to describe the extent of the coupon geometry, hole, and crack. Current inputs were modeled as point sources. Potentials at the location of the DCPD voltage leads were then determined for an array of crack lengths. Crack length versus voltage results were then expressed as a correlation of crack size a in terms of voltage as a function of crack length $V(a)$:

$$a(x) = 0.5(W - D)\left(-0.0516x + 0.98633x^2 - 2.14607x^3 + 3.70705x^4 - 1.49664x^5\right) \quad (4)$$

where W is the coupon gage width (44.5 mm), D is the hole diameter (7.09 mm), and:

$$x = \left(\frac{V(a)}{V(a=0)} - 1\right)^{(1/4)} \quad (5)$$

Because the initial DCPD measurements were taken with a notch in the coupon of length a_n, a nonlinear root-finding routine is required to determine $V(a = 0)$ from a_n and $V(a = a_n)$.

3.2.4.5 Crack Growth Rate Determination.

To determine FCGR from measured pairs of (a, N) data, a method was needed that could achieve two specific goals. First, the method needed to compute FCGR when it is small compared to crack length uncertainty (u_a) divided by inspection-frequency ΔN (i.e., $da/dN \ll u_a/\Delta N$) to filter the effects of noise in crack length measurements early in the test. Second, the method needed to be able to calculate FCGR in areas of high FCGR gradient, caused in this case by the open hole geometry and residual stress present. It was found that the polynomial regression method described in ASTM E647 [4] did not achieve the aforementioned goals, and instead the modified incremental method of Larsen, Jira, and Ravichandran [54] was adapted for this work. The modified incremental method uses regression intervals based on intervals in crack length (Δa) rather than intervals being based on a number of points, as in ASTM E647. Each regression interval is separated from the previous and subsequent intervals by Δa and includes a range of data $\pm 3\Delta a$ (see figure 23). All data points within the $\pm 3\Delta a$ interval are used in a regression for which the FCGR is calculated at the center based on the slope of a polynomial fitted to the data. If the regression interval ended up with fewer than seven points, the interval range was incrementally increased by $\pm\Delta a$ until seven points were included.

To work better with data from the open hole tests, two changes were made to the modified incremental method. First, a cubic polynomial was used for regression because it was found to estimate slope better than the quadratic polynomial used by Larsen, et al. [54] in areas of high

FCGR gradient (see figure 24[a]) and work equally as well as the quadratic in areas of low FCGR gradient. A second change was required because collecting crack length data at even intervals of ΔN leads to sparse data at long crack lengths with high FCGR, causing intervals of $\pm 3\Delta a$ to have many points over the $-3\Delta a$ half-interval and few points in the $+3\Delta a$ half-interval. In the present research, some $\pm 3\Delta a$ intervals had only a single data point in the $+3\Delta a$ half-interval, which led to an imbalanced weighting of the regression and, consequently, erroneously small values of FCGR (see figure 24[b]). To obtain a more balanced distribution of points, the $\pm 3\Delta a$ interval was increased on the high side until the $+3\Delta a$ half-interval included two points, which was found to provide good estimates of FCGR. As a final step following FCGR computation at intervals of Δa, FCGR is interpolated at the measured crack lengths and corresponding even intervals of ΔN.

Trial and error was used to find a value for Δa that would provide useful trends of FCGR for all tests in this study, and the trials provided a value of Δa of 0.05 mm.

3.2.4.6 LEFM Predictions.

To predict the crack growth history from an initial crack length of 0.381 mm to a final length of 7.62 mm, LEFM was used. For a set of steps in crack length, SIFs are calculated for applied and residual stress distributions using the weight function approach developed by Wu and Carlsson [61], but based on new FE models specific to the present coupon geometry. The Wu and Carlsson approach requires the crack-line stress in the uncracked geometry under a reference loading $S(x)$, and the SIF as a function of crack size for that geometry and loading $K(a)$. For the open hole single crack geometry, Wu and Carlsson include power series expressions for $S(x)$ and $K(a)$ for coupons with gage width-to-hole diameter ratios (W/D) ranging from 2–5. For the present coupon, with $W/D = 6.27$, it was simple to develop FE analysis results for $S(x)$ and $K(a)$, and to use the new results in the approach by Wu and Carlsson to define the weight function. The SIFs from the weight function for $W/D = 6.27$ were roughly 2% different from the SIFs computed from the weight function for $W/D = 5$, which is significant considering the rough power-law dependence between SIF and FCGR.

A superposition of the SIFs for applied and residual stress provided values of ΔK and R:

$$\begin{aligned} K_{tot,\max} &= K_{app,\max} + K_{RS} \\ K_{tot,\min} &= K_{app,\min} + K_{RS} \\ R &= K_{tot,\min}/K_{tot,\max} \\ \Delta K &= K_{tot,\max} - K_{tot,\min} \end{aligned} \tag{6}$$

where $K_{tot,\max}$ and $K_{tot,\min}$ are the maximum and minimum total SIFs, $K_{app,\max}$ and $K_{app,\min}$ are the maximum and minimum applied SIFs, and K_{RS} is the residual SIF.

The resulting ΔK and R values are used to find FCGR from a scheme based on crack closure concepts and a piecewise log–log fit for FCGR as a function of the effective SIF ΔK_{eff}. This scheme is based on methods described in detail by Newman [62]. Stress ratio dependence of FCGR is given in terms of ΔK_{eff}. The ratio between the crack opening stress (S_o) and maximum applied cyclic stress ($S_{\max}$) is expressed as a polynomial function of stress ratio [63]:

$$S_o/S_{\max} = 0.32566 + 0.0819R + 0.85923R^2 - 0.26679R^3 \tag{7}$$

ΔK_{eff} is related to ΔK, R, and $S_o/S_{\max}$ by:

$$\Delta K_{eff} = \Delta K \left(\frac{1 - S_o/S_{\max}}{1 - R} \right) \tag{8}$$

Equation (7) is derived from equations provided by Newman [63] with the fitting parameters $S_{\max}/\sigma_o$ and α set to 0.3 and 2, respectively. Data from FCGR tests in 7075-T6 sheet at stress ratios ranging from -1.0 to 0.8 [1, 63–65] are shown on a log-log plot of FCGR vs. ΔK_{eff} in figure 25, and demonstrate the ability of equations (7) and (8) to correlate FCGR at a wide range of R. A piecewise log-log curve is shown above the data, and is defined by the points given in table 6. Given these points, FCGR is then determined from ΔK and ΔK_{eff} using piecewise log–log interpolation:

$$\frac{da}{dN} = \frac{C_{1_i} \left(\Delta K_{eff} \right)^{C_{2_i}}}{1 - \left(\frac{\Delta K}{60(1-R)} \right)^2} \tag{9}$$

where FCGR is in units of m/cycle and ΔK and ΔK_{eff} are in units of MPa m$^{1/2}$. The coefficients C_{1i} and C_{2i} correspond to lines connecting the points in table 6, and the denominator in equation 9 accounts for elevation in FCGR as fatigue crack growth transitions to fracture.

The history of crack length a and cycle count N is calculated from FCGR as a function of crack length using numerical integration. Because of a large variation in crack growth rates for small crack lengths, small increments of growth are taken in the integration for small crack lengths.

3.3 RESULTS.

3.3.1 Residual Stress Measurements.

Residual stress distributions (2D; figure 26) along the crack plane (see figure 21[b]) show that the residual stress varies as a function of thickness and width position (x and y, respectively; figure 27). The distributions are fairly symmetrical through the thickness with generally higher (more tensile) residual stress levels at the mid-thickness and lower (more compressive) residual stress levels on the faces. Through-thickness average of the residual stress measurements simplify the 2D distributions to allow trends to be more easily understood as a function of length along the crack plane (x) (see figure 28). On average, thickness-average residual stress distributions are compressive for the first 2.0 mm from the edge of the hole, after which the residual stress distribution is mildly tensile. A minimum (compressive) residual stress of -452 MPa is measured at the hole with a maximum (tensile) residual stress of 42.2 MPa

occurring at 3.56 mm from the hole, after which point the distribution tapers to residual stress values of about 30 MPa. Little difference exists between the stress distributions from the left and right sides of the holes, bare and clad materials, and replicate tests (see figure 28). Consequently, an average of the six residual stress distributions from the left and right sides and bare and clad material conditions was taken as a representative residual stress distribution for crack growth analysis.

It is difficult to access accuracy of the contour method and the repeatability of the cold working directly. Accepting the present coupons as identical, a statistical analysis of the measurements allows for some understanding of overall variability. The standard deviation of the through-thickness average residual stress for the six residual stress distributions, taken at a given position in x, is less than 40 MPa (see figure 29), with the most variability near the hole. To aid in understanding how the variation in measured residual stress contributes to variation in crack growth behavior, we will carry forward a variation of ±10% in K_{rs} to bound expected variability. These values correspond approximately to the maximum standard deviation (40 MPa) divided by the maximum average residual stress magnitude (-452 MPa).

3.3.2 Crack Length Measurement Method.

For tests on bare sheets, the DP and DCPD methods crack length data were in agreement (see figure 30). The DCPD is better than DP for these tests for a variety of reasons, including easier system automation and data reduction methods, but most importantly, because DP is unable to resolve crack tip locations for coupons in clad material due to microcracking on the coupon surface that obscures the crack tip location (see figure 31). All subsequent results here are based on DCPD crack length data.

3.3.3 Observed and Predicted Crack Growth Behavior.

Geometry factors used in the LEFM predictions are illustrated in figure 32. K_{app} is normalized by applied gross stress and K_{RS} is normalized by material strength and is the negative of flow stress. The average between yield and ultimate strengths is -476 MPa.

Crack growth behavior observed in AM coupons is consistent with earlier literature data and the piecewise log–log fit of figure 25, as shown in figure 33. The NASGRO equation, a more simple relationship, does not fit the data well (see figure 33).

Fatigue crack growth history predicted by LEFM yields a smooth, increasing crack growth rate with crack extension in all coupon conditions (see figures 34–37). The prediction for AM coupons exhibits a steady increase in crack growth rate with the rate of increase larger for shorter cracks (<1.5 mm) than for longer cracks. By comparison, the prediction for CX coupons exhibits a trend similar to AM coupons, but with a much faster increase of FCGR with crack length for shorter cracks.

Crack growth behavior of bare and clad samples is nearly identical for all coupon conditions (see figures 34–37). Consequently, the bare and clad material conditions are considered together when comparing predicted and observed crack growth behavior among variations of stress ratio

and residual stress. Material condition is included in the coupon number and reported in plot legends, with *B* for bare and *C* for clad coupons.

For AM $R = 0.1$ coupons, experimental results compare very well with LEFM in both lifetime and FCGR (see figure 34). On average, cracks for the experimental results grew from 0.381 mm to 5.08 mm (the crack length range to define lifetime in these tests) in 147,000 cycles, with a range in lifetime from 132,000–163,000 cycles. The LEFM model predicts a lifetime of 148,000 cycles, which agrees with the average of the experimental results. Experimental FCGR data agree well with the LEFM predictions for the range of crack size.

For AM $R = 0.5$, experimental results also compare very well with LEFM in both lifetime and FCGR (see figure 35). On average, cracks for the experimental results grew from 0.381 mm to 5.08 mm in 197,000 cycles with a range in lifetime from 171,000–227,000 cycles. The LEFM model predicts a lifetime of 204,000 cycles, which agrees with the average of the experimental results. Experimental FCGR data agree well with the LEFM predictions for the range of crack size.

For CX $R = 0.1$ coupons, some noteworthy behavior exists in the experimental results (see figure 36). Initial crack length measurements for C080-08 show negative crack growth, and was the only instance of this behavior in our tests, which was likely due to drift in the DCPD signal. On average, cracks grew from 0.381 mm to 5.08 mm in 86,000 cycles with a range in lifetime of 29,000–160,000 cycles (see figure 36[a]). The LEFM model predicts a lifetime of 74,000 cycles, which is conservative by 14% when compared to the average of the experimental results. A ±10% variation in K_{rs} provides an LEFM lifetime prediction of between 36,000–163,000 cycles, which is in agreement with the range of observed coupon lifetime. The LEFM FCGR predictions are similar to experimental data for the range of crack size (see figure 36[b]).

For CX $R = 0.5$ coupons, experimental results compare fairly well with LEFM for FCGR, but are slightly nonconservative for lifetime (see figure 37). On average, cracks grew from 0.381 mm to 5.08 mm in 192,000 cycles with a range in lifetime from 128,000–261,000 cycles (figure 37 [a]). LEFM predicts a lifetime of 223,000 cycles, which is nonconservative by 16% when compared to the average of the experimental results. A -10% change in K_{rs} produces a lower bound life of 96,000 cycles, which is in reasonable agreement with the shortest observed life. A +10% change in K_{rs} results in $K_{\max} < 0$, a prediction of crack arrest and infinite life, which is obviously nonconservative. The LEFM predicts FCGR that is similar to, but higher than, most of the experimental results throughout the range of crack length (figure 37[b]).

Trends in variability of the experimental data are also evident. For purposes of discussion, we define variability as the range of observed lifetimes (maximum minus minimum) divided by the average lifetime. For AM coupons, variability at $R = 0.1$ and 0.5 was similar, being 21% and 28%, respectively. For CX coupons, variability at $R = 0.1$ and 0.5 was 152% and 69%, respectively. The greater variability for CX coupons compared to AM coupons is apparently due to variability of residual stress among the coupons, and may also be influenced by a greater degree of crack-face contact occurring in the presence of the compressive residual stresses (which is consistent with the significantly reduced variability found in CX coupons tested at $R = 0.5$ relative to CX coupons tested at $R = 0.1$).

3.4 DISCUSSION.

3.4.1 Correlation of Observed and Predicted Lifetime Variability.

An expected variation in predicted fatigue crack growth life of CX coupons was calculated based on variability of measured residual stress. Although residual stress variability is not the only source of variation in crack growth history, it appears to be a dominant factor in the present tests because variability in AM tests was very small (21%–28%). This observation is consistent with previous work on CX coupons [30]. At $R = 0.1$, the observed variation of ±10% in measured residual stress (see figure 28) is predicted to produce lifetime variation of 170%, which compares well to the 152% observed variation. At $R = 0.5$, the same residual stress variation provides a lower bound of lifetime that is in reasonable agreement with the experimental results (see figure 37), but an upper bound of infinite lifetime (crack arrest) that is nonconservative. Clearly, accurate estimates of the average and variability of residual stress induced by CX are fundamental to understanding crack growth behavior in CX materials.

3.4.2 Prediction Verification.

To ensure that predictions would be accurate, a number of verification steps were taken. Predictions were first made for the AM cases, then compared to two commercial software packages, AFGROW [66] and NASGRO [45]. Geometry factors for the predictions matched exactly to the NASGRO solution and were within a few percentage points of the AFGROW geometry factors. Custom software was developed instead using commercially available products for a number of reasons. AFGROW did not offer weight function solutions for the open hole geometry with a single-sided crack, whereas NASGRO limits residual stress distribution inputs to a finite-sized array, thus limiting resolution. Furthermore, it is unclear whether each commercial package can determine FCGR from ΔK and R using the closure-based piecewise scheme suggested by Newman [62] and given by equations (6–9). Custom software allowed for the verification and understanding of all aspects of the LEFM predictions. The two commercial codes, NASGRO and AFGROW, should provide similar results to those reported here (provided the user carefully selects model options and supplies accurate input data).

3.4.3 Crack Growth Rate Correlation.

The specific choice of correlation for FCGR with ΔK and R strongly affects the predicted crack growth history. The closer the correlation fits the FCGR data, the more accurate the predicted crack growth history. Since some materials, like the 7075-T6 Al used in these tests, have complicated relationships between FCGR, ΔK, and R, a piecewise FCGR-ΔK_{eff} relationship provides a better fit than simpler expressions, such as the NASGRO equation (see figure 33). For the test conditions here, a revised analysis using the NASGRO equation resulted in lifetimes 50% to 200% longer than those found here using the piecewise fit, for which longer lives result because the NASGRO equation falls below the crack growth data (and piecewise fit) when $4 \leq \Delta K_{eff} \leq 9$ MPa m$^{1/2}$ (see figure 33).

3.4.4 Methodological Complications.

3.4.4.1 The DCPD Signal Drift From Electrical Connections.

Drift in voltage signals created variability in DCPD crack length measurements early in the tests. This problem was exacerbated by the bolted electrical lead connections. While not the preferred method, the bolted electrical lead connections were necessary because of the difficulty in soldering to 7075-T6 Al. The drift problems were much worse in areas of high strain, making reference voltage measurements taken on the same coupon unusable. The location of the main voltage measurement leads close to the hole effectively shielded them from strain and, consequently, drift. Attempts to reduce drift using a conductive grease or epoxy were both unsuccessful. In later tests of similar, but thicker, open hole coupons, Molex pins inserted into the holes provided a connection with much less variability and drift, and are recommended over the bolted connections used here.

3.4.4.2 Crack Growth Rate Determination.

A number of methods for FCGR calculation are used in the literature with the calculated FCGR values varying significantly, depending on the method used [43]. As described earlier, the method recommended in ASTM E647 was inadequate to reduce data sets here because data was collected frequently as compared to the measurement precision. The improvement in the level of smoothness for the modified incremental method developed in this work results in a more typical seven-point incremental polynomial algorithm as shown in figure 38.

3.5 SUMMARY.

The work reported in this section is significant because it shows that LEFM with superposition is an effective model for predicting fatigue crack growth history in cold-expanded coupons under constant amplitude loading, despite the opposite often being concluded in the literature. It also suggests likely shortcomings in some earlier work that may have led to conclusions regarding inaccuracies of LEFM. In this work, parameters for predictions and experiments were carefully chosen and analyzed to ensure a thorough and accurate evaluation of LEFM with superposition as a predictor of crack growth history. Coupons were designed to make for simply formulated SIFs due to the growth of a single, through-thickness crack per coupon. Residual stresses were measured using a new technique (the contour method) to accurately determine their distribution and replicate measurements were made to understand variability in residual stress. Because bare and clad materials exhibited similar behavior, results for tests of four coupons per test variation were available to understand average and variability of crack growth behavior. The FCGR was determined from crack length using a modified incremental method to achieve more useful FCGR values than provided by more commonly used methods. The SIF calculations were verified against NASGRO and AFGROW commercial codes. The FCGR was determined from ΔK and R using a piecewise power-law correlation between FCGR and ΔK_{eff} that was established from a range of published FCGR data, which accurately fit the complicated behavior of 7075-T6 Al. Each of these factors had a role in the good agreement found here between observed crack growth and LEFM predictions.

Nearly as significant as the accurate prediction of crack growth histories for cold-expanded coupons is the accurate prediction of variability in the results. For industry to pursue broader adoption of life-enhancing residual stress processes in design, engineering methods are needed that guard against nonconservative predictions and can forecast variability in observed crack growth behavior. In this study, the observed crack growth in CX specimens exhibited significant variability, which is consistent with other published work. However, this work offers a new observation: that the variability in lifetime was reasonably predicted from the observed variation of residual stresses measured in multiple coupons. Therefore, conservative safety factors used in design might be replaced by analytically derived factors based on residual stress variability. The ability of LEFM with superposition to accurately predict mean crack growth history and its variation in CX material under constant amplitude loading is an important step toward a complete accounting of residual stresses in damage-tolerant design.

3.6 TABLES.

Table 4. Mechanical Properties for Clad and Bare 0.080-Inch 7075-T6 Aluminum Sheet

	Clad	Bare
Ultimate tensile stress (MPa)	503	538
Yield stress (MPa)	448	483
Young's modulus (MPa)	71000	71000
Poisson's ratio (ν)	0.33	0.33

Table 5. Maximum Applied (gross) Stress Levels for the Four Different Test Variations

	AM	CX
$R = 0.1$	$S_{max} = 47.2$ MPa	$S_{max} = 142$ MPa
$R = 0.5$	$S_{max} = 65.0$ MPa	$S_{max} = 136$ MPa

Table 6. Points to Create Piecewise Log–Log FCGR-ΔK_{eff} Tabular Lookup Curve for 7075-T6 Al

ΔK_{eff}, MPa m$^{1/2}$	FCGR, m/cycle
1.00	1.50e-13
1.50	9.95e-10
3.36	8.03e-9
4.87	8.36e-8
13.52	9.31e-7
39.63	3.44e-5

3.7 FIGURES.

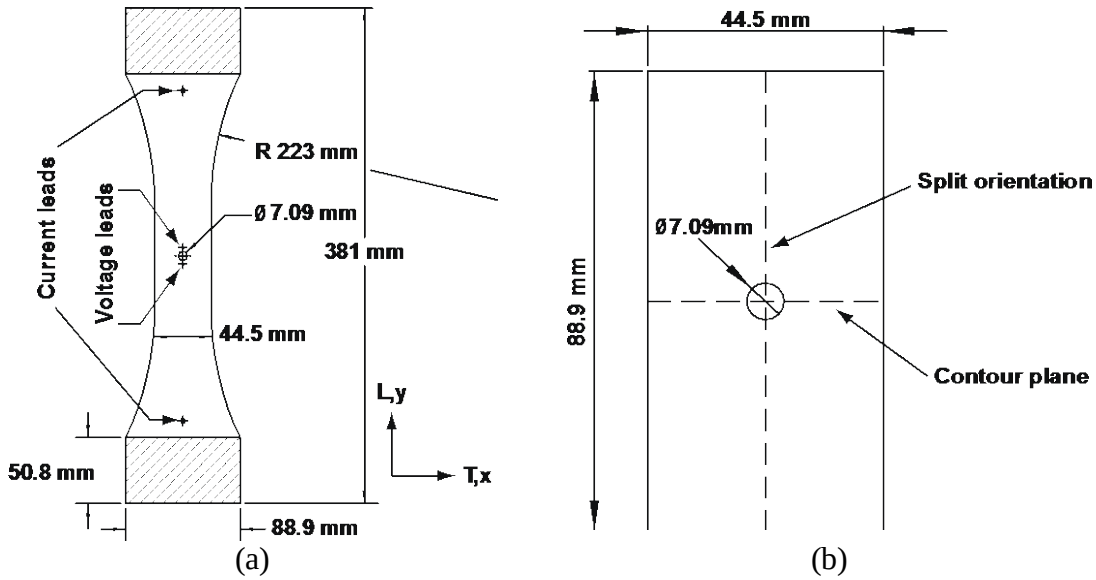

Figure 21. Open Hole Coupons Used in This Study: (a) Fatigue Coupon Dimensions and DCPD Lead Locations and (b) Coupon Blanks Used for Residual Stress Measurements

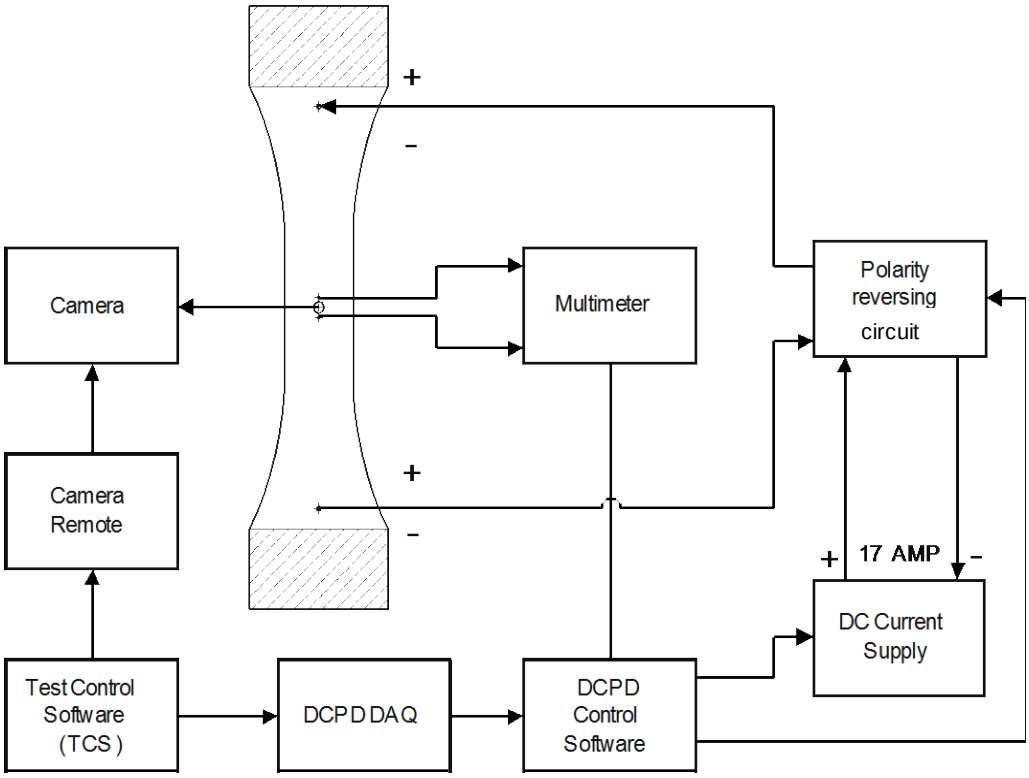

Figure 22. Crack Length Measurement System Diagram

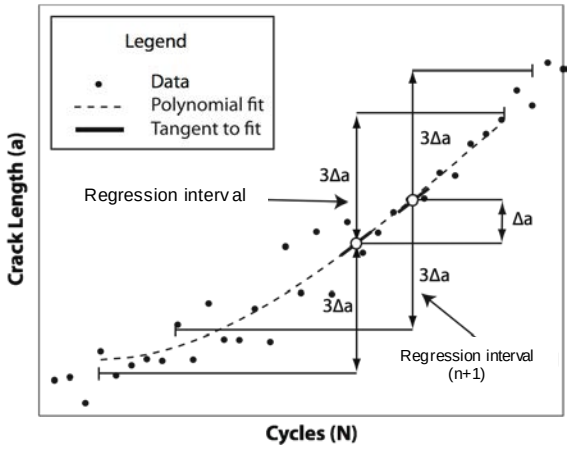

Figure 23. Regression Intervals for the Modified Incremental Method

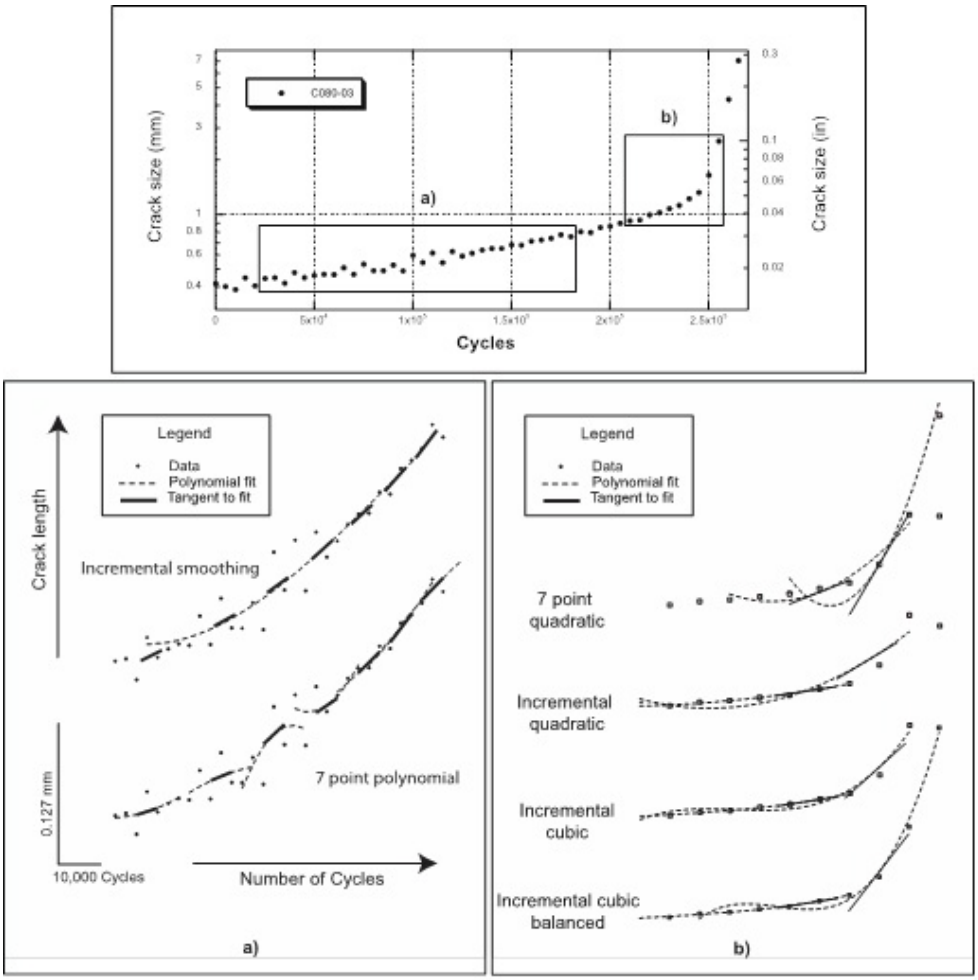

Figure 24. Data From Test of Coupon C080-03, With Semi-Log Plot of Crack Size vs. Cycles Above and Comparison of FCGR Calculation Methods Below: (a) at Low FCGR Where Noise is High Compared to FCGR, and (b) at Long Crack Length With High FCGR Gradient

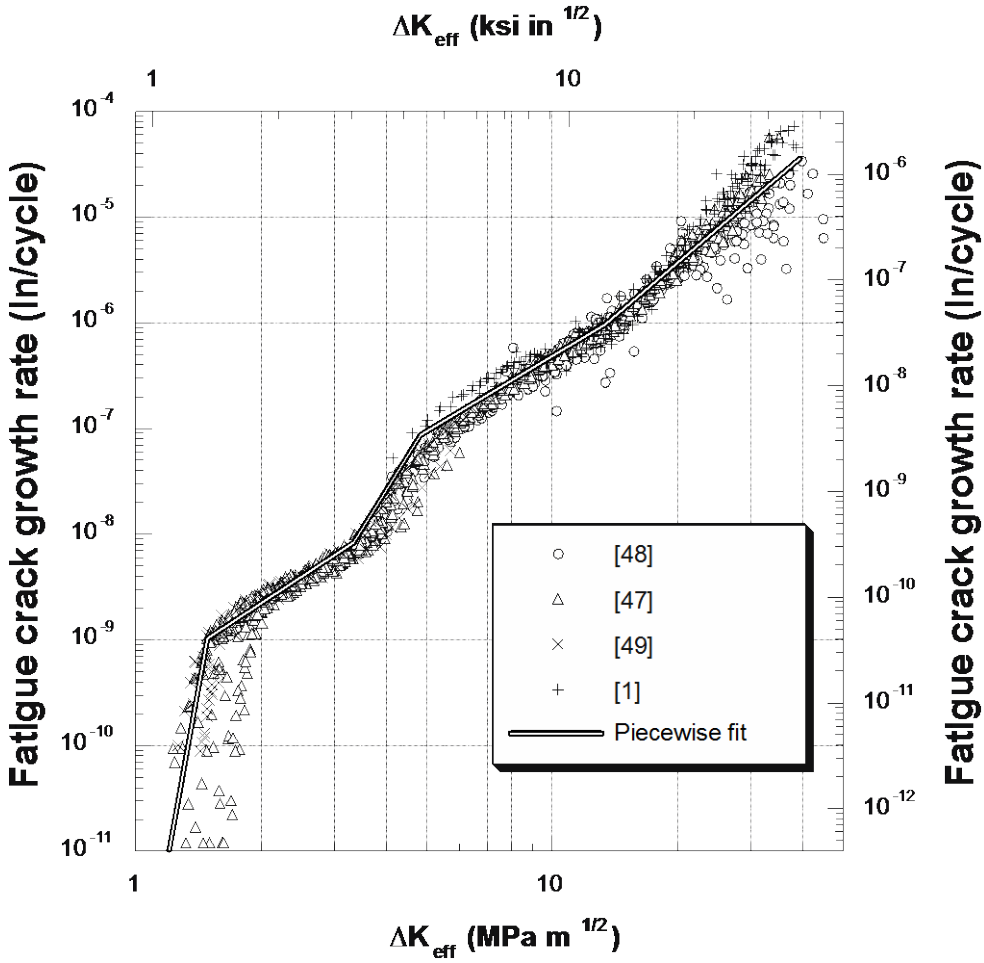

Figure 25. The FCGR vs. ΔK_{eff} Data From the Literature (R ranging from -1 to 0.82) and Piecewise Log–Log Fit

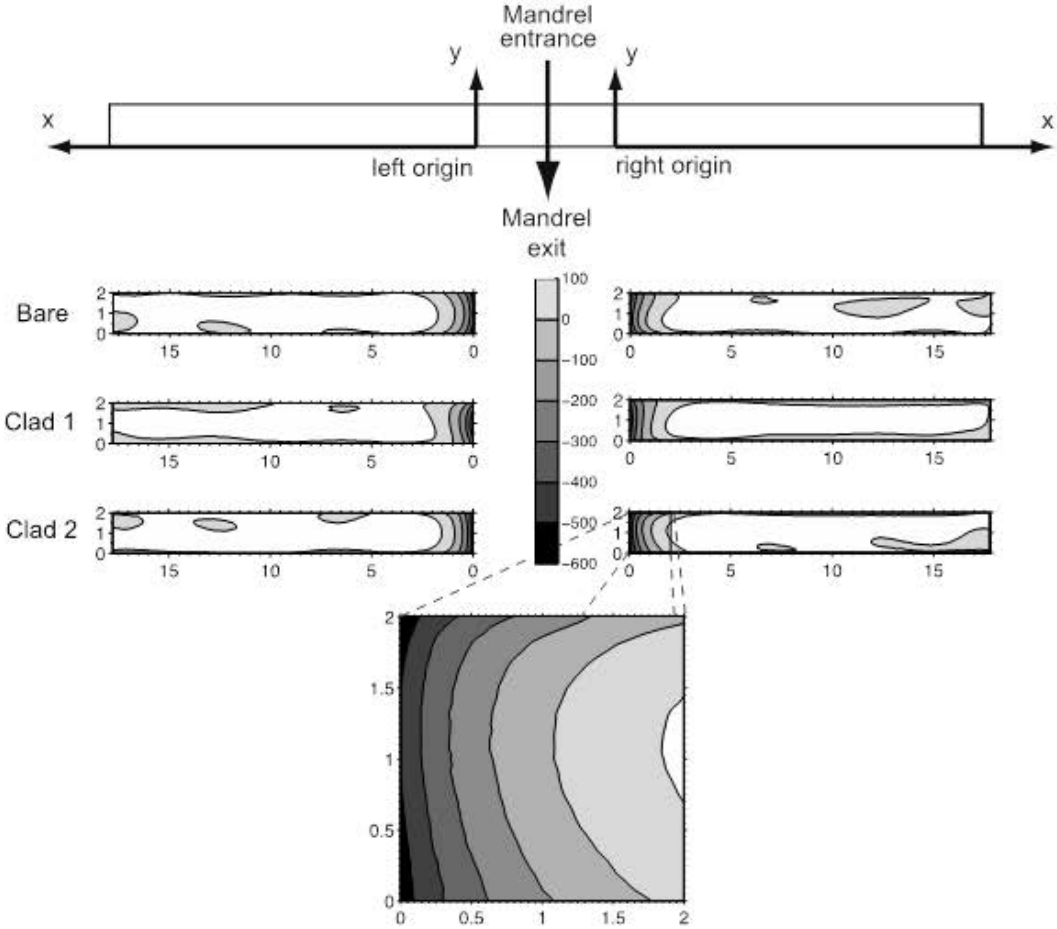

Figure 26. Contour Measurement Results Illustrating 2D Stress Distributions for the Left and Right Side of Cold-Expanded Coupons (one bare, two clad);
(linear scales in mm, color scale in MPa)

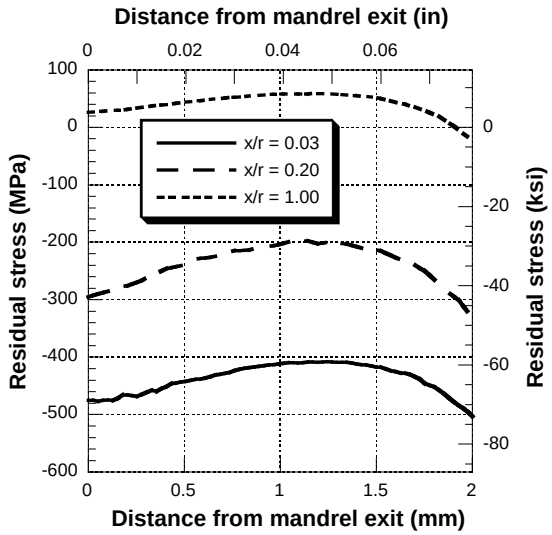

Figure 27. Through-Thickness Residual Stress Distribution at Three Different Positions for the Bare Residual Stress Coupon

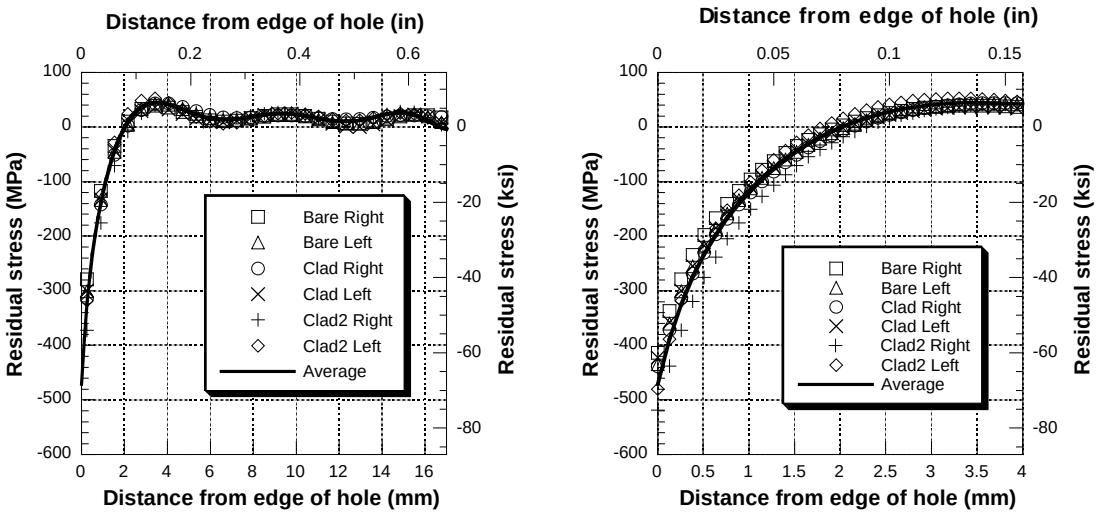

(a) (b)

Figure 28. Through-Thickness Average Residual Stress for the Left and Right Sides of the Three Residual Stress Coupons

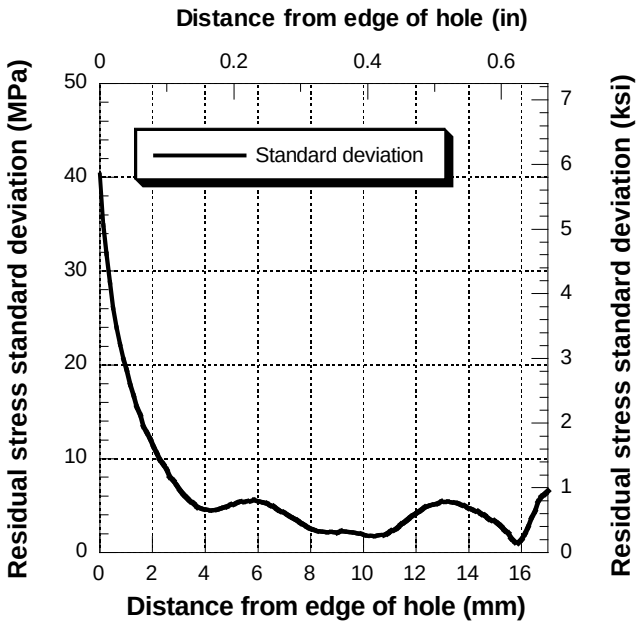

Figure 29. Standard Deviation in Residual Stress for the Set of Six Stress Distributions in Figure vs. the Distance From the Edge of the Hole

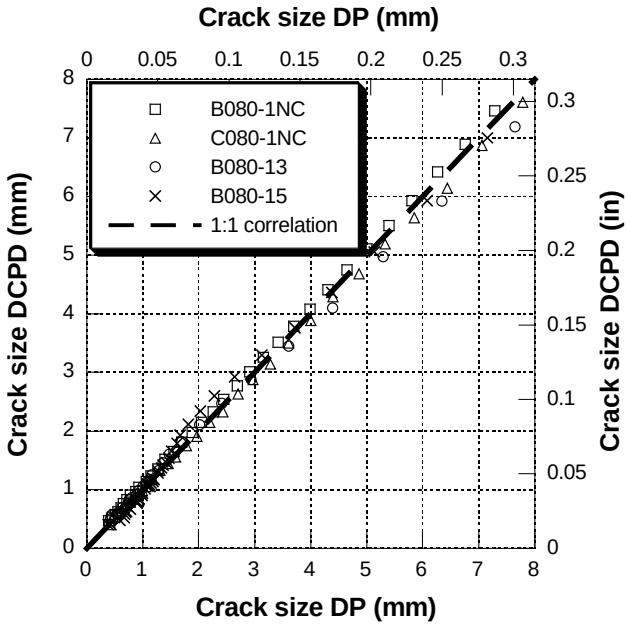

Figure 30. Comparison of DCPD and DP Crack Length Measurements Made on the Same Coupons

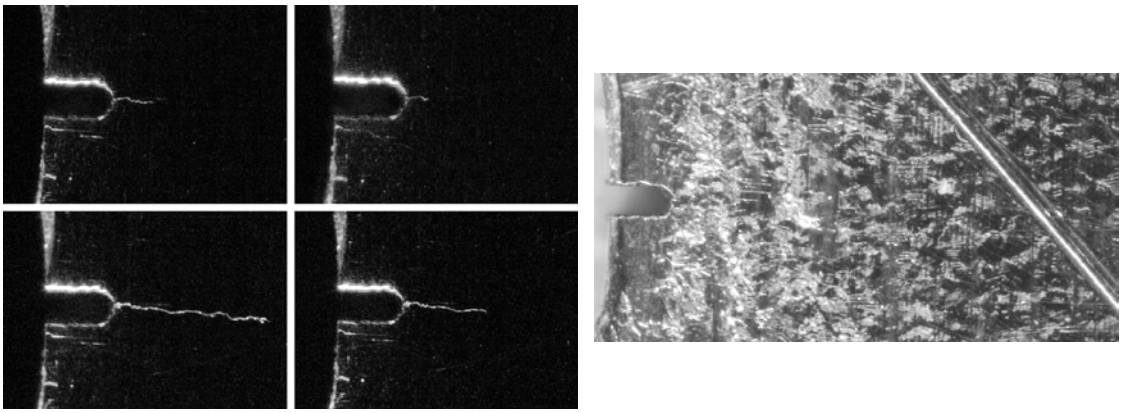

(a) (b)

Figure 31. Comparison of Coupon Surface After Fatigue for Clad and Bare Coupons: (a) a Bare Coupon With Clearly Visible Crack Tip Locations and (b) a Clad Coupon With Microcracking Obscuring the Crack Tip Location

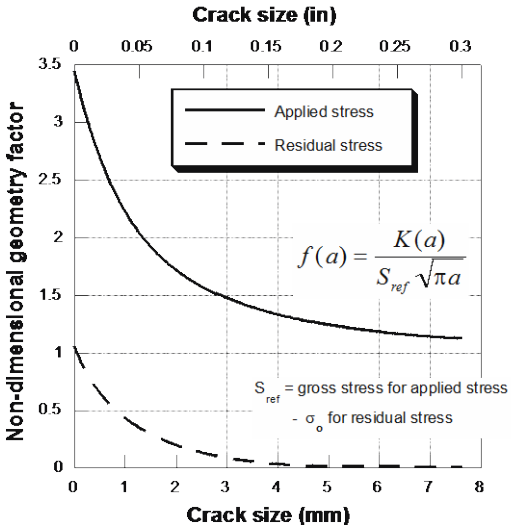

Figure 32. Nondimensional Geometry Factors for Applied and Residual Stresses for Given Crack Sizes; Reference Stress for Applied Stress Is Gross Applied Stress; Reference Stress for Residual Stress Is Negative Flow Stress (-476 MPa)

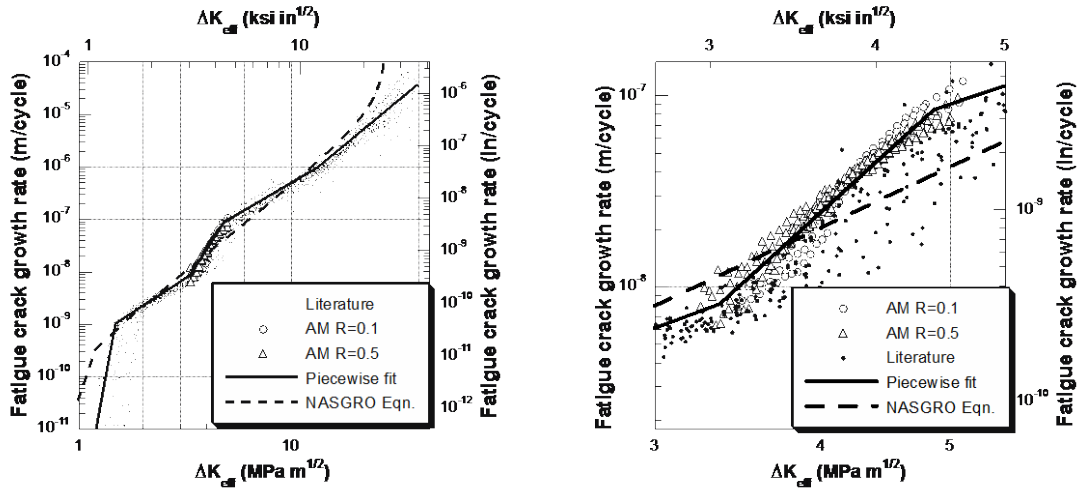

(a) (b)

Figure 33. The FCGR-ΔK_{eff} Literature Data (R ranging from -1 to 0.82), Current Results for AM Coupons (R = 0.1 and 0.5), and the Tabular-Lookup Compared to That for Experimental Data

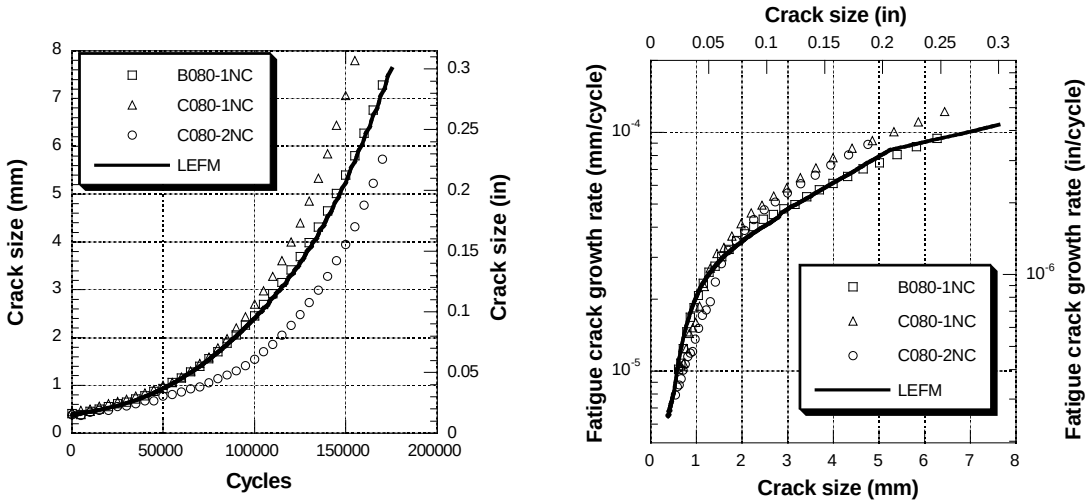

(a) (b)

Figure 34. The AM Coupons, R = 0.1, S_{max} = 47.2 MPa: (a) Crack Length as a Function of Life (a vs. N) and (b) Crack Growth Rate as a Function of Crack Length (da/dN vs. a)

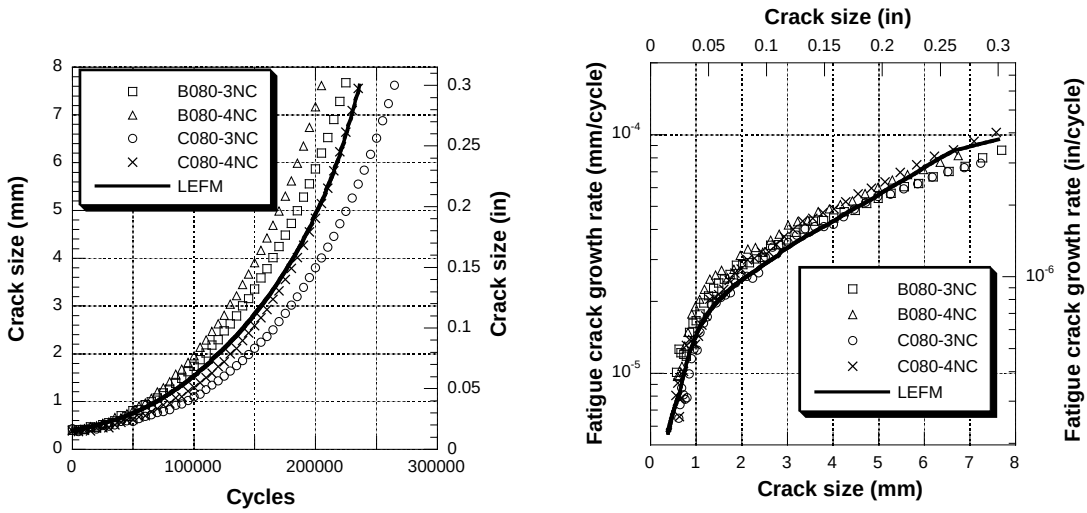

(a) (b)

Figure 35. The AM Coupons, R = 0.5, and S_{max} = 65.0 MPa: (a) Crack Length as a Function of Life (a vs. N) and (b) Crack Growth Rate as a Function of Crack Length (da/dN vs. a)

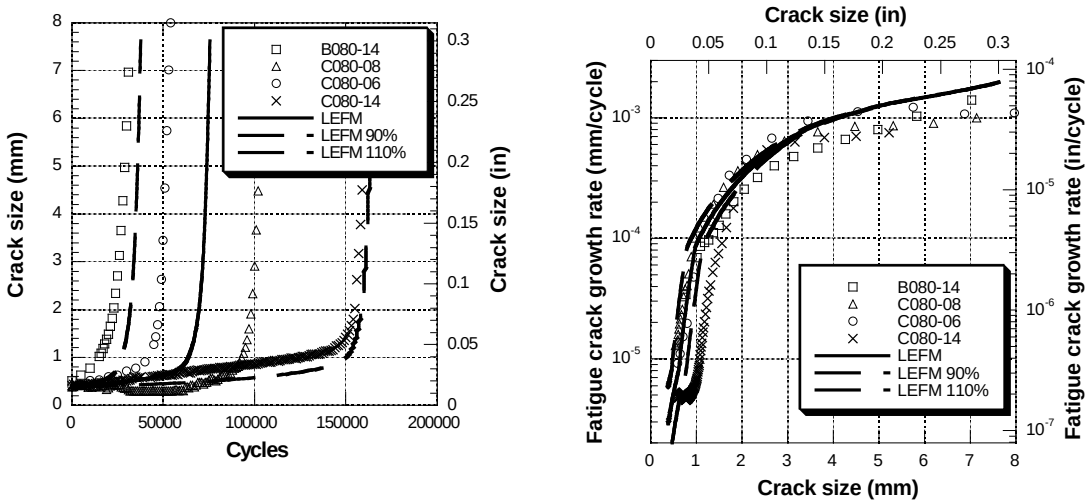

(a) (b)

Figure 36. The CX Coupons, R = 0.1, and S_{max} = 142 MPa: (a) Crack Length as a Function of Life (a vs. N) and (b) Crack Growth Rate as a Function of Crack Length (da/dN vs. a)

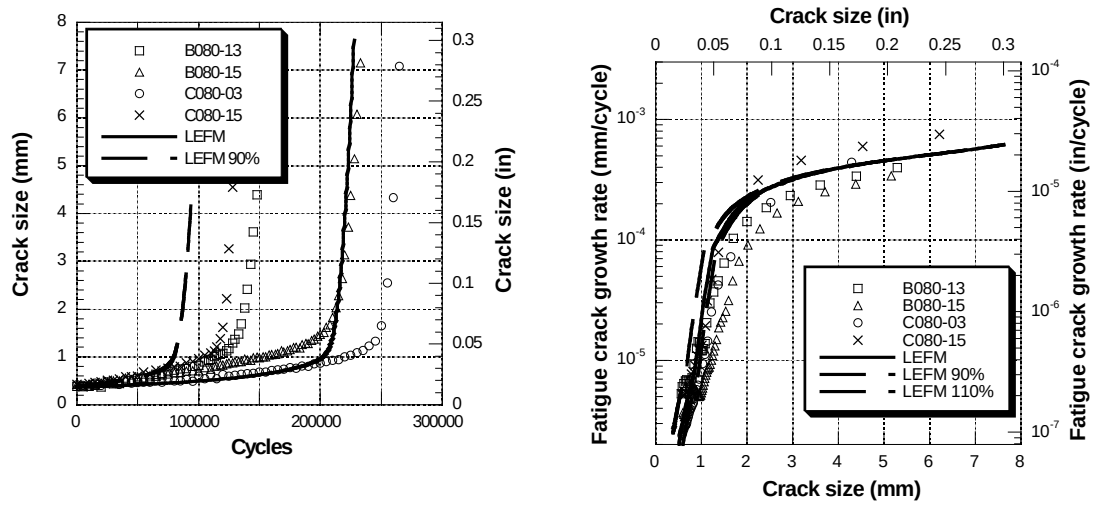

(a) (b)

Figure 37. The CX Coupons, R = 0.5, and S_{max} = 136 MPa: (a) Crack Length as a Function of Life (a vs. N) and (b) Crack Growth Rate as a Function of Crack Length (da/dN vs. a)

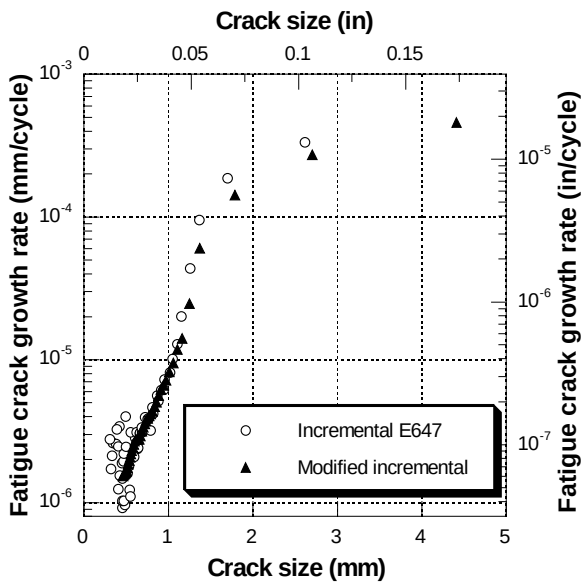

Figure 38. A Comparison Between the Seven-Point Incremental Polynomial Smoothing Algorithm and the Modified Incremental Smoothing Algorithm (C080-03, CX, R = 0.5)

4. THE 2D CRACK GROWTH AT COLD-EXPANDED OPEN HOLES.

4.1 INTRODUCTION.

This section presents experimental and analytical work regarding the growth of 2D cracks from CX holes in thick coupons. As stated in section 1, the cold-hole-expansion process is used in the aircraft industry to improve the fatigue life of components with fastener holes because it is effective in retarding crack growth from fastener holes.

To predict the 2D fatigue crack growth history of thick coupons without residual stresses, LEFM has been widely used with good success [27, 29, 34, 37, 67]. In these cases, handbook-type solutions, in which crack front shape evolution is based on SIFs at two points on the external faces connected by a quarter elliptical (QE), were used. References to "QE LEFM" for the rest of this report refer to analyses based on just two points as opposed to other 2D analyses, such as finite element methods (FEMs), at which the crack shape evolves based on multiple points along the crack front. To make the same type of predictions in coupons containing residual stresses, LEFM is used in conjunction with the principle of superposition, for which SIFs are determined from the sum of the SIFs due to applied and residual stresses. Few if any studies exist in which QE LEFM predictions with superposition were compared to experimental results. Most early attempts at QE LEFM with superposition were given up because of the lack of SIF solutions at the time [34, 37], while recently developed predictions using QE LEFM have not been validated against experimental results [68, 69]. It should be noted that FEM-based analyses have been compared to experimental results [3], but only in a small number of papers.

One problem with QE LEFM is that crack front shapes at corners are assumed to be QE, while experimental results in the literature point to the evolution of significantly different shapes in CX materials [2]. In the literature, two types of shapes have been identified (see figure 39): one in which growth is severely retarded part way down the bore, causing the front to bulge out into the coupon [30, 70], and one in which cracks grow in a semicircular shape near the front face, but with very quick crack growth near the surface of the bore leading to a p-shaped crack [3, 30, 71]. It is likely that the difference in these shapes is due to a variance in the residual stress fields, applied stress levels, and coupon thicknesses [30].

A second caution when using QE LEFM for CX holes arises from significant through-thickness residual stress variation [30]. A through-thickness average of the residual stress field can over-estimate the magnitude of compressive residual stress at corner cracks starting near the mandrel entrance face, where stresses tend to be significantly lower than near the mandrel exit face. Thus, a 2D residual stress characterization is likely needed, such as a 3D FE simulation or contour method measurements, for accurate predictions.

The primary objective of this section is to evaluate QE superposition-based LEFM for prediction of crack growth at CX holes in thick sheet against experimental results. This approach is investigated over an FEM-based approach because of the ease and computational economy of implementation and the availability of commercial software to conduct analyses. As described in section 3, many fatigue tests in the literature contain confounding factors in their experiments and analysis that affect the accuracy of their results. To ensure accuracy, the following secondary objectives have been set. Fatigue coupons, initial notch size, and applied stress levels are carefully chosen to ensure the steady propagation of a single crack from the hole. Multiple replicate tests for each test variation are performed to understand experimental trends. Crack front shapes are implicitly analyzed using surface and through-thickness average crack size measurements. Experimental FCGR is carefully determined from the test data. Crack growth rates for predictions are determined from tabular lookup FCGR-ΔK relationships based on literature data from various stress ratios (see table 9). Lastly, residual stresses are measured on multiple coupons using the contour method because of its relatively high accuracy and ability to measure through-thickness residual stress variation.

4.2 METHODS.

4.2.1 Coupon Geometry and Material.

Thick open hole coupons were manufactured in the same way as the thin coupons from the previous section but from 4.83 mm- (0.190 in) thick 7075-T6 aluminum sheet. Equal numbers of coupons were cut from clad and bare sheets, with coupon designations including *C* for those cut from clad sheet and *B* for those cut from bare sheet. Mechanical properties for 7075-T6 sheet are listed in table 7, as found in MIL-HDBK-5H [72]. Coupon geometry was the same as for thin coupons, save thickness (see figure 40[a]). The sheet thickness is typical of thick sections of rotorcraft fuselage structure and is thick enough to ensure that cracks will grow two dimensionally. Split sleeve cold hole expansion was used to induce residual stress at the hole in half of the coupons. As with geometry, CX and AM parameters mirrored those of the thin coupons. A fatigue starter notch at the edge of the hole on the mandrel entrance face was cut using a wire EDM. The notches were triangular-shaped with a length of 1.27 mm down the bore and 1.27 mm on the front face of the coupons and had an out-of-plane height of 0.127 mm.

4.2.2 Residual Stress Measurement.

The 2D residual stress distributions from CX are measured along the crack plane using the contour method. As with the thin coupons, small coupon blanks (sized 88.9 x 44.5 mm) without notches were fabricated specifically for residual stress measurements (see figure 40[b]) using the same methods employed for fatigue coupons. Those blanks were also measured using the same methods as for the thin coupons. Measurements of residual stress were performed on three coupon blanks, one bare and two clad, to quantify average residual stress from CX and its variability; because each measurement included residual stress fields on two sides of the hole (which we refer to as left and right sides), the measurements provided six distributions of residual stress for further analysis. Full details regarding the contour method for residual stress measurement are available in the literature [17, 18], whereas details pertaining to the measurements for this test are described in section 3. Measurements within 0.1 mm of the coupon edges were discarded because of large uncertainty in contour measurements directly at edges.

4.2.3 Fatigue Testing.

Fatigue crack growth tests were performed at constant amplitude stress using a servo-hydraulic computer-controlled load frame with the same set up procedures as described in section 3. Three variables were investigated in the test matrix to determine the influence of each variable on crack growth history. Residual stress condition was compared by testing CX and AM coupons, applied stress ratios were compared by testing coupons at $R = 0.1$ and $R = 0.5$, and material condition was compared by testing clad (*C*) and bare (*B*) coupons (which were found to be equivalent in section 3). To understand variability, at least one replicate test was performed for each of the four test variations. Applied stress levels (based on gross section area) for each of the test variations were chosen to achieve lifetimes of around 200,000 cycles and were based on preliminary residual stress estimates and LEFM predictions. Initial tests were performed to iterate stress levels and ensure useful test durations. Final stress levels are shown in table 8.

4.2.4 Crack Length Measurement.

During fatigue cycling, tests were stopped at inspection periods to collect crack size data. Front and back face crack length measurements were taken using the Krak-Gage (KG) system [73], bore measurements were taken using surface replicas (SRs), while through-thickness average crack length measurements were taken using the DCPD method. This combination of measurements allows for the measurement of the crack growth on each surface of the coupon and a through-thickness average crack size.

Test control software (TCS [see figure 41]) was developed to pause cycling at each inspection period, open the crack mouth by applying 80% of the maximum applied cyclic stress, trigger measurements, and continue cycling once measurements were complete.

4.2.4.1 The DCPD Crack Length Measurement.

The DCPD crack length measurement method and data reduction method for the thick coupons remained largely the same as for the thin coupons in section 2, except for the use of different voltage measurement lead connections and lack of isolation plates (which in the thin tests were found to provide no benefit). The #0-80 fasteners used for the thin coupons were replaced with 1.57 mm diameter, gold-plated Molex pins pressed into the holes. These pins were soldered to lead wires and replaced for every test to minimize measurement drift associated with fretting at the connectors. A finite element (FE) correlation was used to convert voltage data into crack length data following methods described by Ritchie and Bath [60]. The correlation used for thick coupons is the same as the one developed for the thin coupons, since the analysis was 2D. The DCPD signal therefore provided a measure of thickness-average crack size.

4.2.4.2 The SR Crack Length Measurement.

The SR method was used to measure crack lengths on the surface of the hole bore. This method involves taking a positive SR by capturing a cast of the crack, which is later measured using a microscope. A small drop of replicating solution (Ladd Research, Williston, VT) was brushed inside the bore of the hole over the crack. A 3.81 mm x 19.1 mm x 0.127 mm strip of acetate tape was then carefully placed over the drop. A pick was used to first apply pressure to the tape, then to roll it flat against the surface of the bore to ensure the tape would adhere to the vertical surface while drying. The replicating solution was allowed to dry for 3 minutes before the tape was removed and taped flat against a microscope slide.

Crack lengths for the replicas were measured under a digital microscope using a motorized stage. To more easily view details on the clear replicas, adjustable fiber optic spotlights were positioned at very oblique angles to the slide to cast a shadow off of the positive crack relief [54]. Crack lengths were measured by recording the difference in stage position counts to move from the crack origin to the crack tip. Measurements were made under 64x optical magnification while using digital crosshairs to line up the locations of the crack origin and crack tip. Stage position counts were calibrated against an optical grid to determine crack length in millimeters.

4.2.4.3 The KG Crack Length Measurement.

The KG crack length measurements were used on the front and back surfaces of the coupon. The KG system is an indirect version of the DCPD crack length measurement method. Instead of exciting current through the whole coupon and measuring a voltage between specific locations directly on the coupon (as in the case of DCPD), the excitation and measurements are performed using a small metallic foil gage attached to, but electrically isolated from, the coupon (see figure 42). KG model BH16250-x12 with cast epoxy backing was chosen for these tests. The gages were applied to both faces of the coupons to measure surface crack lengths on both the front and back faces, where the starter notch was on the front face.

The KGs were affixed to the coupons using typical procedures for attaching metallic foil strain gages with a cyanoacrylate adhesive. The gages were positioned on the coupons so that there would be no overhang into the bore of the hole (instead of the recommended placement with a slight overhang [73]) and the KGs would not interfere with the SR measurements. The distance between the bore and gage edge was measured under a microscope and added to the KG crack length measurements to obtain physical crack size. Excitation and voltage measurement wires were connected to the gages using shielded grounded wires via solder connections and strain relief pads.

The measurements for the KG method were triggered through the TCS and controlled through the DCPD Control Software (DCPD CS). The DCPD CS in turn triggered a FRACTOMAT to make KG measurements (see figure 41). The FRACTOMAT is an off-the-shelf piece of equipment, designed specifically to work with KG, that performs continuous excitation, signal conditioning, and voltage reading during tests. At each inspection period, the DCPD CS recorded measurements at 1000 Hz for the duration of one second from the voltage output on the FRACTOMAT, which is sufficiently long to average out power-line noise.

4.2.4.4 The KG Data Reduction and Length Correlation.

Each model of KG comes with a tabular voltage to crack length correlation. From this tabular correlation, a piecewise polynomial equation was created for use in data-reduction software. The measured KG voltage at each inspection period is correlated to a crack length using the piecewise relation.

4.2.4.5 Through Thickness Crack Length Determination From Surface Measurements.

Surface crack length measurements are combined to determine through-thickness average crack length, where thickness average crack length is defined as the cracked area divided by the coupon thickness. The SR and KG crack length measurements correspond to the intersection of the crack front with the surface. Cracked area is then computed using one of two area calculation methods: a straight-line area or a QE area. The straight-line area is determined based on a triangular or trapezoidal crack shape, which is created by connecting the points on the bore a and front face c during the corner crack regime (CCR), then the rear face c_t and front face c in the through-thickness regime (see figure 43). The transition from corner crack to through-thickness regimes was specified as the point where the SR bore measurement was equal to the coupon thickness. Quarter-ellipse area is formulated similarly, using a quarter ellipse

connecting the front face c and bore a measurements during the CCR. For the through-thickness regime, the area was defined using a QE with an origin at the notched corner and intersections at the front c and rear faces c_t crack length measurements (see figure 43).

4.2.4.6 Crack Growth Rate Determination.

Crack growth rates were determined using the same methods developed for the thin coupons: a modified incremental polynomial method based on the work of Larsen, Jira, and Ravichandran [54] but using cubic polynomial regression and a weighting modification (details provided in section 3). Regression intervals of 0.133 mm were found to be suitable for computing the crack growth rate in the thick coupons.

4.2.4.7 LEFM Predictions.

The LEFM was used to predict the crack growth history. Numerical integration is used to determine the number of loading cycles required to extend the crack from an initial corner crack with $a = c = 1.27$ mm to a final through-thickness average size of 11 mm. For every step in crack length, SIFs were calculated at the two intersections of the crack front and the surfaces of the coupon. For AM coupons, two models were used to make predictions corresponding to the two different crack growth regimes in the test, first as a corner crack and secondly as a through-thickness crack (see figure 43). The CCR was modeled using SIF solutions from Newman and Raju [74] with corrections implemented based on more recent FEM work by Fawaz and Andersson [75]. This model determines the nondimensional SIFs as a function of parametric angle based on crack length, crack depth, thickness, and hole radius. In implementing this solution, two corrections that are frequently used in the literature [45, 69] were used to improve agreement with experimental results. The first is a constraint correction factor:

$$C_{cr} = 0.9 + 0.2R^2 - 0.1R^4 \tag{10}$$

that multiplies ΔK to account for the loss of constraint at the free surfaces [76]. The second correction is the use of parametric offset angles to avoid FEM-based boundary layer errors from the reference solutions. Offset angles were chosen to be the same as those used in NASGRO [45] so that non-dimensional SIFs for c and a positions are calculated at parametric angles ϕ of 0° and 80°, respectively (see figure 43). The through-thickness crack regime (TTCR) was modeled using SIFs from a part-elliptical through-thickness solution developed by Fawaz [77]. The FE reference solutions were fit so that SIFs could be determined in a way similar to the corner crack model. To determine the rear face crack length (c_t), a virtual crack was grown from the bore beyond the thickness of the coupon. The intersection of the quarter ellipse connecting the c and a lengths and the rear face of the coupon defines the crack length on the rear face of the coupon c_t (see figure 43).

For CX coupons, a 2D weight function solution was used to investigate crack growth in the CCR. A solution from the crack analysis program NASGRO was investigated: the CC10 corner crack solution for bivariant stress [45, 68]. This solution takes the same approach as the corner crack solution; nondimensional SIFs are calculated as a function of angular position along a QE. Applied SIFs were calculated based on the built-in stress distribution for remote tension stress and residual SIFs were calculated based on the 2D residual stress distribution measured using the

contour method. The SIF solutions from NASGRO at parametric angles of 3° and 87° were used for this model.

Superposition of the SIFs for applied and residual stress provided values of ΔK and R at the a and c locations:

$$K_{\max} = K_{app,\max} + K_{RS}$$
$$K_{\min} = K_{app,\min} + K_{RS}$$
$$R = K_{\min}/K_{\max}$$
$$\Delta K = K_{\max} - K_{\min} \tag{11}$$

where $K_{\max}$ and $K_{\min}$ are the maximum and minimum total SIFs, $K_{app,\max}$ and $K_{app,\min}$ are the maximum and minimum applied SIFs, and K_{RS} is the residual SIF.

The resulting ΔK and R values were used to determine the fatigue crack growth rate (FCGR) from a scheme based on crack closure concepts and a piecewise log–log fit for FCGR as a function of the effective SIF ΔK_{eff}. This scheme is based on methods described in detail by Newman [69] and its derivation and application to these tests is identical to that described in section 3.

Cycle counts were calculated from FCGR as a function of crack size using numerical integration. Because of a large variation in crack growth rates for small crack sizes, small growth increments were taken early in the integration and larger increments were taken at a later time to increase the accuracy of numerical integration.

4.3 RESULTS.

4.3.1 Residual Stress Measurements.

The 2D residual stress distributions (see figure 44) along the crack plane (see figure 40[b]) show that the residual stress varies as a function of thickness and width position, x and y, respectively. The distribution close to the bore is asymmetric with a minimum value of compressive stress (-519 MPa) occurring near the mandrel exit face that is approximately 40% higher than that occurring at the entrance face (-369 MPa, figure 45). Farther from the bore, the residual stresses are fairly uniform through the thickness.

The mid-thickness average of the residual stress measurements simplifies the 2D distributions to allow trends to be more easily understood as a function of length along the crack plane x (see figure 46). Little difference exists between the stress distributions from the left and right sides of the holes, bare and clad materials, and replicate tests (see figure 46). Consequently, an average of the six residual stress distributions from the left and right sides and bare and clad material conditions was taken as a representative residual stress distribution for crack growth analysis (see figures 44 and 46). On average, the mid-thickness average residual stress distribution is compressive for the first 1.8 mm from the edge of the hole, after which the residual stress distribution is mildly tensile. A minimum (compressive) thickness average residual stress of -470 MPa is measured at the hole with a maximum (tensile) residual stress of 52.2 MPa

occurring at 3.02 mm from the hole (see figure 46), after which the distribution tapers to residual stress values of about 10 MPa.

It is difficult to assess accuracy of the contour method and the repeatability of the cold-working directly. Accepting the present coupons as identical, a statistical analysis of the measurements allows for some understanding of overall variability. The standard deviation of the mid-thickness average residual stress for the six residual stress distributions, taken at a given position in x, is less than 40 MPa (see figure 47) with the most variability near the hole. To aid in understanding how the variation in measured residual stress contributes to variation in crack growth behavior, we will carry forward a variation of ±10% in K_{rs} to bound expected variability. These values correspond approximately to the maximum standard deviation (40MPa) divided by the maximum average mid-thickness residual stress magnitude (-470 MPa).

4.3.2 Crack Length Measurement Methods.

The KG crack length measurements were verified by comparing DCPD measurements (previously validated in section 2) on a thin sample with through-thickness crack growth. Measurements using each method were in agreement (see figure 48).

4.3.3 Observed and Predicted Crack Growth Behavior.

Crack growth behavior of bare and clad samples is nearly identical for all coupon conditions (see figures 49–56). Consequently, the bare and clad material conditions are considered together when comparing predicted and observed crack growth behavior among variations of stress ratio and residual stress. Material condition is included in the coupon number, reported in plot legends, with *B* for bare and *C* for clad coupons.

The SIFs for the CX coupons were found to be very low at the initial crack size, which resulted in near-threshold crack growth rates at the bore. As the LEFM model proceeds, the crack is predicted to grow along the front face, but not along the bore. The a/c crack length ratio continues to decrease as c grows and a stays fixed until the ratio is out of the range of the SIF solution, which is valid for $a/c > 0.5$ [68]. The crack length on the bore remains at approximately 1.27 mm, whereas the length along the face is predicted to grow to 1.84 mm in 19,000 cycles before growing beyond the range of validity; this is in contrast to the observed crack growth behavior, which exhibited similar crack growth rates along both the bore and face. In the development of an LEFM analysis of 1D cracking, it is possible to determine crack growth rate (but not lifetime) predictions for a case in which crack growth is near zero because of threshold level SIFs. It is not possible to develop an analogous solution for QE LEFM because the evolution of a and c are intrinsically tied together. Because of the lack of predicted crack growth along the bore, QE LEFM for the CX coupons could not be further evaluated.

To evaluate the LEFM model for AM tests, crack growth rates and lifetimes from the front face and bore; the ratio of growth on the bore to the front face (or back face to front face for the through-thickness regime); and crack growth rates based on through-thickness average crack lengths were investigated. These crack growth measurements were each investigated individually and were also combined to assist in understanding crack shape evolution. To differentiate between the two models used in the predictions, a solid line was used to plot results

for the corner crack model, with a dashed line for the through-thickness model. For purposes of discussion, we define variability as the range of observed lifetimes (maximum minus minimum) divided by the average lifetime.

Front face crack growth rate and lifetime LEFM predictions correlate fairly well with AM $R = 0.1$ experimental results and very well with $R = 0.5$ results (figures 49 and 50, respectively). Lifetime predictions (cycles to achieve crack lengths of 10 mm) are within the range of experimental results for AM $R = 0.1$ tests and slightly conservative for $R = 0.5$. In the CCR, LEFM and observed rates agree for $R = 0.1$ for very short cracks, LEFM over-predicts rates at the transition, and the two correlate well again for long cracks. Predictions of rate for $R = 0.5$ generally correlate well with the data for all crack lengths. Variability in AM lifetimes is small at 34% for $R = 0.1$ and 15% for $R = 0.5$.

Crack growth rates on the front face for CX coupons increase quickly during corner crack growth, then taper for through-thickness crack growth (see figures 51 and 52). Variability of CX lifetimes is substantially larger than corresponding AM lifetimes: 125% for both $R = 0.1$ and $R = 0.5$ (3.7x and 8.3x more variable than the AM tests, respectively).

As for the front face, LEFM predictions for crack growth rates in the bore of the hole and lifetimes (to crack breakthrough at $a = 4.83$ mm) correlate well with AM experimental results (see figures 53 and 54). Lifetime predictions are approximately equal to the average of the experimental data for both $R = 0.1$ and $R = 0.5$. The AM experimental bore FCGR data have significant variability for each coupon and between coupons. Variability in AM lifetimes is significant at 58% for $R = 0.1$ and small at 16% for $R = 0.5$. Crack growth rates down the bore for CX coupons differ from the AM measurements in that the behavior is less consistent. Cracks from the bore initially grew at a given rate after which growth would become exponential, for which the crack length at which exponential growth would occur varied between coupons (see figures 55 and 56). Variability of CX lifetimes is slightly larger than corresponding AM lifetimes for $R = 0.1$ at 79% and substantially larger for $R = 0.5$ at 127% (1.4x and 7.9x more variable, respectively).

The history of the ratio of crack length measurements on the bore and front face (a/c), then rear face and front face (c_t/c), provide for the understanding of crack shape evolution (see figure 57). For AM $R = 0.1$ coupons, experimental a and c lengths were found to grow at the same rate in the CCR and while a was predicted to grow faster than c. The AM $R = 0.5$ experimental results were more in line with predictions for which a grew faster than c in the CCR. In the through-thickness regime, predicted growth along the back face (c_t) agrees with that observed for $R = 0.5$, but for $R = 0.1$, c_t is predicted to catch up to c faster than the experimental data illustrate. For CX coupons, cracks grew slightly faster down the bore (a) than cracks on the front face (c) until approximately halfway through the bore (see figure 57), at which point growth on the bore would slow and growth along the front face would accelerate. Through-thickness cracking occurs once the front face crack length reaches approximately 8 mm, after which the back face crack length (c_t) quickly catches up to that of the front face (c).

Through-thickness average crack lengths, as defined by straight-line area, QE area, and DCPD, provide an indication of the crack front shape internal to the coupon. The DCPD measurements,

which correspond to the exact amount of cracked area, can be compared to either the straight line or QE measurements to determine when the crack front shape is more linear or more elliptical. This is important in verifying the corner crack LEFM model because of its assumption of an elliptical crack front shape. To illustrate trends, one coupon from each test variation was chosen to be representative of behavior for each variation (see figure 58). At the beginning of the test in AM and CX coupons, the DCPD measurements are close to the straight line because the starter notch is triangular. In the AM coupons, the shape evolves until it becomes essentially QE at around 0.3 mm, then falls between the two models for the rest of the test. In the CX coupons, the DCPD measurements are, on average, close to the straight-line model until the through-thickness transition, then are generally closer to the elliptical measurements. A lack of QE shape in the CX coupons would explain, at least in part, why the QE LEFM model did not provide useful estimates of initial crack growth for the CX coupons.

Surface measurements and through-thickness average lengths based on surface measurements are useful measures of crack growth. However, because uncertainty exists in the internal crack front shape, each measurement (or a combination in the form of a through-thickness length) only acts as an estimate of cracking behavior. Because DCPD is a direct measurement of the average crack length instead of an indirect one based on external measurements, DCPD was chosen to evaluate LEFM predictions in general. The following sections use DCPD through-thickness average lengths for crack lengths and growth rates. The LEFM predictions use through-thickness average crack lengths and growth rates based on areas defined by a, c, and a QE, as described earlier.

For AM $R = 0.1$ coupons, experimental results correlate fairly well with LEFM in both lifetime and FCGR (see figure 59). On average, cracks for the experimental results grew from 0.167 mm to 10 mm (the crack length range to define lifetime in these tests) in 350,000 cycles with a range in lifetime from 286,000–406,000 cycles. The LEFM model predicts a lifetime of 300,000 cycles, which is just on the lower end of the experimental results. Because of the nature of using the combination of two separate models to predict crack growth during the two different crack regimes, discontinuities in rate are observed at the transition point (see figure 59). The LEFM FCGR predictions generally agree during the CCR, and are slightly high for most of the through-thickness regime, with the greatest difference seen at the transition discontinuity.

For AM $R = 0.5$ coupons, experimental results correlate fairly well with LEFM in both lifetime and FCGR (see figure 60). On average, cracks for the experimental results grew from 0.167 mm to 10 mm in 370,000 cycles, with a range in lifetime from 351,000–412,000 cycles. The LEFM model predicts a lifetime of 331,000 cycles, which is slightly lower than the range of experimental data, but only a 10% difference from the average. As with the $R = 0.1$ results, LEFM FCGR predictions agree fairly well for the CCR and TTCR regimes.

For CX $R = 0.1$ coupons, on average, cracks for the experimental results grew from 0.167 mm to 10 mm in 213,000 cycles, with a range in lifetime from 87,000–351,000 cycles. Very little variability exists for FCGR experimental results in this test variation.

For CX $R = 0.5$ coupons, on average, cracks for the experimental results grew from 0.167 mm to 10 mm in 217,000 cycles, with a range in lifetime from 97,000–369,000 cycles. Very little variability exists for FCGR experimental results in this test variation.

Trends in lifetime variability of the experimental data are also evident. For AM coupons, variability at $R = 0.1$ and $R = 0.5$ was similar, being 34% and 16%, respectively. For CX coupons, variability at both $R = 0.1$ and $R = 0.5$ was 125%. The greater variability for CX coupons compared to AM coupons is apparently due to the variability of residual stress among the coupons and is consistent with trends seen in thin coupon testing (see section 3).

4.4 DISCUSSION.

4.4.1 Crack Length Measurements.

A variety of methodological complications regarding crack size measurement occurred during testing. The move from a thin coupon (as described in section 3) to one that was nearly twice the thickness effectively reduced the electrical resistance of the coupons by half, thereby halving measured voltage and, hence, DCPD resolution. This made it harder to measure small cracks and slow crack growth rates. Conversely, the use of Molex pins reduced noise and drift experienced with the fastener connections used with the thin coupons. The Molex pins act as springs inside the holes and experience less strain amplitude (and therefore fretting) than ring terminal connections did on the surface of thin coupons.

A variety of problems were experienced using the KG system. First, it was found that the ability of the gages to crack concurrently with the coupon is very sensitive to bond quality and the backing material of the gage. A fiberglass backing was used in the trial tests but was found to have more problems with concurrent cracking than the more brittle cast epoxy backing. Placing the gage so that it overhangs the location of crack initiation helps to ensure that the gage and coupon would crack concurrently. This was not possible for the back-face gages, because to do so would interfere with the ability to take replica measurements down the bore of the hole. This resulted in two problems: some distance would be left between the bore edge and the edge of the gage in which back-face crack lengths could not be measured and, second, there was less confidence in initial coincidence of the crack in the KG and the coupon.

It was difficult to make high-quality replica measurements down the bore of the hole. This resulted from a number of factors. First, the placement of the acetate tape on a curved surface (the bore) proved difficult and required an experienced operator to ensure that the replicating solution would hold the tape up against gravity and the tape's tendency to lay flat. Second, despite a final post ream, the surface of the bore was fairly irregular, which made crack-tip identification difficult. Both of these factors resulted in variable crack length measurements and, hence, noisy FCGR data (see figures 53–56).

In these tests, it was difficult to measure accurately the transition of the corner crack to a through-thickness crack. In some cases, crack initiation occurred on the back face just prior to the bore crack size reaching through-thickness. Despite this initial crack growth measured by the back side KG, bore measurements were used to define consistently through-thickness average length at transition.

4.4.2 Prediction Verification.

To ensure predictions would be accurate, a number of verification steps were taken. Predictions were first made for the AM cases and compared to solutions from a commercial software package (NASGRO [45]) for the CCR. Geometry factors for the predictions matched exactly with the NASGRO solution. The CC10 SIF solutions from NASGRO that were used for CX predictions were verified by modeling AM conditions. The AM SIFs from CC10 were similar to those of the CCR predictions when run with identical parametric angles. Some difference is expected because the two models are based on different reference solutions [68, 75].

4.4.3 The SIF Formulation.

The examination of the crack front shape evolution for the AM coupons shows that the crack front is not always a QE as assumed in the prediction model. Since SIFs are based on the assumption of QE geometry, the actual SIFs will be different than those approximated by the QE corner crack solution. Fortunately, the crack transitions from linear to QE quickly, leading to fairly accurate predictions for AM coupons.

The use of the two different models to predict growth in the CCR and TTCR regimes led to a discontinuity in FCGR at the transition in the form of a growth rate spike. As this growth rate spike is not present in the DCPD measurements (see figures 59 and 60), the models are not apparently accurate at transition. Certainly, the small ligament present as the crack transitions from part- to through-thickness has a material state quite different from the highly constrained crack-tip state assumed in LEFM. This difference in stress state is consistent with lower observed growth rates and may account for the difference between the predictions and experiments.

The CX coupons (see figures 61 and 62) exhibited DCPD crack lengths more similar to straight-line than QE crack lengths. As described earlier, results for CX cracks from the literature point to a p-shaped crack front evolution. If a p-shaped crack were present, such as in figure 39(b), DCPD measurements would indicate a crack size smaller than for QE and close to that of a straight line, which is consistent with the observed data. Because crack shape evolution is important, a method of measuring it (e.g., marker banding) should be used in further tests.

The SIFs calculated for CX coupons indicate that there should be almost zero crack growth along the bore of the hole considering the applied and residual stress distributions in these tests. This is contrary to the experimental results gathered, in which crack growth along the bore of the hole clearly occurs. This discrepancy is likely because the crack front evolution in the model is constrained to a QE shape. Forcing the QE shape does not allow the crack to follow least resistance, which leads to slower crack growth (and potentially crack arrest) than would occur in experiments.

4.5 SUMMARY.

This work is significant because it is the only work in the literature that attempts to validate a QE LEFM model with residual stresses against experimental results (where QE LEFM refers specifically to crack front evolution based on two surface lengths connected by a QE). Like

other results in the literature, QE LEFM is seen to accurately predict crack growth in AM coupons. However, the QE LEFM predictions with residual stresses break down for these tests because of the relatively high level of residual stress and apparently inaccurate shape assumptions in SIF determination. In both AM and CX, it can be seen from an analysis of crack front shape that SIF formulation errors are due to the inaccuracy of the assumed QE crack front shape. Because QE LEFM for AM coupons could be used as an effective tool in industry, predictions for CX holes clearly require a method in which crack front shape evolves naturally. A number of papers point to FE methods that include arbitrary crack front shape evolution schemes as a promising means to model 2D crack growth [3, 30]. The FE methods should be pursued in followup work.

4.6 TABLES.

Table 7. Material Properties for Clad and Bare 0.19-Inch 7075-T6 Aluminum Sheet

	Clad	Bare
Ultimate tensile stress (MPa)	517	538
Yield Stress (MPa)	462	489
Young's modulus (MPa)	71000	71000
Poisson's ratio (ν)	0.33	0.33

Table 8. Applied Stress (gross stress) Levels for the Four Different Test Variations

	AM	CW
$R = 0.1$	$S_{max} = 47.2$ MPa	$S_{max} = 130$ MPa
$R = 0.5$	$S_{max} = 65.0$ MPa	$S_{max} = 136$ MPa

Table 9. Points to Create Multilinear (in log–log space) FCGR-ΔK_{eff} Tabular Lookup Curve for 7075-T6 Al

ΔK_{eff} MPa m$^{1/2}$	Rate, m/cycle
1.00	1.5×10^{-13}
1.50	9.95×10^{-10}
3.36	8.03×10^{-9}
4.87	8.36×10^{-8}
13.52	9.31×10^{-7}
39.63	3.44×10^{-5}

4.7 FIGURES.

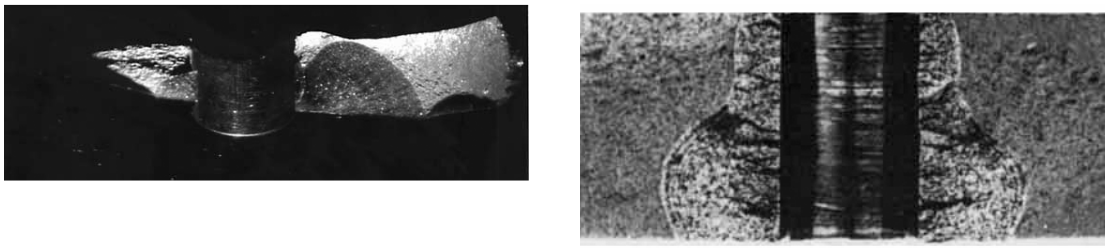

(a) (b)

Figure 39. Crack Front Shapes for a CX Coupon as Illustrated by (a) Clark and Johnson [70] and (b) Pell et al. [71]

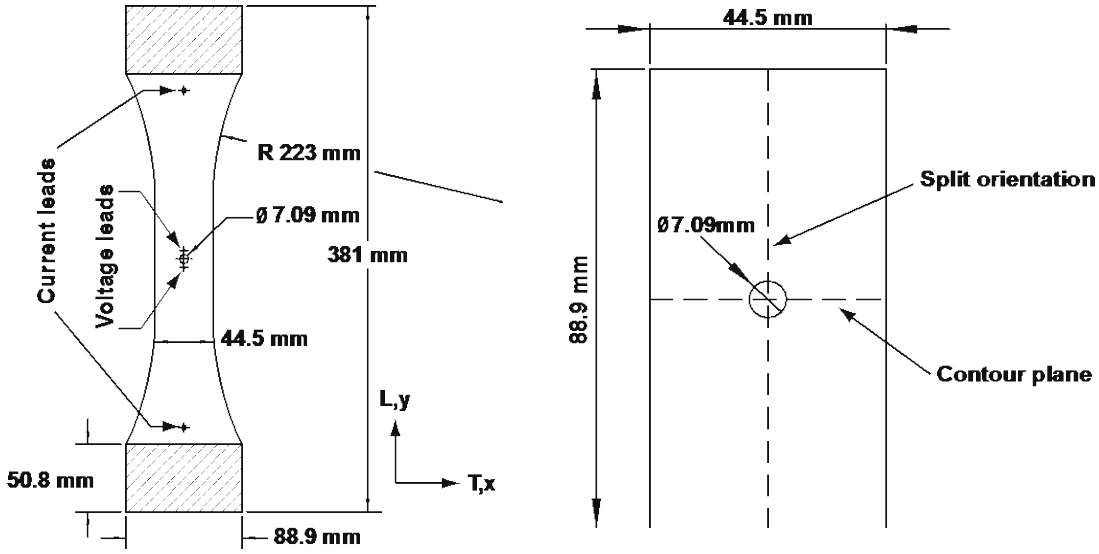

(a) (b)

Figure 40. Open Hole Coupons Used in This Study: (a) Fatigue Coupon Dimensions and DCPD Lead Locations, and (b) Coupon Blanks Used for Residual Stress Measurements

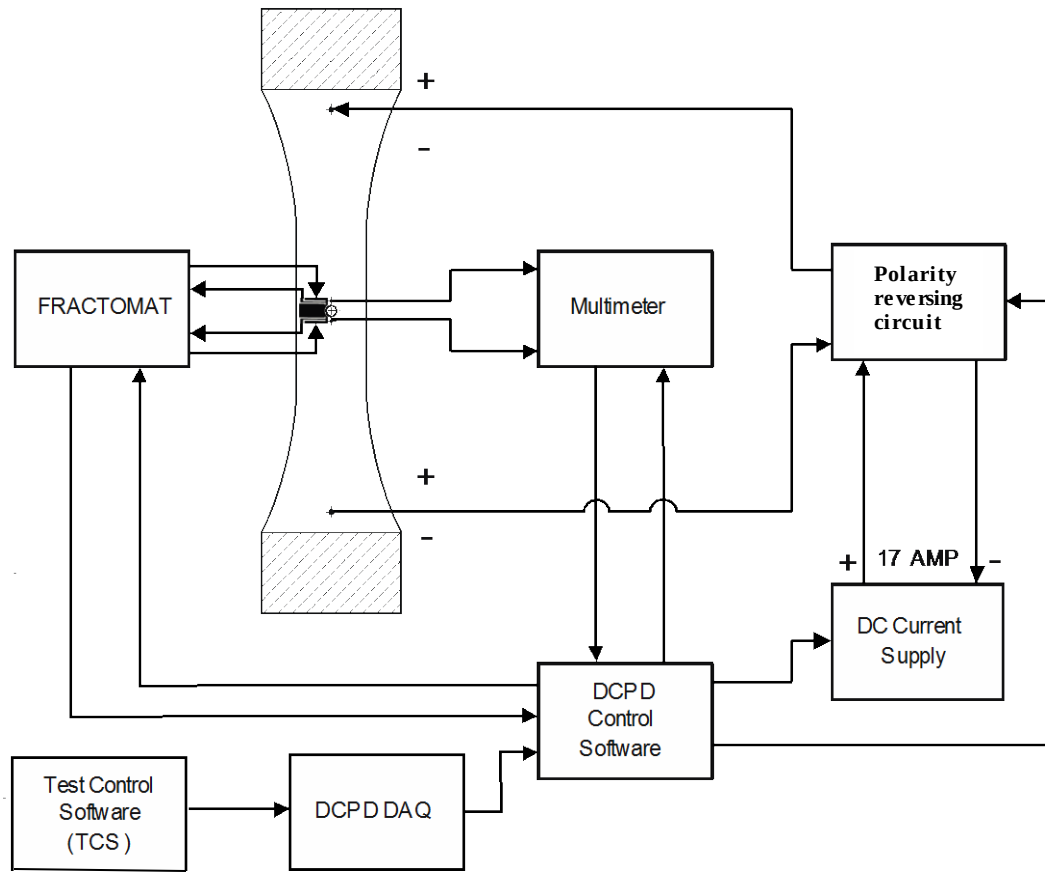

Figure 41. Crack Length Measurement System Diagram

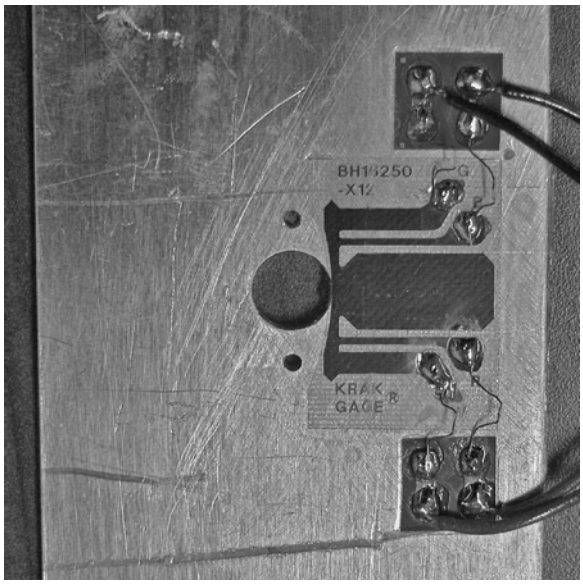

Figure 42. The KG and Strain Relief Pad Positioning

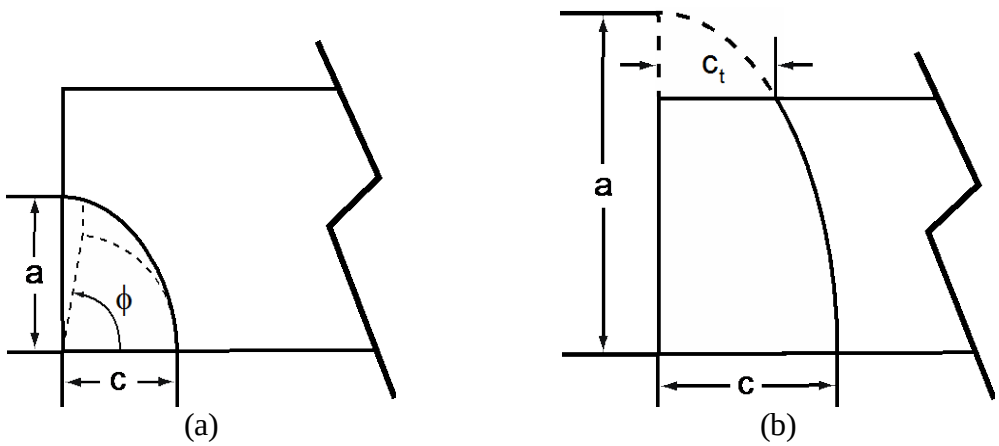

Figure 43. Dimension Definitions for (a) the Corner Crack SIF Solution and (b) the Part-Elliptical Through-Thickness SIF Solutions

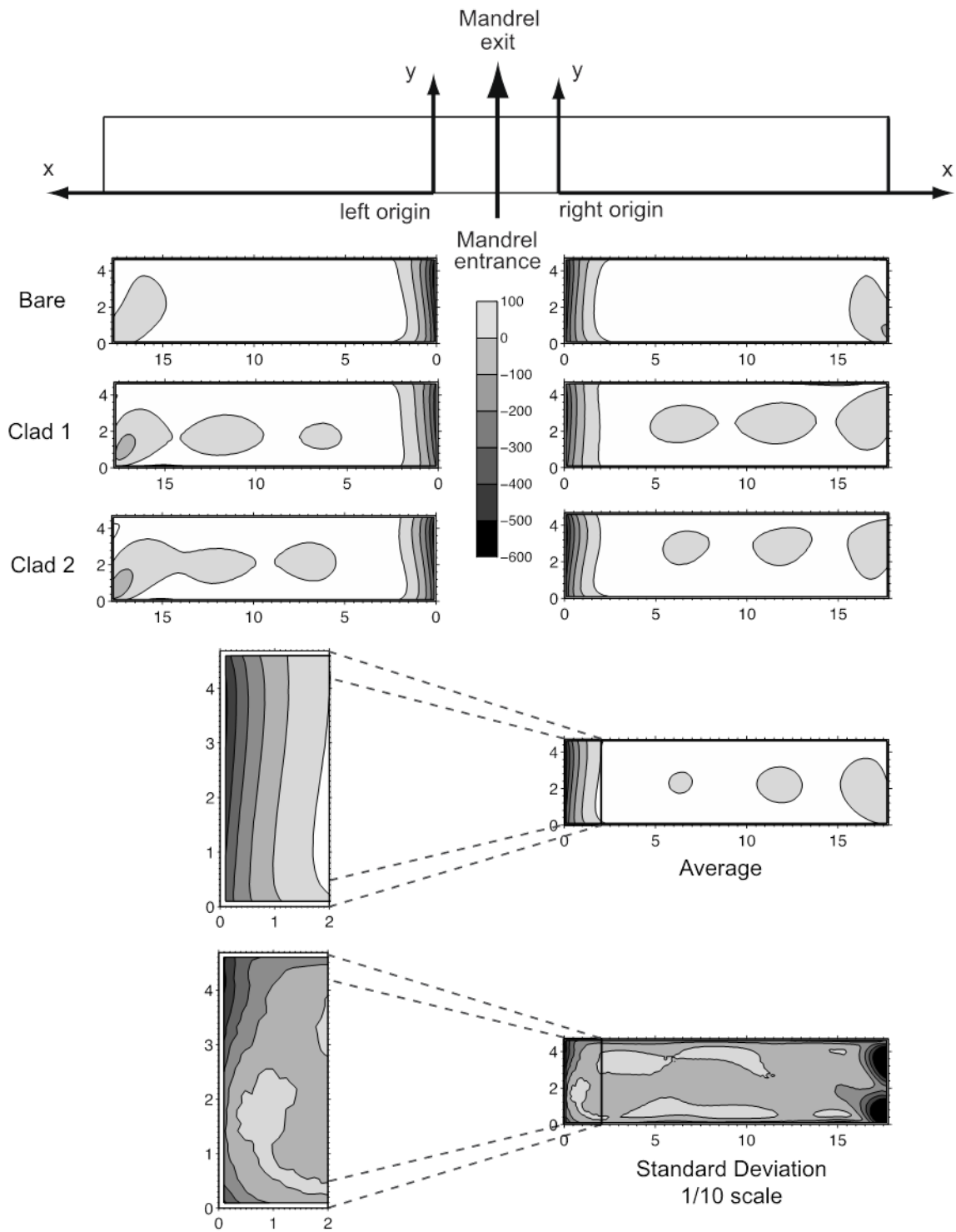

Figure 44. Contour Measurement Results Illustrating 2D Stress Distributions for the Left and Right Side of CX Coupons (1 bare, 2 clad) (white border around each coupon reflects uncertainty of contour measurements within 0.1 mm of edges)

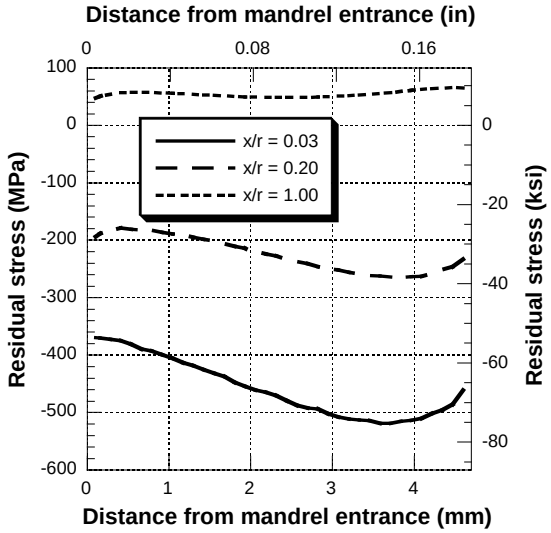

Figure 45. Through-Thickness Residual Stress Distribution at Three Different Positions for the Bare Residual Stress Coupon

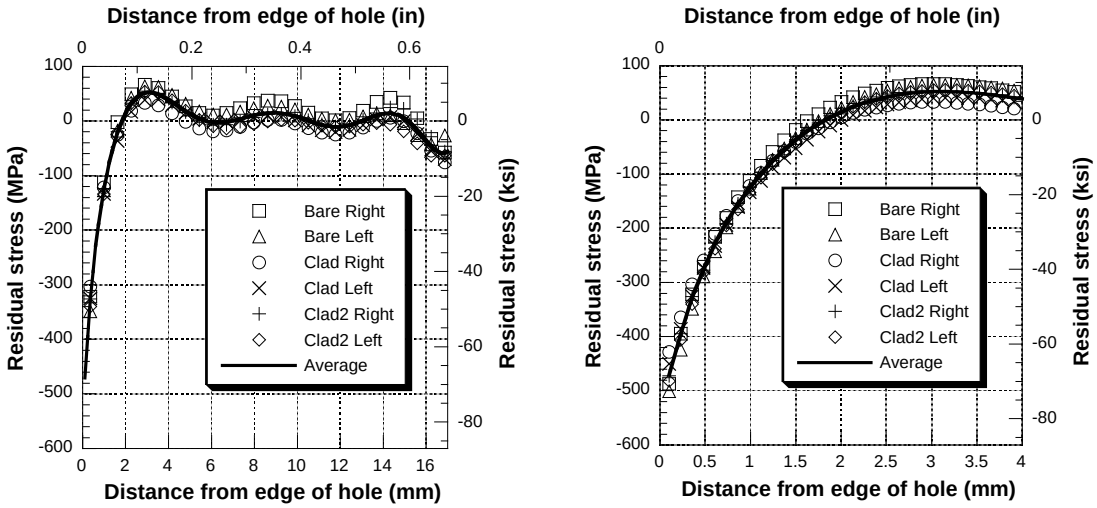

(a) (b)

Figure 46. Mid-Thickness Average Residual Stress for the Left and Right Sides of the Three Residual Stress Coupons

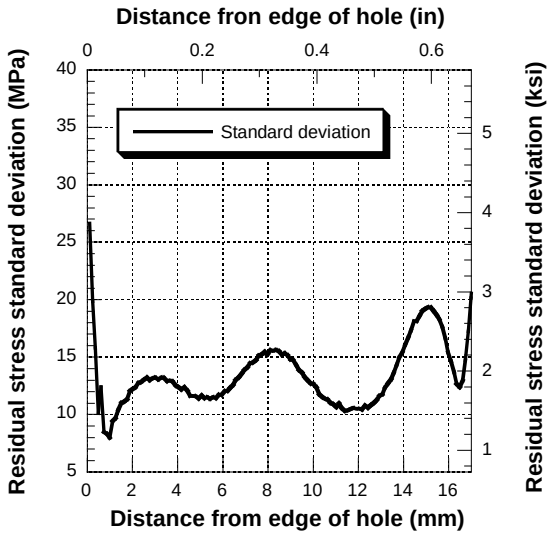

Figure 47. Standard Deviation in Residual Stress for the Set of Six Stress Distributions in Figure vs. the Distance from the Edge of the Hole

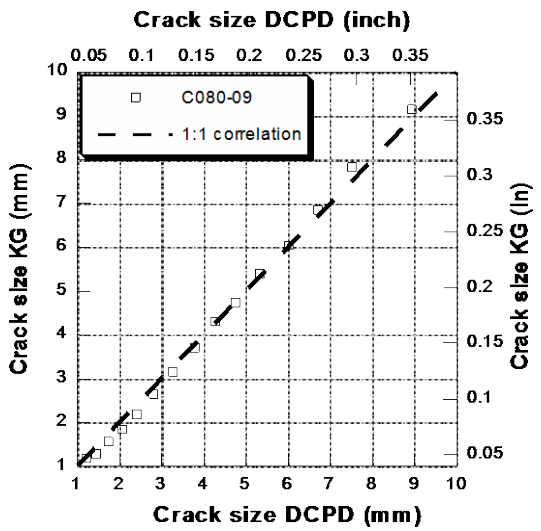

Figure 48. Comparison of DCPD to KG Crack Length Measurements Made on the Same Thin Coupon

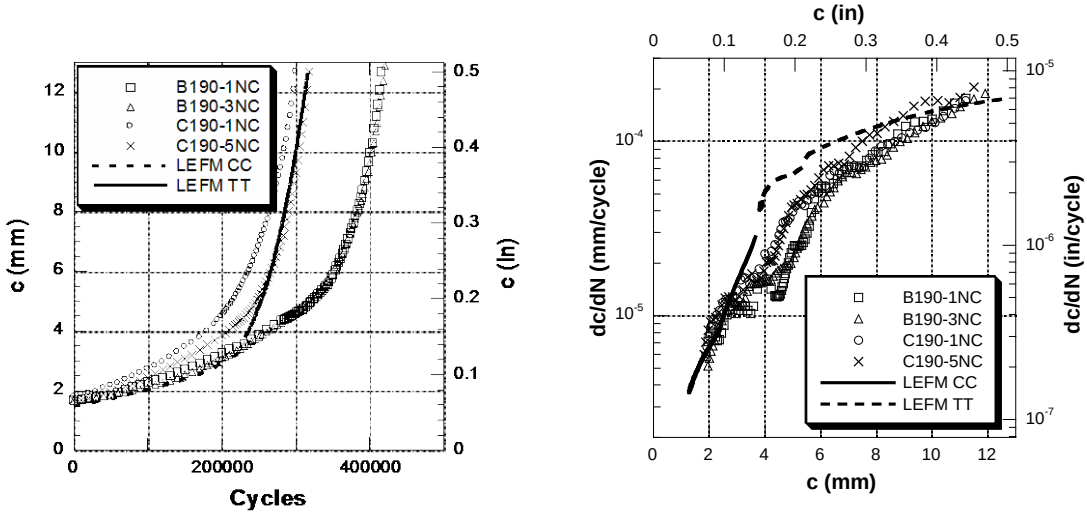

(a) (b)

Figure 49. The AM coupons, R = 0.1 and S_{max} = 47.2 MPa: (a) Front Face Crack Length as a Function of Life (c vs. N), and (b) Front Face Crack Growth Rate as a Function of Front Face Crack Length (dc/dN vs. c)

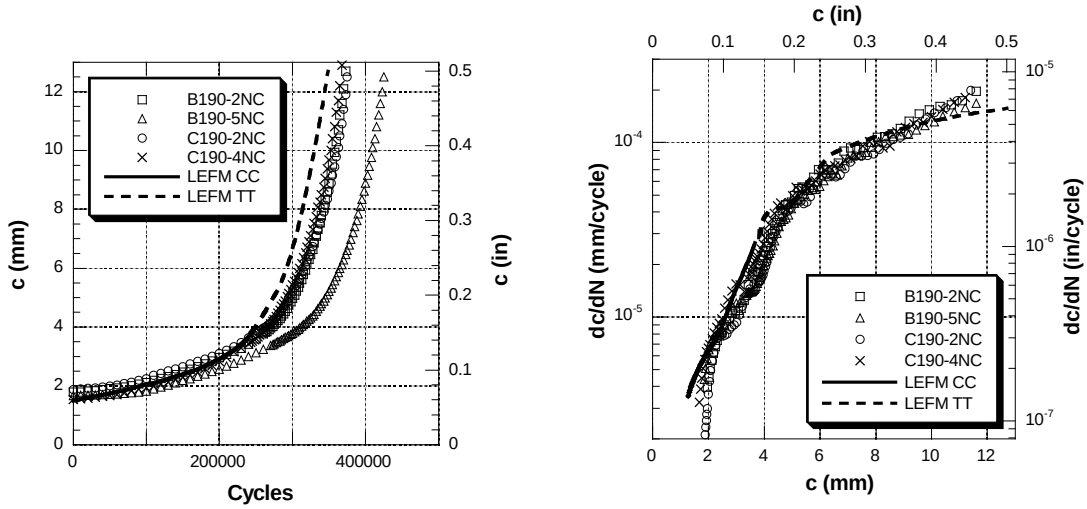

(a) (b)

Figure 50. The AM Coupons, R = 0.5 and S_{max} = 65.0 MPa: (a) Front Face Crack Length as a Function of Life (c vs. N), and (b) Front Face Crack Growth Rate as a Function of Front Face Crack Length (dc/dN vs. c)

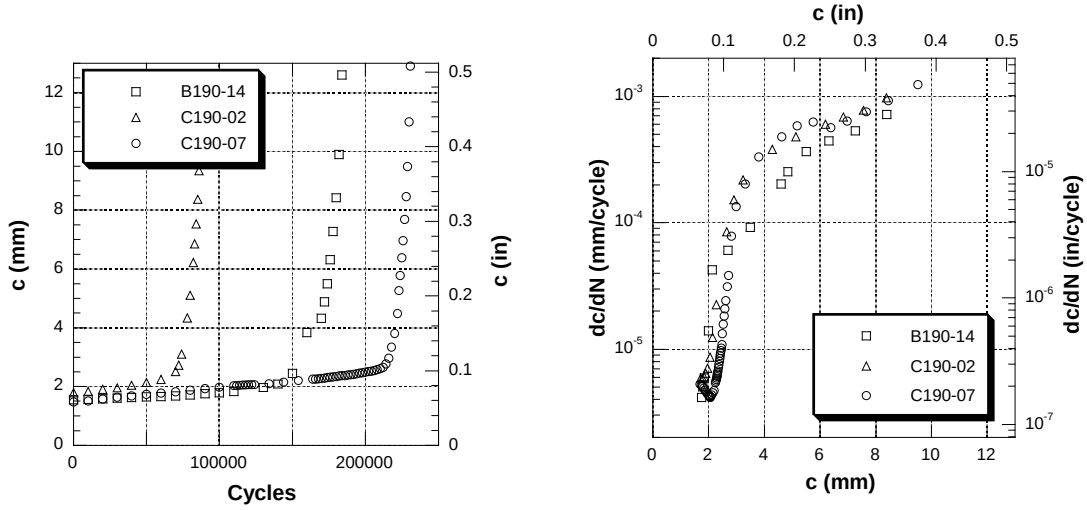

(a) (b)

Figure 51. The CX Coupons, R = 0.1 and S_{max} = 130 MPa (a) Front Face Crack Length as a Function of Life (c vs. N), and (b) Front Face Crack Growth Rate as a Function of Front Face Crack Length (dc/dN vs. c)

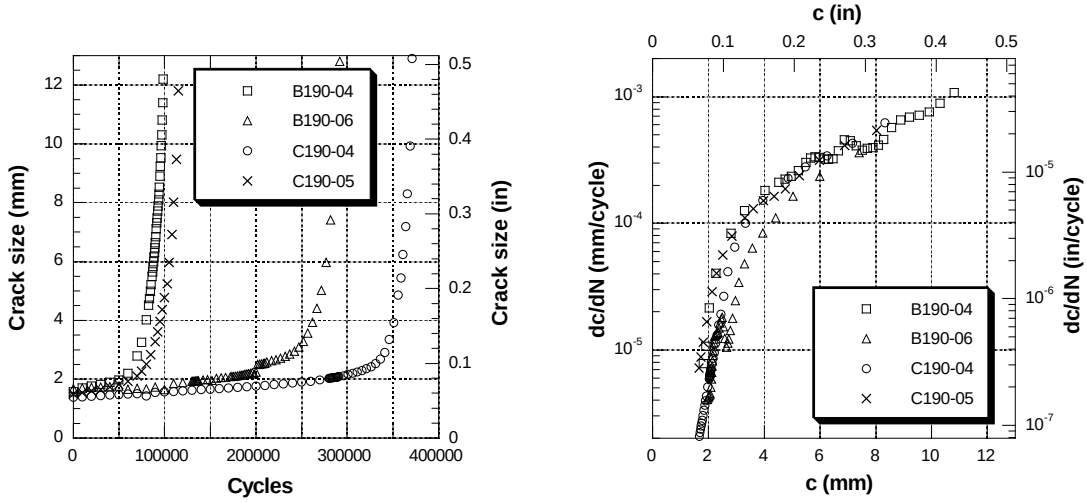

(a) (b)

Figure 52. The CX Coupons, R = 0.5 and S_{max} = 135 MPa (a) Front Face Crack Length as a Function of Life (c vs. N), and (b) Front Face Crack Growth Rate as a Function of Front Face Crack Length (dc/dN vs. c)

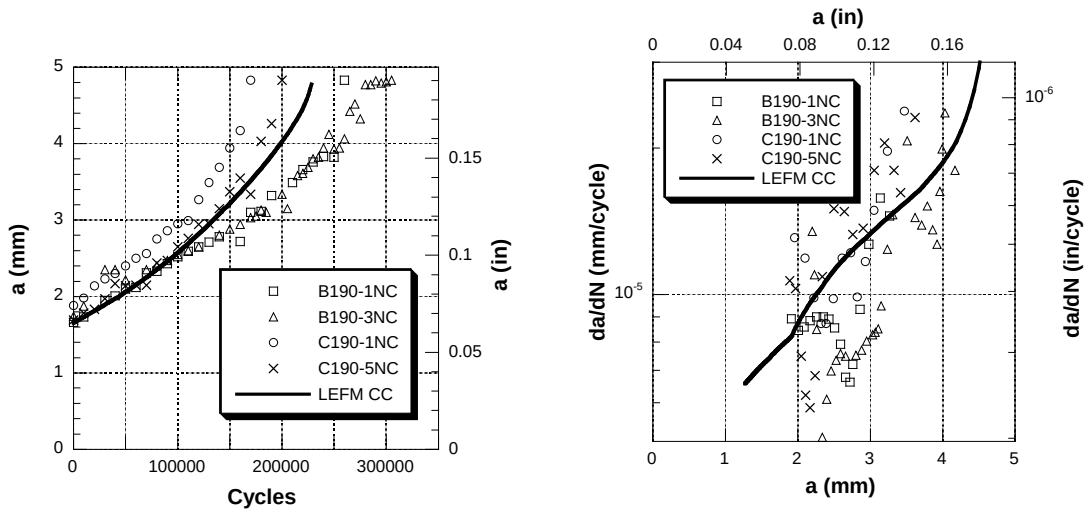

(a) (b)

Figure 53. The AM Coupons, R = 0.1 and S_{max} = 47.2 MPa (a) Bore Crack Length as a Function of Life (a vs. N), and (b) Bore Crack Growth Rate as a Function of Front Face Crack Length (da/dN vs. a)

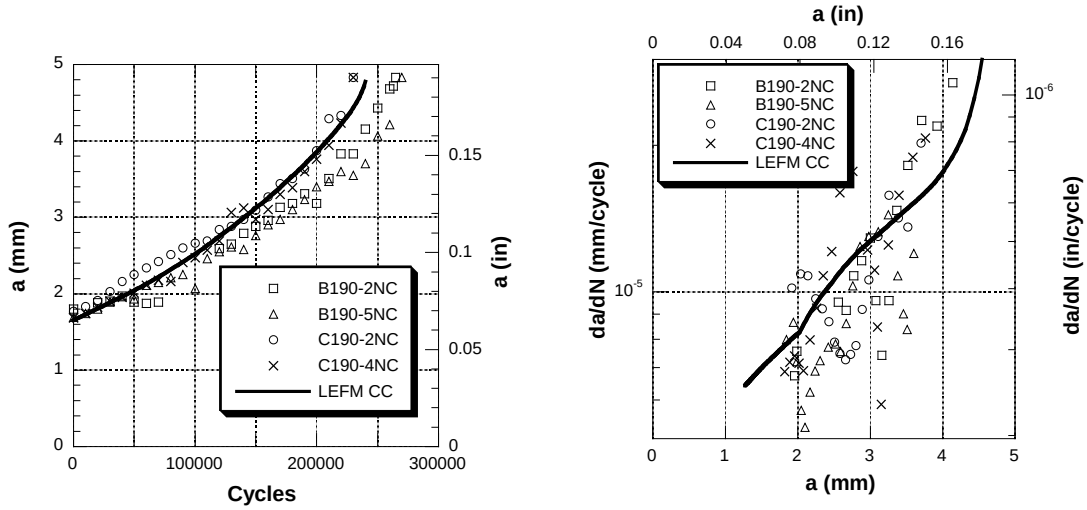

(a) (b)

Figure 54. The AM Coupons, R = 0.5 and S_{max} = 65.0 MPa (a) Bore Crack Length as a Function of Life (a vs. N), and (b) Bore Crack Growth Rate as a Function of Front Face Crack Length (da/dN vs. a)

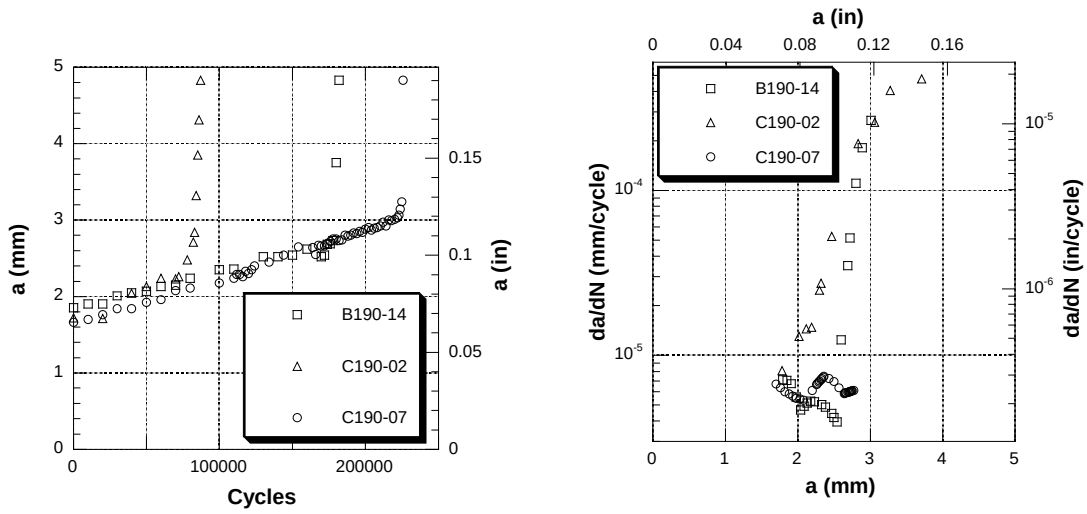

(a) (b)

Figure 55. The CX Coupons, R = 0.1 and S_{max} = 130 MPa (a) Bore Crack Length as a Function of Life (a vs. N), and (b) Bore Crack Growth Rate as a Function of Front Face Crack Length (da/dN vs. a)

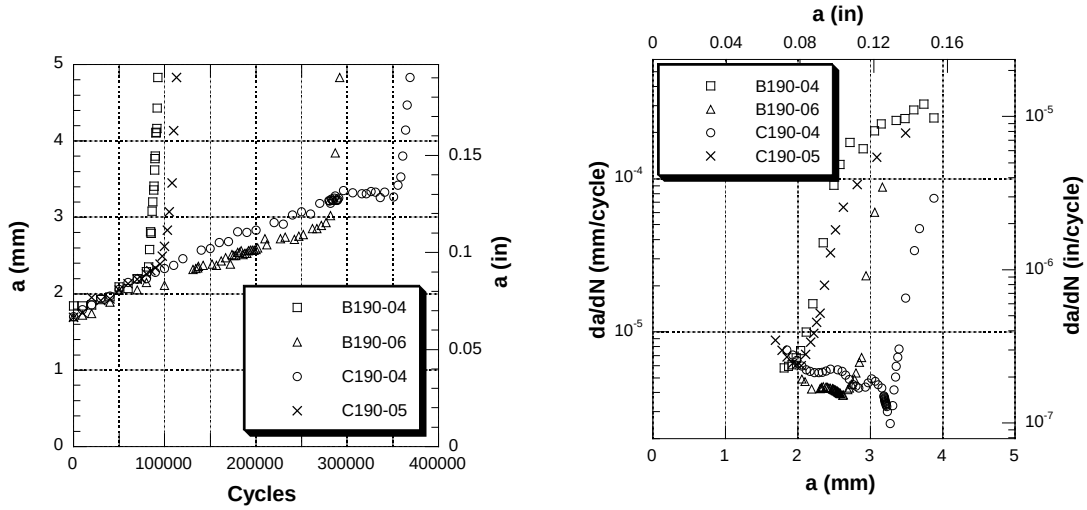

(a) (b)

Figure 56. The CX Coupons, R = 0.5 and S_{max} = 141 MPa (a) Bore Crack Length as a Function of Life (a vs. N), and (b) Bore Crack Growth Rate as a Function of Front Face Crack Length (da/dN vs. a)

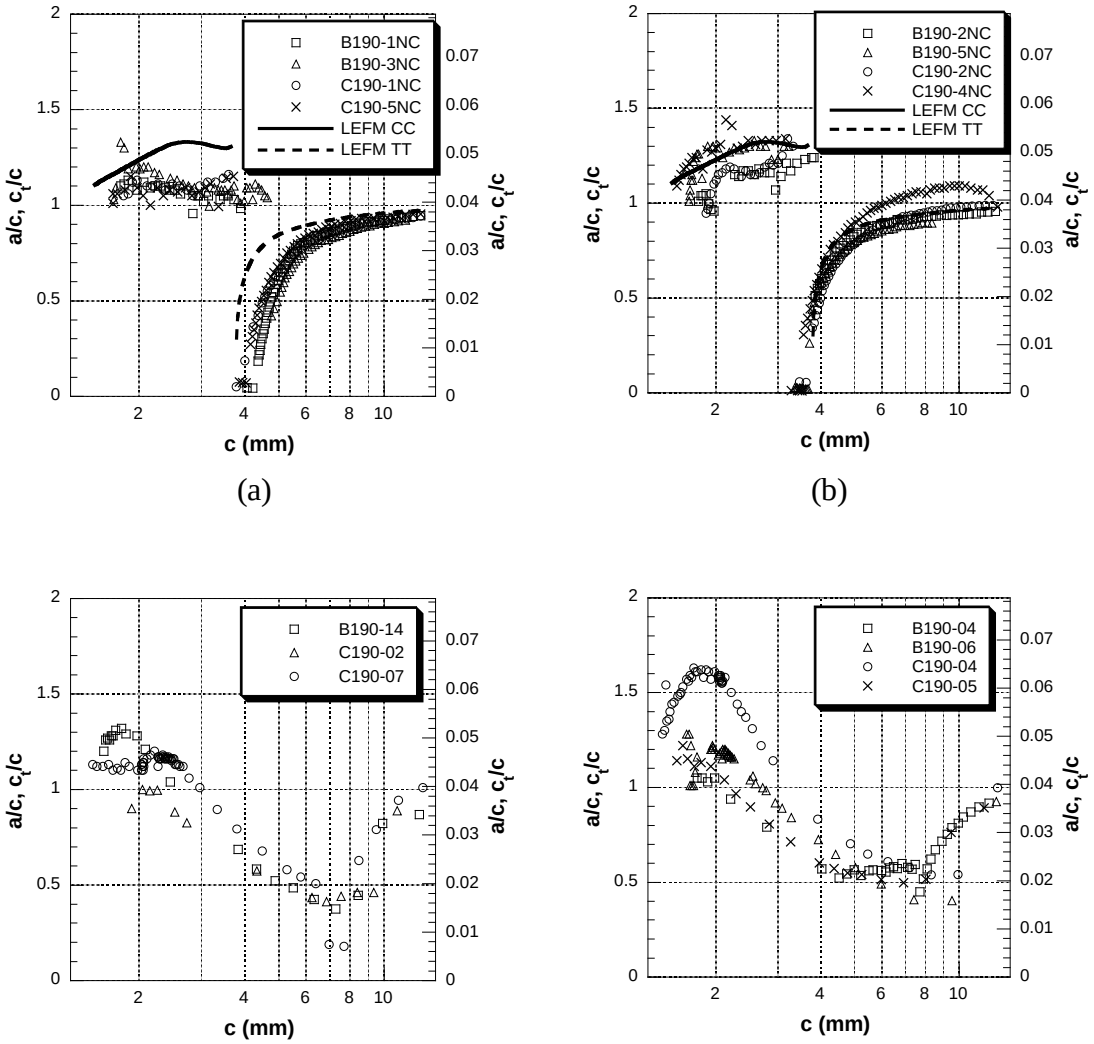

Figure 57. Ratio of Crack Length on the Bore or Back Face to Crack Length on the Front Face (a/c, c_t/c vs. N) as a Function of Life for Each Test Variation: (a) AM R = 0.1, (b) AM R = 0.5 (c) CX R = 0.1, and (d) CX R = 0.5

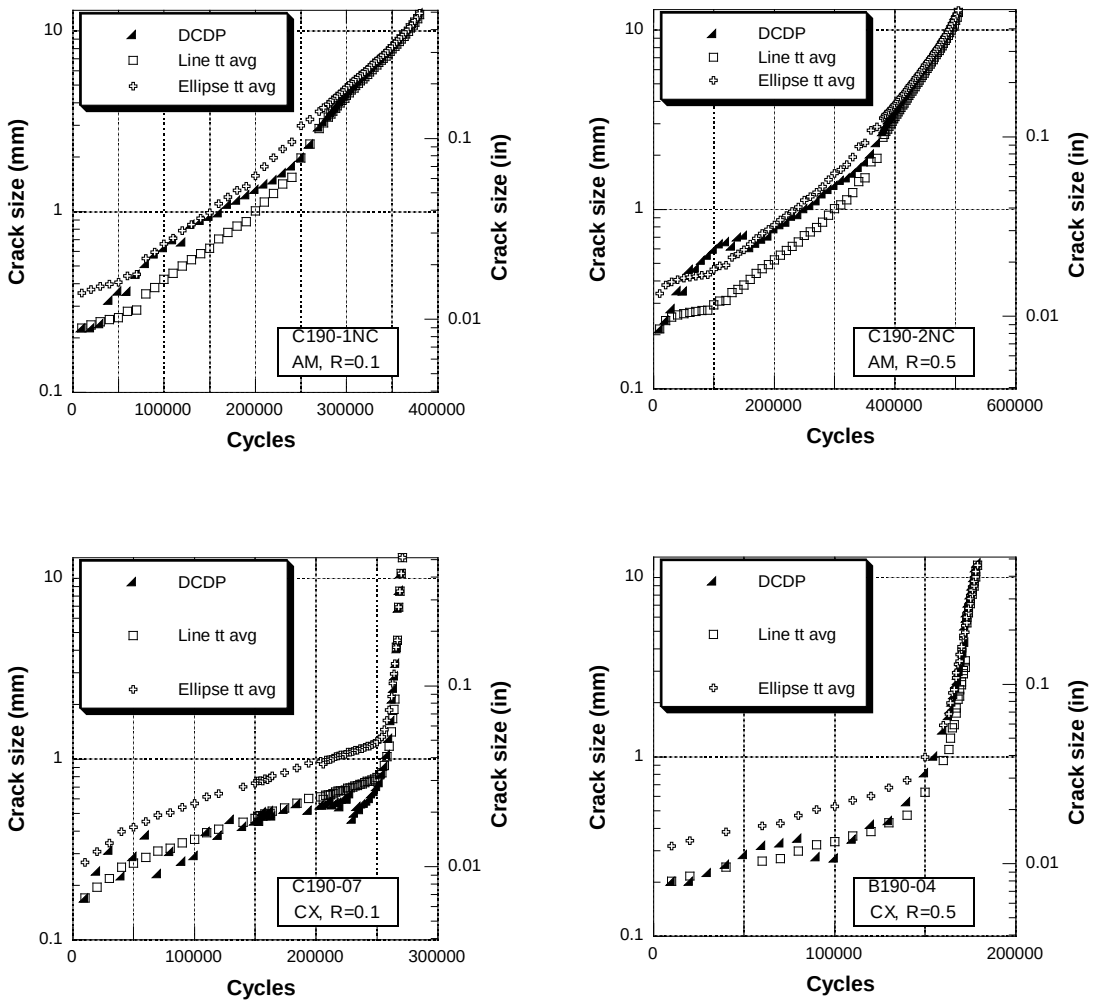

Figure 58. Through-Thickness Average Crack Length as a Function of Loading Cycles for the Four Test Variations Measured by DCPD or Computed From Surface Measurements Using a Crack-Front Model Based on a Straight Line or Part Ellipse

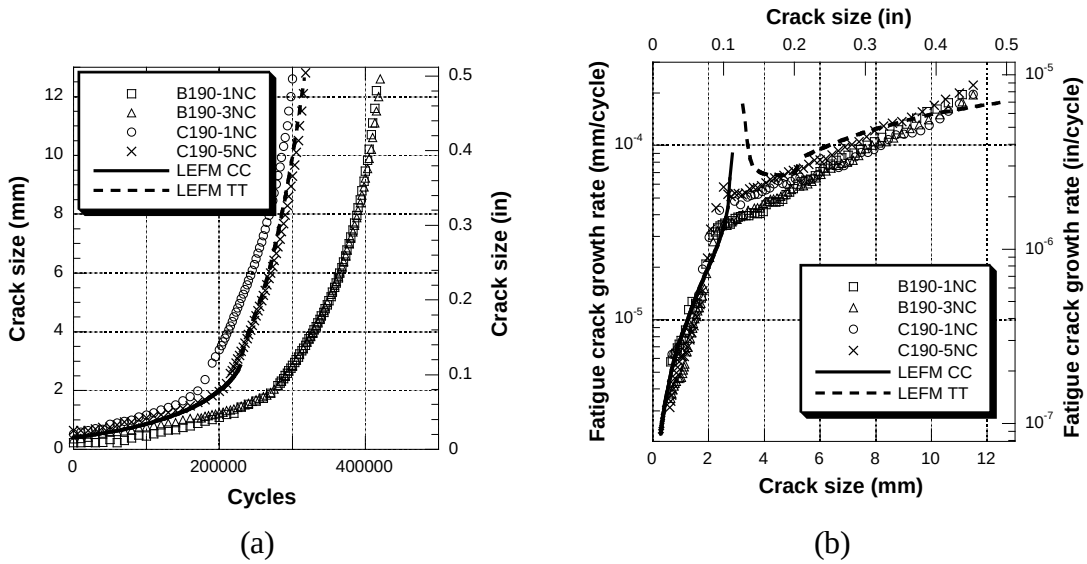

(a) (b)

Figure 59. The AM Coupons, R = 0.1 and S_{max} = 47.2 MPa: (a) DCPD Crack Length as a Function of Life (a vs. N), and (b) DCPD Crack Growth Rate as a Function of Front Face Crack Length (da/dN vs. a)

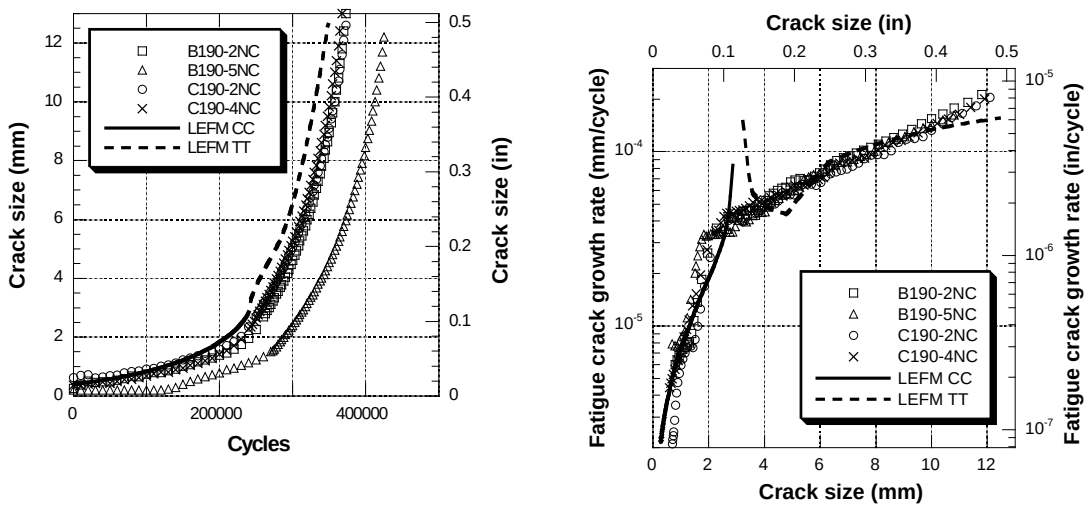

(a) (b)

Figure 60. The AM Coupons, R = 0.5 and S_{max} = 65.0 MPa: (a) DCPD Crack Length as a Function of Life (a vs. N), and (b) DCPD Crack Growth Rate as a Function of Front Face Crack Length (da/dN vs. a)

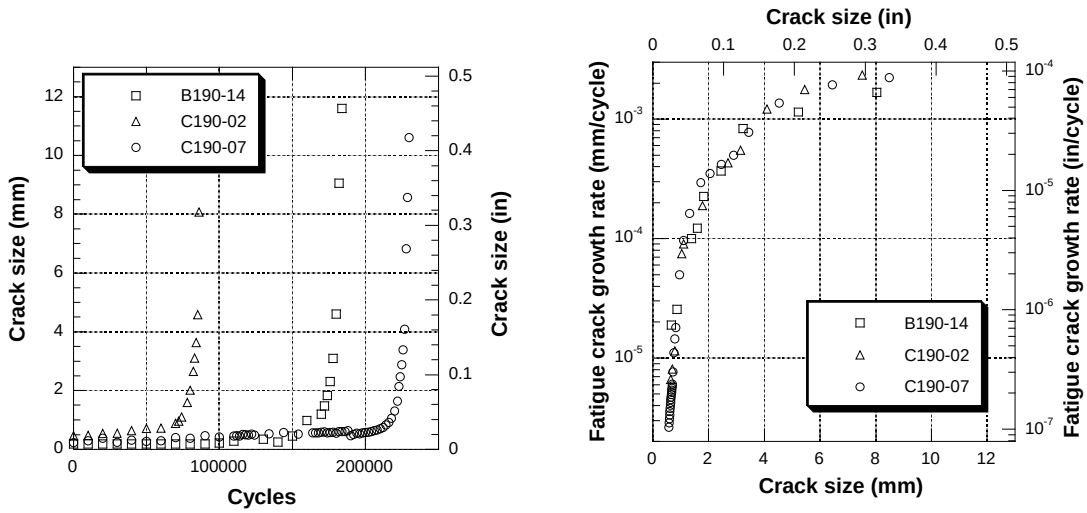

(a) (b)

Figure 61. The CX Coupons, R = 0.1 and S_{max} = 130 MPa: (a) DCPD Crack Length as a Function of Life (a vs. N), and (b) DCPD Crack Growth Rate as a Function of Front Face Crack Length (da/dN vs. a)

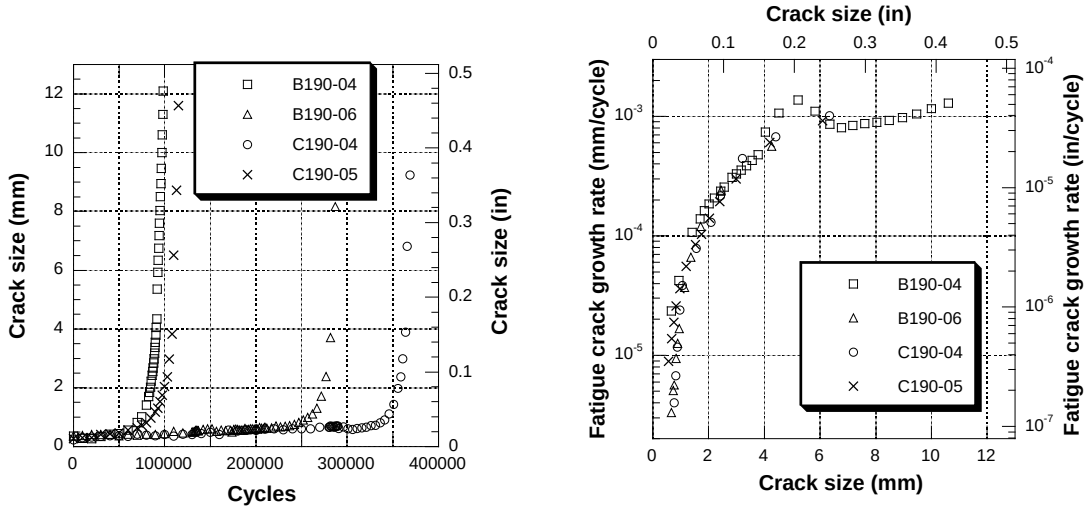

(a) (b)

Figure 62. The CX Coupons, R = 0.5 and S_{max} = 135 MPa: (a) DCPD Crack Length as a Function of Life (a vs. N), and (b) DCPD Crack Growth Rate as a Function of Front Face Crack Length (da/dN vs. a)

5. THE 1D CRACK GROWTH AT COLD-EXPANDED LOADED HOLES UNDER CONSTANT AMPLITUDE LOADING.

5.1 INTRODUCTION.

This section addresses loaded fastener holes. Much of the published experimental work related to loaded holes directly addresses the residual strength of a large array of fasteners [78–80]. Although the basis of many damage-tolerant design guidelines, this work does not investigate crack growth from a single loaded hole. Furthermore, of the work performed on single loaded holes [81–87], only one study [87] included the effects of residual hoop stress.

The main objective of the current section is to demonstrate an LEFM approach to loaded hole crack growth prediction for holes with and without residual stress from CX. To accomplish this, an applied SIF solution provided by the AFGROW crack modeling software [88] was used to calculate an applied SIF. Data from section 3 were used to calculate residual SIFs for coupons with 3% cold mandrel expansion. A superposition-based approach was then used to predict crack growth.

The second objective was to validate the crack growth predictions. For this, predictions of crack growth in AM coupons were compared to test data to evaluate the accuracy of the model and applied SIF. Similarly, predictions of crack growth in CX coupons were compared to test data to examine the effects of residual stress. Testing of both coupon configurations was performed under two stress ratios and multiple applied load levels to investigate the correlation of data for different levels of applied stress.

5.2 METHODS.

5.2.1 Material.

A set of identical loaded hole tensile coupons was cut from a single sheet of 2.03 mm-thick 7075-T6 clad aluminum. The sheet thickness was chosen because it is typical of an airframe structure and thin enough to obtain a constant crack length through the thickness of the coupon. Coupons were cut so the long axis was along the sheet rolling direction (L direction). The mechanical properties of 7075-T6 aluminum sheet in the L direction are listed in table 10 [89].

5.2.2 Geometry.

Loaded hole coupon design is shown in figure 63. The coupons have a total length of 212.7 mm with a 71.4 mm long by 44.5 mm wide gage area on one end. A 7.1 mm diameter hole was located in the gage area on the vertical centerline of the coupon, 22.2 mm from the edge. A large, 89 mm wide grip area was provided on the coupon, tapering from the gage area with a 222.3 mm radius. Additional width in the grip area reduces the opportunity for fretting failure at the grips seen in the earlier tests of constant-width coupons [51].

5.2.3 Hole Preparation.

Residual stresses were introduced on a subset of the loaded hole coupons via 3% split-sleeve CX of the hole diameter. The other half of the coupons did not undergo a residual stress treatment, remaining in the AM condition.

After coupons were cut from the sheet, holes were introduced by first drilling a 6.35 mm diameter pilot hole in the location described above. For CX coupons, a 3% CX of the pilot hole diameter was then performed. The CX starts by placing a split sleeve in the hole with the split running parallel to the length of the coupon. This sleeve is sized to provide a 3% interference fit with the tapered mandrel. After mandrel expansion, holes were reamed to a final diameter of 7.1 mm, removing material around the hole perimeter that may have been damaged by the CX process. For AM coupons, the pilot hole was reamed to 7.1 mm, resulting in the proper hole diameter and low levels of residual stress.

5.2.4 Residual Stress Fields.

Residual stress measurements for identically prepared CX coupons were reported in sections 3.2.2 and 3.3.1, and the residual stress fields in the open hole and loaded hole coupons were assumed to be identical. A plot of residual stress versus radial distance from the hole perimeter is given in figure 64, which includes error bars showing the variation of measured residual stress. The residual stresses are highly compressive at the perimeter of the hole, measuring approximately -460 MPa; sharply decrease in magnitude with radial distance; become tensile approximately 2.1 mm from the hole edge (which is to be expected from force equilibrium); and decrease to a negligible level far from the hole. Crack growth predictions for open hole CX coupons included a ±10% variation of residual stress that provided useful bounds to the experimental data, and the same bounds were used in predictions for loaded hole CX coupons.

5.2.5 Test Matrix.

The effects of two variables on fatigue crack growth were investigated. The AM crack growth was compared to CX crack growth to evaluate the effects of residual stress. The effects of applied stress ratio were evaluated by comparing results from tests performed at $R = 0.1$ and $R = 0.5$. The AM coupons were tested at a variety of maximum applied stresses (S_{max}) to evaluate LEFM predictions at multiple stress levels. One AM coupon was improperly calibrated and tested at $R = 0.14$. Additional LEFM predictions were performed to compare against these results, as described in section 5.2.7.

5.2.6 Crack Growth Testing.

Fatigue crack growth testing was performed by applying a constant amplitude time varying bearing stress to the loaded hole using a servo-controlled hydraulic load frame. The bearing stress was applied to the coupon by a 6.35 mm diameter high-strength steel loading pin. This pin was passed through the coupon hole and loaded by a clevis that allowed visual inspection (see figure 65). A 10 mm long 660 Bronze bushing with a 6.35 mm inner diameter and 7.1 mm outer diameter was placed between the loading pin and coupon hole to mitigate fretting. Cracks were grown from the notch to a measured crack length of 7.62 mm. The test was terminated at this

length to enable post-test inspection. Reported crack lengths (see table 13) varied slightly from the termination crack length due to DCPD calibrations made following post-test crack length measurements, discussed below.

A fatigue crack starter notch was cut into the perimeter of each hole using wire electric discharge machining (wire EDM). The notches were perpendicular to the length of the coupon. A 0.77 mm-long notch was cut into the CX coupons and a 0.25 mm-long notch was cut into the AM coupons. The CX and AM samples used different notch lengths to mitigate fretting failure seen in initial CX testing, as discussed below. The distance between the opposing notch faces (notch height) was 0.127 mm. Microscopic measurements of the notch front were made to ensure constant length through the coupon thickness. These measurements were made on the fracture surface following completion of crack growth testing, using the five-point measurement technique described in ASTM E399-90 [90], section 8.2.2.

Fatigue pre-cracking was accounted for during data analysis. This differed from the standard approach suggested by ASTM [4], which is not suitable for CX coupons. The standard pre-cracking method requires a pre-crack extending from the notch length (a_n) that is as long as the notch height, 10% of the coupon thickness (0.203 mm), or 1 mm, whichever is greater. These requirements tend to eliminate most of the data collected within the compressive residual stress region (see figure 64). Instead, crack length data was collected immediately off of the notch tip and any data affected by the notch (characterized by a decreased FCGR) were eliminated. This resulted in initial crack lengths (a_i) of 0.508 and 1.016 mm (from the hole edge) for the AM and CX tests, respectively, satisfying two of the three pre-cracking criteria.

5.2.7 Load Level Determination.

Predictions were made using an LEFM model to approximate the level of S_{max} needed for a test duration of roughly 200,000 cycles. The loads applied to achieve the levels of stress predicted by LEFM were calculated using strength of materials. The values of S_{max} (gross section stress) and subsequent values of applied load based on this prediction are provided in table 11. Adjustments to the load levels were made during initial tests to achieve the desired test duration.

5.2.8 Test Frame Calibration.

The load frame was statically aligned [52] to eliminate bending in the coupon. Bending was measured using strain gages that were symmetrically placed at the bottom of the gage area. Gages were placed on the front and back face and on the left and right sides of the coupon. Bending was measured as the difference between the front and back, and left and right strain measurements under a monotonically applied load.

The system was dynamically calibrated [53] to verify that the proper stress levels were being applied at the test frequency. Strains were measured on the coupon face using strain gages under a cyclic load applied at 10 Hz. Peak and valley stresses were calculated from the strain measurements using uniaxial stress-strain relations. The applied load levels were adjusted until the proper stress levels were achieved at the 10 Hz test frequency. Along with the target load levels calculated for each S_{max}, table 11 also lists the commanded load levels resulting from

dynamic calibration. Sample N2 was improperly tested at $R = 0.14$. The target stresses listed in table 11 for this sample were calculated from the commanded loads.

5.2.9 Data Collection Instrumentation.

Crack length was measured using the indirect current potential drop (DCPD) measurement technique and the KG system [73]; details were identical to those used for surface crack length measurements on thick, open hole coupons (see section 4.2.4.3). Two gages (KG model BH 16250 X12) were bonded to the coupon, one on the front and back surfaces, overlapping the notch, a minimal distance from the hole perimeter and covering the expected path of the fatigue crack. Crack length measurements were made on the front and back surfaces to verify 1D crack growth. Figure 66 illustrates the placement of the KG on the coupon.

Crack plane bending was monitored throughout the tests by taking the difference between strain measurements made on the front and back face of the coupon. Strain gages with a gage length of 1.57 mm were placed adjacent to the hole opposite the notch. The gages were placed 1.5 mm from the hole perimeter, as shown in figure 66. Early tests showed that unmonitored crack plane bending caused undesirable through-thickness variations in crack length (to be discussed in section 5.4.2.1).

5.2.10 Data Collection.

Crack length and strain data were collected every 1000 cycles by holding the test at 80% S_{max}. This was done to ensure that the crack faces were completely separated during data collection. A set of 30 measurements was made during each inspection period and was averaged to reduce the effects of noise.

5.2.11 Post-Test Measurements.

Numerous post-test measurements were taken to verify the data. Microscopic measurements were made of the initial notch length and final physical crack length. These measurements were taken using a microscope with a motorized stage that was used to linearly correct DCPD measurement, as suggested in section A6.3 of ASTM E647 [4].

Crack angularity was verified per ASTM E399-90 [90] section 8.2.2, using photogrammetric measurements of the surface crack length. Photogrammetric measurements were also made on the fracture surface to verify 1D crack growth, per ASTM E647 [4], section 8.8.3.

5.2.12 DCPD Correlation.

A mathematical relationship was used to correlate DCPD voltage measurements to physical crack length. The relationship was developed from FE analysis results similar to those discussed by Ritchie and Bathe [60]. The analysis used a commercial code [91]. The problem domain was a 2D description of the KG boundary (as shown in figure 66). A constant current boundary condition was defined at each current lead and Laplace's equation was solved over the domain to provide the voltage difference between the voltage lead locations. Results were obtained for a series of crack lengths, with the crack length increasing perpendicular to the applied stress (i.e., a

0° crack). A second set of results was obtained with the crack at 15° to understand how crack angle affects voltage.

A power series was used to fit the FE results. Normalized voltage was defined as:

$$\gamma(a) = \left\lfloor \left(V(a) - V_0\right) / \left(V_f - V_0\right) \right\rfloor \tag{12}$$

where $V(a)$ is the voltage on the KG with a crack length of a, V_o is voltage for $a = 0$, V_f is voltage for $a = a_f$, and a_f is a final crack size of 12.7 mm (specified by the gage manufacturer). The power series for crack length in terms of normalized voltage is:

$$a / a_f = \sum_{i=1}^{5} \alpha_i \left(\gamma\right)^{i/2} \tag{13}$$

An inverse relation is given by:

$$\gamma = \left[\sum_{j=1}^{5} v_j \left(a / a_f\right)^j \right]^2 \tag{14}$$

Coefficients α_i and v_j are listed in table 12 for cracks at 0° and 15°. The power fits to the numerical data are plotted in figure 67(a) for both the 0° and 15° cracks that fit the results to an R^2 value of 1.0000. Figure 67 also illustrates the effect of crack angle on DCPD calibration, noted by the divergence in the relationships at longer crack lengths.

Controlled DCPD measurements were made to validate the numerical DCPD calibration, as suggested by Ritchie and Bathe [60], and Hicks and Pickard [92]. Measurements were made by mounting KGs on coupon material, carefully slitting them to a set of crack lengths, and recording measured voltage. The resulting data, which show good agreement between the DCPD measurements and the power series fit to the numerical results at both crack angles, are given in figure 67(b).

5.2.13 Crack Growth Predictions.

Crack growth predictions were made using an LEFM approach. The AFGROW solution [88] for the SIF at a loaded lug due to applied pin load was used in the analysis. The AFGROW solution includes a hole-edge boundary condition that accounts for the neat-fit pin used to apply the load in these tests. Other solutions for lug geometry, such as those used by NASGRO [45] and earlier versions of AFGROW, assume a pin-hole pressure-loading distribution that ignores contact effects. In computing the SIF, it was important to account for the difference in reference stress used here (gross section stress, which uses gross section area (width times thickness)), and that used by AFGROW (bearing stress, which uses hole area [diameter times thickness]). The residual SIF (K_{RS}), as a function of crack length, was calculated using the weight function method suggested by Wu and Carrlson, et al. [22] adapted to the present geometry, as described in section 3.2.4.6. The combination of applied and residual SIF (K_{tot}) and combined stress ratio

(R_{tot}) were calculated using superposition. The FCGR was predicted from ΔK_{tot} and R_{tot} using the ΔK_{eff} correlation developed earlier by Newman et al. [93] and also described in detail in section 3.2.4.6.

5.3 RESULTS.

5.3.1 Fatigue Crack Growth Predictions.

A plot of geometry factor versus crack length, for both applied and residual stress, is shown in figure 68. The geometry factor for applied stress is greatest close to the hole and steadily decreases with crack length because of stress concentration. The geometry factor for residual stress has a maximum absolute value of approximately -1 close to the hole and approaches zero at a crack length of 4 mm. Because of an error in the AFGROW software package, applied geometry factor is not reported for crack lengths less than 0.47 mm. Even though AM initial notches (a_n) were 0.25 mm long, compensation for fatigue pre-cracking (discussed in section 5.2.6) corresponded to an initial crack length (a_i) of 0.508 mm, avoiding the erroneous values at short crack lengths.

For loading of $S_{\max}$ = 60.33 MPa and R = 0.1, $K_{app,\max}$ is plotted as a function of crack length in figure 69, along with K_{RS}, $K_{tot,\max}$, and $K_{tot,\min}$. The $K_{app,\max}$ is at its minimum value of approximately 12.5 MPa m$^{1/2}$ near the hole. At a crack length of 1.4 mm, $K_{app,\max}$ peaks at 14.2 MPa m$^{1/2}$, then decreases with crack length. The K_{RS} decreases sharply with crack growth as compressive residual stresses begin to take effect. The K_{RS} reaches a minimum value of -12 MPa m$^{1/2}$ at a crack length of approximately 0.5 mm. Following the minimum value, K_{RS} approaches zero as residual compressive stresses diminish. The $K_{tot,\max}$ and $K_{tot,\min}$ both start at minimum values close to the hole perimeter, highlighting the effects of residual stress. The $K_{tot,\max}$ and $K_{tot,\min}$ approach the values of $K_{tot,\max}$ and $K_{tot,\min}$ with crack length, as the crack tip grows beyond the CX material.

5.3.2 Fatigue Crack Growth Test Data Compared to LEFM Predictions.

Fatigue lives measured during AM R = 0.1 and R = 0.5 tests are provided with LEFM fatigue life predictions (for the same test conditions) and key test parameters in table 13. Fatigue life predictions were compared to test data by examining the ratio of observed to predicted cycles (N_{obs}/N_{pred}) to grow a crack from the initial crack length of 0.508 mm to the final crack lengths listed in table 13. For AM tests at R = 0.1, fatigue life ratios ranged between 0.76 and 1.63, with an average of 1.06. For tests at R = 0.5, fatigue life ratios ranged between 0.72 and 1.31, with an average of 0.84.

Crack growth and FCGR measured during each AM test have been plotted against LEFM predictions in figures 70 and 71 for tests conducted at R = 0.1 and 0.5, respectively. These plots show constant crack growth during AM testing. The LEFM predictions remained very close to the test data, indicating that LEFM accurately predicted fatigue crack growth in the AM coupons.

Fatigue lives measured during CX R = 0.1 and 0.5 tests have been compared with LEFM fatigue life predictions in table 13. The average ratio of observed to predicted cycles (at 100% residual stress) for R = 0.1 tests ranged between 0.79 and 1.58, with an average of 1.27. The observed

data are contained within the upper and lower bounds, resulting from 10% residual stress variability. For $R = 0.5$ tests, fatigue life ratio varied between 0.85 and 3.11, with an average of 1.99. The variability in residual stresses provided a useful lower bound to the test data, but three of the five coupons exceeded the corresponding upper bound.

Observed crack growth and FCGR through CX coupons are plotted with LEFM predictions in figures 72 and 73 for $R = 0.1$ and 0.5, respectively. These plots show slow crack growth early in the test, as the crack grows through the compressive residual stresses. Between the crack lengths of 1.2–2.0 mm, the growth rate increases significantly because of the larger crack size and decreasing K_{rs}. Crack growth measured during $R = 0.1$ testing is contained within the upper and lower limits of the crack length predictions. This is contrasted by the LEFM predictions of $R = 0.5$ crack growth, which provided an accurate lower bound to the crack length measurements, but contained only two of the five tests within the upper bound. Also seen in figures 72 and 73, FCGR measured during $R = 0.1$ tests agreed more closely with the LEFM predictions than that measured for $R = 0.5$. The $R = 0.5$ predictions generally fell above the measured FCGR data. These data indicate that LEFM accurately predicted CX $R = 0.1$ crack growth behavior between the limits of residual stress variability and provided mixed results for the $R = 0.5$ crack growth predictions.

5.4 DISCUSSION.

5.4.1 Correlation Between Observed and Predicted Behavior.

The good correlation between observed and predicted fatigue cracking in AM coupons (see figures 70 and 71) supports the LEFM model used. That model relies on both the AFGROW SIF solution [66] and the closure-based correlation between FCGR, ΔK, and R suggested by Newman [62]. These findings are consistent with similar work on loaded lug coupons that also showed good correlation between observed and predicted fatigue cracking [85]. The good correlation (for loaded hole coupons) also agrees with results for open hole coupons (section 3).

The LEFM model was dependent on the applied stress ratio and could not always provide a good correlation for CX coupons. Observed fatigue cracking of CX coupons tested at $R = 0.1$ (see figure 72) were in good agreement with predictions in terms of the average of all test data and ±10% variations of residual stress. These accurate predictions suggest that the residual stress distributions used in the calculations and their use in the LEFM analyses (weight function method, superposition of applied and residual SIFs) provided good results. For CX coupons tested at $R = 0.5$ (see figure 73), the results were somewhat less successful. Observed crack growth rates were lower than predicted for three of the five CX $R = 0.5$ tests, resulting in longer-than-predicted fatigue lives. The differences in crack growth rate are for mid-range crack lengths (from 2–4 mm crack length in figure 73[b]). The other two tests experienced similarly low crack growth rate at shorter crack lengths, but rose above the predicted rates at longer crack lengths so that life predictions were more accurate.

The discrepancies between CX $R = 0.5$ predictions and test data are puzzling when considering the successful prediction of crack growth for all other test configurations. Similarly conservative predictions were noted in section 3.3.3 for open hole CX coupons at $R = 0.5$. However, those predictions were closer to the test data (figure 37[b]).

5.4.2 Methodological Difficulties.

5.4.2.1 Asymmetric Crack Growth.

Significant differences between measured front and back face crack length occurred during initial CX testing. If left unattended, this difference violated ASTM limits for 1D crack growth [4], as shown in figure 74.

Achieving 1D crack growth was essential to match modeling predictions. The 1D crack growth was achieved by using higher loads, eliminating initial crack plane bending, and correcting asymmetric crack growth. Higher stress levels were used to reduce the effects of crack closure. Initial crack plane bending was eliminated by placing 0.025 mm thick steel shim stock between the clevis saddle and loading pin (fixturing highlighted in figure 65), until the difference in front and back crack plane strain (measured by the strain gages shown in figure 66) was within 3% of the average. As illustrated in figure 75, even though initial bending was eliminated, asymmetric crack growth still occurred. Therefore, the difference between front and back crack length was monitored throughout testing. If the difference exceeded 0.4 mm, the shims were adjusted to apply a tensile bending stress on the side of the coupon with a shorter crack length. The effect of this adjustment can be seen in figure 75 at an average crack length of approximately 2.2 mm. Seen here is the change in strain as the shims are adjusted and the resulting change in front and back crack lengths that occurred with further crack growth.

Asymmetric crack growth was not noticed during loaded hole AM testing or during any of the open hole tests. This observation suggests that asymmetric crack growth is the result of through-thickness residual stress variations, absent in AM coupons, coupled with the sharp residual and applied stress gradients along the loaded hole ligament. Although forcing 1D crack growth did enable useful correlation with 1D LEFM analysis, further investigation would be useful to understand the natural crack growth behavior.

5.4.2.2 Fretting Damage.

Initial CX tests experienced significant fretting around the hole perimeter, which initiated a fatigue crack opposite the notch. A photograph of this can be seen in figure 76. This behavior was noted during other loaded hole testing [85] and was avoided in that work by shortening the termination crack length. Fretting failure was avoided in the present testing by using a slightly lower stress level. This negated some of the adjustments made to resolve 2D crack growth, therefore requiring a balance between the two influences. The lower S_{max} also required a longer crack starter notch in CX coupons. The bronze bushing installed between the pin and coupon further reduced fretting damage by providing a layer of compatible material between the contact surfaces. This reduced relative friction and provided a sacrificial layer, thereby reducing fretting damage on the coupon.

5.5 TABLES.

Table 10. Mechanical Properties for Clad 0.080-Inch 7075-T6 Aluminum Sheet

	Clad
Ultimate tensile strength (MPa)	503
Yield strength (MPa)	448
Young's modulus (MPa)	71000
Poisson's Ratio (ν)	0.33

Table 11. Target Stresses and Loads for Fatigue Testing

Material Condition	S_{max} (MPa)	R	Target P_{max} (kN)	Target P_{min} (kN)	Commanded P_{max} (kN)	Commanded P_{min} (kN)
AM	37.92	0.1	3.43	0.34	3.32	0.33
AM	32.75	0.1	2.96	0.30	3.06	0.49
AM	31.03	0.1	2.80	0.28	2.87	0.48
AM	23.40	0.14	2.11	0.30	2.46	0.29
AM	60.33	0.5	5.45	2.72	5.31	2.68
AM	48.26	0.5	4.36	2.18	4.40	2.20
AM	37.92	0.5	3.43	1.71	3.37	1.73
CX	60.33	0.1	5.45	0.54	5.52	0.77
CX	62.05	0.5	5.60	2.80	5.58	2.90

Table 12. Coefficients to the Power Series Defining Correlations Between DCPD and Crack Length for Cracks at 0º and 15º; Valid for $a \leq 13.2$ mm and 9.5 mm, Respectively

	0°		15°	
i or *j*	α_i	ν_j	α_i	ν_j
1	0.3976	2.5491	0.4601	2.3820
2	0.3552	-3.9888	-0.2851	-1.9217
3	-0.8713	4.3007	1.2934	-2.9571
4	2.6450	-2.5241	-0.3733	8.3613
5	-1.5237	0.6615	-0.3199	-4.8013

Table 13. Test Number, Key Test Parameters, Measurements Made of Test Results, and Prediction Data

									Predicted Cycles			
Coupon	Material Condition	R	S_{max} (MPa)	a_n	a_i	a_f	Angle	Observed Cycles	100% RS	90% RS	110% RS	N_{obs}/N_{pred}
N1	AM	0.1	37.9	0.254	0.508	7.569	16	52,104	60,209	NA	NA	0.87
N2	AM	0.14	23.4	0.254	0.508	7.620	9	602,200	796,730	NA	NA	0.76
N3	AM	0.1	32.8	0.254	0.508	7.584	19	152,300	93,208	NA	NA	1.63
N4	AM	0.1	31.0	0.254	0.508	7.267	21	123,250	118,630	NA	NA	0.94
N5	AM	0.5	60.3	0.254	0.508	7.458	13	33,066	46,117	NA	NA	0.72
N6	AM	0.5	48.3	0.254	0.508	7.058	14	71,142	78,366	NA	NA	0.91
N8	AM	0.5	37.9	0.254	0.508	6.406	19	363,730	299,480	NA	NA	1.31
N9	AM	0.5	37.9	0.254	0.508	6.633	18	322,640	314,240	NA	NA	1.03
A12	CX	0.1	60.3	0.762	1.016	7.308	20	143,290	92,675	52,529	165,870	1.55
A13	CX	0.1	60.3	0.762	1.016	7.469	12	112,220	93,620	53,480	166,360	1.20
A14	CX	0.1	60.3	0.762	1.016	6.744	15	72,144	90,917	50,780	164,100	0.79
A15	CX	0.1	60.3	0.762	1.016	7.330	13	146,290	92,742	52,596	165,930	1.58
A19	CX	0.5	62.1	0.762	1.016	7.521	14	277,550	129,640	81,566	223,740	2.14
A21	CX	0.5	62.1	0.762	1.016	7.337	13	144,290	128,390	80323	222,500	1.12
A22	CX	0.5	62.1	0.762	1.016	7.438	12	109,220	129,080	81,006	223,180	0.85
A23	CX	0.5	62.1	0.762	1.016	7.204	11	396,790	127,490	79,421	221,590	3.11
A24	CX	0.5	62.1	0.762	1.016	7.025	14	369,740	126,270	78,202	220,370	2.93

5.6 FIGURES.

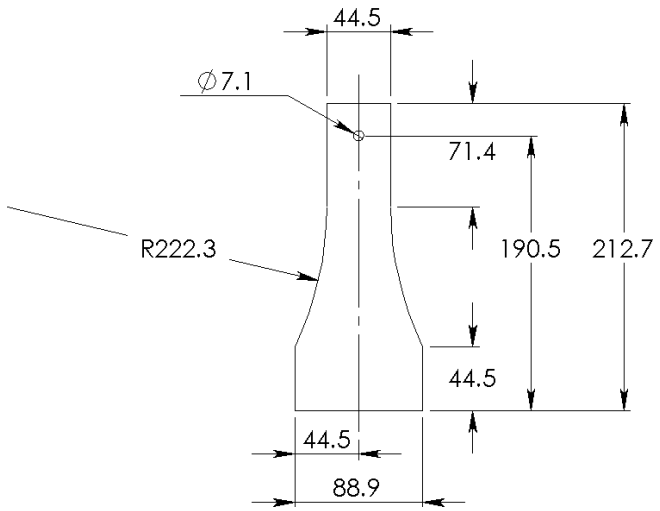

Figure 63. Loaded Hole Coupon Geometry (dimensions in mm)

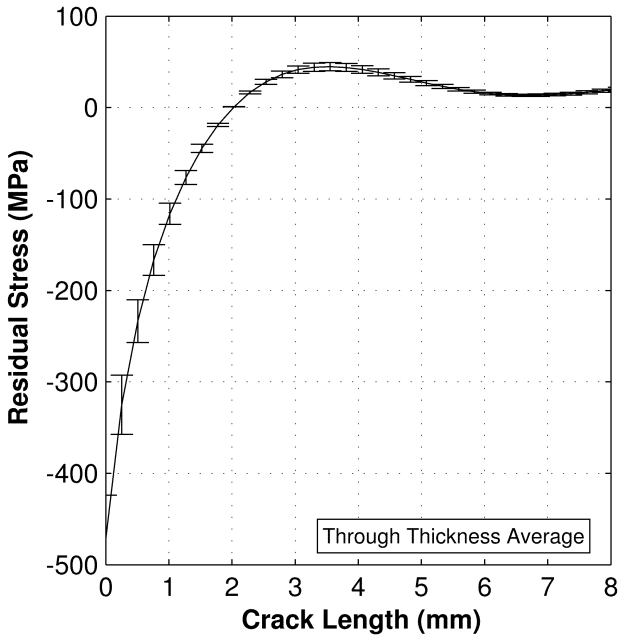

Figure 64. Residual Stress Versus Radial Distance From the Loaded Hole Perimeter (coincident with crack length), Error Bars Marking Residual Stress Variability

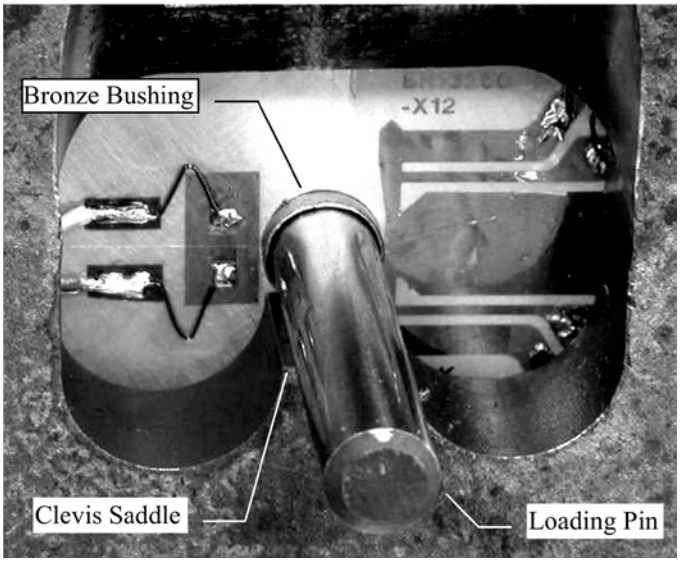

Figure 65. Loaded Hole Instrumentation as Seen Through Inspection Window of Clevis, With the DCPD KG (right) and Strain Gage (left), Highlighting the 6.35 mm Diameter Loading Pin and Bronze Bushing

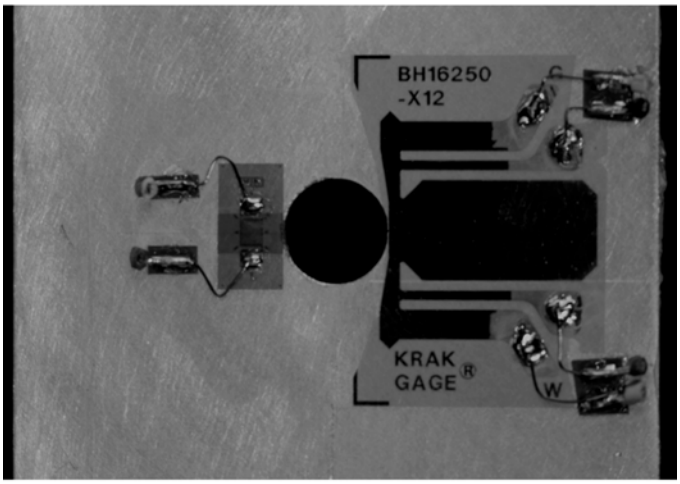

Figure 66. Loaded Hole Instrumentation: KG (right) and Strain Gage (left)

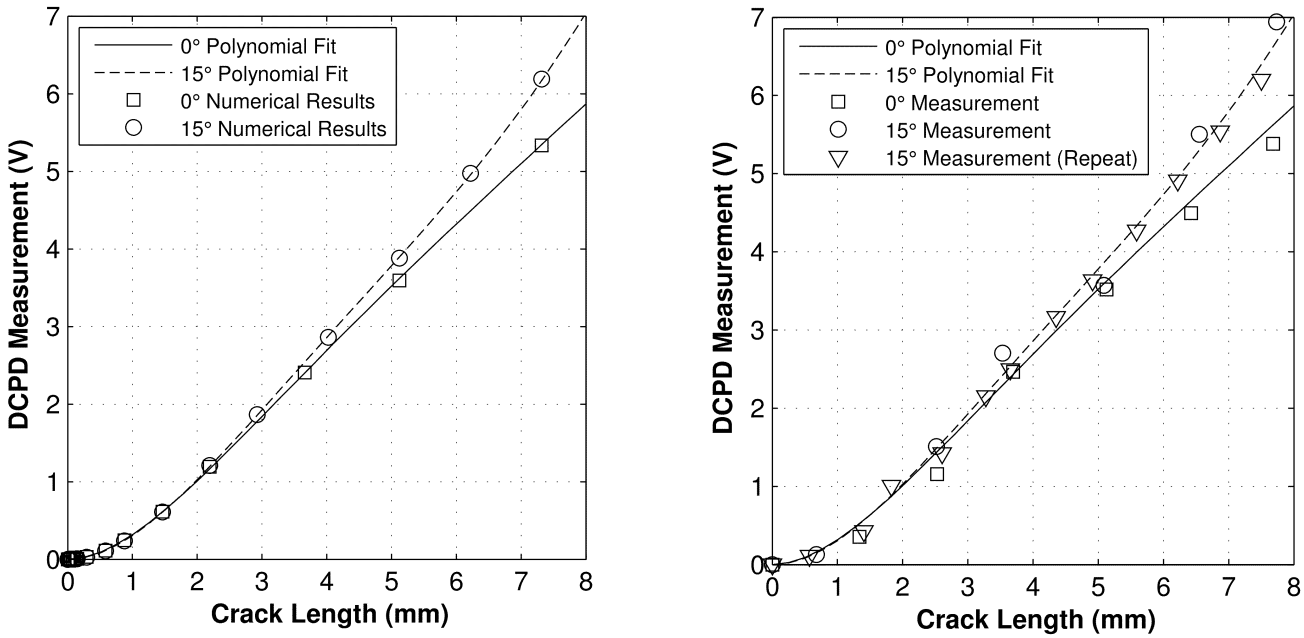

(a) (b)

Figure 67. Resulting Polynomial Relationship Describing DCPD Voltage to Crack Length for Crack Angles of 0° and 15° Plotted Against (a) Data From the Numerical Results and (b) Data From Controlled DCPD Measurements

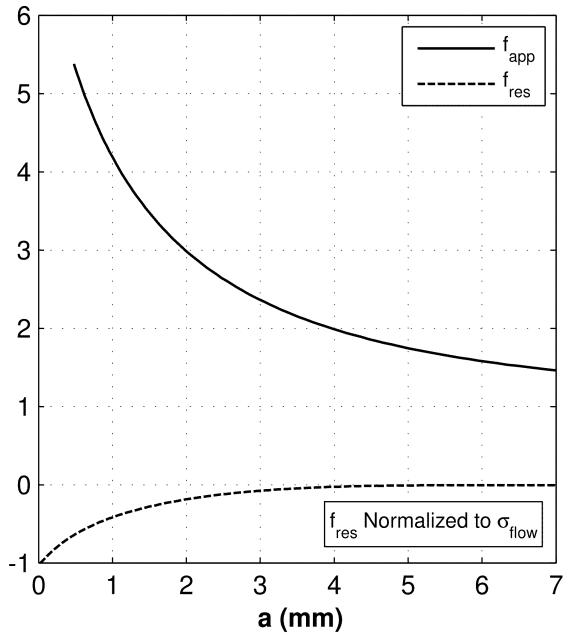

Figure 68. Geometry Factors vs. Crack Length for Applied and Residual Stresses, Normalized by Applied Gross Section Stress and Flow Stress (476 MPa), Respectively

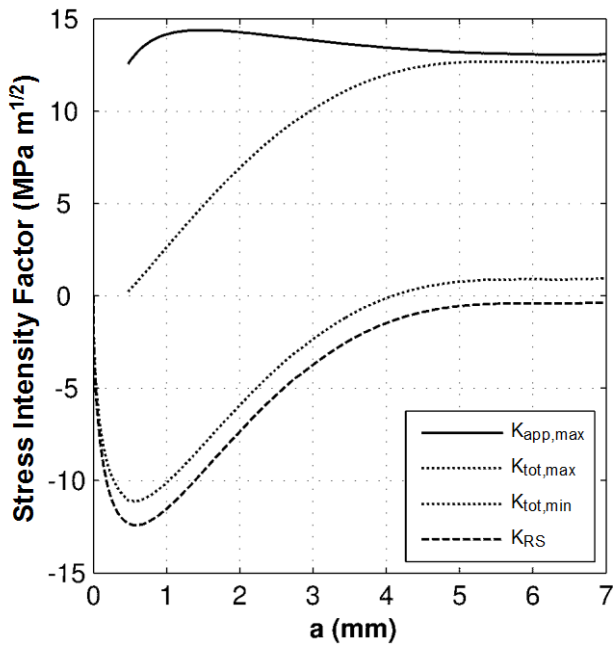

Figure 69. The SIF vs. Crack Length for Applied and Residual Stresses for $S_{app,\max}$ = 60.33 MPa and R = 0.1

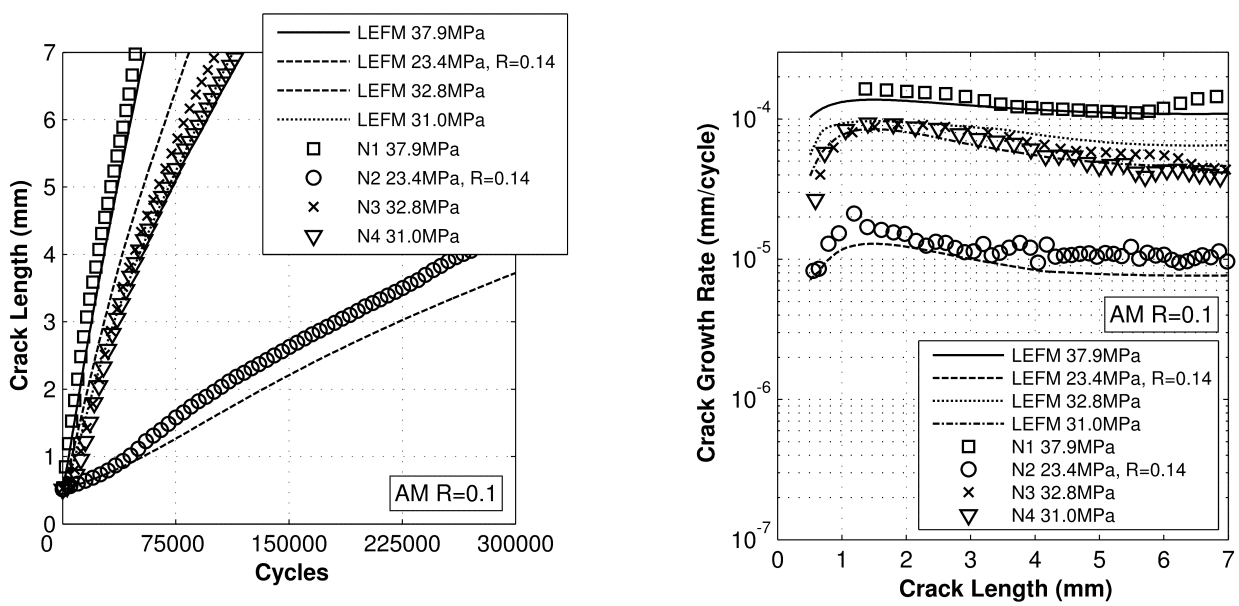

(a) (b)

Figure 70. The AM R = 0.1 Crack Growth Data Plotted With LEFM Crack Growth Predictions of (a) Crack Length as a Function of Cycles and (b) FCGR as a Function of Crack Length

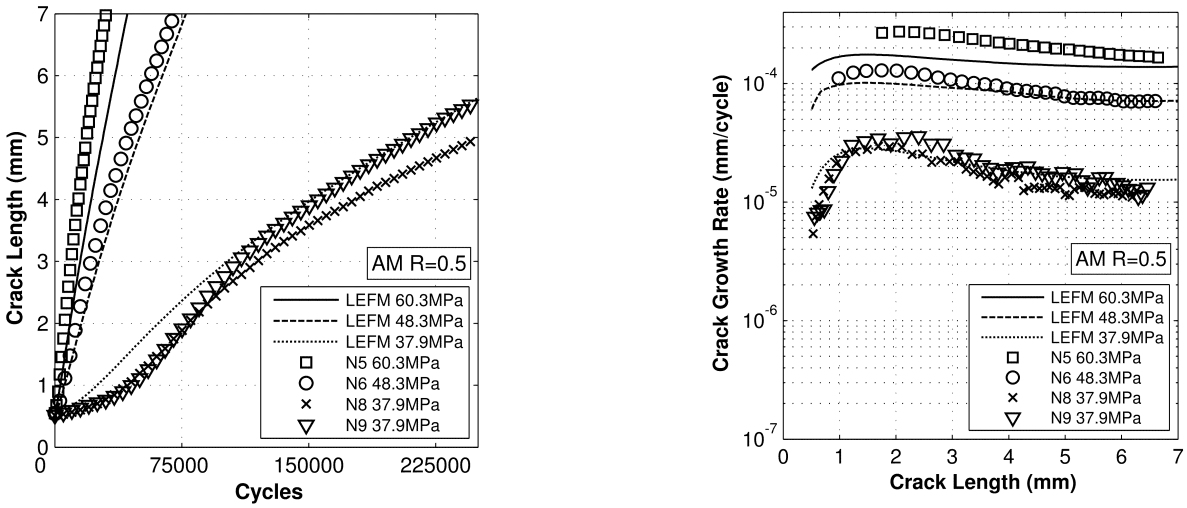

(a) (b)

Figure 71. The AM R = 0.5 Crack Growth Data Plotted With LEFM Crack Growth Predictions of (a) Crack Length as a Function of Cycles and (b) FCGR as a Function of Crack Length

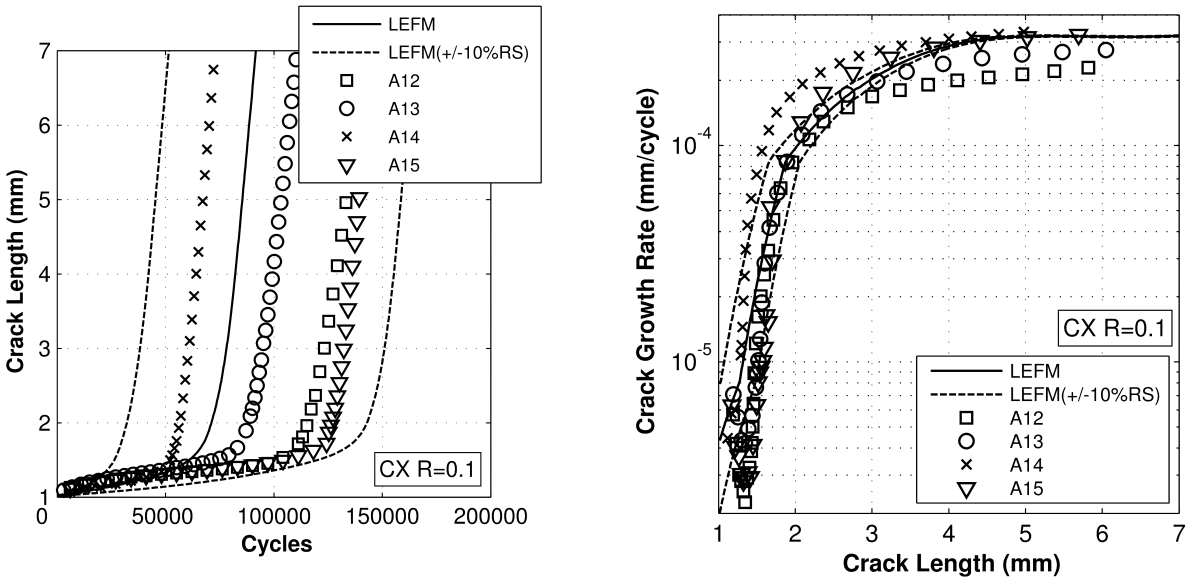

(a) (b)

Figure 72. The CX R = 0.1 Crack Growth Data Plotted With LEFM Crack Growth Predictions of (a) Crack Length as a Function of Cycles and (b) FCGR as a Function of Crack Length at an S_{max} = 60.33 MPa

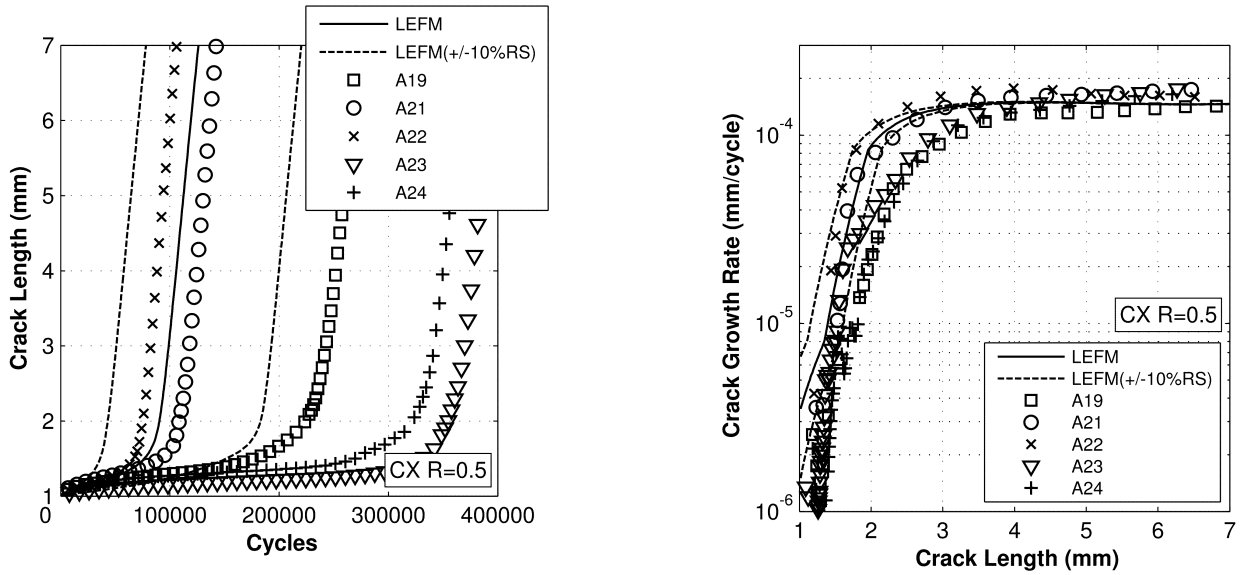

(a) (b)

Figure 73. The CX R = 0.5 Crack Growth Data Plotted With LEFM Crack Growth Predictions of (a) Crack Length as a Function of Cycles and (b) FCGR as a Function of Crack Length at an S_{max} = 62.0 MPa

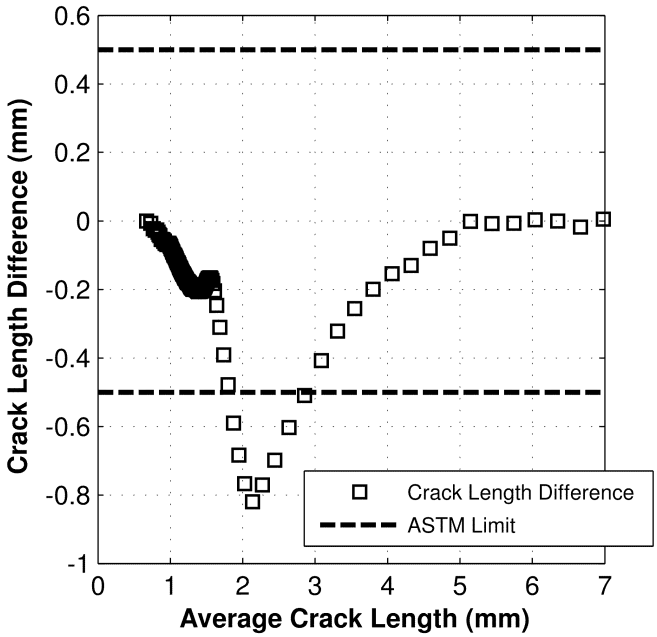

Figure 74. Difference in Front and Back Crack Lengths Measured During the Test of Coupon A8

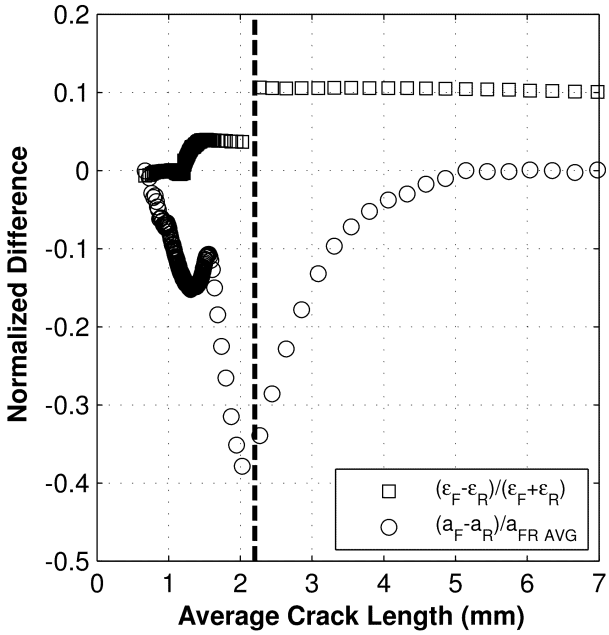

Figure 75. Normalized Front (F) and Rear (R) Strain and Crack Size Differences Plotted as a Function of Average Crack Length; (a) the Vertical Line Identifies Shim Adjustment and the Response of Strain and Crack Growth

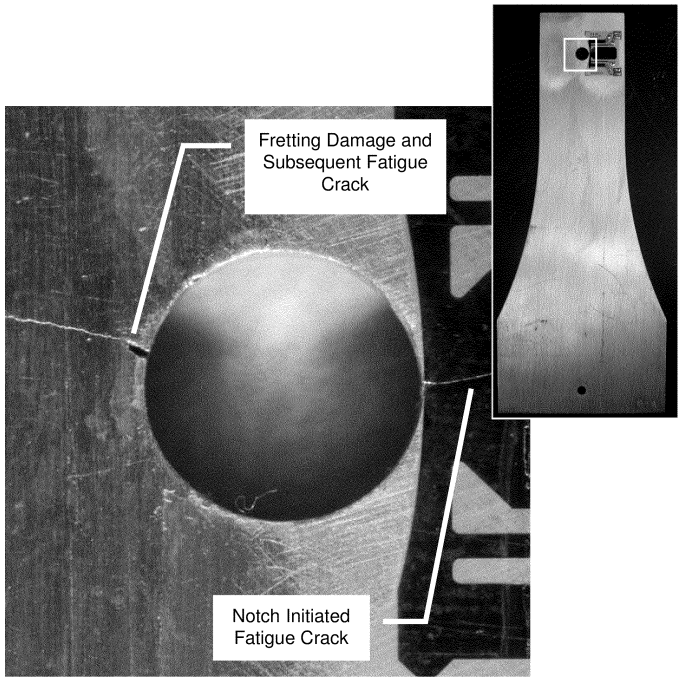

Figure 76. Fretting Failure at the Perimeter of the Loaded Hole Experienced During Initial Testing Without a Bushing

6. THE 1D CRACK GROWTH AT COLD-EXPANDED LOADED HOLES UNDER VARIABLE AMPLITUDE LOADING.

6.1 INTRODUCTION.

Previous sections show that LEFM with superposition can be used to predict the growth of 1D cracks in open hole and loaded hole coupons treated with CX under constant amplitude loading (sections 3 and 5). Although constant amplitude load test data provide valuable information for the development of CX lifing techniques, variable amplitude loading is typical of aircraft operations, has significant effects on crack growth, and negatively affects the accuracy of engineering methods for crack growth prediction [94–98]. Despite the common use of CX, there is a lack of published work on crack growth at CX holes tested under variable amplitude loading. Therefore, this section investigates 1D crack growth in loaded hole coupons, with and without CX, under variable amplitude loading.

The first objective is to construct a variable amplitude block-loading program representative of rotorcraft operation. This is done by rainflow counting and binning in-flight rotorcraft strain gage data along with developing a representative block-loading program. The second objective is to extend the LEFM techniques used to predict crack growth under constant amplitude loading (described in sections 3.2.5 and 5.2.13) to predict crack growth under a variable amplitude block-loading program. The third objective is to validate the predictions against test data.

6.2 METHODS.

6.2.1 Block Loading Program.

The block loading program was developed from in-flight strain gage data collected during normal rotorcraft operations. The subject rotorcraft was an Erickson Air-crane S-64E, originally manufactured by Sikorsky for military use but modified by Erickson Air-crane for industrial use in a variety of missions (including firefighting, construction, and logging)[*]. The in-flight data were collected during logging operations and reflect a significant number (greater than 10) of dispatch, lift, return, and release cycles. Strain was measured adjacent to a fatigue-critical nested angle joint connecting the pylon to the tail boom, a feature known to have exhibited stable fatigue cracking in past operations. Stress as a function of time was calculated from the strain data using uniaxial stress-strain relations. Cycles were normalized to the maximum in-flight stress and are plotted as a function of time in figure 77(a). The normalized cycles were rainflow counted using methods suggested by ASTM [99] and binned into 26 by 28 equally spaced bins over the range of stress mean and amplitude (σ_m and σ_a), respectively. The cycles contained within each bin were assumed to have a σ_m and σ_a equal to the maximum values defining the bin. Consistent with other variable amplitude testing [100, 101], these cycles were arranged in order of ascending σ_m, then σ_a, and are plotted against cycle number in figure 77(b). Damage per bin was calculated using an equivalent damage approach based on the Walker equation and Paris relationship, as described by Dowling [102].

[*] The authors are grateful for the interest, assistance, and support of Dale Roberts and Arild Barrett of Erickson Aircrane.

Following the initial binning and damage calculation, the bins were refined. Cycles in the lower 7.7% of the σ_a range were judged to be insignificant and were eliminated. The remaining cycles were re-binned into 16 bins, defined by the boundaries listed in table 14. The number of cycles per bin was adjusted until the damage caused by each of the 16 bins equaled the damage caused over the same σ_m and σ_a range in the original 26 by 28 binning scheme. Of the 16 refined bins, 5 did not contain any cycles.

Maximum and minimum stress limits were recognized when assembling the final block-loading program. Buckling and fixture design restricted testing to tensile loading only; therefore, $S_{\min}$ was limited to 0.002. Binning resolution resulted in cycles with $S_{\max}$ slightly larger than the maximum in-flight stress level; therefore, $S_{\max}$ was limited to 1.0. In both cases, the corresponding peak or valley stress and number of cycles per bin were unaltered. The block loading program for fatigue testing is given in table 15 and plotted in figure 78.

6.2.2 Coupon Preparation.

The loaded hole coupons used for variable-amplitude loading tests are identical to the coupons used for constant amplitude loading tests. Details of the coupon material, geometry, hole preparation, and instrumentation were detailed in sections 5.2.1, 5.2.3, and 5.2.9.

6.2.3 Test Equipment and Calibration.

Variable amplitude loading tests were performed on the same equipment used for constant amplitude loaded hole tests (section 5.2). No changes were made to the machine; therefore it remained in static alignment (section 5.2.8).

Dynamic calibration was performed to ensure the proper stress levels were being applied at the test frequency of 10 Hz. To do this, peak and valley strain was measured using the instrumented loaded hole coupon (described in section 5.2.8). Peak and valley stress was computed from strain using uniaxial stress-strain relations. The applied loads were adjusted until the measured stresses were within 0.5% of the desired stresses. Dynamic calibration was performed under a constant amplitude loading at $R = 0.002$, 0.11, 0.579 and 0.76, the exact stress ratios for 7 of the 11 bins, and for an array of $S_{\max}$ between 34.5 and 86.2 MPa. The remaining bins, which had the $R = 0.14$, 0.33, 0.43, and 0.62, were judged to be close enough to the $R = 0.11$, 0.579, 0.579, and 0.76 bins, respectively, to use the same dynamic calibration relationships. A linear curve was fit to the calibration data to provide a continuous relationship between desired $S_{\max}$ and commanded load for each block.

The most critical feature of the block loading program was the transition between blocks. This was because the block transitions apply the critical overloads and underloads, which were difficult to control with the servohydraulic control loop at high frequency. Therefore, to ensure proper load application during block transitions, testing during transitions was slowed to 0.5 Hz. Additionally, an automatic feature of the test control software [103] continuously monitored the peak and valley loads. Any difference between the applied and commanded loads was compensated for by an amount proportional to the difference. This compensation is stored by the software and applied during the next similar cycle. This feature ensured that actual peak- and valley-applied stresses were within 3.5 MPa of the corresponding desired stress levels.

6.2.4 Data Collection.

Crack growth data were collected during variable amplitude tests as they were for constant amplitude tests (described in section 5.2.9 and 5.2.10) at the end of every block loading program. Post-test crack measurements showed that cracks grew at an average angle of 12º from horizontal, with crack angle ranging from 7º–15º on different coupons. The average crack angle during variable amplitude loading tests was considered to be close enough to the average crack angle during constant amplitude loading tests to use the same polynomial relationship between DCPD measurements and crack length (described in section 5.2.12). Errors associated with small coupon-to-coupon variations in crack angle are roughly accounted for through the data reduction procedure, which offsets and scales the DCPD signal so that it provides the correct crack sizes at the beginning and end of the test (which were measured fractographically) [53].

Fatigue pre-cracking was accounted for during data analysis using the same methods used during loaded hole constant amplitude testing (refer to section 5.2.6), which differs from the methods suggested by the ASTM standard [4]. This resulted in the initial crack lengths (a_i) of 0.630 and 1.270 mm (from the hole edge) for the AM and CX tests, respectively, which satisfied the first two elements of the standard.

6.2.5 The FCGR Calculation.

The FCGR was calculated from measurements of crack length using the modified incremental method of Larsen, Jira, and Ravichandran [54], as adapted to open hole coupons (see section 3.2.4.5). The FCGR was calculated from LEFM prediction outputs as the difference in crack growth over one block-loading program, using the secant method, and assuming that the FCGR occurred at the block mean crack length.

6.2.6 Test Matrix.

Variable amplitude tests were performed on loaded hole coupons with and without CX. The effects of compressive residual hoop stresses were evaluated by comparing AM and CX crack growth. Cracks were grown from the initial notch to a crack length of 7.62 mm. A total of six loaded hole coupons—three AM and three CX—were tested. By duplicating constant amplitude test conditions (except for loading), the effects of variable amplitude loading were isolated.

6.2.7 The LEFM Predictions of Crack Growth Under Variable Amplitude Loading.

An LEFM approach was used to predict crack growth under variable amplitude loading. This approach involved many of the same techniques used by the constant amplitude predictions (described in section 5.2.13), with additions to account for the effects of variable amplitude loading, often called load interaction effects.

The three main parts to the LEFM approach are: a solution for SIF as a function of crack length, a material model, and numerical integration. The solutions used for applied and residual SIF (K_{app} and K_{RS}, respectively) were developed earlier (see section 5.2.13), where superposition was used to combine K_{app} and K_{RS}, forming K_{tot}. For the variable amplitude model, an additional

term was included in this sum, effectively reducing the SIF to account for crack closure from prior large "overload" cycles. This term is referred to as K_{red}.

K_{red} is calculated using the Generalized Willenborg Model (GWM) proposed by Gallagher [104]. The GWM assumes that stress intensity is reduced by an amount related to the size of the plastic region ahead of the crack tip. The radius of this region (Z_{ap}, figure 79) is calculated using a relationship developed by Newman [21]:

$$Z_{ap} = \frac{\pi}{8}\left(\frac{K_{tot,\max}^{ol}}{\alpha_g \sigma_{ys}}\right)^2 \tag{15}$$

Here, σ_{ys} is the material yield strength and $K_{tot,\max}$ is the superposition of the maximum applied and residual SIFs. The use of $K_{tot,\max}$ was an assumption made for this study, to include residual stress effects, and is a significant difference from the standard GWM [21], which uses K_{app} and does not consider residual stress. The variable α_g is a constraint factor that compensates Z_{ap} for plane stress or strain via:

$$\alpha_g = 1.15 + 1.4e^{-0.95\left(\frac{K_{tot,\max}}{\sigma_{ys}\sqrt{t}}\right)^{1.5}} \tag{16}$$

where t is the material thickness.

The GWM simply states that if Z_{ap} is completely contained within a plastic region formed by a previous overload cycle (Z_{ol}, figure 79), stress intensity is reduced by K_{red}:

$$K_{red} = \Phi\left(K_{tot,\max}^{ol}\left(1 - \frac{\Delta a}{Z_{ol}}\right)^{0.5} - K_{tot,\max}\right) \tag{17}$$

Here, Δa is the difference in crack length between the current cycle and the overload cycle (a_{ap} and a_{ol}, figure 79) and $K_{tot,\max}^{ol}$ and $K_{tot,\max}$ are the maximum total SIF during the overload cycle and current cycle, respectively. The term Φ is a modification to the GWM proposed by Brussat [21]. By adding Φ, the GWM becomes the Modified Generalized Willenborg Model (MGWM). The term Φ is added to reduce K_{red} in the event of an underload following the overload [21], which has been shown to reduce load interaction effects. The Φ is computed as:

$$\Phi = \mathrm{Min}\{1.0,\ 2.523\Phi_o/(1.0 + 3.5(0.25 - R_u)^{0.6})\} \qquad \text{for } R_u \le 0.25 \tag{18}$$

$$\Phi = 1.0 \qquad \text{for } R_u > 0.25 \tag{19}$$

where Φ_o is a tuning parameter, discussed further below, and R_u is the underload ratio:

$$R_u = \frac{\sigma_{ul}}{\sigma_{\max}^{ol}} \tag{20}$$

where σ_{ul} is the minimum applied stress during the underload cycle and $\sigma_{\max}^{ol}$ is the maximum stress applied during the overload cycle. The use of a stress-based underload ratio is consistent with the MGWM, but is perhaps unexpected for CX crack growth modeling, which typically substitutes SIF for stress into the formulae used to predict crack growth. The influence of the underload formulation is discussed later.

The resulting value of K_{red} is then combined with the total SIFs to account for load interaction via:

$$K_{MGWM,\max} = K_{tot,\max} - K_{red} \qquad \text{for } R_u \leq 0.25 \tag{21}$$

$$K_{MGWM,\min} = Max\left\{\left(K_{tot,\min} - K_{red}\right), 0\right\} \qquad \text{for } K_{tot,\min} > 0 \tag{22}$$

$$K_{MGWM,\min} = K_{tot,\min} \qquad \text{for } K_{tot,\min} \leq 0 \tag{23}$$

This method results in values of stress ratio (R_{MGWM}) and an SIF range (ΔK_{MGWM}) that effectively account for load interaction and applied and residual stresses:

$$R_{MGWM} = K_{MGWM,\min}/K_{MGWM,\max} \tag{24}$$

$$\Delta K_{MGWM} = K_{MGWM,\max} - K_{MGWM,\min} \tag{25}$$

Given the values of R_{MGWM} and $\Delta K_{MGWM,}$ a crack growth increment is computed using the FCGR model presented in section 3.2.5 and numerical integration. After updating the crack size, the MGWM analysis is repeated until the termination crack length is reached.

The number of cycles over which to integrate crack growth was determined through iteration. The number of cycles was halved until predicted fatigue life differed by no more than 0.5%. This occurred between 25 and 12 cycles. Therefore, for computational efficiency, crack growth was incremented by 25 cycles or the number of cycles in the block, whichever was smaller.

6.2.8 Tuning the MGWM Model to Test Data.

The MGWM model was tuned to AM test data [21]. This is typically done to adjust the model for a specific sequence of variable amplitude loading. Tuning was performed by adjusting Φ_o, until the difference between the predicted and measured fatigue life (at two AM stress levels) was minimized. This occurred at $\Phi_o = 0.6$, which is within the range suggested by NASGRO [21] and near the value of $\Phi_o = 0.5$, which was used by Sander and Richard [95] for MGWM spectrum predictions of crack growth in 7075-T6 aluminum.

6.3 RESULTS.

All coupons were tested using the block-loading program given in table 15 and plotted in figure 78. The scale of the block program applied during each test ($S_{\max}$) is listed in table 16 and reflects the gross-section stress. The number of block programs applied during each test to grow

the crack to a length of 7.62 mm is referred to as the fatigue life and is compared with LEFM predictions and other parameters in table 16. To quantify the correlation between observed and predicted life, the fatigue life ratio is calculated as the number of block programs observed (B_{exp}) divided by the number predicted (B_{pred}). Values greater than one indicate a conservative prediction. The average loaded hole AM fatigue life ratio was 0.99 and ranged between 0.92–1.11. The AM crack growth and FCGR is plotted as a function of block programs in figure 80. Both plots include complementary LEFM predictions, which correlate well with the AM crack growth data. An LEFM prediction without load-interaction effects (i.e., not using MGWM) is also reported in figure 80 for one stress level, and for all stress levels in table 16, and shows that load interaction effects are significant.

The CX fatigue lives are provided in table 16 along with other parameters. Also provided in table 16 are the corresponding values of fatigue life ratio, which averaged to 1.52 and ranged between 1.43–1.66. The crack length and FCGR measured during CX testing is plotted as a function of block programs in figure 81. Included in the plots and tabulated results are corresponding LEFM predictions, including predictions that do not consider load interaction.

The MGWM conservatively predicted CX fatigue life, which is indicated by a fatigue life ratio greater than 1.0 for all tests (see table 16). Measured FCGR agrees with MGWM predictions to a crack length of approximately 2.0 mm (see figure 81), at which point test data slowed well below predictions, but continued to accelerate with crack length. The results show crack growth history for two of the three tests falling between crack growth predictions with ±10% residual stress (see figure 81), the expected variation in 3% CX residual stress, as described in section 5.2.4. The third test had a longer fatigue life than predicted by the +10% residual stress prediction. Not taking into account load interaction effects provides grossly conservative predictions.

6.4 DISCUSSION.

6.4.1 Correlation Between Observed and Predicted Loaded Hole Crack Growth.

There is good correlation between the observed and predicted crack growth in AM coupons under variable amplitude loading. This is highlighted by an average fatigue life ratio of 0.99 and the close proximity of the crack growth predictions to test data (see figures 80 and 81). Therefore, it can be concluded that the MGWM accurately predicts AM spectrum crack growth, which is expected because the model was tuned to the test data. These findings are consistent with other work that compares MGWM predictions to test data [21, 94–96, 105] in coupons without residual stress.

For CX coupons, the correlation between observed and predicted crack growth under variable amplitude loading is of lower quality than found for AM coupons. All three fatigue lives were conservatively predicted by LEFM (see table 16), two of which remained bound by the limits of RS variability (see figure 81), but the mean fatigue life is under-predicted by a factor of 1.5. The lack of correlation of FCGR is greatest for large crack length (>2 mm in figure 81[b]), which suggests a systematic issue. Considering superposition, FCGR in AM and CX coupons should be identical for cracks longer than 4 mm where K_{RS} is negligible (see figure 81). Comparing AM and CX tests at 82.7 MPa (see figures 80 and 81), the FCGR at 4 mm crack length is a factor of

approximately 2 lower for CX coupons than for AM coupons. The source of this discrepancy is unknown.

6.4.2 Effects of Load Interaction.

The effects of load interaction significantly affected predictions of fatigue life and crack growth (see table 16; figures 80 and 81), for which ignoring interaction led to a much shorter predicted life for AM and CX tests. These results are consistent with previous variable amplitude testing [94–98] and show that compensating for load interaction is essential for accurate predictions of variable amplitude crack growth.

Variable amplitude testing experienced remarkably consistent crack growth. The CX fatigue lives varied less than 17%, compared to the more than 300% measured during constant amplitude CX testing (see section 5.3). Even less scatter was observed during AM testing at 68.9 MPa (see figure 80), for which crack growth was nearly identical in two coupons. Consistent test behavior under variable amplitude loading suggests that future validation of modeling techniques would be better accomplished with spectrum tests than with constant amplitude tests.

6.4.3 Underload Calculation.

Consistent with the MGWM, the underload ratio was calculated based on the applied stress ($R_u(\sigma)$, equation [9]) [21]. This may appear atypical of LEFM modeling of residual stress-bearing material, which often employs the total SIF to account for residual stresses. Predictions that use a SIF-based underload ($R_u(K)$) are plotted with test data and predictions using the stress-based underload in figure 82(a). This figure shows that using an SIF-based underload ratio results in significantly shorter predictions of fatigue life than predicted using the stress-based underload ratio.

The shorter fatigue life predicted when using $R_u(K)$ is the result of an overprediction of crack growth rate at short crack lengths (see figure 82[b]). This occurs because of a negative underload ratio in the presence of high-magnitude compressive residual stress. At short crack lengths, K_{ul} is negative and has a negative underload ratio. This results in predicting a significant underload effect, thereby increasing FCGR [21]. This is contrasted with the stress-based underload ratio, which remains positive (no compressive stresses are applied), resulting in a slower FCGR.

6.4.4 Loaded Hole Fatigue Performance With and Without CX.

Cold mandrel expansion was shown to increase the fatigue performance of loaded hole coupons under variable amplitude loading. This is expected and agrees with the findings of earlier CX testing. A side-by-side comparison of CX effects is offered by the AM and CX tests performed at 82.7 MPa (see table 16; figures 80 and 81), for which the CX tests had 5.5 times longer fatigue life.

6.5 TABLES.

Table 14. The Bin Boundaries Defining the Refined Binning Scheme Along Stress Amplitude (σ_a) and Mean Stress (σ_m), Respectively

σa	0.04	0.16	0.3	0.4	0.6
σm	-0.12	0.2	0.4	0.6	0.92

Table 15. Variable-Amplitude Block-Loading Program Listed per Bin Number, Maximum and Minimum Stress (σ_m and σ_a, respectively), Stress Ratio (R), and the Number of Cycles per Bin

Bin	σmax	σmin	R	Cycles per Bin
1	0.360	0.040	0.11	430
2	0.560	0.240	0.43	1762
3	0.760	0.440	0.58	1069
4	1.000	0.760	0.76	30
5	0.500	0.002	0.00	4
6	0.700	0.100	0.14	100
7	0.900	0.300	0.33	29
8	1.000	0.620	0.62	1
9	0.800	0.002	0.00	29
10	1.000	0.002	0.00	2
11	1.000	0.002	0.00	1

Table 16. Data From Fatigue Crack Growth Tests for Loaded Hole Coupons Under Variable Amplitude Loading

							Block Program Predictions				
							With Load Interaction Effects			Without Load Interaction Effects	
Coupon Number	Material Condition	$S_{app,\max}$ (MPa)	a_n (mm)	a_i (mm)	a_f (mm)	Measured Block Programs	100% RS	90% RS	110% RS	AM or 100% RS	B_{exp}/B_{pred}
N11	AM	82.7	0.254	0.630	7.620	41	37	NA	NA	18	1.11
N12	AM	68.9	0.254	0.630	7.620	73	78	NA	NA	39	0.94
N10	AM	68.9	0.254	0.630	7.620	72	78	NA	NA	39	0.92
A11	CX	86.2	0.762	1.270	7.620	213	149	103	229	41	1.43
A17	CX	82.7	0.762	1.270	7.620	217	149	103	229	41	1.46
A18	CX	82.7	0.762	1.270	7.620	248	149	103	229	41	1.66

6.6 FIGURES.

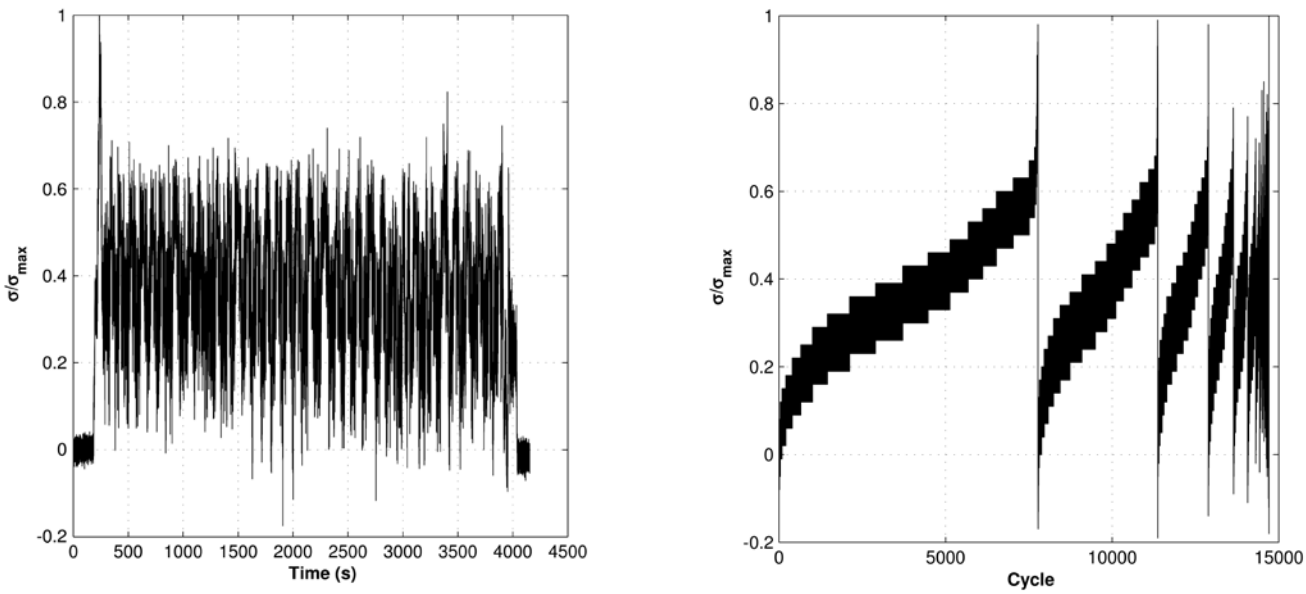

(a) (b)

Figure 77. In-Flight Stress Calculated From Collected Strain Data: (a) Plotted as a Function of Time and (b) Binned Into a 26 x 28 Binning Scheme and Sorted by Increasing Mean Stress and Stress Amplitude (σ_m and σ_a respectively)

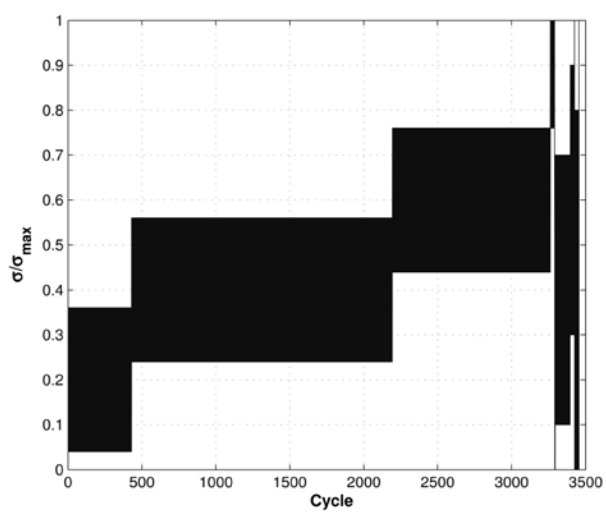

Figure 78. Plot of the Final Block Loading Program as a Function of Cycles Used to Test Loaded Hole Coupons

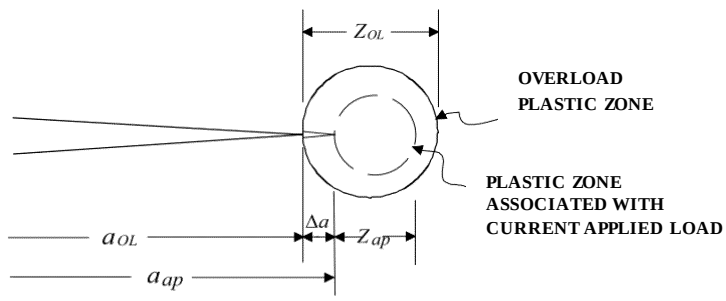

Figure 79. Dimensions Used by the MGWM to Define Features at the Crack Tip [34]

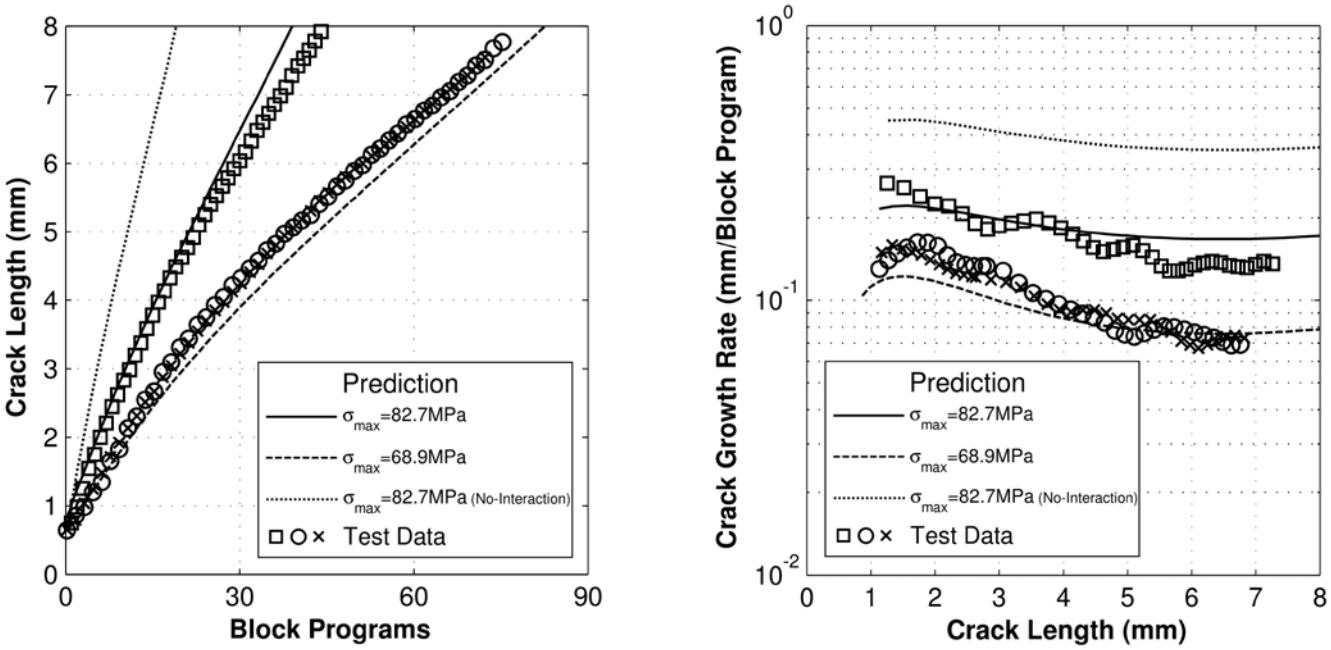

(a) (b)

Figure 80. Crack Growth Through Loaded Hole AM Coupons With LEFM Predictions Plotted as (a) Crack Length as a Function of Block Programs and (b) Crack Growth Rate as a Function of Crack Length

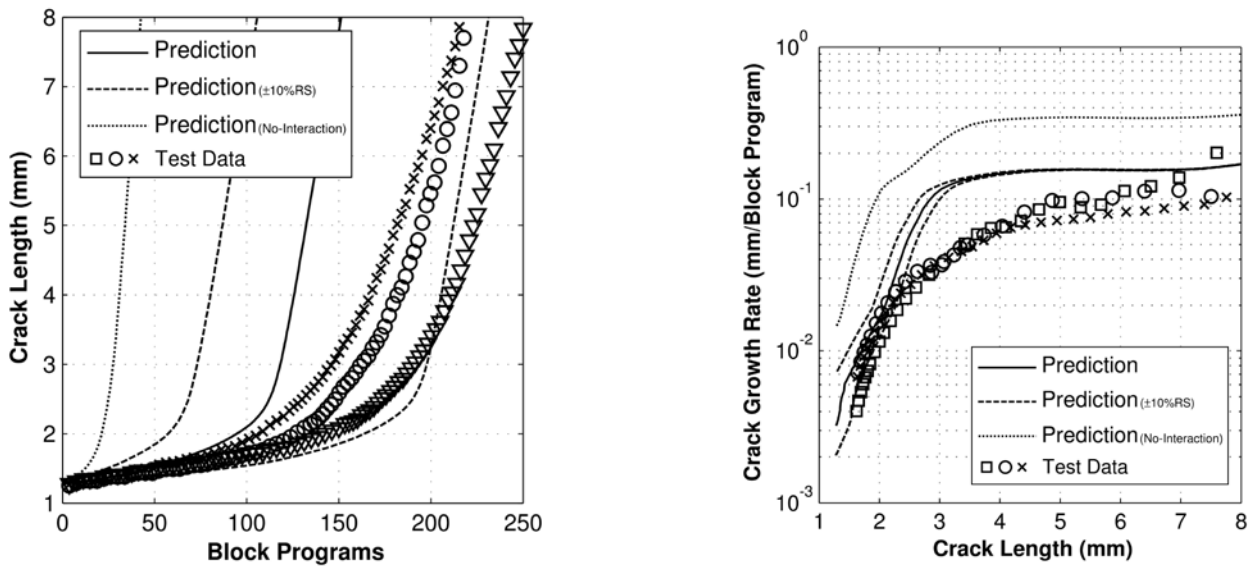

(a) (b)

Figure 81. Crack Growth Through Loaded Hole CX Coupons With LEFM Predictions Plotted as (a) Crack Length as a Function of Block Programs and (b) Crack Growth Rate as a Function of Crack Length at 82.7 MPa

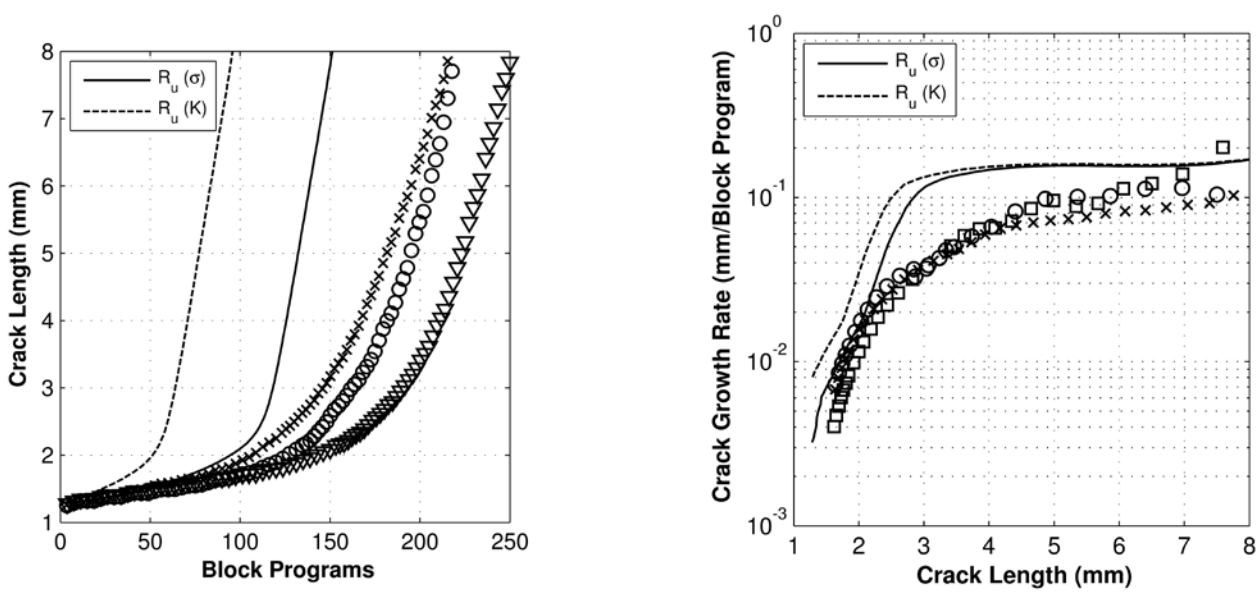

(a) (b)

Figure 82. Predictions of CX Crack Growth Using a Stress-Based Underload Ratio ($R_u(\sigma)$) or a K-Based Underload Ratio ($R_u(K)$) Plotted as (a) Crack Length as a Function of Block Programs and (b) Crack Growth Rate as a Function of Crack Length

7. CRACK GROWTH IN NESTED ANGLES UNDER ALTERNATING CONSTANT AMPLITUDE BLOCK LOADING AND VARIABLE AMPLITUDE LOADING.

7.1 INTRODUCTION.

Nested-angle splice joints are common features of rotorcraft fuselages. Nested angles join two structural members through a series of mechanical fasteners, thereby providing a reliable and serviceable connection. An example of this type of joint is illustrated in figure 83, in which eight mechanical fasteners join the two pieces at the extruded angle. The load case at each of these fastener holes is a unique combination of bypass stress and bearing stress. Work reported in earlier sections of this report shows that cold expansion of holes improves fatigue life under a pure bypass stress (open holes) and pure bearing stress (loaded holes). These findings suggest potential fatigue life improvement of nested angles by treating the fastener holes with CX.

Despite the potential benefits of CX to nested angle fatigue, only a limited volume of work has been performed beyond the basic open hole and loaded hole cases. Most relevant was an investigation of the fatigue behavior of AM nested angles performed by the industrial partner on this project [106]. The current study builds on that earlier work by developing fatigue crack growth data for coupons in AM and CX conditions.

Earlier sections have demonstrated a correlation between LEFM predictions and data from crack growth tests of AM and CX open holes (section 3) and loaded holes (sections 5 and 6). The results showed isolated crack growth due to a pure bypass stress (open holes) and pure bearing stress (loaded holes). These are essential elements for understanding crack growth in nested angles near the fastener holes, which falls between the bypass and bearing stress cases. Nested angles are also complicated by such factors as friction, fastener preload (from tightening the fasteners), tilting of the fastener due to shear loading, and local bending of the joined pieces. The objective of this work is to collect crack growth data on AM and CX nested-angle coupons exposed to alternating constant amplitude block loading and variable amplitude block loading representative of in-flight stresses. Data from AM and CX coupons were compared to evaluate the effects of CX. Data collected under variable amplitude loading was used to investigate the effects of load interaction. The data collected support the development of methods for damage-tolerant assessment of nested-angle features, but crack growth predictions are left for follow-on work.

7.2 METHODS.

7.2.1 Material.

Nested-angle coupons were made from extruded, clad 7075-T651 aluminum alloy with the material properties (in the extruded direction) listed in table 17 [89]. Nested-angle coupons are made from two separate pieces, each having different cross-sectional dimensions (see figure 83). All pieces of each size were cut from a single extrusion.

7.2.2 Geometry.

Geometry of the nested-angle coupon is shown in figure 83 and is similar to coupons from the earlier fatigue tests performed by the industrial partner [106]. Assembled coupons were 394 mm long (left side of figure 83) and made from two L-angle pieces, each 254 mm in length (right side of figure 83). The larger of the two pieces has an angle leg length of 41.3 mm and the smaller piece has a leg length of 31.8 mm. Drilled into one end of each piece are two rows of four 4.8 mm fastener holes. Cut into the opposite end are two 19.1 mm diameter holes used to accommodate loading grip hardware.

7.2.3 Fastener Hole Manufacturing.

A portion of the nested angles had fastener holes treated with CX to introduce local compressive residual hoop stresses. The rest of the nested angles remained in the AM condition. Most fastener holes on the CX coupons were treated with a 5% expansion of the hole diameter. The two fastener holes closest to the end of the smaller piece had the highest local stress (first fastener, smallest section), and one of these holes was denoted the critical fastener hole (indicated in figure 83). In CX coupons, this hole was treated with 3% CX (rather than 5%) to help control the location of cracking. In both AM and CX coupons, a fatigue crack starter notch was used to ensure cracking from the critical hole, as explained below.

The fastener holes were prepared simultaneously on both nested-angle pieces while the pieces were clamped together. The 5% CX holes were drilled and reamed to a diameter of 4.3 mm. A split sleeve, sized to provide a 5% interference with the tapered mandrel, was placed through the holes with the split positioned at 12 o'clock or 6 o'clock relative to the coupon length. After CX, a 4.8 mm diameter ream was used to clean up and finish the fastener holes. The same process was used for 3% CX holes, except that a 4.4 mm diameter pilot hole was used and the sleeve was sized to provide a 3% interference with the mandrel. The AM nested angles had all eight holes drilled and reamed to a 4.8 mm diameter.

7.2.4 Residual Stress Measurement.

Residual stresses surrounding the three types of holes (AM, 3% CX, and 5% CX) were measured using the contour method. Measurements were made in two AM and two CX coupons and provided a map of residual stress around eight fastener holes: four AM holes, two 3% CX holes, and two 5% CX holes. Measurements were made of only the small section piece, with no fasteners in place.

7.2.5 Initial Notch.

A 45º initial corner-notch was cut in the fatigue test articles—at the critical fastener hole on the smaller L-section—where the edge of the hole meets the surface that contacts the larger L-section (called the faying surface) to initiate a 2-D crack typical of aircraft splice joints [74 and 107–109]. The notch was cut perpendicular to the coupon length and toward the internal corner of the angle. The notch was cut using wire EDM threaded with 0.10 mm diameter wire and measured 1.27 mm along the faying surface and 1.27 mm along the hole bore.

7.2.6 Coupon Assembly.

To remove surface asperities that may have had the potential to initiate fatigue cracks away from the fastener hole, the faying surfaces of the coupons were flattened by block sanding using a series of 320, 400, then 1500 grit silicone carbide sand paper. Coupons were then assembled using eight Hi-Loc HL 20-6-3 fasteners, which are common in aircraft assemblies and include integral breakaway collars that provide a constant fastener preload (torque). The fasteners are inserted through the fastener holes from the outer face of the large angle. All fastener collars, except at the critical fastener, are tightened until the hex has been sheared off (full torque). The collar at the critical fastener is tightened to 1.1 N-m, essentially a hand-tight condition, to reduce faying-surface friction. This was required for consistent crack growth from the initial notch, which was not achieved with full torque at the critical fastener (as discussed below).

7.2.7 Grips.

Custom two-piece grips were manufactured to apply the tensile force during nested-angle testing (see figure 84). The grips are designed to clamp 66.7 mm of either end of the nested angle. To compensate for a small difference in angle between the 90° grip faces and nested-angle pieces, 19-mm-wide, 51-mm-long, and 0.3-mm-thick shims were installed between the inner gripping surface of the larger coupon piece and the grip. These shims were installed with the long dimension running parallel to the coupon length and against the free edge of the coupon. A layer of 0.25-mm-thick, 8111 aluminum foil was placed between the steel grips and coupon grip area to mitigate fretting failures along the gripped area experienced during initial fatigue tests. On the gripped area with the shims, the foil was placed between the grip and the shims. The coupon is secured in the grip by two 19.1 mm diameter bolts that pass through one grip piece, through the large coupon holes, through the second grip piece, and are finally secured with a nut. The bolts were torqued to 203 N-m, which provided enough friction to transfer the load from the grip to the coupon without loading the coupon through the bolts; tests with lower levels of torque exhibited cracking in the grip (where the 19.1 mm bolts passed through the coupon).

7.2.8 Fatigue Loading.

Nested-angle coupons were tested under alternating constant amplitude load and under variable amplitude load. Alternating constant amplitude load tests were performed at a specific value of maximum stress (S_{max}). The reference S_{max} used during nested-angle testing is defined from the gross cross-sectional area of the smaller coupon piece. Blocks of constant amplitude applied load alternated between $R = 0.1$ and $R = 0.5$. All blocks were 10,000 cycles. The alternating stress ratio was used to develop marker bands on the fracture surface, as described below. Variable amplitude load tests used the block loading program applied during loaded hole variable amplitude tests (described in section 5.2.8), which was developed from in-flight strain gage data.

7.2.9 Load Frame Alignment and Calibration.

Static alignment of the specimen and load frame was performed to ensure a minimum amount of coupon bending [52]. Bending and axial stresses were assessed using an instrumented nested angle. The coupon was instrumented using six strain gages (two groups of three), which had an

active grid 1.52 mm long and 0.81 mm wide. All gages were placed on the internal faces of the L angles. One group was placed on the large piece and the other on the small piece, each on a plane perpendicular to the long axis of the coupon, 36.7 mm along the coupon length from the edge of the overlap of the pieces (see figure 83). At each location along the coupon length, two gages were mounted on the inner surface of the coupon 12.7 mm from the edge of the large piece and 19.8 mm from the edge of the small piece so that the two gages were at the same location on each cross section relative to the L angle center (see figure 85). The third gage in each group was placed on the internal radius at the center of the L angle. The placement of the gages was assumed to be sufficiently far enough away from the gripping area and lap joint so as not to be influenced by stress gradients caused by either detail.

Strains were measured under a monotonic load and bending moments were calculated about the section principal axes (see figure 85) using strength of materials and uniaxial stress–strain relations (see appendix A). Bending strains and stresses in each section were calculated at the points furthest from the section centroid (shown in figure 85), corresponding to the location of the highest bending stress. This provided a conservative characterization of bending stress in the coupon, which was greater than bending stress near the fastener holes, which are close to the section centroid.

Bending due to the moment about the section *X*-axis (see figure 85) was minimized relative to the axial stress by adjustment of concentric and angular alignment of the load frame. Axial stress was calculated using the strain measurements and strength of materials (see appendix A). Once aligned, bending stress was less than 5% of axial stress at the maximum fiber of the gage plane in either section of the coupon. Additional analysis indicated that residual bending stress is a result of the additional moment applied by the offset centroids of the small and large pieces of the coupon along the *Y*-direction. This cannot be eliminated through machine adjustment.

For alternating constant amplitude tests, the load frame was dynamically calibrated [53] to ensure that the appropriate values of S_{max} and S_{min} were being applied at the test frequency of 8 Hz. The same calibration procedure was used for nested-angle alternating constant amplitude testing as was for loaded hole constant amplitude testing (see section 5.2.8). Nested-angle calibration was performed at $R = 0.1$ and for an array of S_{max} ranging between 43.1–117.2 MPa. The calibration data was fit to a quadratic curve to provide a continuous dynamic calibration relationship for constant amplitude loading. Post-test calibration was also performed for the loads applied by the block loading program at the test frequency of 8 Hz. This procedure is described in appendix A.

7.2.10 Test Matrix.

Tests were performed on multiple coupons for each material condition, and the effects of CX were evaluated by comparing the AM and CX test data. The effects of load interaction were evaluated by comparing alternating constant amplitude test data to variable amplitude test data. Alternating constant amplitude tests were performed on three AM and two CX coupons. An additional three AM and two CX coupons were tested under the block-loading program.

7.2.11 Initial Load Levels.

Load levels were determined during initial tests to achieve fatigue lives of approximately 1 million cycles. This required a balance between applying enough load to overcome faying surface friction and achieve a reasonable test duration and applying too much load, which could result in failure at the grips.

7.2.12 Fatigue Testing.

Remote tensile loads were applied by a computer-controlled servohydraulic load frame. Custom software was engineered to apply the alternating constant amplitude time-varying sinusoidal loading. The same software was adapted to apply the block-loading program (described in section 6.2.1).

7.2.13 In-Situ Surface Crack Size Measurement.

Testing was paused periodically to measure surface crack length under a monotonic load of 80% S_{max}. This ensured there was no crack face contact. Alternating constant amplitude tests were paused after each 10,000-cycle block to collect data. Variable amplitude tests were paused during the ramp-up of the final cycle in the program (which had a peak of 100% S_{max}) so that load interaction was not affected.

Surface crack length was measured using the KG system [73] and used the same instrumentation and methods as used for loaded hole coupons (refer to section 5.2.9), except for a modification to the gage itself. A single KG (model BH 16250 X20) was bonded to the side of the hole nearest the L section interior radius, over the expected path of the crack growing from the notch at the faying surface. The gage was modified so that it fit between the fastener and the L section interior radius by removing 5.5 mm from the end (see figure 86). The start of the gage foil was placed at 1.86 mm from the hole perimeter to avoid contact with the fastener collar. Typical gage installation is shown in figure 86. At this position, the gage measured free-surface crack length after a crack emerged from behind the fastener head (referred to as crack breakthrough).

A mathematical relationship was used to correlate DCPD voltage measurements to physical crack length, as done for the loaded hole tests (see section 5.2.12). The earlier FE analysis was modified to account for the new gage boundaries (including the trimming of the gage, as described above). Additional analysis was performed to provide a DCPD to crack length correlation for the average crack angle measured during constant amplitude and variable amplitude nested-angle testing (15° and 7°, respectively). The coefficients of the power series for normalized crack size and normalized voltage in the modified crack gage are provided in table 18 for 15°, 7°, and 0° cracks, for which the equations between voltage and crack size are given in section 5.2.12. For all crack angles, the power series fit the numerical results with an R^2 value of 1.0000.

Tests were terminated when a crack extended 7.62 mm from the hole edge, as measured on the inner surface of the L-angle in the coupon by the KG. Post-test measurements of surface crack length were used to adjust DCPD crack length data. Measurements of the distance between the hole perimeter and the KG foil, and of the final crack length, were made using a microscope with

a motorized stage. The distance between the hole and the foil was used to offset crack length measurements to account for gage placement. Initial and final crack length measurements were used to linearly adjust the DCPD signal, per section A6.3 of ASTM E647 [4].

7.2.14 Post-test Through-thickness Crack Size Measurement.

Marker bands generated on coupon fracture surfaces (by the alternating constant amplitude blocks or by the variable amplitude loading) were measured by breaking the coupons open and imaging the surfaces with a Zita 20, 3-D through focus microscope. The microscope provided a scaled, 2-D image of the fracture surface in which marker bands could be identified.

The marker bands were measured photogrammetrically using image manipulation software [58]. For each marker band, crack lengths were determined along the hole bore (a) along the faying surface (c) and along the free surface (c_t). In cases where marker bands did not form completely through to the coupon-free surfaces, bands were projected to the surfaces by lines perpendicular to the coupon edge. The cracked area, enclosed by each marker band, was also determined and included the area made by projecting the marker bands to the coupon surface.

7.2.15 Fatigue Crack Growth Rate Calculations.

Free surface fatigue crack growth rate (FCGR) was calculated from DCPD measurements of crack length. Average alternating constant amplitude FCGR was calculated for each block of cycles by fitting data collected during the block to a quadratic curve, differentiating it with respect to cycles, and evaluating the derivative at the median crack length of the block. Variable amplitude surface FCGR (per block) was calculated from DCPD crack length data using the modified incremental method of Larsen, Jira, and Ravichandran, et al. [54], with modifications developed during open hole testing (see section 3.2.4.5). Cracked area growth rate was calculated from marker band measurements and computed using the modified incremental method.

7.2.16 Data Verification.

To assess the accuracy of the reported crack length, free surface KG and marker band measurements were compared.

7.3 RESULTS.

7.3.1 Residual Stress Measurements.

Contour plots of measured residual stress near each hole are provided in figure 87, showing more compressive stresses near the CX holes than the AM holes and illustrating the variations measured in each coupon. Comparing plots for AM and CX holes indicates that CX holes have a narrow region of high magnitude compressive residual stress near the hole, which is typical of CX. Residual stress fields near 3% and 5% CX holes are similar. There is a negligible difference between the left and right sides of the holes (as shown in figure 87).

To compare the AM and CX material conditions, statistical analysis was performed on the residual stress data. The spatial distribution of the average residual stress in each condition, and its standard deviation, was computed along specific trajectories through the coupon. Because residual stresses were similar on both sides of the holes (i.e., the left and right sides of each contour plot in figure 87), results from both sides were grouped together for analysis. Replicate data for each material condition were also grouped together. The group size was eight for the AM condition (two sides of each hole, two holes per coupon, and two coupons) and four for the 3% CX and 5% CX conditions (two sides, one hole, two coupons).

Average residual stress in each material condition along a trajectory running through the thickness and 0.1 mm from the hole edge is shown in figure 88. Error bars indicate the standard deviation at each position. These results show a roughly parabolic distribution of residual stress through the thickness, which is more symmetric at the AM holes than at the CX holes. The results for AM holes are typical of extruded shapes, with more compressive residual stress at the outer surfaces and tension on the interior. Results for CX holes are typical of CX, with compression through the thickness and an asymmetry that results from the mandrel pull direction. The average through-thickness residual stress is similar for both CX conditions (-282.2 MPa for 3% CX holes and -316.3 MPa for 5% CX holes), but 5% CX holes had significantly more variability than 3% CX holes.

Average residual stress along the mid-thickness of the section in each condition is plotted as a function of distance from the hole edge in figure 89. Error bars again provide the standard deviation. Results for AM holes are typical of extruded shapes, with a low level of compressive stress near the hole, which results from the drill and ream operations. Results for the CX holes are typical of CX. They had highly compressive residual stresses at the hole edge that decreased in magnitude with distance from the hole and became tensile at some distance. The average residual stress is -427.1 MPa at the edge of 3% CX holes and -417 MPa at the edge of 5% CX holes. The transition from compressive to tensile residual stress occurred 0.58 mm and 0.67 mm from the edge of 3% and 5% CX holes, respectively.

The through-thickness average residual stress near 3% CX nested-angle holes is compared to data from 3% CX open holes in thin material in figure 90. Open hole coupons had a roughly 15% greater magnitude of residual stress at the hole edge and compressive residual stress extending about three times farther from the hole edge (2.0 mm versus 0.7 mm). Therefore, the results indicate that residual stresses from CX may have a much more limited effect on crack growth in these nested-angle coupons than was found in the tests of open hole and loaded hole coupons described in previous sections.

7.3.2 Crack Growth Under Alternating Constant Amplitude Loading.

7.3.2.1 Fatigue Life.

Alternating constant amplitude tests were performed at S_{max} = 62.0 MPa. Fatigue life was defined as the number of cycles to grow a crack from the initial notch (without pre-cracking) to a crack length of 7.62 mm, as measured by the KG; results are listed in table 19. The average alternating constant amplitude AM nested-angle fatigue life was 804,000 cycles with lifetimes ranging from 547,000–1,110,000 cycles. The average of the two CX fatigue lives was 873,000

cycles, with lives of 618,000 and 1,130,000 cycles. The average fatigue lives in each material condition were within 8.6% of each other and the range of fatigue lives overlap; therefore, there is no significant difference between the total fatigue lives (cycles spent in initiation [from the notch] and crack growth) of the AM and CX coupons.

7.3.2.2 Free Surface Crack Growth.

The shortest crack length measured by DCPD on the coupon-free surface was restricted by the radius of the fastener collar, which limited the proximity of the KG to the hole perimeter (as explained in section 7.2.13). Crack growth on the free surface is reported as crack size versus cycles from crack breakthrough, defined as the first detection of crack growth at the KG. Cycles to crack breakthrough are reported in table 18 for each coupon.

Free surface crack growth during alternating constant amplitude AM nested-angle testing is plotted as a function of cycles in figure 91. The corresponding FCGR for blocks at $R = 0.1$ and $R = 0.5$ are plotted as a function of crack length in figure 92. Similar plots for CX coupons are provided in figures 93 and 94. Crack length (figures 91 and 93) is reported every 10,000 cycles, corresponding to changes in stress ratio.

These results show similar free-surface fatigue crack growth behavior in AM and CX coupons. Typical variations in FCGR were measured between stress ratios, with slower crack growth for $R = 0.5$ blocks than for $R = 0.1$ blocks. Variations in crack growth at the same R are likely a result of the shallow angle between the crack front and the coupon surface along with intermittent tearing of the thin ligament near the coupon surface, which is picked up as alternating low and high FCGR by surface DCPD.

7.3.2.3 Marker Band Crack Size Data.

Multiple microscopic techniques were used in attempts to resolve the marker bands on the coupon fracture surfaces. Marker bands were only visible under light, projected at a specific angle of incidence, which is thought to highlight a macroscopic accumulation of shadows cast by microscopic striations. Therefore, without light scanning, electron microscopy was unsuccessful, and conventional optical and confocal techniques, which cannot focus the entire 3D fracture surface, were unable to resolve continuous marker bands across the surface. Marker bands were successfully revealed using a Zita 20 3D through focus microscope, as shown in figure 95, in which marker bands are highlighted by superimposed curves. Blocks of $R = 0.5$ cycles formed very narrow bands and, for clarity, the figures show only the transition from $R = 0.1$ to $R = 0.5$. Marker bands did not always form completely through the thickness of the coupon and marker bands at short crack lengths did not form in some coupons, especially CX coupons (perhaps as a result of the compressive residual stresses).

Among tests of coupons in the same condition, the marker bands show inconsistent crack front geometry. The marker bands suggest that cracks initiated at different locations along the notch front during each test (see figure 95), with surfaces for coupons NC C and CW 11 suggesting crack initiation across the entire notch and surfaces for coupons NC A, NC B, and CW 10 suggesting crack initiation at the intersection of the notch and the faying surface. At longer crack lengths, all coupons had similar crack front shapes.

Marker bands were measured in two ways. The first was to estimate surface crack lengths at the bore (a), the faying surface (c), and the free surface (c_t). The second was to measure the cracked area enclosed by each marker band.

Data from marker band surface crack lengths are plotted in figure 96. The distance down the hole bore and along the free surface was normalized to the distance along the faying surface and plotted as a function of crack length along the faying surface. Short cracks tended to grow faster along the faying surface than the bore of the hole during the test of coupons NC C and CW 11. The opposite behavior was noted on all other coupons. This discrepancy is due to the difference in initiation locations, thus crack front, as noted above. The data are also impacted by the quality of the marker bands at short crack lengths, the end points of which had to be projected a relatively long distance to the respective coupon surfaces. Once the crack breaks through to the free surface, faster crack growth is noted along the free surface than along the faying during all tests, as the crack grows toward a uniform (1D) through-thickness crack.

Cracked area is plotted as a function of faying surface crack length (c) in figure 97 and the corresponding cracked area growth rate is plotted against c in figure 98. Cracked area shows smooth, constantly increasing crack growth that is similar for all tests, with no consistent difference among AM or CX conditions.

To validate the crack length data, free surface crack length measured using DCPD is plotted with free surface crack length measurements from the marker band images (see figure 99). Figure 99(a) shows crack length data for NC A from both optical and DCPD methods as a function of cycles to illustrate the general agreement between the measurement methods over the test. Figure 99(b) shows a correlation between marker band and DCPD crack length data for all tests. The general trend is that the two crack length measurement methods are in agreement, although better agreement would be preferred.

7.3.3 Crack Growth Under Variable Amplitude Loading.

7.3.3.1 Fatigue Life.

Variable amplitude block loading tests were performed at S_{max} = 117.2 MPa. Post-test dynamic calibration showed differences between intended and achieved cyclic stress (similar differences were not found in the load-hole variable amplitude tests described in section 6). Achieved maximum stresses were similar to those intended; however, achieved minimum stresses were significantly different than those intended. The corresponding normalized maximum and minimum achieved stress levels for all blocks of the variable amplitude program are given in table 20. These stress levels are useful for follow-on efforts in modeling crack growth observed in the tests.

The number of block programs required to grow a crack from the initial notch to the length of 7.62 mm during variable amplitude testing is provided for all coupons in table 21. The AM fatigue life ranged from 451–514 block loading programs, with an average of 488 programs. Because of damage that occurred to the gage placed on coupon CW 16, fatigue lives were available for only two of the CX coupons, which were 525 and 573 blocks loading programs, with an average of 549 programs. The average fatigue life in CX coupons was 12.5% longer

than the average life in AM coupons; the minimum CX fatigue life was 16% longer than the minimum AM fatigue, indicating the difference may be statistically significant but additional data points would be needed to confirm and quantify the difference. Certainly, CX did not provide a large life increase in this experimental protocol (coupon geometry, CX process, assembly detail, and load spectrum).

7.3.3.2 Free Surface Crack Growth.

As with alternating constant amplitude tests, free surface crack length and per-program-FCGR, measured by DCPD, was plotted against the number of block programs following crack break-through in figures 100 and 101 for AM and CX coupons, respectively. The number of block programs to crack breakthrough is also provided in table 21. These data show steadily increasing crack growth rates and a negligible difference between AM and CX coupons, as was found in alternating constant amplitude tests.

7.3.3.3 Marker Band Crack Size Data.

No marker band crack size data were available. Marker bands were not visible across the fracture surface of the coupons tested under variable amplitude loading using any of the microscopy techniques used with the coupons tested under alternating constant amplitude loading.

7.4 DISCUSSION.

7.4.1 The AM Versus CX Test Results.

The tests showed no significant differences between fatigue crack growth behavior in AM and CX nested-angle coupons. Similarly, there were no consistent differences observed between AM and CX crack-front geometry in the alternating constant amplitude coupons. The factor likely contributing to the similar crack growth behavior was the limited extent of residual stress in the CX coupons. This, combined with the long notch length needed to ensure consistent crack growth, would have resulted in low levels of residual stress effect at the notch tip. The results here are atypical of the CX process, which has been shown by other work to introduce significant residual stress fields that significantly affect fatigue cracking (e.g., [2] and earlier sections of this report). The contrast between results in these tests and those in other CX work suggest that the benefits of CX may be limited to crack initiation and short crack growth, which were not discernable with the current test design.

The industrial partner, using the same techniques applied to in-service rotorcraft, performed CX of the nested angles. The low levels of residual stress in these nested angles suggests the need for future work to improve CX practice so that it may more significantly affect long-crack growth in nested-angle coupons. Future CX nested-angle testing should be accompanied by modeling to support the findings and could make use of the data presented here.

7.4.2 Photogrammetric Measurement of Marker Bands.

Although difficult to produce, the photogrammetric measurements of the alternating constant amplitude marker bands provided useful crack size data. Accurate measurements are highly dependent on the microscopic technique and careful photogrammetric work. However, because of the flexibility offered by photographically based measurements, a similar technique might be applied to other test configurations.

Marker bands were not seen on the variable amplitude coupons, which did not experience the long cycle blocks at high stress levels necessary to accumulate wide, distinct regions of striations (as formed during alternating constant amplitude testing). This highlights a fundamental technical need for reliable and accurate through-thickness crack growth measurements for 3D cracks, such as the nested angle coupons, that fully quantify observed crack growth.

7.4.3 Methodological Difficulties.

7.4.3.1 Clamping Stress.

During coupon installation, significant clamping stress was measured in the corners of the angle and was found to be a function of the torque applied to the grip bolts. This was a result of differences in the angle between the extruded pieces and the machined grips. Clamping stress was minimized by installing shims between the inner face of the coupon and the grip (which is detailed in section 7.2.7) and consistently tightening the grips to 203 N-m.

7.4.3.2 Uncontrolled Locations of Cracking.

Nested-angle tests were designed to grow a crack from the critical fastener hole, but this was difficult to achieve and several iterations were required to develop a successful test protocol. While the tests reported above used a hand-tight critical fastener, initial trial tests used a critical fastener at full torque. With full torque, faying surface friction dominated the stress state in the neighborhood of the critical fastener, shielding the fatigue starter notch from cyclic stress. At stress levels below approximately 62.0 MPa and with a fully torqued critical fastener, cracks would not form at the fastener hole, and the coupons would either run out (at 10^6 cycles) or fail because of fretting at the coupon-grip interface, as shown in figure 102(a). Failure at the coupon-grip interface was alleviated by using aluminum foil between the coupon and the grip. At higher applied stress, the coupon would break free of the grip clamping, resulting in loading at the large holes of the coupon beneath the grips and hidden fatigue crack initiation (see figure 102[b]). High-contact stresses at the faying surface near the critical fastener also caused crack initiation at asperities on the faying surface prior to crack initiation at the notch, which caused fracture away from the hole (see figure 102[c]). That was alleviated by block sanding the faying surfaces prior to coupon assembly. Finally, using a hand-tight critical fastener decreased friction enough to allow reliable crack initiation at the fatigue starter notch.

The measures used to control fatigue cracking affected crack growth and may have reduced the effects of residual stresses from CX. Therefore, future improvements to test methods, aimed at capturing natural crack initiation and early crack growth, would complement the current work and future lifing efforts by better quantifying CX effects.

7.4.4 Difference Between Test Results and Field Observations.

Nested-angle coupons were designed to mimic typical splice joints, such as at the pylon-to-tail boom transition used in rotorcraft. This feature is known to be highly susceptible to fatigue and has shown fatigue crack growth directly from the fastener holes, with crack growth along the same approximate crack path as observed in these tests. It may be that anti-corrosion surface treatments used on rotorcraft (such as anodizing and painting) give rise to low friction in fielded rotorcraft joints, such that this type of cracking occurs with fully torqued fasteners. Laboratory coupons did not include typical anti-corrosion surface treatments, but follow-on tests could easily include them. However, long-crack growth behavior might not be significantly affected by the level of fastener torque so that some of the conclusions from present tests may be useful in understanding the potential effects of CX in nested-angle joints of rotorcraft. As mentioned previously, future work would benefit from improved CX processes and measurements of earlier (smaller) crack growth.

7.5 TABLES.

Table 17. Mechanical Properties of Extruded, Clad 7075–T651 Aluminum (extrusion direction)

	Clad
Ultimate tensile strength (MPa)	558
Yield strength (MPa)	496
Young's modulus (MPa)	71706
Poisson's ratio (ν)	0.33

Table 18. Power Series Coefficients for DCPD to Crack Length Correlation With Modified (trimmed) KG for 0°, 15°, and 7° Cracks (valid for cracks less than 8.26 mm long)

	0°	0°	15°	15°	7°	7°
i or j	α_i	ν_j	α_i	ν_j	α_i	ν_j
1	0.4010	2.4354	0.4519	2.3191	0.4150	2.4022
2	0.4920	-2.5416	-0.1006	-1.1324	0.3339	-2.1323
3	-2.0744	-1.1869	0.4517	-6.2953	-1.4100	-2.7513
4	5.6488	5.0753	1.0435	14.0363	4.4392	7.8510
5	-3.8672	-2.1467	-1.1589	-7.8820	-3.1422	-3.9561

Table 19. Fatigue Life Measured During Alternating Constant Amplitude Nested-Angle Testing at S_{max} = 62.0 MPa

Coupon	Material Condition	Fatigue Life (cycles)	Cycles to Break Through
NC A	AM	554,315	355,685
NC B	AM	749,320	629,999
NC C	AM	1,114,261	1,037,287
CW 10	CX	618,140	479,842
CW 11	CX	1,128,300	980,147

Table 20. Normalized Stress Levels Achieved During Variable Amplitude Nested-Angle Testing Calculated From Strains Measured During Post-Test Dynamic Calibration

Bin	σ_{max}	σ_{min}	R	Cycles Per Bin
1	0.356	0.058	0.16	430
2	0.559	0.317	0.57	1762
3	0.770	0.582	0.76	1069
4	1.022	0.981	0.96	30
5	0.548	0.009	0.02	4
6	0.705	0.139	0.20	100
7	0.920	0.420	0.46	29
8	0.814	0.003	0.00	1
9	0.814	0.008	0.01	29
10	1.007	-0.007	-0.01	2
11	0.356	0.058	0.16	1

Table 21. Fatigue Life Measured During Variable Amplitude Nested-Angle Testing at S_{max} = 117.0 MPa

Coupon	Material Condition	Fatigue Life (Programs)	Programs to Break Through
NC D	AM	451	272
NC E	AM	499	344
NC G	AM	514	359
CW 18	CX	525	391
CW 21	CX	573	397

7.6 FIGURES.

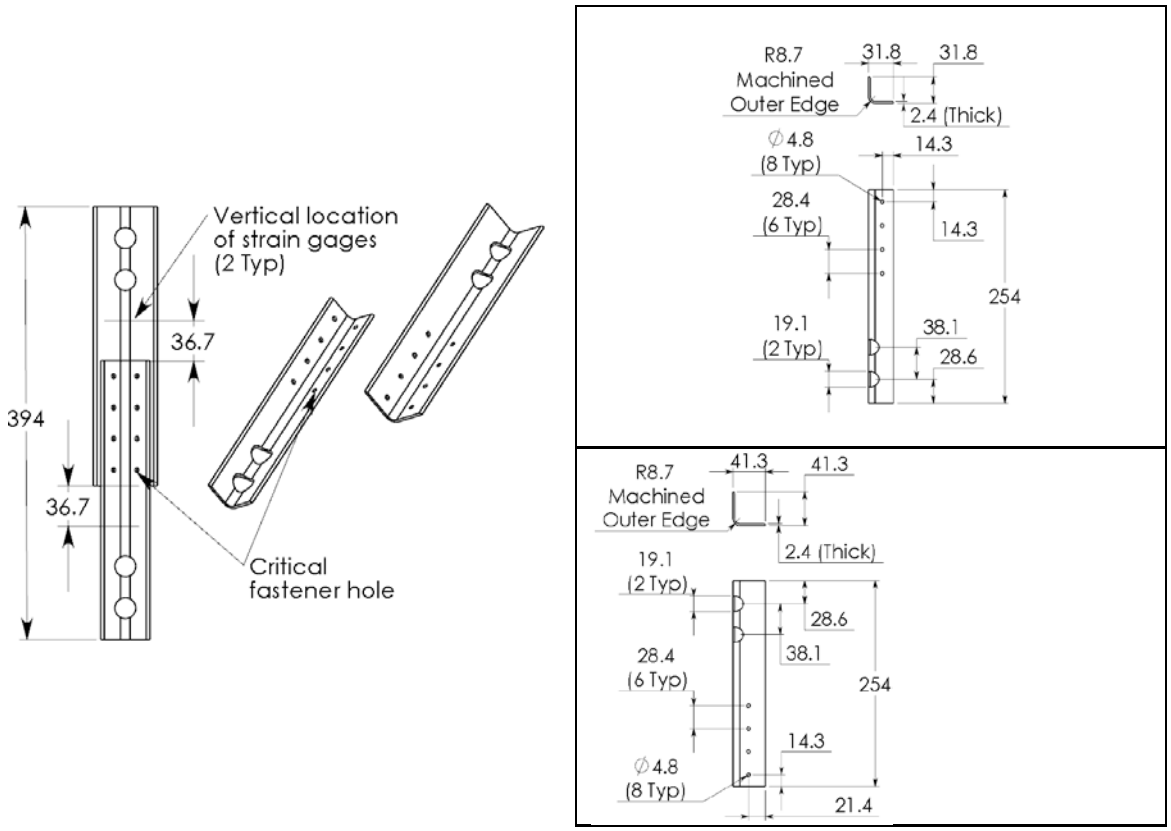

Figure 83. Dimensions of the Nested-Angle Coupon Assembly (left), the Small Piece (top right), and the Large Piece (bottom right)

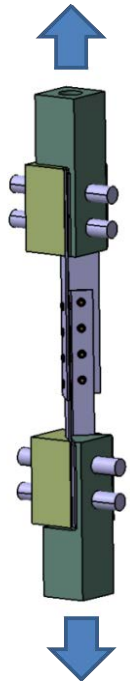

Figure 84. Nested-Angle Coupon Shown Gripped at Either End as During Testing, With Arrows Highlighting the Direction of the Applied Force

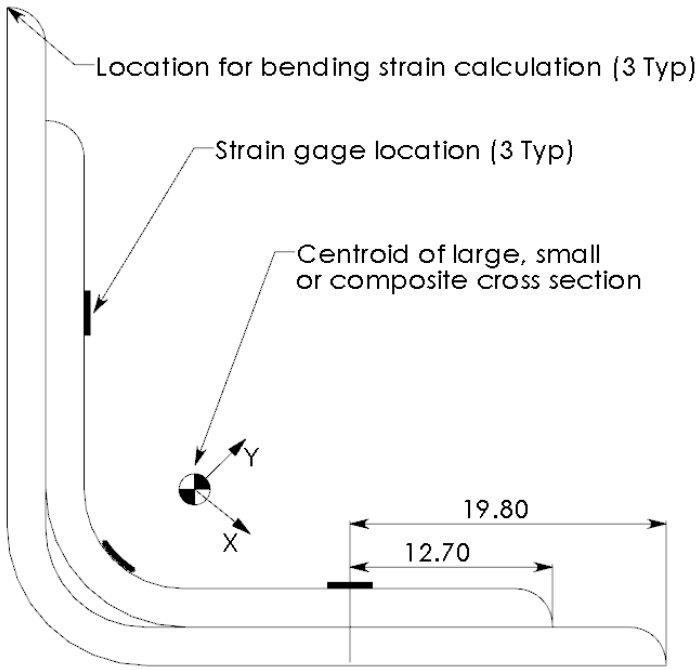

Figure 85. Cross Section of a Nested Angle, Definition of the Cross-Sectional Centroid and Principal Axes, and the Location of the Strain Gages and Bending Characterization

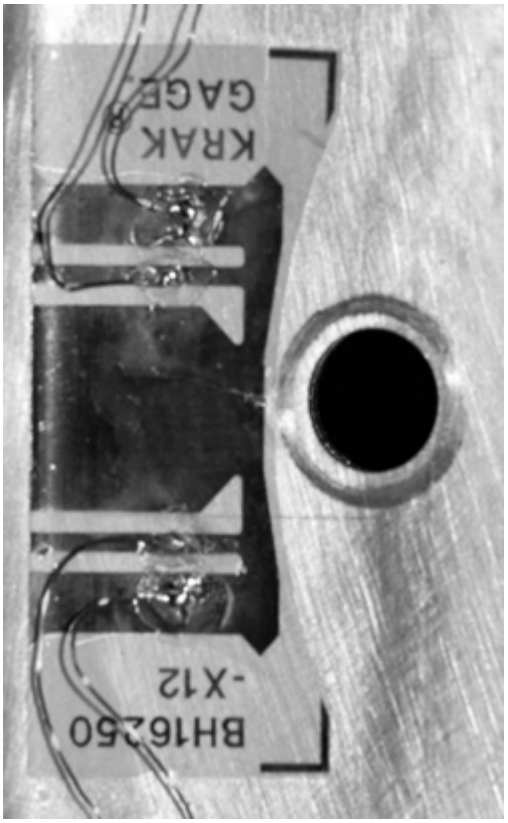

Figure 86. Trimmed KG Placed Between the Critical Fastener Hole (right) and the Coupon Bend (to the left of the image); Note the Marking Made by the Fastener Collar and Its Proximity to the KG Foil (scale provided by 4.8 mm diameter hole)

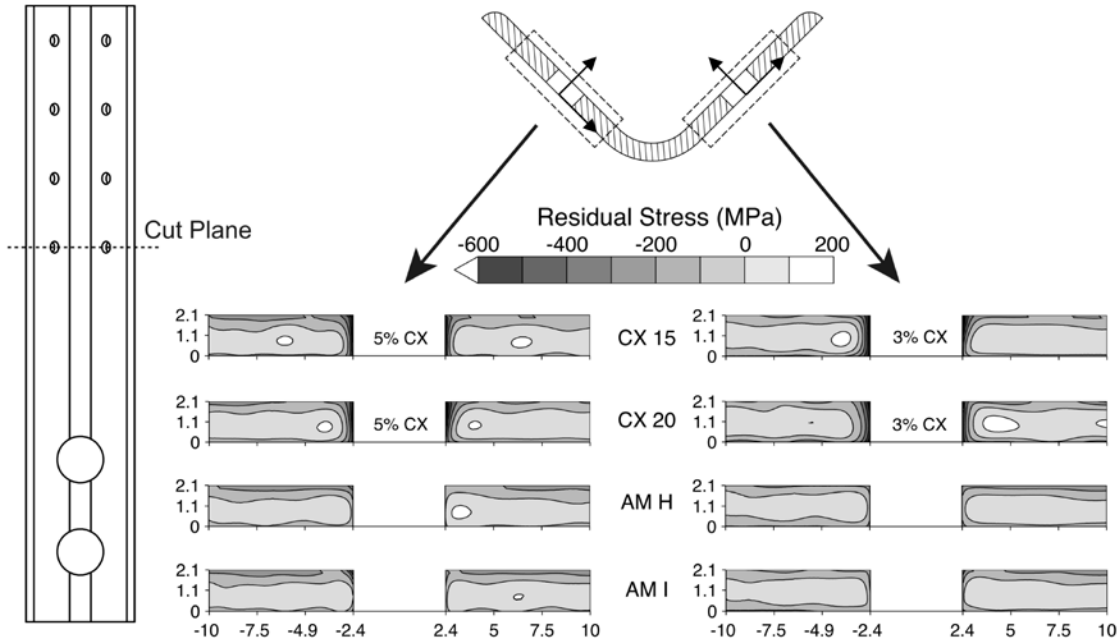

Figure 87. Contour Plots of Residual Stress Measured for Two AM and Two CX Coupons Along the Cut Plane and Axes Provided on the Top Left and Top Middle of the Figure, Respectively (linear scales in mm)

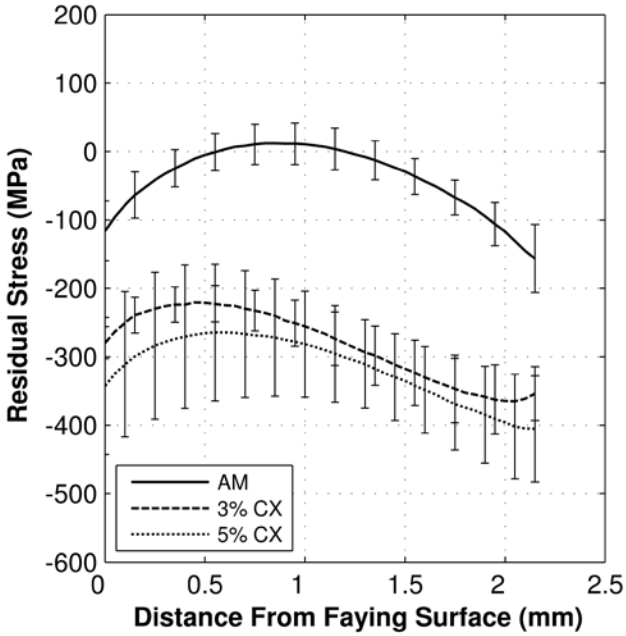

Figure 88. Variation of Residual Stress Through the Specimen Thickness With Error Bars Providing the Standard Deviation

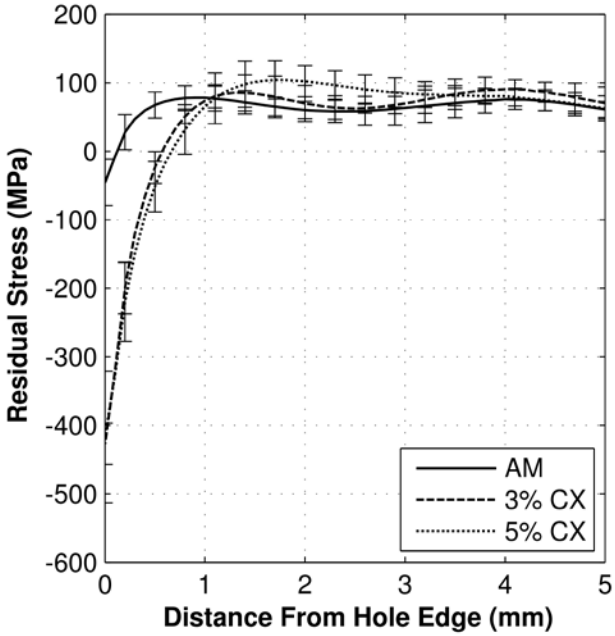

Figure 89. Average Mid-Thickness Residual Stress Plotted With Standard Deviation

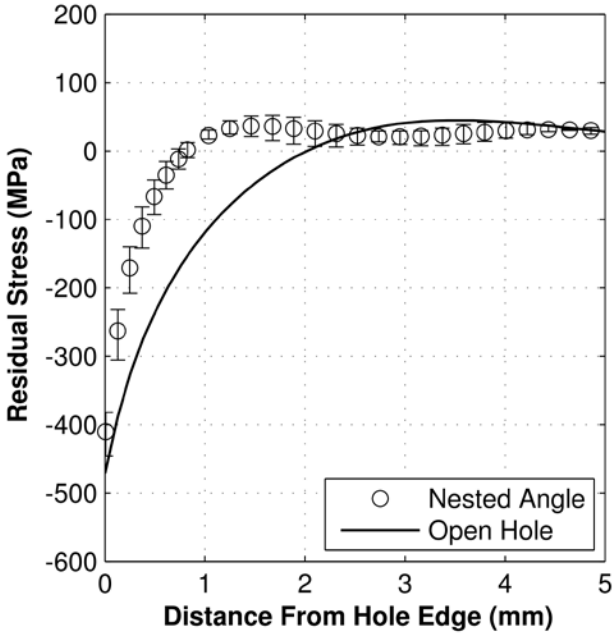

Figure 90. Through-Thickness Average Residual Stress for Nested-Angle and Thin Open Hole Coupons

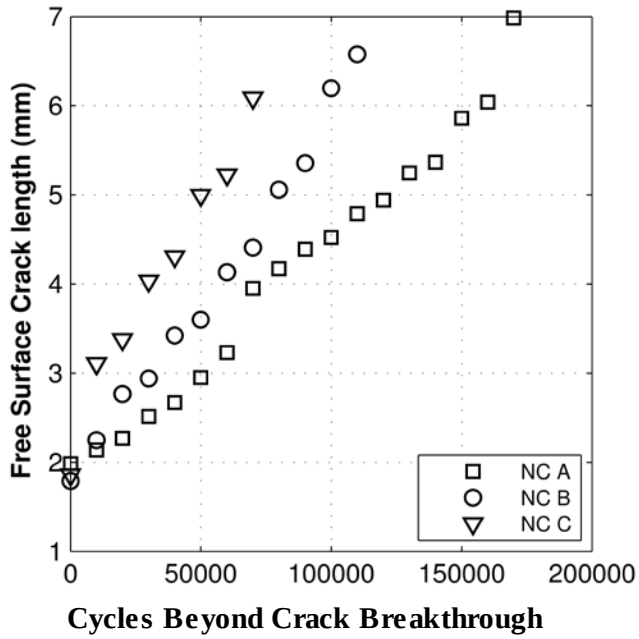

Figure 91. Crack Growth History Following Crack Breakthrough for Coupons NC A, B, and C

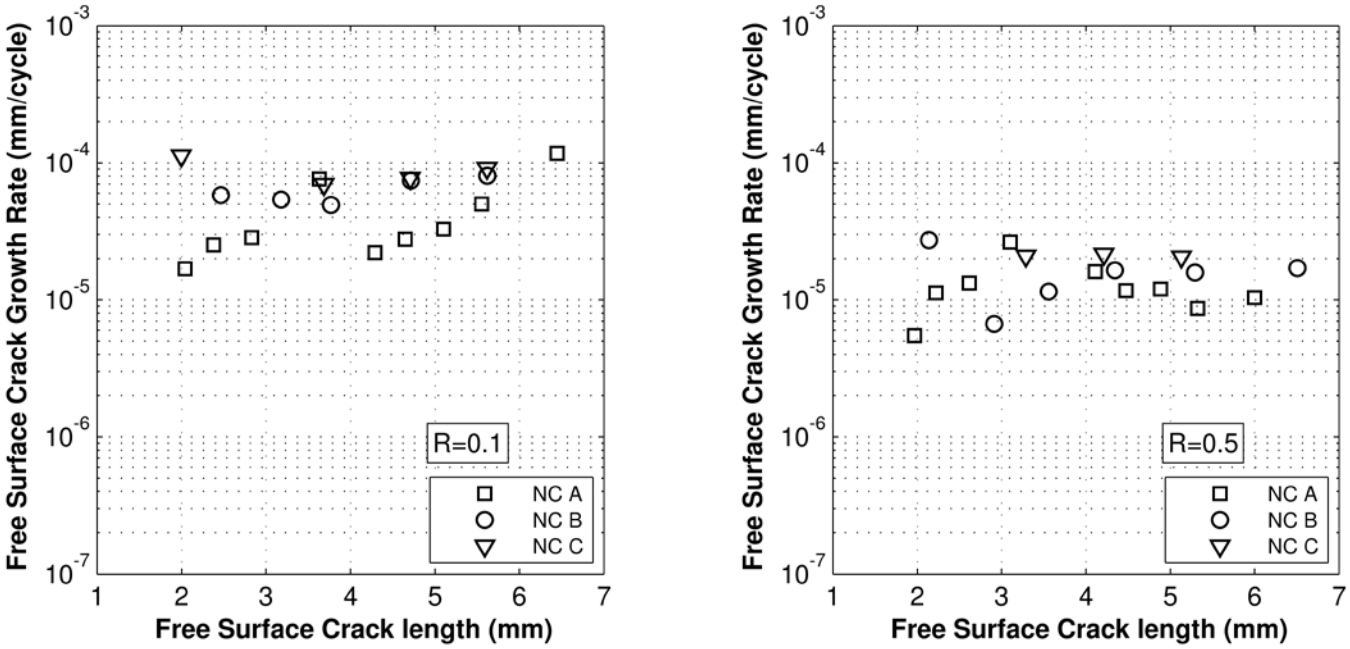

(a) (b)

Figure 92. The FCGR Following Crack Breakthrough as a Function of Free Surface Crack Length for Coupons NC A, B, and C During Blocks With (a) $R = 0.1$ and (b) $R = 0.5$

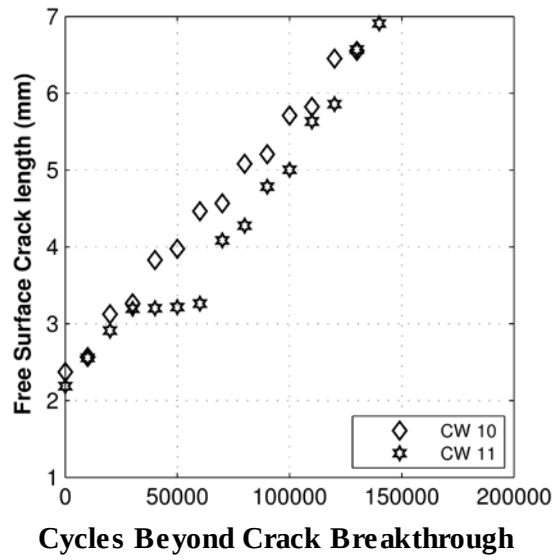

Figure 93. Crack Length as a Function of Cycles From Crack Breakthrough for Coupons CW 10 and 11

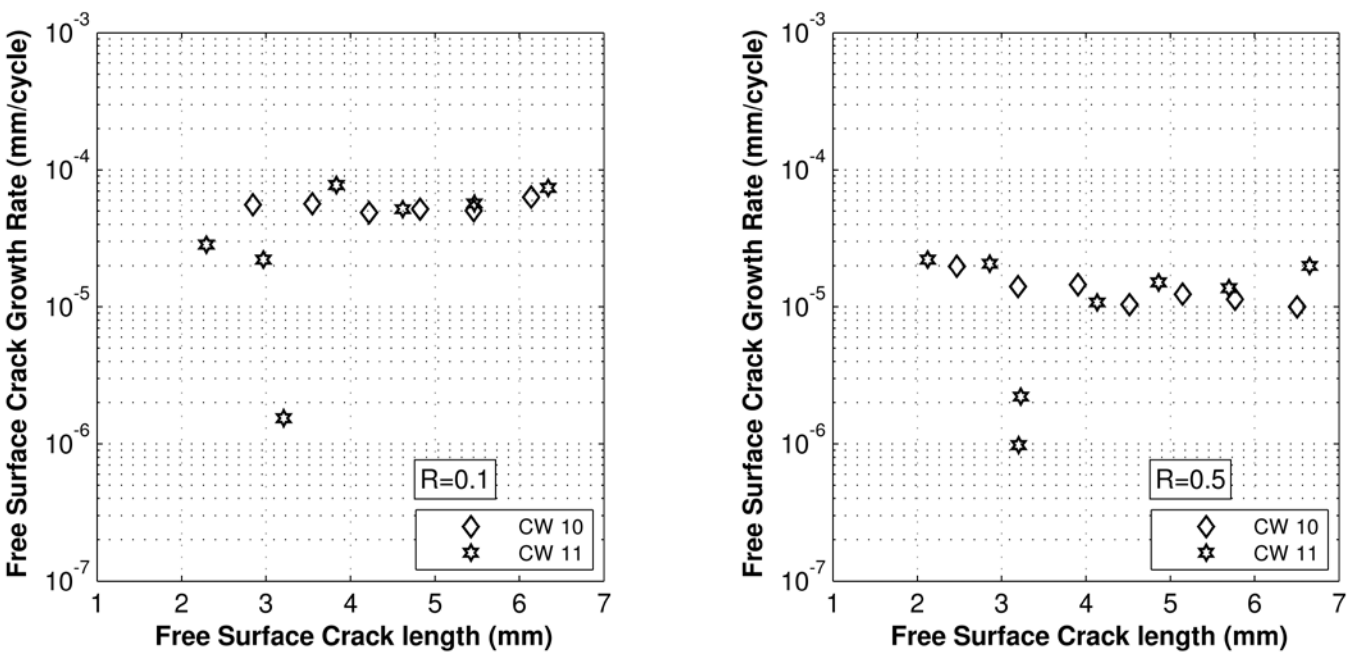

(a) (b)

Figure 94. The FCGR From Crack Breakthrough as a Function of Free Surface Crack Length, for Coupons CW 10 and 11 During Blocks With (a) R = 0.1 and (b) R = 0.5

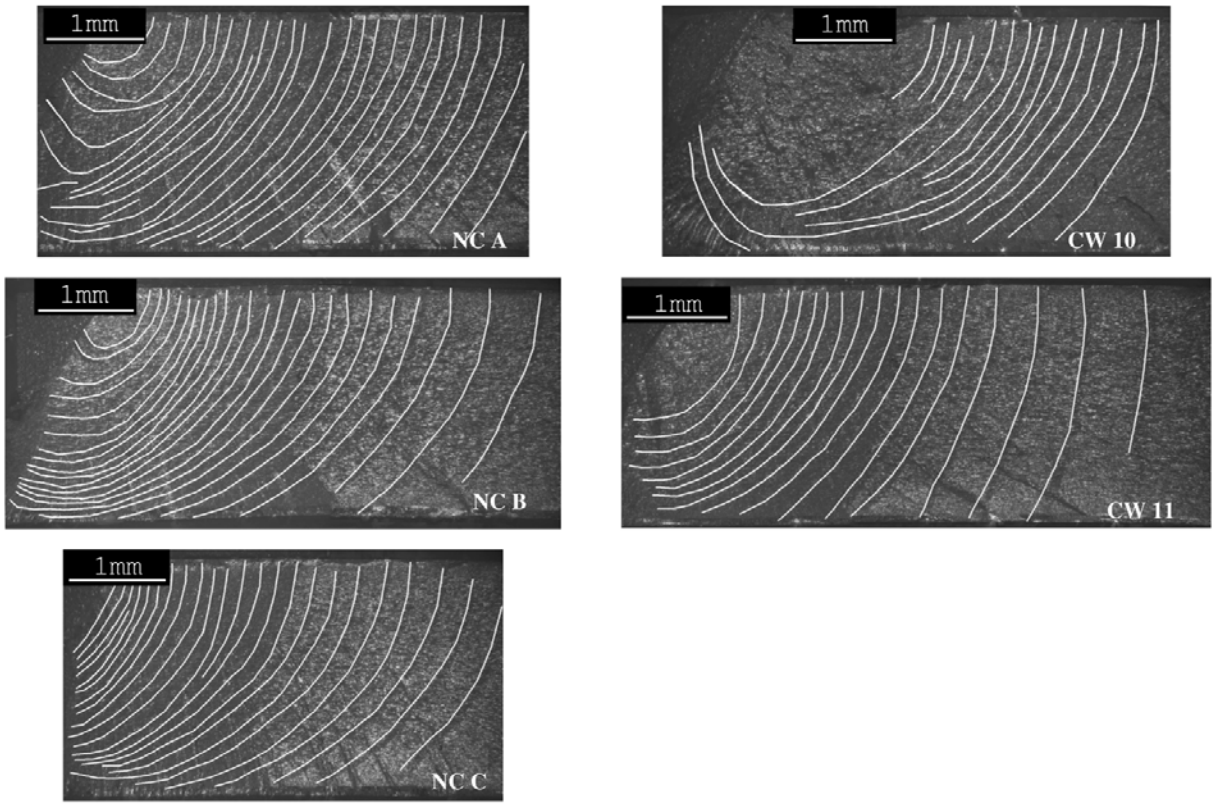

Figure 95. Marker Bands for Cracks Initiated at Different Locations Along the Notch Front Where NC C and CW 11 Show Crack Initiation Across the Entire Notch and NC A, NC B, and CW 10 Show Crack Initiation at the Intersection of the Notch and the Faying Surface

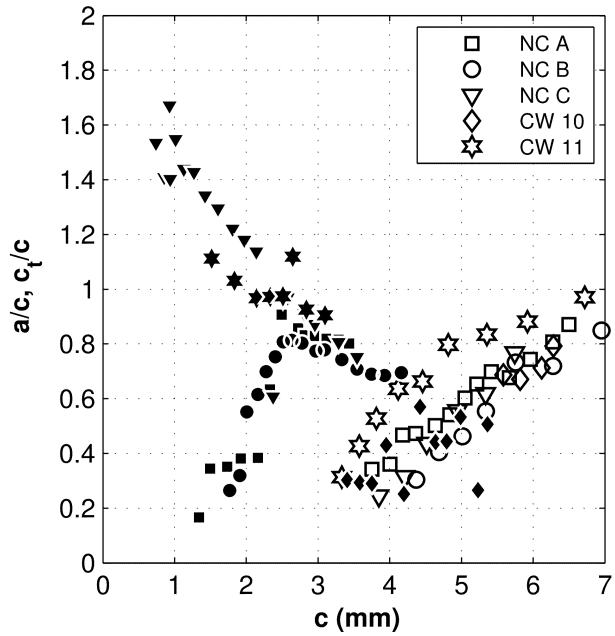

Figure 96. Crack Length Down the Bore of the Hole Normalized by Faying Surface Crack Length (a/c) (filled symbols) and Free Surface Crack Length Normalized by Faying Surface Crack Length (c_t/c) (open symbols) as a Function of Faying Surface Crack Length (c)

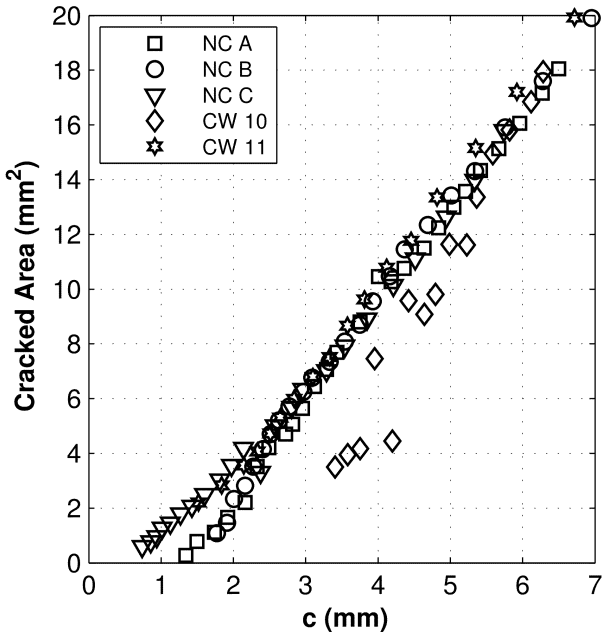

Figure 97. Cracked Area vs. Faying Surface Crack Length (c)

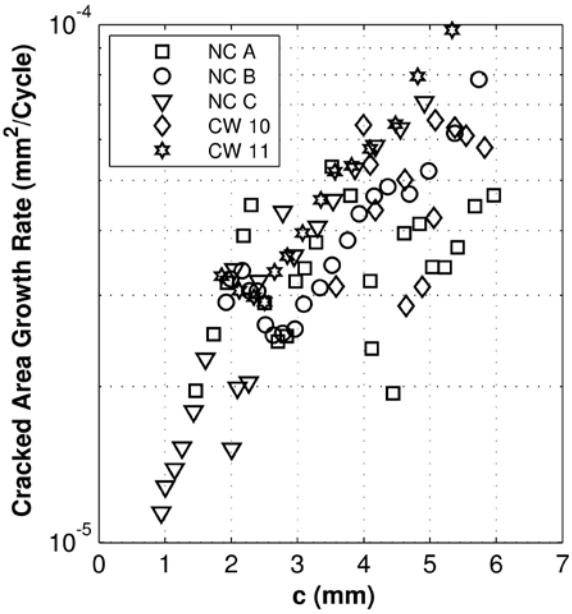

Figure 98. Cracked Area Growth Rate vs. Faying Surface Crack Length (c)

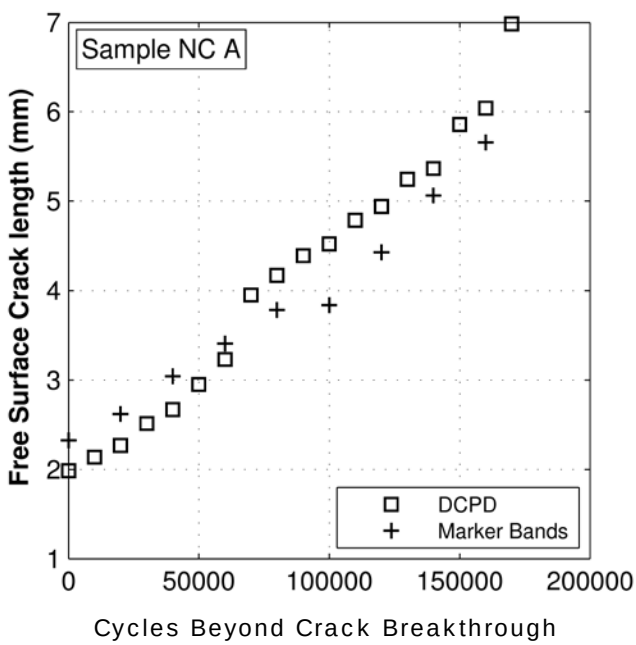

(a)

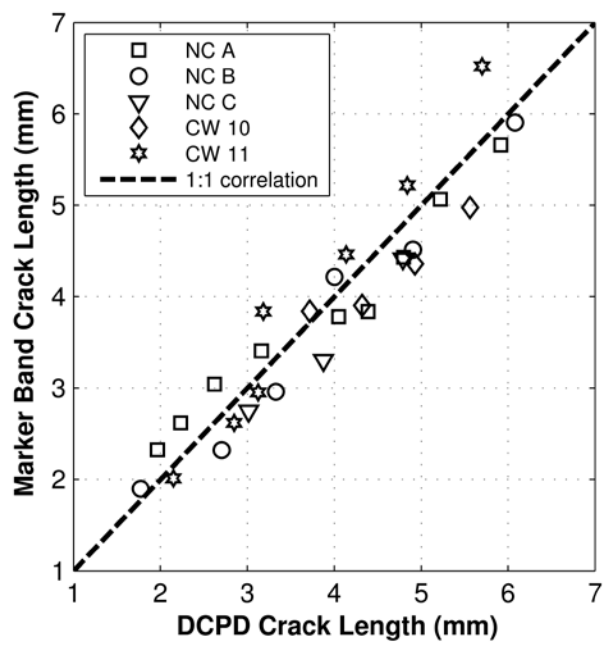

(b)

Figure 99. Crack Length Beyond Breakthrough Measured Using Surface DCPD and Marker Bands Plotted as a (a) Function of Cycles for Sample NC A and (b) Marker Band Measurements Versus DCPD Measurements (perfect correlation results in a 1:1 correlation)

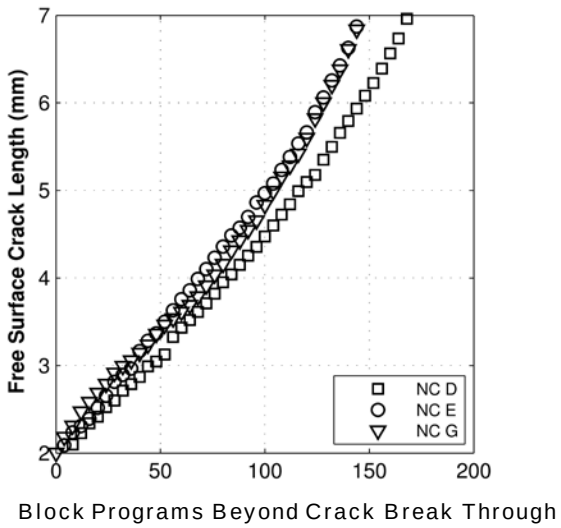

(a)

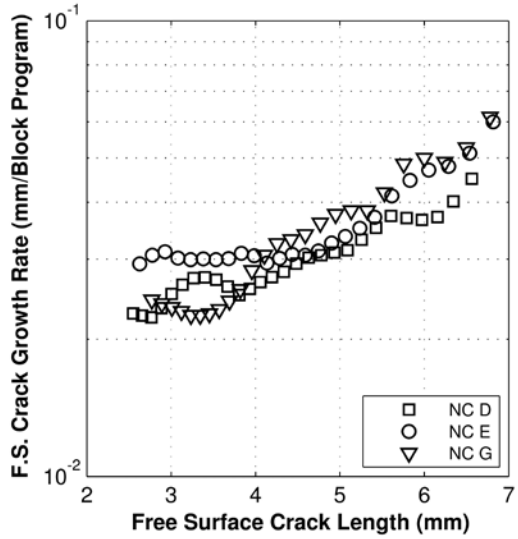

(b)

Figure 100. The AM Nested-Angle Crack Growth Data Plotted as (a) a Free Surface Crack Length as a Function of Block Programs Beyond Crack Break Through and (b) a Free Surface Crack Growth Rate as a Function of Free Surface Crack Length

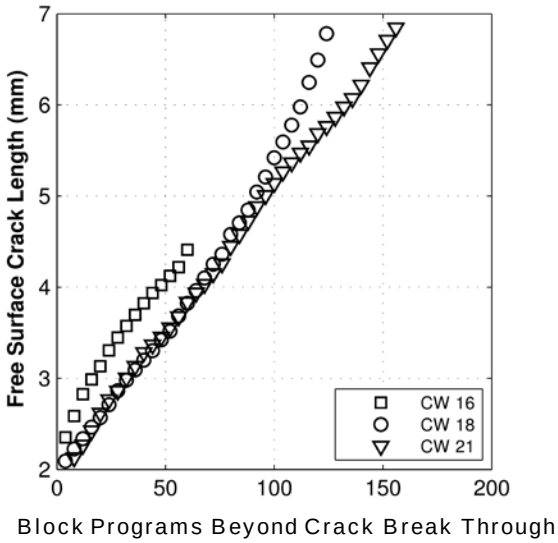

(a)

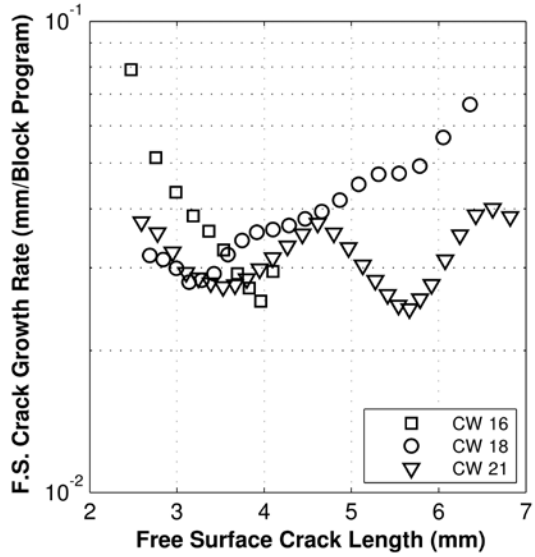

(b)

Figure 101. The CX Nested-Angle Crack Growth Data Plotted as (a) a Free Surface Crack Length as a Function of Block Programs Beyond Crack Breakthrough and (b) a Free Surface Crack Growth Rate as a Function of Free Surface Crack Length

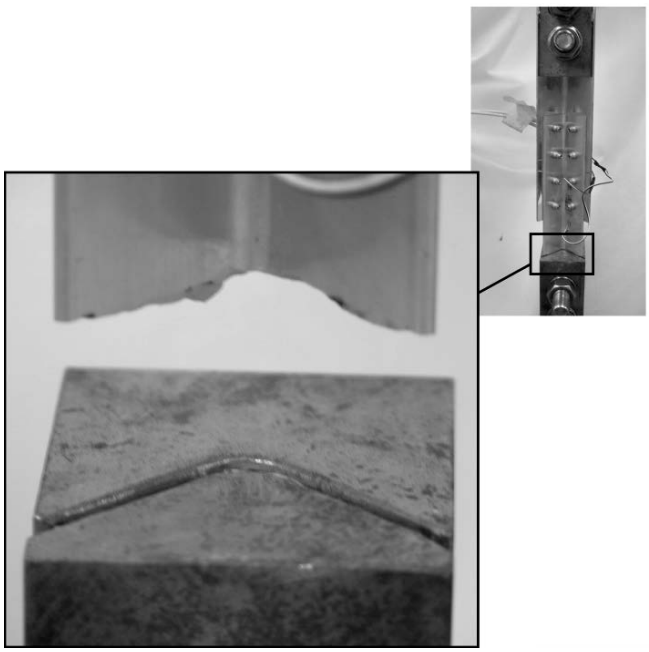

(a)

(b)

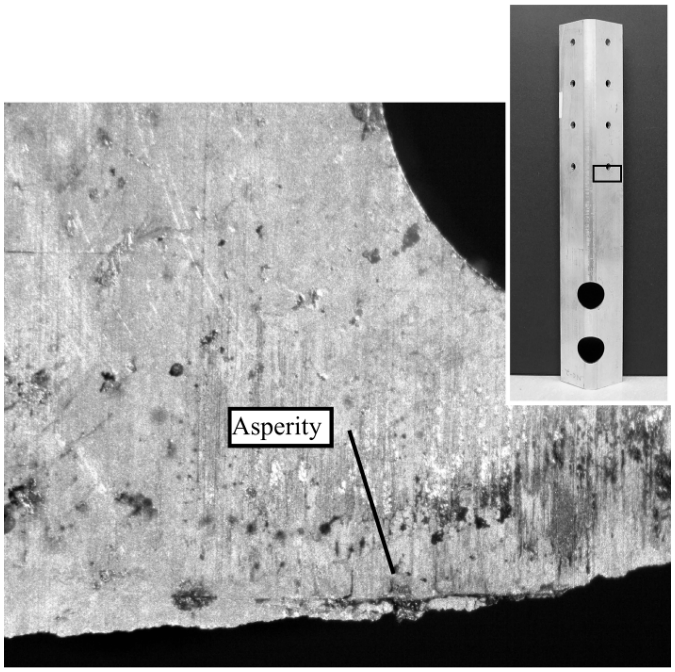

(c)

Figure 102. Coupon Failures Due to (a) Fretting at the Coupon Grip, (b) Stress at Large Holes Under the Coupon Grip (as the result of coupon slipping), and (c) Asperity on the Faying Surface

8. CONCLUSION.

This report describes a range of tests and analyses of fatigue crack growth in a variety of coupons in both as-machined (AM) and residual stress bearing conditions. The work is unique because of the methods employed for residual stress measurements and in its attention to a number of analytical and experimental details for assessing the fatigue crack growth. A number of methodological issues were identified and resolved during the course of this work, and these observations are reported in detail to provide useful insights for further research. Linear elastic fracture mechanics (LEFM) with superposition of known applied and measured residual stress fields was found to provide useful estimates of one-dimensional (1D) fatigue crack growth. For two-dimensional (2D) crack growth at open holes, the typical approach based on a quarter-elliptical QE crack shape provided useful results for AM coupons (without residual stress), but did not provide useful results for residual stress-bearing (cold-expanded [CX] hole) coupons. Tests of nested-angle coupons with a lap-shear joint provided useful data for follow-on benchmarking of tools that predict fatigue crack growth for such complicated structural details.

Some observations drawn from the test data are:

- Tension-loaded coupon geometries with an enlarged grip area proved useful and eliminated grip-related failures common to straight gaged coupons.

- The slitting method provided a useful and repeatable method for characterizing a 1D SIF in laser shock peened compact tension coupons.

- The contour method provided a useful and repeatable method for characterizing 2D residual stress fields in laser shock peened compact tension coupons, flat test coupons with CX holes, and nested-angle coupons with CX holes.

- The LEFM with superposition of known applied and measured residual stresses provided predictions of 1D fatigue crack growth that were in reasonable agreement with test data for compact tension coupons, tension-loaded open hole coupons, and pin-loaded hole coupons.

- Bounds of predicted 1D fatigue crack growth in open hole and loaded hole coupons with CX holes were developed from variability in measured residual stresses and the bounds agreed with observed variability.

- Predicted and observed crack growth for pin-loaded coupons tested under variable amplitude loading had a similar degree of correlation as found for coupons tested under constant amplitude loading.

- The LEFM provided accurate predictions of the growth of 2D fatigue cracks at as-machined open holes in tension loaded coupons but did not provide useful predictions for 2D cracks at CX holes.

9. REFERENCES.

1. Skinn, D.A., Gallagher, J., Berens, A.P., Huber, P.D., and Smith, J., "Damage Tolerant Design Handbook," Wright-Patterson Air Force Base, Ohio, 1994.

2. McClung, R.C., "A Literature Survey on the Stability and Significance of Residual Stresses During Fatigue," *Fatigue & Fracture of Engineering Materials & Structures*, Vol. 30, No. 3, 2007, pp. 173–205.

3. Jones, K.W. and Dunn, M.L., "Predicting Corner Crack Fatigue Propagation From Cold Worked Holes," *Engineering Fracture Mechanics*, Vol. 76, No. 13, 2009, pp. 2074–2090.

4. *Annual Book of ASTM Standards*, "E 647-00 Standard Test Method for Measurement of Fatigue Crack Growth Rates," West Conshohocken, Pennsylvania, ASTM International, 2004.

5. Paris, P.C., Tada, H., and Donald, J.K., "Service Load Fatigue Damage—A Historical Perspective," *International Journal of Fatigue*, Vol. 21, 1999, pp. S35–S46.

6. Ghoshal, A., Kim, H.S., "Damage Tolerance Management for Aircraft and Rotorcraft Structural Components," *Journal of Aircraft*, Vol. 43, No. 6, pp. 1676–1684.

7. Everett, R.A. and Elber, W., Jr., "Damage Tolerance Issues Related to Metallic Rotorcraft Dynamic Components," *Journal of the American Helicopter Society*, Vol. 45, No. 1, 2000, pp. 3–10.

8. Niu, M.C.Y., "Airframe Structural Design," (2nd edition), Hong Kong Conmilit Press Ltd., 1999.

9. Iyyer, N., Sarkar, S., Merrill, R., and Phan, N., "Aircraft Life Management Using Crack Initiation and Crack Growth Models – P-3C Aircraft Experience," *International Journal of Fatigue*, 29, 2007, pp. 1584–1607.

10. Rodopoulos, C.A., Curtis, S.A., del los Rios, E.R., and SolisRomero, J., "Optimisation of the Fatigue Resistance of 2024-T351 Aluminum Alloys by Controlled Shot Peening – Methodology, Results and Analysis," *International Journal of Fatigue*, Vol. 26, 2004, pp. 849–856.

11. Clark, D.A. and Johnson, W.S., "Temperature Effects on Fatigue Performance of Cold Expanded Holes in 7050-T7451 Aluminum Alloy," *International Journal of Fatigue*, Vol. 25, 2003, pp. 150–165.

12. Fujimoto, W., "Strategies for Improving the Damage Tolerance of Rotorcraft Components," *Annual Forum Proceedings - AHS International*, v II, *AHS International 62nd Annual Forum - Vertical Flight: Leading through Innovation – Proceedings*, 206, pp. 1180–1199.

13. Department of Transportation, "Metallic Materials Properties Development and Standardization," 2003.

14. Pistochini, T., M.S. Thesis, "Fatigue Life Optimization in Laser Peened 7050-T7451 and 300M Steel," Department of Mechanical and Aeronautical Engineering, University of California, Davis, 2003.

15. Luong, H., M.S. Thesis, "Fatigue Life Extension and the Effects of Laser Peening on 7050-T7451 Aluminum, 7085-T651 Aluminum and Ti-6Al-4V Titanium Alloy," Department of Mechanical and Aeronautical Engineering, University of California, Davis, 2006.

16. Cuellar, S., M.S. Thesis, "Fatigue Crack Growth Applications of Laser Peened Titanium," Department of Mechanical and Aeronautical Engineering, University of California, Davis, 2005.

17. Prime, M.B., "Cross-Sectional Mapping of Residual Stresses by Measuring the Surface Contour After a Cut," *Journal of Engineering Materials and Technology*, Vol. 123, 2001, pp. 162–168.

18. Prime, M.B., Sebring, R.J., Edwards, J.M., Hughes, D.J., and Webster, P.J., "Laser Surface-Contouring and Spline Data-Smoothing for Residual-Stress Measurement," *Experimental Mechanics*, Vol. 44, No. 2, 2004, pp. 176–184.

19. Schindler, H.J. and Bertschinger, P., "Some Steps Towards Automation of the Crack Compliance Method to Measure Residual Stress Distributions," *Fifth International Conference on Residual Stress*, Linköping, 1997.

20. "NASGRO Material File M7HA03AB1"; 7075-T6 Clad Sheet; L-T, T-L; Lab Air, 2006.

21. NASGO Fracture Mechanics and Fatigue Crack Growth Software Reference Manual, Version 5.1 alpha, 2006.

22. Wu, X.R. and Carlsson, J., 1991, "Weight Functions and Stress Intensity Factor Solutions," 1st ed, Oxford; New York: Pergamon Press.

23. Schajer, G.S. and Prime, M.B., "Residual Stress Solution Extrapolation for the Slitting Method using Equilibrium Constraints," *Journal of Engineering Materials and Technology*, Vol. 129, No. 2, 2007, pp. 227–232.

24. Wang, G.S., "A Strip Yield Analysis of Fatigue Crack Growth in the Residual Stress Field," *International Journal of Fatigue*, Vol. 96, 1999, pp. 247–277.

25. Cathey, W.H. and Grandt, Jr., A.F., "Fracture Mechanics Consideration of Residual Stresses Introduced by Coldworking Fasterner Holes," *Journal of Engineering Materials and Technology*, Vol. 102, No. 1, 1980 pp. 85–91.

26. Clark, G., "Modelling Residual Stresses and Fatigue Crack Growth at Cold-Expanded Fastener Holes," Fatigue and Fracture of Engineering Materials and Structures, Vol. 14, No. 5, 1991, pp. 579–589.

27. Ball, D.L. and Lowry, D.R., "Experimental Investigation on the Effects of Cold Expansion of Fastener Holes," *Fatigue and Fracture of Engineering Materials and Structures*, Vol. 21, No. 1, 1998, pp. 17–34.

28. Pavier, M.J., Poussard, C.G.C., and Smith, D.J., "Effect of Residual Stress Around Cold Worked Holes on Fracture Under Superimposed Mechanical Load, " *Engineering Fracture Mechanics*, Vol. 63, No. 6, 1999, pp. 751–773.

29. Kokaly, M.T., Ransom, J.S., Restis, J.H., and Reid, L., "Predicting Fatigue Crack Growth in the Residual Stress Field of a Cold Worked Hole," *Journal of ASTM International*, Vol. 2, No. 5, 2005, p. 31.

30. Kokaly, M.T., Ransom, J.S., Restis, J.H., and Reid, L., "Observations and Analysis of Fatigue Crack Growth From Cold Worked Holes," *In: Proceedings of the 8th Joint FAA/DoD/NASA Aging Aircraft Conference*, Palm Springs, California, 2005.

31. Saunder, T.J. and Grandt, A.F., "The Effect of Edge Distance on Cold Working Fastener Holes," *Proceedings of the Fourth Joint DoD/FAA/NASA Conference on Aging Aircraft*, 2000.

32. Toor, P.M., "Cracks Emanating From Precracked Coldworked Holes," *Engineering Fracture Mechanics*, Vol. 8, No. 2, 1976, pp. 391–395.

33. Wang, Z. and Zhang, X., "Predicting Fatigue Crack Growth Life for Cold-Worked Holes Based on Existing Closed-Form Residual Stress Models," *International Journal of Fatigue*, Vol. 25, 2003, pp. 1285–1291.

34. Hsu, T.M. and McGee, W.M., "Extended Study of Flaw Growth at Fastener Holes," Tech Report AFFDL-TR-77-83: Wright-Patterson Air Force Base, Ohio, 1977.

35. Stefanescu, D., "Measurement and Prediction of Fatigue Crack Growth From Cold Expanded Holes Part 1: The Effect of Fatigue Crack Growth on Cold Expansion Residual Stresses," *Journal of Strain Analysis for Engineering Design*, Vol. 39, No. 1, 2004, pp. 25–40.

36. Gaerke, J., Zhang, X., and Wang, Z., "Life Enhancement of Fatigue-Aged Fastener Holes Using the Cold Expansion Process," *Proceedings of the Institution of Mechanical Engineers, Part G: Journal of Aerospace Engineering*, Vol. 214, No. 5, 2000, pp. 281–293.

37. Hall, L.R., Shah, R.C., and Engstrom, W.L., "Fracture and Fatigue Crack Growth Behavior of Surface Flaws and Flaws Originating at Fastener Holes V1 Results and Discussion," Technical Report AFFDL-TR - Air Force Flight Dynamics Laboratory (United States), 1974.

38. Pasta, S., "Fatigue Crack Propagation From a Cold-Worked Hole," *Engineering Fracture Mechanics*, Vol. 74, No. 9, 2007, pp. 1525–1538.

39. Zhang, Y., Fitzpatrick, M.E., and Edwards, L., "Analysis of the Residual Stress Around a Cold-Expanded Fastener Hole in a Finite Plate," *Strain-International Journal for Experimental Mechanics*, Vol. 41, No. 2, 2005, pp. 59–70.

40. Chandawanich, N., and Sharpe, W.N., Jr., "Experimental Study of Fatigue Crack Initiation and Growth From Coldworked Holes," *Engineering Fracture Mechanics*, Vol. 11, No. 4, 1979, pp. 609–620.

41. de Matos, P.F.P., Moreira, P.M.G.P., Nedbal, I., and de Castro, P.M.S.T., "Reconstitution of Fatigue Crack Growth in Al-Alloy 2024-T3 Open Hole Specimens Using Microfractographic Techniques," *Engineering Fracture Mechanics*, Vol. 72, No. 14, 2005, pp. 2232–2246.

42. Lacarac, V.D., Garcia-Granada, A.A., Smith, D.J., and Pavier, M.J., "Prediction of the Growth Rate for Fatigue Cracks Emanating From Cold Expanded Holes," *International Journal of Fatigue*, Vol. 26, No. 6, 2004, pp. 585–595.

43. Wei, R.P., Wei, W., and Miller, G.A., "Effect of Measurement Precision and Data Processing Procedure on Variability in Fatigue Crack Growth Rate Data," *Journal of Testing and Evaluation*, Vol. 7, 1979.

44. Lacarac, V.D., Smith, D.J., and Pavier, M.J., "The Effect of Cold Expansion on Fatigue Crack Growth From Open Holes at Room and High Temperature," *International Journal of Fatigue*, Vol. 23, 2001, pp. S161–S170.

45. NASGRO Reference Manual (Version 5.0), NASA Johnson Space Center and Southwest Research Institute, 2006.

46. Stefanescu, D., Bouzina, A., Dutta, M., Wang, D.Q., Fitzpatrick, M.E., and Edwards, L., "Comparison of Residual Stress Measurements Using Neutron and X-Ray Diffraction Around Cold Expanded Holes," *Journal of Neutron Research*, Vol. 9, No. 2, 2001, pp. 399–403.

47. Smith, D.J., Poussard, C.G.C., and Pavier, M.J., "Assessment of the Sachs Method for Measuring Residual Stresses in Cold Worked Fastener Holes," *Journal of Strain Analysis for Engineering Design*, Vol. 33, No. 4, 1998, pp. 263–274.

48. Zhang, Y., Fitzpatrick, M.E., and Edwards, L., "Measurement of the Residual Stresses Around a Cold Expanded Hole in an EN8 Steel Plate Using the Contour Method," *Proceedings of the 7th International Conference on Residual Stresses: Materials Science Forum*, 2004, pp. 294–299.

49. Ismonov, S., Daniewicz, S.R., Newman, J.C., Jr., Hill, M.R., and Urban, M.R., "Three Dimensional Finite Element Analysis of a Split-Sleeve Cold Expansion Process, *Journal of Engineering Materials and Technology*, 2009, Vol. 131, No. 3.

50. DoD. MIL-HDBK-5H: "Metallic Materials and Elements for Aerospace Vehicle Structures," 1998, pp. 3–371, 373–376.

51. LaRue, J.E., Masters Thesis, "The Influence of Residual Stress on Fatigue Crack Growth," Department of Mechanical Engineering, Starkville, Mississippi, Mississippi State University, 2005.

52. "E 1012-99, Standard Practice for Verification of Specimen Alignment Under Tensile Loading," *Annual Book of ASTM Standards*, West Conshohocken, Pennsylvania, ASTM International, 2000.

53. "E 467-98a Standard Practice for Verification of Constant Amplitude Dynamic Forces in an Axial Fatigue Testing System," *Annual Book of ASTM Standards*, West Conshohocken, Pennsylvania, ASTM International, 2004.

54. Larsen, J.M., Jira, J.R., and Ravichandran, K.S., "Measurement of Small Cracks by Photomicroscopy: Experiments and Analysis, " In: J.M L, J.E. A, eds., *Small-Crack Test Methods ASTM STP 1149*, Philadelphia, Pennsylvania, American Society for Testing and Materials, 1992, pp. 57–80.

55. De los Rios, E.R., and Brown, M.W., "Microscope Techniques," In: Marsh KJ, Smith RA, Ritchie RO, eds., *Fatigue Crack Measurement: Techniques and Applications: EMAS*, 1991, pp. 289–313.

56. Adobe Photoshop CS3 Extended (version 10.0.1), Adobe Systems Inc, 2007.

57. Donald, J.K. and Ruschau, J., "Direct Current Potential Difference Fatigue Crack Measurement Techniques," In: Marsh KJ, Smith RA, Ritchie RO, eds., *Fatigue Crack Measurement: Techniques and Applications*, 1991, pp. 11–37.

58. Catlin, W.R., Lord, D.C., Prater, T.A., and Coffin, L.F., "Reversing D-C Electrical Potential Method," In: Cullen WH, Landgraf RW, Kaisand LR, Underwood JH, eds. *Automated Test Methods for Fracture and Fatigue Crack Growth ASTM STP 877*, Pittsburgh, Pennsylvania, ASTM, 1985, pp. 67–85.

59. Tupta, M.A., "Alternating and Direct Current Measurement Techniques for Low Power Nanotech and Other Sensitive Devices," Materials Evaluation, Vol. 65, No. 2, 2007, pp. 113–119.

60. Ritchie, R.O. and Bathe, K.J., "On the Calibration of the Electrical Potential Technique for Monitoring Crack Growth Using Finite Element Methods," *International Journal of Fracture*, Vol. 15, No. 1, 1979, pp. 47–55.

61. Wu, X.R. and Carlsson, J.A., "Weight Functions and Stress Intensity Factor Solutions," Oxford: Pergamon Press, 1991, Chapter 14, pp. 264–286.

62. Newman, J.C., Jr., "Analyses of Fatigue-Crack-Growth Databases for Use in Damage-Tolerance Approach for Aircraft Propellers and Rotorcraft," DOT/FAA/AR-07/49, December 2007.

63. Newman, J.C., Jr, Wu, X.R., Venneri, S.L., and Li, C.G., "Small-Crack Effects in High-Strength Aluminum Alloys," a NASA/CAE Cooperative Program: NASA RP-1309. Langley Research Center; 1994, p. 116.

64. Hudson, C.M. and Scardina, J.T., "Effect of Stress Ratio on Fatigue-Crack Growth in 7075-T6 Aluminum-Alloy Sheet," *Engineering Fracture Mechanics*, Vol. 1, No. 3, 1969, pp. 429–446.

65. Wu, X.R., Newman, J.C., Zhao, W., Swain, M.H., Ding, C.F., and Phillips, E.P., "Small Crack Growth and Fatigue Life Predictions for High-Strength Aluminium Alloys: Part I - Experimental and Fracture Mechanics Analysis," *Fatigue and Fracture of Engineering Materials and Structures*, Vol. 21, No. 11, 1998, pp. 1289–1306.

66. Harter, J.A., "AFGROW User's Guide and Technical Manual v 4.0012.15, AFRL-VA-WP-TR-2008," Wright-Patterson Air Force Base, Ohio, 2008.

67. George, K., Reemsnyder, H.S., Donald, J.K., and Bucci, R.J., "Development of a DCPD Calibration for Evaluation of Crack Growth in Corner-Notched, Open Hole Specimens," In: McKeighan PC, Ranganathan N, eds., *Fatigue and Testing and Analysis Under Variable Amplitude Loading Conditions, ASTM 1439*, West Conshohocken, Pennsylvania, American Society for Testing and Materials, 2003, pp. 81–95.

68. Lee, Y-D., McClung, R.C., and Chell, G.G., "An Efficient Stress Intensity Factor Solution Scheme for Corner Cracks at Holes Under Bivariant Stressing, " *Fatigue and Fracture of Engineering Materials and Structures*, Vol. 31, No. 11, 2008, pp. 1004–1016.

69. Newman, J.C., Jr., Johnson, S.W., and Zhao, W.. "Assessment of Residual Streses and Hole Quality on the Fatigue Behavior of Aircraft Structural Joints," DOT/FAA/AR-07/56,V1., 2009.

70. Clark, D.A. and Johnson, W.S., "Temperature Effects on Fatigue Performance of Cold Expanded Holes in 7050-T7451 Aluminum Alloy," *International Journal of Fatigue*, Vol. 25, No. 2, 2003, pp. 159–165.

71. Pell, R.A., Beaver, P.W., Mann, J.Y., and Sparrow, J.G., "Fatigue of Thick-Section Cold-Expanded Holes With and Without Cracks," *Fatigue and Fracture of Engineering Materials and Structures*, Vol. 12, No. 6, 1989, pp. 553–567.

72. MIL-HDBK-5H, "Metallic Materials and Elements for Aerospace Vehicle Structures," US Department of Defense, 1998. pp. 3–371, 373–376.

73. Instruction Manual - "FRACTOMAT and KRAK-GAGE," Eden Prairie, Minnesota, TTI Division, Hartrun Corporation.

74. Newman, J.C., Jr., and Raju, I.S., "Stress Intensity Factor Equations for Cracks in Three Dimensional Finite Bodies Subjected to Tension and Bending Loads," NASA-TP-85793, NASA Langley Research Center, Virginia, 1984.

75. Fawaz, S.A. and Andersson, B., "Accurate Stress Intensity Factor Solutions for Corner Cracks at a Hole," *Engineering Fracture Mechanics*, Vol. 71, Nos. 9–10, 2004, pp. 1235–1254.

76. Newman, J.C., Jr. and Raju, I.S., "Prediction of Fatigue Crack-Growth Patterns and Lives in Three-Dimensional Cracked Bodies," *Proceedings of the Sixth International Conference on Fracture*, New Delhi, India, Pergamon Press, 1984, pp. 1597–1608.

77. Fawaz, S.A., "Stress Intensity Factor Solutions for Part-Elliptical Through Cracks," *Engineering Fracture Mechanics*, Vol. 63, No. 2, 1999, pp. 209–226.

78. Seshadri, B.R., and Newman, J., Jr., "Residual Strength Analyses of Riveted Lap-Splice Joints," Technical Report, NASA/TM-2000-209856, Hampton, Virginia, Langley Research Center, National Aeronautics and Space Administration, 2000.

79. Samavedam, G., Hoadley, D., and Thomson, D., "Full-Scale Testing and Analysis of Curved Aircraft Fuselage Panels," DOT/FAA/CT-93/78, 1992.

80. Vlieger, H. and Ottens, H., "Uniaxial and Biaxial Tests on Riveted Fuselage Lap Joint Specimens," Technical Report DOT/FAA/AR-98/33, Washington, DC, Office of Aviation Research, 1998.

81. Nicoletto, G., "Experimental Characterization of Cracks at Straight Attachment Lugs," *Engineering Fracture Mechanics*, Vol. 5, No. 22, 1985, pp. 829–38.

82. Liu, S.B. and Tan, C.L., "Two-Dimensional Boundary Element Contact Mechanics Analysis of Pin-Loaded Lugs with Single Cracks," *Engineering Fracture Mechanics*, Vol. 48, 1994, pp. 711–725.

83. Brussat, T.R., Kathiresan, K., and Rudd, J., "Damage Tolerance Assessment of Aircraft Attachment Lugs," *Engineering Fracture Mechanics*, Vol. 23, 1986, pp. 1067–1084.

84. Schijve, J. and Hoeymakers, A., "Fatigue Crack Growth in Lugs," *Fatigue of Engineering Materials and Structures*, Vol. 1, 1979, pp. 185–201.

85. Child, D., Moyle, N., and Grandt, A., "Experimental Validation of Stress Intensity Factor Solutions for the Pin Loaded Lug," In: Bos MJ, ed. ICAF 2009, *Bridging the Gap Between Theory and Operational Practice, Proceedings from the 25th ICAF Symposium*, Rotterdam, The Netherlands, 2009, pp. 871–898.

86. Ball, D.L., "The Development of Mode I Linear-Elastic Stress Intensity Factor Solutions for Cracks in Mechanically Fastened Joints," *Engineering Fracture Mechanics*, Vol. 27, 1987, pp. 653–681.

87. Newman, J., Jr., Johnson, S, and Zhao, W., "Assessment of Residual Stresses and Hole Quality on the Fatigue Behavior of Aircraft Structural Joints," Technical Report , U.S. DOT FAA, DOT/FAA/AR-07/56, Washington, DC, Air Traffic Organization Operations Planning Office of Aviation Research and Development, 2009.

88. Harter, J., "AFGROW User's Guide and Technical Manual," AFGROW version 4.0012.15. AFRL-VA-WP-TR-2008, 4.0012.15 ed, Wright-Patterson Air Force Base, Ohio, 2008.

89. "MIL-HDBK-5J: Metallic Materials and Elements for Aerospace Vehicle Structures," US Department of Defense, 2003.

90. "E 399-90 Standard Test Method for Plane-Strain Fracture Toughness of Metallic Materials" (Reapproved 1997), *Annual Book of ASTM Standards*, West Conshohocken, Pennsylvania, ASTM international, 1997.

91. "FlexPDE 5 User Manual," Spokane Valley, Washington, PDE Solutions Inc, 2008.

92. Hicks, M.A. and Pickard, A.C., "A Comparison of Theoretical and Experimental Methods of Calibrating the Electrical Potential Drop Technique for Crack Length Determination," *International Journal of Fracture*, Vol. 20, 1981, pp. 91–101.

93. Newman, J.C., Jr., Wu, X.R., Venneri, S.L., and Li, C.G., "Small-Crack Effects in High-Strength Aluminum Alloys," A NASA/CAE Cooperative Program, NASA RP-1309, Langley Research Center, 1994, p. 116.

94. Zhuang, W. and Molent, L.. "Block-by-Block Approaches for Spectrum Fatigue Crack Growth Prediction," *Engineering Fracture Mechanics*, Vol. 75, 2008, pp. 4933–4947.

95. Sander, M. and Richard, H.A., "Lifetime Predictions for Real Loading Situations-Concepts and Experimental Results of Fatigue Crack Growth," *International Journal of Fatigue*, Vol. 25, 2003, pp. 999–1005.

96. Bao, R. and Zhang, X., "Fatigue Crack Growth Behaviour and Life Prediction for 2324-t39 and 7050-T741 Aluminum Alloys Under Truncated Load Spectra," *International Journal of Fatigue*, Vol. 32, 2010, pp. 1180–1190.

97. Skourpa, M., Machniewicz, T., Schijve, J., and Skorupa, A., "Application of the Strip-Yield Model From the NASGRO Software to Predict Fatigue Crack Growth in Aluminum Alloys Under Constant and Variable Amplitude Loading," *Engineering Fracture Mechanics*, 2007, pp. 291–313.

98. Celik, C.E., Vardar, O., and Kalenderoglu, V., "Comparison of Retardation Behaviour of 2024-T3 and 7075-T6 Al Alloy," *Fatigue and Fracture of Engineering Materials and Structures*, 2004, pp. 713–722.

99. "E 1049-85 Standard Practices for Cycle Counting in Fatigue Analysis," *Annual Book of ASTM Standards*, West Conshohocken, Pennsylvania, ASTM International, 1997.

100. McKeigham, P.C. and McMaster, F.J., "A Framework for a Standardization Effort for Fatigue Crack Growth Testing Under Variable Amplitude Spectrum Loading," *Journal of ASTM International*, Vol. 1, 2004, pp. 36–52.

101. Halfpenny, A., "Methods for Accelerating Dynamic Durability Tests," *9th International Conference on Recent Advances in Structural Dynamics*, Southamption, United Kingdom, 2006.

102. Dowling, N.E., "Mechanical Behavior of Materials," Upper Saddle River, New Jersey, Pearson Prentice Hall, 2007, pp. 577–580.

103. TestStar II, Version 4.0C, MTS, 1997.

104. Gallagher, J.P., "A Generalized Development of Yield Zone Models," AFFDL-TM-FBR-74-28, Air Force Flight Dynamics Laboratory, Wright-Patterson AFB, Ohio, January, 1974.

105. Newman, J., Brot, A., and Matias, C., "Crack-Growth Calculations in 7075-T7351 Aluminum Alloy Under Various Load Spectra Using an Improved Crack-Closure Model," *Engineering Fracture Mechanics*, Vol. 71, 2004, pp. 2347–2363.

106. Urban, M.R., "Analysis of the Fatigue Life of Riveted Sheet Metal Helicopter Airframe Joints," *International Journal of Fatigue*, Vol. 25, 2003, pp. 1013–1026.

107. Newman, J.C., Jr., Harris, C.E., Piascik, R.S., and Dawicke, D.S., "Methodology for Predicting the Onset of Widespread Fatigue Damage in Lap-Splice Joints," Technical Report NASA/TM-1998-208975, Hampton, Virginia, NASA Langley Research Center, 1998.

108. Piascik, R.S. and Willard, Scott A., "The Characteristics of Fatigue Damage in the Fuselage Riveted Lap Splice Joint," Technical Report NASA/TP-97-206257, Hampton, Virginia, National Aeronautics and Space Administration, Lockheed Martin Engineering & Sciences Company, 1997.

109. Harris, C., Piascik, R., and Newman, J., Jr., "A Practical Engineering Approach to Predicting Fatigue Crack Growth in Riveted Lap Joints," Technical Report NASA/TM-2000-210106, Hampton, Virginia, NASA Langley Research Center, 2000.

APPENDIX A—DETERMINATION OF LOADS APPLIED TO THE NESTED-ANGLE COUPON FOR ALIGNMENT AND STATIC AND DYNAMIC CALIBRATION

A.1 Alignment and Calibration for the Nested-Angle Coupon

Alignment of the load frame and static and dynamic calibration for the nested angle was performed using an instrumented coupon. The overall coupon geometry, strain gage locations, and loading fixtures are described in section 7 of this report. The coupon cross section and locations of the strain gages are shown in figure A-1. This two-dimensional view shows the small and large L angle pieces and their position relative to one another. At different positions along the coupon length, the coupon has the small L angle alone (small cross section), the large L angle alone (large cross section), or both sections together (i.e., composite cross section), as shown in figure A-1. Figure A-1 also defines a single set of coordinate axes (X, Y) that are used to locate specific points. For each cross section, loads are defined in terms of the principal axes of the section, which are parallel to the (X, Y) axes, but have their origins at the section centroid. The first step of the static calibration was to develop the equations relating loads at each section (axial force P_Z, and bending moments M_X and M_Y, in the section principal axes) to strains measured on the instrumented coupon. A second step uses the section loads to determine bending stress at the extreme fibers on the cross section where bending stresses are maximized. Normalizing the bending stress at each location by the axial stress allowed adjustment of load frame alignment until the bending stresses were as small as possible. Repeated cycles of coupon installation into the fixture, application of applied load, strain measurement, unloading, and removal of the coupon allowed verification of static alignment and variability of applied loads. Loading the instrumented coupon in fatigue allowed for dynamic calibration and verification of the cyclic stresses achieved during fatigue testing.

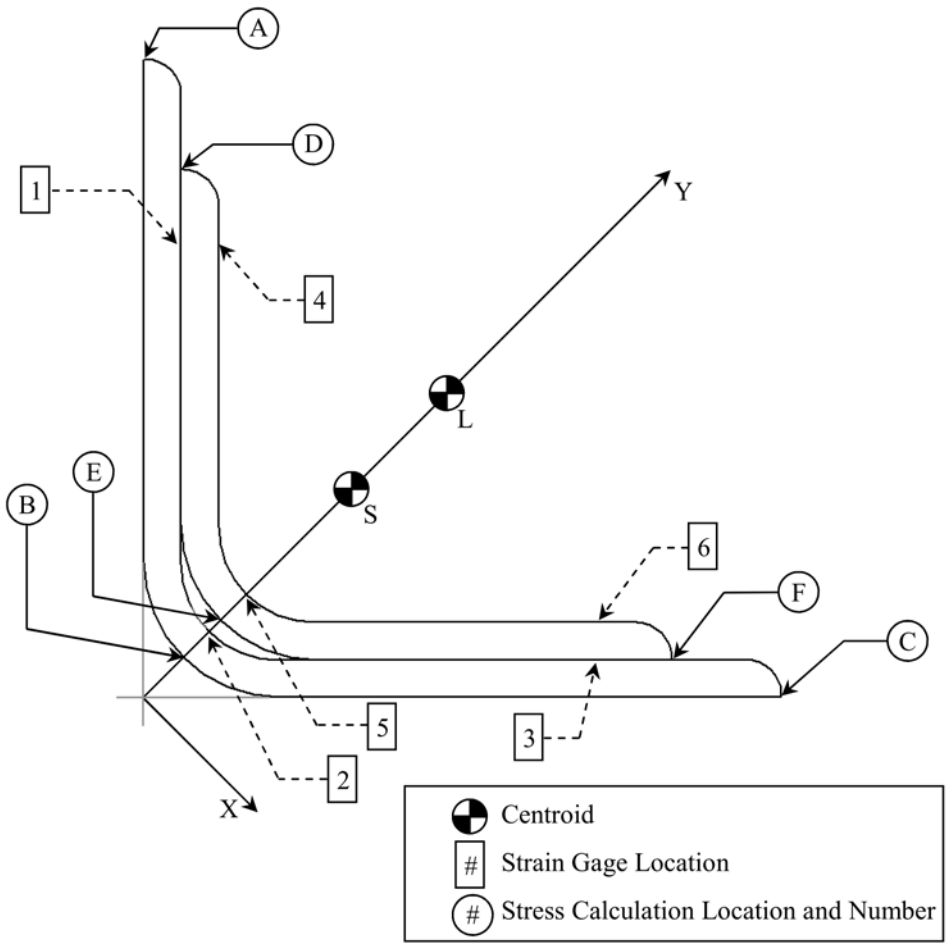

Figure A-1. Cross Section of the Nested-Angle Coupon Showing Locations of Strain Gages and Calculated Bending Stress; L and S Signify Locations of the Large and Small Centroids, Respectively, but the Locations of L and S Are Not to Scale

A.2 Determination of Loads from Strain

Using the coordinates in figure A-1, strains in the large cross section (locations 1–3) can be calculated from the section loads using a strength of materials approach:

$$\begin{Bmatrix} \varepsilon_1 \\ \varepsilon_2 \\ \varepsilon_3 \end{Bmatrix} = \begin{bmatrix} \frac{1}{EA} & \frac{Y_1 - \overline{Y}}{EI_{XX}} & \frac{X_1 - \overline{X}}{EI_{YY}} \\ \frac{1}{EA} & \frac{Y_2 - \overline{Y}}{EI_{XX}} & \frac{X_2 - \overline{X}}{EI_{YY}} \\ \frac{1}{EA} & \frac{Y_3 - \overline{Y}}{EI_{XX}} & \frac{X_3 - \overline{X}}{EI_{YY}} \end{bmatrix} \begin{Bmatrix} P_z \\ M_x \\ M_y \end{Bmatrix} \tag{A-1}$$

where the section properties (A, I_{XX} and I_{YY}), centroidal location ($\overline{X}$, $\overline{Y}$), and strain gage locations (X_i , Y_i) are provided in table A-1 and table A-2. A similar expression can be written for the small cross section, with locations 1, 2, and 3 replaced by locations 4, 5, and 6, and using the cross sectional properties for the small section.

Table A-1. Centroidal Locations and Cross Sectional Properties of Small, Large, and Composite Cross Section

Cross Section	Location of Centroid		Moment of Inertia		Area
	$\bar{X}$ (mm)	$\bar{Y}$ (mm)	I_{XX} (mm^4)	I_{YY} (mm^4)	A (mm^2)
Large	0.0	16.6	11238.2	52028.9	186.5
Small	0.0	16.3	4578.5	22060.3	139.4
Composite	0.0	16.4	15816.8	74089.2	325.2

Table A-2. Location of Strain Gages Used for Coupon Alignment, Figure A-1

Location	X (mm)	Y (mm)
1	-13.5	16.9
2	0.0	6.0
3	13.5	16.9
4	-11.8	18.6
5	0.0	8.7
6	11.8	18.6

In the matrix notation, A-1 is represented by the following:

$$\{\varepsilon\} = [C]\{F\} \tag{A-2}$$

Substituting the values for the section properties (table A-1) and gage locations (table A-2), the matrix $[C]$ for the large section is:

$$[C]_L = \begin{bmatrix} 0.07492 & 0.37058 & -3.59701 \\ 0.07492 & -13.14683 & 0.0000 \\ 0.07492 & 0.37058 & 3.59701 \end{bmatrix} \tag{A-3}$$

where the forces and moments are given in N and N-m, respectively, and strains are in $\mu\varepsilon$ (1 x 10^{-6} m/m). Similarly, for the small section:

$$[C]_S = \begin{bmatrix} 0.10026 & 6.96293 & -7.47008 \\ 0.10026 & -22.43652 & 0.0000 \\ 0.10026 & 6.96293 & 7.47008 \end{bmatrix} \tag{A-4}$$

Inverting equation A-1, the section forces can be calculated from strain. For the large section, this relationship is:

$$\begin{Bmatrix} P_z \\ M_x \\ M_y \end{Bmatrix}_L = \begin{bmatrix} 6.4908 & 0.3659 & 6.4908 \\ 0.0370 & -0.0740 & 0.0370 \\ -0.1390 & 0.0000 & 0.1390 \end{bmatrix} \begin{Bmatrix} \varepsilon_1 \\ \varepsilon_2 \\ \varepsilon_3 \end{Bmatrix} \tag{A-5}$$

where strains are in $\mu\varepsilon$ and section forces are in N and N-m. For the small section, this relationship is:

$$\begin{Bmatrix} P_z \\ M_x \\ M_y \end{Bmatrix}_S = \begin{bmatrix} 3.8059 & 2.3622 & 3.8059 \\ 0.0170 & -0.0340 & 0.0170 \\ -0.0669 & 0.0000 & 0.0669 \end{bmatrix} \begin{Bmatrix} \varepsilon_4 \\ \varepsilon_5 \\ \varepsilon_6 \end{Bmatrix} \tag{A-6}$$

A.3 Determination of Stress at Maximum Fibers

Given the section forces, stress at the extreme fibers of each cross section were calculated using:

$$\sigma(x, y) = \frac{P_z}{A} + \frac{M_x\left(Y - \overline{Y}\right)}{I_{xx}} + \frac{M_y\left(X - \overline{X}\right)}{I_{yy}} \tag{A-7}$$

Stresses at extreme fibers of the large section were calculated at A, B, and C (see figure A-1) using location data in table A-3:

$$\begin{Bmatrix} \sigma_A \\ \sigma_B \\ \sigma_C \end{Bmatrix} = \begin{bmatrix} 0.000505 & 0.002722 & -0.001339 \\ 0.000505 & -0.002768 & 0.000000 \\ 0.000505 & 0.002722 & 0.001339 \end{bmatrix} \begin{Bmatrix} P_Z \\ M_X \\ M_Y \end{Bmatrix} \tag{A-8}$$

For the small section, stresses were calculated at locations D, E, and F:

$$\begin{Bmatrix} \sigma_D \\ \sigma_E \\ \sigma_F \end{Bmatrix} = \begin{bmatrix} 0.000676 & 0.004962 & -0.002441 \\ 0.000676 & -0.005078 & 0.000000 \\ 0.000676 & 0.004962 & 0.002441 \end{bmatrix} \begin{Bmatrix} P_Z \\ M_X \\ M_Y \end{Bmatrix} \tag{A-9}$$

Defining axial stress as:

$$\sigma_{ax} = \frac{P_Z}{A} \tag{A-10}$$

the amount of bending stress normalized by axial stress (% σ_{bend}) was defined at each location. For example, at location A:

$$\%\sigma_{bend,A} = 100\% \frac{\left(\sigma_A - \sigma_{ax}\right)}{\sigma_{ax}} \tag{A-11}$$

Table A-3. Locations Where Bending Stress Is Computed to Evaluate Coupon Alignment, Figure A-1

Location	X (mm)	Y (mm)
A	-29.3	29.3
B	0.0	3.6
C	29.3	29.3
D	-22.4	26.0
E	0.0	6.3
F	22.4	26.0

A.4 Verification of Load Frame Alignment

Load frame concentric and angular alignments were adjusted with the instrumented coupon under load to minimize bending stress. Following alignment, repeated cycles of coupon installation into the fixture, application of static applied load, strain measurement, unloading, and removal of the coupon allowed verification of static alignment. Results of four such cycles are tabulated in table A-4. These results show that the bending stresses were limited to less than 5% of axial stress at the extreme fibers of the coupon. Further evaluation of the data shows that the largest bending stress contributions are from M_X in each section, which arise from the offset of the two sections relative to one another and do not depend on load frame alignment. Bending strains near the fasteners (locations of crack growth) are significantly lower than 5%, as the fasteners are close to the centroidal X-axis of all sections.

Table A-4. Bending Stress, as Percent of Axial Stress, Calculated at Each Coupon Installation Location for Figure A-1

Installation	$\%\sigma_{bend,A}$	$\%\sigma_{bend,B}$	$\%\sigma_{bend,C}$	$\%\sigma_{bend,D}$	$\%\sigma_{bend,E}$	$\%\sigma_{bend,F}$
1	0.66	0.15	-0.94	-0.38	3.78	-7.01
2	6.29	-3.19	-0.03	-1.73	3.34	-4.81
3	3.47	-0.29	-2.89	0.59	3.27	-6.99
4	0.52	-1.84	3.10	-0.38	1.42	-2.40
Average	1.90	-0.54	-0.84	-0.41	2.69	-4.85
Standard Deviation	2.70	1.92	2.33	0.75	0.97	1.92

A.5 Dynamic Calibration

The instrumented coupon was used for dynamic calibration. First, the alignment of the coupon was determined by installing the coupon, applying a static load, and using gages on the small section (4, 5, and 6) to establish the small-section forces. Second, the middle gage (5) was used to provide a dynamic record of axial load on the small section (assuming proportionality of the three section forces as established during the initial static loading). Finally, dynamic axial stress was determined from axial load using equation A-10.